Super-Resolution Spatial, Temporal and Functional Characterisation of Voltage-Gated Calcium Channels Involved in Exocytosis

Katia Hiersemenzel

Degree of Doctor of Philosophy

School of Engineering and Physical Sciences

Heriot Watt University

October 2014

Abstract

The process of information transfer between neurons or endocrine cells is one of the most important, intricate and temporally precise processes in the body. Exocytosis, which is central to the process of excitation-secretion coupling, is triggered by calcium signalling through voltage-gated calcium channels. Super-resolution imaging offers the possibility to fully understand the spatial relationship between the SNARE proteins involved in exocytosis, vesicles and the associated voltage-gated calcium channels.

In this thesis the focus is on exploring the trigger for exocytosis, specifically the spatial and functional role that voltage-gated calcium channels play in this process. Super-resolution imaging techniques have been applied to measure the interaction between $Ca_v2.2$ calcium channels and the syntaxin1a SNARE protein, where binding was found to affect the overall channel distribution. A novel method of caged dye conjugated ω-conotoxin GVIA binding was developed for live cell single molecule imaging of $Ca_v2.2$ calcium channels. An innovative approach to analyse channel functionality and the distribution of calcium events at the plasma membrane was developed to create a temporal-spatial map of calcium activity across the cell. These developments, combined with newly developed techniques in optical patching and simultaneous calcium and vesicle imaging reveal the functional relationship of voltage-gated calcium channel and exocytosis at unprecedented spatial and temporal scales.

Acknowledgment

I would like to express my gratitude first and foremost to my supervisors Prof. Rory Duncan and Dr. Colin Rickman for the opportunity to undertake this PhD project, alongside their expertise, help and guidance throughout. I was fortunate to have the opportunity to collaborate with Dr. Euan Brown on the optical patching work and would like to thank him for the advice and assistance for the experimental work and the many in depth discussions. I would also like to extend my thanks and appreciation to Dr. Paul Dalgarno for the collaboration on the calcium image processing work and the countless scientific discussions and guidance.

Invaluable throughout the time in the lab was the constant support, through advice and assistance, of members of the lab, and in particular I am grateful to Dr. Ali Dun for the technical assistance on the microscope.

A special thank you goes out to my parents Inge and Andreas, my brother Jan and my twin sister Florine for their unwavering support and encouragement throughout. I also would like to thank Oliver for his unfailing support during the four years of this PhD.

ACADEMIC REGISTRY
Research Thesis Submission

Name*:*	Katia Hiersemenzel		
School/PGI:	School of Engineering and Physical Sciences		
Version: *(i.e. First, Resubmission, Final)*	Final	Degree Sought (Award **and** Subject area)	Degree of Doctor of Philosophy In Physics

Declaration

In accordance with the appropriate regulations I hereby submit my thesis and I declare that:

1) the thesis embodies the results of my own work and has been composed by myself
2) where appropriate, I have made acknowledgement of the work of others and have made reference to work carried out in collaboration with other persons
3) the thesis is the correct version of the thesis for submission and is the same version as any electronic versions submitted*.
4) my thesis for the award referred to, deposited in the Heriot-Watt University Library, should be made available for loan or photocopying and be available via the Institutional Repository, subject to such conditions as the Librarian may require
5) I understand that as a student of the University I am required to abide by the Regulations of the University and to conform to its discipline.

* *Please note that it is the responsibility of the candidate to ensure that the correct version of the thesis is submitted.*

Signature of Candidate*:*		Date:	

Submission

Submitted By *(name in capitals):*	Katia Hiersemenzel
Signature of Individual Submitting:	
Date Submitted:	

For Completion in the Student Service Centre (SSC)

Received in the SSC by *(name in capitals):*			
Chapter 1 *ethod of Submission* *(Handed in to SSC; posted through internal/external mail):*			
Chapter 2 *-thesis Submitted (**mandatory for final theses)***			
Signature:		Date:	

Table of Contents

List of Figures

Publication

Hiersemenzel K, Brown ER, Duncan RR (2013) Imaging large cohorts of single ion channels and their activity. Front. Endocrinol. 4:114.

Chapter 1 Introduction

This thesis develops new and novel experimental and analytical techniques to study the spatial configuration and function of voltage-gated calcium channels, particularly for their role in exocytosis. In this introduction a background to the nature of cell communication, membrane biophysics and voltage-gated calcium channels is presented. The established understanding of exocytosis and the role that voltage-gated calcium channels play in that process is also discussed. Finally, the existing and established microscopy methods, including state-of-the-art super-resolution techniques, are discussed, including their application to functional imaging.

1.1 Cellular Secretion of Hormones and Neurotransmitters

The normal functioning nervous system relies on the perfect timing of synaptic neurotransmitter release and detection between neurons. While efficient long distance intercellular communication requires the release of hormones and other molecules into the circulation, it is the concentration and timing of this release, which is critical for normal endocrine function. These processes are collectively known as excitation-secretion coupling and a complete understanding of peptide secretion is central to a step-by-step reconstruction of the entire process. Such detailed information would help to distinguish between normal function and various disease states that impact the excitation-secretion coupling process.

Central to this process is exocytosis, which is the controlled release of molecules from a cell through vesicle fusion. Within the cell, neurotransmitter molecules, polypeptides or other cargo are packaged into membrane-bound vesicles, which locate and dock to the plasma membrane. Triggered by a signal, usually a local increase in calcium concentration through the opening of voltage-gated calcium channels, the vesicular membrane fuses with the plasma membrane through the action of several soluble N-ethylmaleimide-sensitive factor attachment protein receptors (SNARE) proteins pulling the two membranes together. This membrane fusion allows the packaged cargo to diffuse into the extracellular space and act on their target, over either a short distance such as across the synaptic cleft or long range in the case of hormones that are released into the blood stream targeting various receptors throughout the body.

Exocytosis has been a topic of interest for a number of decades since it provides the key information to understanding the many diseases and disorders, of which signalling issues are core, such as diabetes, Alzheimer's and Parkinson's disease.

One major research target associated with exocytosis is calcium signalling. Calcium signalling happens on a time scale of 10s of milliseconds and causing diverse cellular actions, not only triggering exocytosis but also muscle contraction, cell growth and enzyme activity. As calcium ions are small in size they can diffuse rapidly from the extracellular medium through opened calcium channels into the cell and hit their target in a matter of nanoseconds before diffusing into the intracellular space. Put into the perspective of neuronal signalling where timing precision is of vital importance, the release of vesicles can happen within a space of milliseconds. Due to the nature of the rapid voltage-dependent calcium signal the best method with the best temporal resolution to analyse the overall cellular calcium signal is through the means of voltage clamping. However, to single out individual fusion events and understand the spatial relationship between SNARE proteins, vesicles and voltage-gated calcium channels,

super-resolution optical imaging offers the only viable methodology and as such, the possibility of providing insights to further understand the process of exocytosis at the fundamental level.

In this thesis the focus is on dissecting out the trigger for exocytosis, specifically the role of voltage-gated calcium channels in this process. In this work super-resolution imaging techniques will be used to measure the interaction between voltage-gated calcium channels and syntaxin1a, a SNARE protein, to localize single N-type voltage gated calcium channels through ω-conotoxin GVIA binding and to measure and analyse calcium channel openings at plasma membrane level in precise relation to vesicle localisation and fusion.

1.2 Cellular Communication of Excitable Cells

1.2.1 Cellular Secretion

Cytology, the study of cells, is a topic of interest that is so broad and complex that it takes decades to single out and understand the molecular mechanisms of individual cellular functions. One of these complex mechanisms is the intercellular communication through small signalling molecules, which was coined exocytosis. Exocytosis, a word derived from the Greek and English words for 'out', 'cell' and 'receptacle', is defined as the secretion of signalling molecules through the fusion of intracellular, peptide and protein containing vesicles with the extracellular plasma membrane.

The discovery of neurons, their unique architecture and the circuits they form by Caliop Golgi and Santiago Ramon y Cajal led to the question of how one cell signals to another cell. Despite the electrical nature of nervous conduction this was found to be through chemical and not electrical information transfer (Palay & Palade 1955). Early electrical recordings and kinetic analysis of transmitter release revealed the quantal or 'packet-like' nature of chemical transmission of pre-synaptic cells to electrical end-plate currents on post-synaptic cells (Barrett & Stevens, 1972; Fatt & Katz, 1951; Valenstein, 2002). The realisation that this process is applicable not only to neurons but other cell types, such as insulin secreting beta cells in the pancreas, raises fundamental questions, as to which proteins are involved and how these interlink. When linked to importance of cell communication to drive evolution in terms of organism development as a whole, this topic becomes an important field of research (Torday & Rehan 2009). In addition to signalling, this mechanism of membrane fusion is adopted for numerous cellular activities such as replenishing extracellular membrane proteins or cell division. With membrane fusion being at the core of cellular communication, it is vital to understand

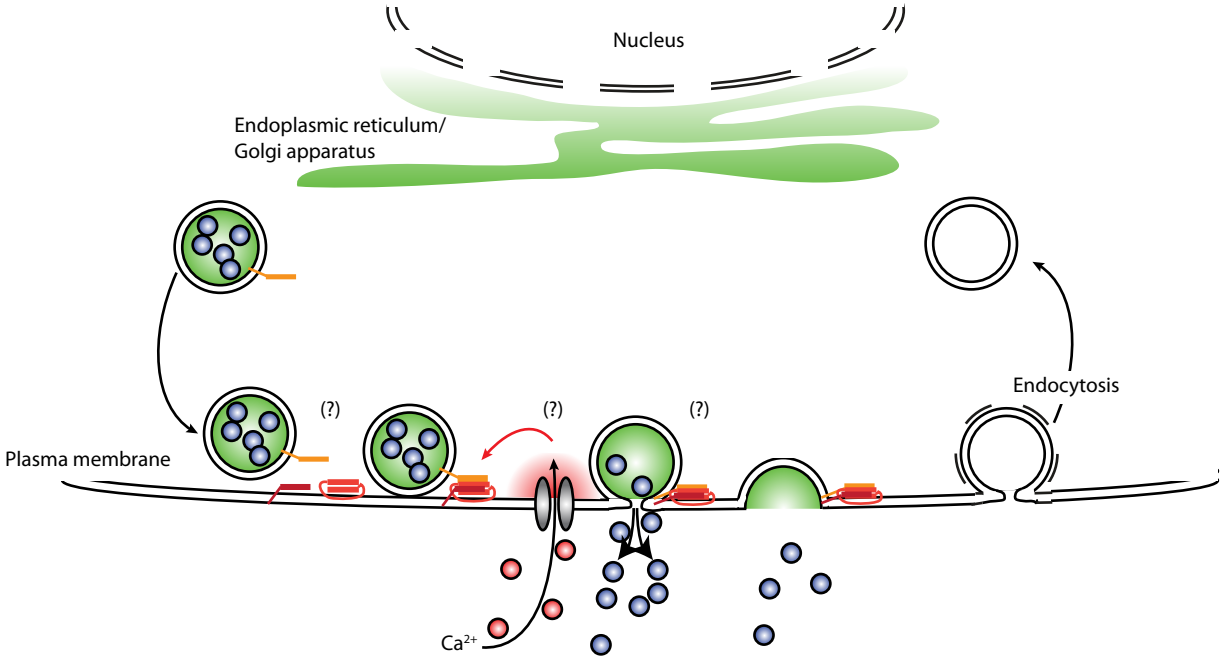

Figure 1.1 **Schematic diagram of regulated exocytosis.** Vesicles (green) filled with secretion peptides (blue dots) translocate from the ER to the plasma membrane where a calcium signal (red dots), triggered by an action potential, elicits the fusion process. The fusion of the vesicle and plasma membranes is mediated through the interaction of three main SNARE proteins, which are the plasma membrane proteins syntaxin1a and SNAP25 (dark red and bright red) and the vesicle membrane protein synaptobrevin (orange). The precise spatial arrangements SNARE proteins to each other and in relation of voltage-gated calcium channels (grey channel) are still unknown. It is also not fully understood where and how active channels are orchestrated in relation to fusion sites. Endocytosis is the process of reforming vesicles from the original fused vesicle membrane in the plasma membrane.

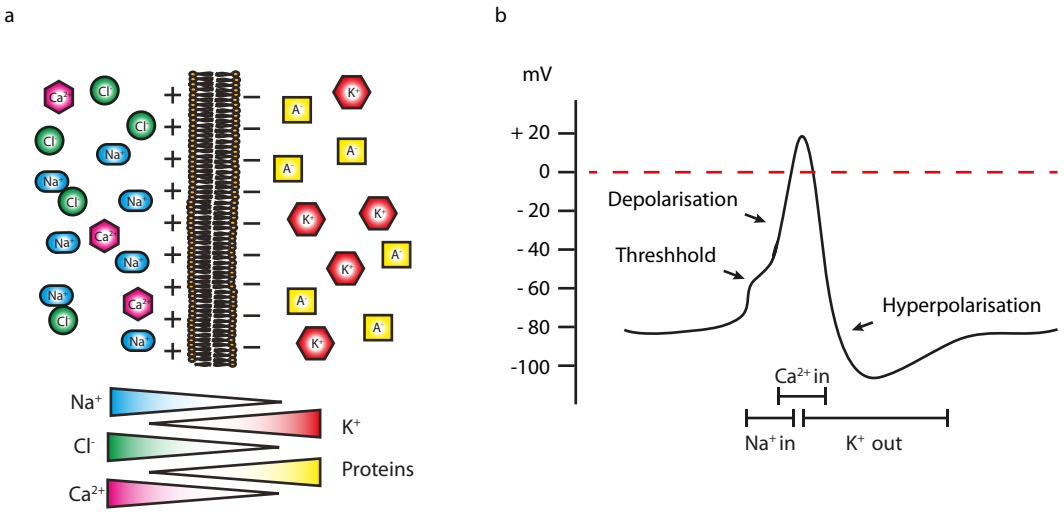

Figure 1.2 **Membrane excitability.** a. The plasma membrane impermeability and ion pumps create ionic concentration gradients and therefore a voltage difference across the membrane. b. The voltage difference is exploited for the excitability of cells, generating action potentials. The depolarisation phase is elicited by the opening of sodium channels until the electrochemical balance is reached, at which point potassium channels open and repolarise the membrane back to the resting potential. Generally, voltage-gated calcium channels have a higher opening probability at depolarised membrane potentials.

excitation were done by Hodgkin and Huxley in 1952, famously using the giant squid axon, and identifying a sodium, potassium and a 'leakage' current. Following on from those experiments many ion channels were identified, initially by electrical and pharmacological characteristics and later through genetic analysis. Now, a library formalised by the International Union of Pharmacology has been created with a systematic approach of numbering taking into account the physiological, pharmacological and genetic characteristics of each channel.

1.2.3 Membrane Potential

The underlying physics of the electrochemical properties of plasma membranes and conductance of voltage-gated channels can be explained by a series of simple equations to illustrate the relationship between current, conductance and voltage described by Ohm's law (equation 1.1). The current (I) is equal to the ratio of the voltage difference (E) to the resistance (R).

$$I = \frac{E}{R} \tag{1.1}$$

The underlying behaviour relies on the fundamental properties of charged particles. As defined by Avogadro's number, one mole contains N = 6.02 x 10^{23} particles, either atoms or molecules. The charge of a single proton is q_e = 1.6 x 10^{-19} C and applied to a mole of monovalent cations the quantity of charge per mole is described by the Faraday constant as F = Nq_e = 6.02 x 10^{23} x 1.6 x 10^{-19} ≈ 10^5 C/mol. For divalent or negatively charged ions, the Faraday constant F is multiplied by the respective ionic charge.

Electrical current, I, measured in Amps (A) is defined as the flow of 1 coulomb per second, which equated to 1 ampere. In a solution of freely moving cations and anions, no electrical current will arise, as there is a net equilibrium of charge distribution throughout the solution. Only with separation through positively and negatively charged electrodes will the ions flow to the oppositely charged electrodes and create an electrical current. The size of the current is determined by the potential difference, the voltage (V), as defined as the energy per unit charge to move a charged particle from one electrode or equivalent to the other electrode in a static electric field, and the electrical resistance between the two electrodes (equation 1.1). The electrical resistance measured in Ohms (Ω) is the difficulty of which the electrons pass through the conductor.

The resistance of a conductor can be measured by the resistivity ρ and shape in terms of area A and length l.

$$R = \frac{\rho l}{A} \tag{1.2}$$

The resistivity for electrolyte solutions can be calculated from known ionic conductors (Robinson and Stockes 1965). By adding of phospholipid bilayers to a solution with a known resistivity of 60 Ωcm, the resistivity increased up to 10^{15} Ωcm, indicating the extremely low conductivity of the bilayer. This simple result leads to the conclusion that the lipid bilayer does not conduct any current and that in fact current flow could only occur through ion channel, which are embedded in it.

As the membrane acts as a separator for internal and external ion solution it can be compared to an electrical capacitor. Capacitance, the ability to store an electric charge, is a measure of how much charge Q needs to be transferred to set up a given potential difference E. This measure is described in Farad (F).

$$C = \frac{Q}{E} \tag{1.3}$$

Re-arranging equation 1.3 for E and differentiating both sides gives Ohm's law for resistance in a capacitor:

$$\frac{dE}{dt} = \frac{I_c}{C} \tag{1.4}$$

From Gauss's law for the electric field within a capacitor, capacitance is given by

$$C = \frac{\varepsilon\varepsilon_0 \mathrm{A}}{d} \tag{1.5}$$

and therefore:

$$\frac{dE}{dt} = \frac{I_c}{C} = -\frac{E}{RC} \tag{1.6}$$

This first order differential equation describes the rate of change of electric potential in a capacitor and can be solved to show an exponential decay of voltage over time.

$$E = E_0 e^{-\frac{t}{RC}} = E_0 e^{-\frac{t}{\tau}} \tag{1.7}$$

RC defines the time constant of the electrical circuit, τ. In an ionic solution, equilibrium is defined as the state at which the tendency to change disappears and there is as much forward flux as there is backwards. For example, if a solution contains a higher concentration of ions on one side compared to the other, the ions will diffuse until uniformly distributed, which is the state of equilibrium. The Boltzmann's equation (1981) describes equilibrium distribution of particles in a force field, by calculating the statistical probability of how much a particle is in state 1 or 2, when the energy difference between them is $u_2 - u_1$. The temperature T is measured in kelvin and k_B is the Boltzmann's constant.

$$\frac{p2}{p1} = e^{-\frac{u_2 - u_1}{k_B T}} \tag{1.8}$$

From Boltzmann's equation, the Nernst equation is derived, taking into account the

charge of the ion particles zF and the intracellular (I_1) and extracellular (I_2) ion concentration.

$$E_{ion} = E_1 - E_2 = \frac{RT}{zF} \ln \frac{[I]_2}{[I]_1} \quad 1.9$$

The Nernst equation, 1.9, describes the voltage difference across the plasma membrane and can be calculated for every ion, together accumulating into the full membrane potential. The above however only consider the potential and concentrations of 1 type of ion alone. If only E_{ion} was taken into consideration, the current would stop once equilibrium has been reached. However, the membrane potential has to be considered as a whole to estimate the current of ions through one type of channel. Hence, the ionic current stands in relation to the net driving force (E - E_{ion}) and conductivity g (the inverse of the resistance, R), in siemens (S), which is a measure of the ease of which electrons pass through the conductor.

$$I_K = g_K(E - E_K) \quad 1.10$$

The analysis of membrane potential, illustrated above, lays the foundation of the field of electrophysiology in exploring cell behaviour from an electrical behaviour in order to reveal single ion currents.

1.2.4 Membrane Biophysics

Early understanding of excitable membranes originated from electrophysiological experiments, using the then technologically advanced setup of inserting one electrode containing glass micropipette into a cell through the penetration of the plasma membrane and having a second reference electrode in the bath. The membrane potential, E_M, is defined as the potential difference between the internal and the external of the cell, with the reference electrode in the bath set at 0 mV. With this innovative setup, voltage and current measurements led to progress in the kinetic description of membrane permeability changes underlying the electrical events of signalling. E_M was found to be slightly more negative than what the calculations for E_K would suggest (Hodgkin and Katz, 1949). This was correctly interpreted to mean that the membrane is permeable not only to K^+ but to other ions at rest (Hodgkin and Katz, 1949; Goldman, 1943).

The two major advances in membrane biophysics were achieved by a British based group (Hodgkin, Huxley and Katz), and an American group (Cole and Curtis). Their work, experimentally proved Bernstein's membrane hypothesis of passive properties along with the concept of propagating action potentials using the squid giant axon as a model.

The squid giant axon served as an excellent model for electrophysiological membrane

measurements (Young 1936). Through electrical stimulation of the axon, action potentials were recorded that were characterised by a supra-threshold depolarisation, followed by a sharp depolarisation beyond 0 mV and finally an exponential repolarisation (Hodgkin and Huxley 1945). The theory of electrical propagation was suggested by Hermann (Hermann 1872; Hermann 1902) who realised that local circuit currents flow in the direction of axon stimulation, but it took until 1937 to verify this theory when Alan Hodgkin published his work showing that the electrical depolarisation spreading ahead of the action potential was enough to stimulate the next section of the nerve fibre (Hodgkin & Huxley, 1939). In 1939 Cole and Curtis answered the question of membrane permeability during excitation with experimental results showing a drop in membrane resistance, but constant membrane capacitance during the action potential (Cole & Curtis 1939). Experiments done by Hodgkin and Huxley in the squid giant axon, before a forced break due to WWII, revealed that during the action potential the membrane potential become transiently positive, up to +45 mV (Hodgkin and Huxley, 1939) and that the potential change was not driven by membrane breakdown. It was only years later that Hodgkin and Katz realised that a reduced extracellular sodium concentration elicited a decrease in the positive potential, that the peak membrane potential change indicated a partial Nernst equilibrium potential for sodium ions (Hodgkin and Katz, 1949). Based on experimental work by Cole in 1949 (Cole 1949), they then went on to fit equations characterising the time course of the potential changes (Hodgkin and Huxley, 1952a; Hodgkin and Huxley, 1952b; Hodgkin and Huxley, 1952c) (Figure 1.2b).

The Nobel Prize award to Hodgkin and Huxley underlined the importance of the understanding of resting membrane potential, current flow and action potentials.

1.2.5 Voltage-Gated Channels

The Hodgkin and Huxley concept of membrane excitability was widely accepted but remained at the point where three different currents were identified as sodium, I_{Na}, potassium, I_K, and 'leakage', $I_{leakage}$, but the mechanisms of the permeability 'changes' were not yet understood. Interdisciplinary approaches were required which encompassed biophysics, pharmacology, protein chemistry and molecular, cellular and genetic biology.

Pharmacological results showed some of the first convincing data that I_{Na} and I_K had separate ionic pathways through the membrane. The addition of tetrodotoxin, a toxin from the puffer fish, abolished the I_{Na} current (Narahashi et al. 1964) as did further experiments with saxitoxin (Nakamura et al. 1965), a toxin produced by marine

dinoflagellates. Both showed a selective, complete and reversible block of the sodium currents. In contrast, tetraethylamonium ion (TEA) injected into the squid giant axon was identified as a selective block of I_K (Armstrong & Binstock 1965; Tasaki & Hagiwara 1957). Nothing however was found to inhibit the leakage current. It was therefore concluded, that there must exist another, separate, ionic pathway.

The terms sodium and potassium "channels" became an accepted terminology and the idea that these channels are voltage-dependent receptors for toxin binding and blocking (Armstrong 1969) was underlined with experimental data showing increased blocking when the membrane was depolarised (Armstrong 1971). Armstrong also managed to deduce that the channels have two distinct parts; a wide mouth, which binds hydrated K^+ or TEA^+ ions, and a narrower part that only accepts fully or partially dehydrated K^+ ions, but not TEA^+ (Armstrong 1971). Modified equilibrium dissociation equations, based on Michaelis-Menten theory of enzyme kinetics (Michaelis & Menten 1913), describing the association and association of toxins to receptor, were established and tested with dose-response experiments at different voltages, from which the receptor density could be estimated (Hille 1968). Through pharmacological and biophysical evidence the ion channel was thought of as being a transmembrane protein with a voltage sensitive region, which allows the channel to pass ions of a certain size through the aqueous filled pore (Hille 1971; Bezanilla & Armstrong 1972).

A more detailed analysis of potassium currents, using different cell types and stimulation patterns, revealed different activation and inactivation kinetics (Giles et al. 1989; Adrian et al. 1970), from which it was deduced that a broad variety of voltage-gated potassium channels must exist and these were later identified (Choe 2002). The same applied to voltage-gated sodium channels, though these were found to be less diverse (Goldin 2001). Another milestone was set when Erwin Neher and Bert Sakmann developed the patch-clamp technique making single channel recording possible (Hamill et al. 1981; Neher & Sakmann 1976). This was backed-up with rapid advances in molecular biology and protein chemistry. Protein purification of single channels revealed subunits as large as 500 kDa and channel encoding DNA sequences were discovered, which revealed a whole family for each ion channel type (Goldin 2001). Then, with the first crystal structure of a K^+ channel subunit obtained by Rob MacKinnon's lab (Doyle et al. 1998), came the important confirmation of the transmembrane pore forming ion channels.

The understanding of the excitability of membranes was enriched greatly by the pharmacological dissection of the overall current of an action potential into sodium and potassium currents. This work proved the ion channel theory before ion channel DNA

analysis, crystal structure acquisition, and single ion channel current recordings further enhanced the understanding. However, it was still unknown how the action potentials drove intercellular signalling as well as cellular secretion.

1.3 Voltage-Gated Calcium Channels

Fatt and Katz discovered by accident during electrical recordings in muscle cells, that some non-propagating action potentials were not elicited by sodium channels (Fatt and Katz, 1953). Follow-up experiments confirmed the above results, explaining it as a 'calcium spike' which they underlined with experimental data showing that higher extracellular concentrations of divalent cations Ca^{2+}, Sr^{2+} and Ba^{2+} increased the rate of rise and the peak of the action potential (Fatt and Ginsborg, 1958). Mg^{2+} and Mn^{2+}, now known to block voltage-gated calcium channels, were found to block the excitability. Later experiments also showed that Ba^{2+} and TEA block K^{+} channels, decreasing the membrane potential and hence increasing the membrane excitability. Internal calcium depletion experiments with the calcium chelator ethylene glycol bis[b-amino-ethylether]-N,N'-tetraacetic acid (EGTA) revealed that the internal calcium concentration had to be below 0.1 μM for an action potential to be produced (Hagiwara and Nakajima, 1966). The calcium hypothesis was confirmed by measurements that proved that the flux of calcium was sufficient to produce an action potential (Hagiwara and Naka, 1964) The overall knowledge of the biophysics of calcium was broadened by the understanding calcium concentrations and flux across the membrane (Figure 1.3).

Further research continued to identify many different classes of voltage-gated calcium channels (Catterall 2000). The accepted theory is now that voltage-gated calcium channels activate through membrane depolarization, whether through an action potential or a sub-threshold depolarization, by a change in molecular confirmation to specifically allow calcium ions through the pore. These channels are located in many different cell types and elicit a number of events, such as contraction, secretion, synaptic transmission and gene expression.

1.3.1 Electrophysiological Properties of VGCCs

Calcium measurements were initially hampered by the fact that the small calcium currents were masked by the much larger potassium currents. Furthermore, there existed the more practical problem that the majority of cells were simply too small for electrophysiological patching experiment. With the invention of the patch-clamp technique (Hamill et al. 1981) combined with selective inhibition of sodium channels through tetrodotoxin (TTX) and potassium channels through Cs^{2+} and TEA, the calcium

current I_{Ca} could be isolated and analysed. The three main initial finding characterising calcium channels in general were, first that the calcium current had slower activation and inactivation kinetics (Kostyuk & Krishtal 1977), second, that the calcium current lasted for the duration on the depolarization (Fenwick et al. 1982) and, thirdly, that the current amplitude was voltage specific, with a depolarisation to +10 mV eliciting the largest current amplitude (Fenwick et al. 1982). In contrast to the low sodium channel depolarisation threshold, the calcium channel currents exposed two thresholds, one at a higher voltage than the other, a characteristic which prompted a division of calcium channels into the high-voltage activated (HVA) calcium channel class and the low-voltage activated (LVA) channel class.

1.3.2 Family of Voltage-Gated Calcium Channels

Voltage-gated calcium channels (VGCC) play a role in many diverse functions, such as muscle contraction and cellular secretion, requiring a broad variety of properties. Initially, VGCCs were grouped into five categories based on pharmacological and electrophysiological properties, known as L-type, N-type, P/Q-type, R-type and T-type channels. Later however, with the analysis of the molecular components, the groups were reconsidered according to the ten different pore-forming α_1 subunit, α_{1A} - α_{1I} (see table 1.1). The L-types were subcategorized to $Ca_v1.1$ through to $Ca_v1.4$, as four molecularly dissimilar α_1 subunits with 75 % homology displaying similar pharmacological and electrophysiological properties. The more neuronal localized types P/Q-, N- and R-types were categorized into Ca_v2, with the ω-agatoxin sensitive P/Q-type channel in $Ca_v2.1$, the ω-conotoxin-GVIA sensitive N-type channel with its α_{1B} subunit in $Ca_v2.2$, and the R-type channel in $Ca_v2.3$. The third group, Ca_v3, encompasses all the T-type channels with the subunits α_{1G} - α_{1I}.

1.3.3 Molecular Structure of Voltage-Gated Calcium Channels

Mammalian voltage-gated Ca^{2+} channels consist of multiple subunits, namely the main α_1, with its secondary subunits $\alpha_2\delta$ (four types), β (four types) and γ (two types) acting as regulatory proteins for the correct PM translocation as well as functional modulation.

The α_1 subunit is the trans-membrane, pore forming and voltage sensitive subunit of 190 kDa in size. The 7000 base pair long cDNA encodes a protein with four equal domain sections (I - IV), each consisting of six trans-membrane helices (S1 - S6). S4 of each domain is the pore lining segment enriched with positively charged amino acids, that can 'sense' a membrane depolarization, change confirmation and thus selectively allow Ca^{2+} ions to pass through the pore (Figure 1.4).

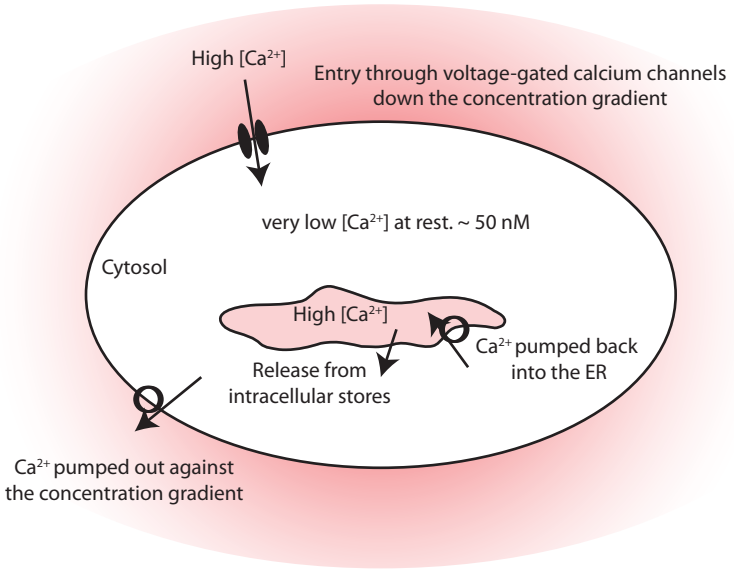

Figure 1.3 **Schematic diagram of Ca^{2+} movement pathways.** The internal cytoplasmic Ca^{2+} concentration is held very low, ~50 nM. Any excess Ca^{2+} is either pumped out against the concentration gradient through plasma membrane pumps, or is stored in intracellular endoplasmic reticulum (ER) compartments. Important for calcium signalling is the rapid external calcium entry through voltage-gated calcium channels down the concentration gradient.

Family of voltage-gated calcium channels

Ca^{2+} channel	Current type	Primary localization	Alpha subunit	Specific blocker	Functions
$Ca_v1.1$	L (Long lasting)	Skeletal muscle	α_{1S}	DHPs	Excitation-contraction coupling Ca^{2+} Homeostasis Gene regulation
$Ca_v1.2$	L (Long lasting)	Cardiac muscle Endocrine cells Neurons	α_{1C}	DHPs	Excitation-contraction coupling Hormone secretion Gene regulation
$Ca_v1.3$	L (Long lasting)	Endocrine cells Neurons	α_{1D}	DHPs	Hormone secretion Gene regulation
$Ca_v1.4$	L (Long lasting)	Retina	α_{1F}	DHPs	Tonic neurotransmitter release
$Ca_v2.1$	P/Q (Purkinje)	Nerve terminals Dendrites	α_{1A}	ω-Agatoxin	Neurotransmitter release Dendritic Ca^{2+} calcium transients
$Ca_v2.2$	N (Neuronal)	Nerve terminals Dendrites	α_{1B}	ω-Conotoxin-GVIA	Neurotransmitter release Dendritic Ca^{2+} calcium transients
$Ca_v2.3$	R (Residual)	Cell bodies Dendrites Nerve terminals	α_{1E}	-	Neurotransmitter release
$Ca_v3.1$	T (Transient)	Cardiac muscle Skeletal muscle Neurons	α_{1G}	-	Repetitive firing
$Ca_v3.2$	T (Transient)	Cardiac muscle Neurons	α_{1H}	-	Repetitive firing
$Ca_v3.3$	T (Transient)	Neurons	α_{1I}	-	Repetitive firing

Adapted from Catterall 2000. DHP – Dihydropyridine

One main function of the cytosolic β subunit, 55 kDa in size, is binding to the α_1 subunit hiding the ER retention signal and increasing the expression level of the channel. The presence of the β and $\alpha_2\delta$ subunits shifts the voltage dependence to a more negative membrane potential and changes the kinetics of gating, usually increasing the rate of inactivation of the channel. The large 170 kDa $\alpha_2\delta$ auxiliary subunits linked by two disulphide bonds also ensures the correct trafficking and targeting of the α_1 subunit to the PM. The γ subunit is another transmembrane modulatory protein that completes some of the Ca_v channel assemblies.

1.4 Exocytosis

1.4.1 Constitutive Exocytosis

Constitutive exocytosis, as the name implies, is fundamental to basic cellular activity, as it replaces old plasma membrane proteins with freshly synthesized ones. Newly synthesized membrane proteins are transported from the endoplasmic reticulum (ER) via the Golgi apparatus in vesicle membranes. With the fusion of vesicles with the plasma membrane the new proteins are now fully integrated into the plasma membrane. These basic functions occur constantly and do not need a precise triggering system.

1.4.2 Regulated Exocytosis

Exocytosis as part of cell communication, unlike constitutive exocytosis, has to be tightly regulated by the cell. Only incoming signals can trigger the fusion of vesicles with the plasma membrane (Figure 1.1). Precision is key for this fast communication pathway, and it is the drive to understand this precision, and specifically the details of the temporal and spatial calcium signal that form the motivation for this thesis.

Secretory proteins and peptides such as neurotransmitter and hormones are generally synthesized in the ER and sorted in the Golgi apparatus (Farquhar & Palade 1981; Dalton & Felix 1956). Through the action of ADP-ribosylation factor 1 (ARF1) biogenesis of secretory vesicles budding from the trans-Golgi network (TGN) is increased, from where the vesicles are transported and targeted to the plasma membrane (Barr & Huttner 1996). Prior to fusion, secretory vesicles are docked at the plasma membrane through protein-protein interaction between vesicular and plasma membrane proteins identified and classified under soluble NSF-attachment protein receptor (SNARE) proteins (Ferro-Novick & Jahn 1994; Rothman 1994). The plasma membrane bound target (t)-SNAREs, and the vesicle bound vesicle (v)-SNAREs bind to each other with high affinity at conserved alpha helical coiled protein structures (Jahn & Scheller 2006; Hayashi et al. 1994). The vesicles are then primed through MgATP hydrolysis which allows rapid fusion within tens of milliseconds upon stimulation, rather than previously unprimed vesicles that take tens of seconds to fuse (Parsons et al. 1995; Jahn et al. 2003). The fusion signal is identified as a marked increase in intracellular calcium concentration (Schneggenburger & Neher 2000), which is 'sensed' by a calcium sensitive protein called synaptotagmin (Dunn & Holz 1983; Borst & Sakmann 1996; Fernandez-Chacon et al. 2001). Through protein-protein interaction the trigger signal is relayed on to the SNARE proteins, which pull together the two bi-lipid membranes and create a fusion pore through which the neurotransmitter peptides or

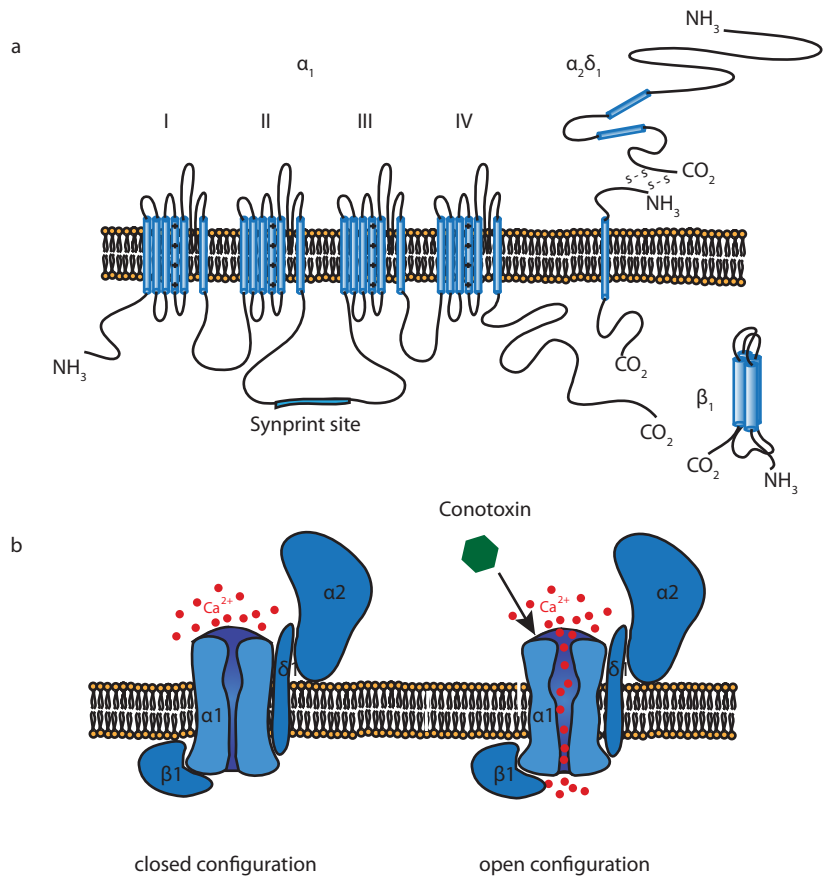

Figure 1.4 **Schematic diagram of the $Ca_v2.2$ calcium channel structure.** a. The α_{1B} subunit of the $Ca_v2.2$ calcium channels is arranged in 4 domains each consisting of 6 transmembrane helices. The synprint site is located on the large intracellular loop between domain II and III. The β subunit is associated with the α_{1B} subunit on the intracellular leaf of the membrane, whereas the $\alpha_2\delta_1$ subunits are a transmembrane protein and an extracellular protein, which associate through two di-sulphide bonds. b. The 4th helix of each domain lines the pore and is voltage-sensitive, causing a conformational change and allowing Ca^{2+} ions to pass through. This is inhibited by ω-conotoxin GVIA, which binds at the extracellular mouth of the channel.

hormones can diffuse into the extracellular space (Cohen et al. 1980; Söllner et al. 1993; Steyer et al. 1997). The majority of experiments trying to elucidate the full mechanism of exocytosis were done either by electron microscopy, various biochemical approaches or patch clamp and patch amperometry measurements (Albillos et al. 1997). Theses techniques reveal a wealth of information about exocytosis in terms of protein-protein interaction and temporal information but lack spatial analysis. Advanced super-resolution imaging has filled this void and has already proven to enhance research in this field (Rickman et al. 2007; Rickman et al. 2010).

1.4.3 SNARE Proteins

The fusion of the secretory vesicles with the plasma membrane relies upon the interaction of a family of proteins, which have been identified and named soluble N-ethylmaleimide sensitive factor attachment protein receptors (SNARE) proteins (Söllner et al. 1993) as well as soluble NSF attachment proteins (SNAP) proteins, or the equivalent Sec1/Munc18-like (SM) proteins, which have a modulatory effect on SNARE proteins for regulation of exocytosis (Sudhof & Rothman 2009). Ca^{2+} stimulation through the ionic binding to a Ca^{2+} sensitive SNARE protein causes these protein complexes to change conformation, and through the hydrolysis of ATP can release the energy required to fuse the two membranes together.

The cytosolic protein N-ethylmaleimide sensitive factor (NSF) was identified to be involved and essential in intracellular fusion processes (Block et al. 1988), as a block of these proteins caused an accumulation of vesicles unable to fuse as well as hindered the fusion required for the ER to Golgi pathway (Söllner et al. 1993). The NSF proteins were found to require additional soluble proteins as well as integral membrane receptors for fusion (Weidman et al. 1989). The soluble proteins were purified and identified as α-SNAP, β-SNAP, and γ-SNAP proteins (Clary & Rothman, 1990), which enabled NSF binding to the Golgi membrane (Clary, Griff, & Rothman, 1990). Integral membrane receptors were first discovered in vesicle membranes, synaptophysin, which is embedded into the vesicle membrane, synapsin, which is associated with the vesicle membrane, and vesicle-associated membrane protein (VAMP), with one transmembrane domain and a proline-rich N-terminus extending into the cytoplasm (Trimble & Scheller 1988). VAMP was found through screening an expression library from the electric lobe of *Torpedo* with an antibody against purified vesicles (Trimble & Scheller 1988) and this protein was later found to be an essential SNARE protein for regulated exocytosis. Through mRNA analysis, a 25 kDa protein was discovered to be enriched in neurons, and located within the presynaptic terminals (Oyler et al. 1989).

This synaptosome-associated protein 25 (SNAP25) was thought to be a SNARE protein associated with the plasma membrane. Experimental results indicated an attachment to membranes (Oyler et al. 1989), even though the polypeptide sequence implied a lack of hydrophobic amino acids required for a transmembrane domain (Eisenberg 1984), suggesting that the SNAP25 attaches through palmitoylation, a linkage through thioester bonds of palmitic acid (Oyler et al. 1989). Through immunoprecipitation, another SNARE protein subset, syntaxin1a and syntaxin1b, was found to bind to a known vesicle-bound synaptic protein p65 [synaptotagmin] (Bennett, Calakos, & Scheller, 1992). It was postulated that vesicles dock at the plasma membrane through the main interaction of a vesicle bound, and a plasma membrane bound SNARE protein, with NSF and SNAP/SM proteins facilitating the interaction (Söllner et al. 1993). Further experiments showed that VAMP, SNAP25 and syntaxin1a associate into weak binary as well as strong ternary complexes, which was revealed by the common feature of proteolyzation of all three SNAREs by clostridial neurotoxins only when the proteins are unbound and not in the intermolecular interaction in a coiled-coil structure (Hayashi et al. 1994). When not assembled, these proteins, especially SNAP25 and synaptobrevin, are in relatively unstructured conformation, but when they interact, in a 1:1:1 manner, they form helical sections, which align along the length of each other (Fasshauer, Otto, Eliason, Jahn, & Bru, 1997; Sutton, Fasshauer, Jahn, & Brunger, 1998). These helices, conserved SNARE motifs, are homologous heptad repeats of 60 - 70 residues located near the membrane anchoring point (Fasshauer, Otto, et al. 1997; Fasshauer et al. 2002; McNew 2008; Stein et al. 2009). SNAP25 and syntaxin1a, located on the plasma membrane, form a complex, increasing the α-helicity of each molecule. Syntaxin1a binds with one α-helix and SNAP25 binds first with one, and then with a second α-helix that gains structure as the first binding happens (Fasshauer, Bruns, et al. 1997). In the docking process of the vesicle, VAMP [synaptobrevin] binds last, forming a four helical structure, which align in a parallel fashion, creating a bundle of about 12nm in length (Sutton et al., 1998). This protein complex is modulated by the NSF and SM/SNAP proteins and with the hydrolysis of ATP (Söllner et al., 1993) the SNARE complex overcomes the energy barrier for membrane fusion (McNew, 2008).

The fusion process, however, needs to be controlled and regulated. With the depolarization of the plasma membrane eliciting the opening of voltage gated calcium channels, the resulting Ca^{2+} ion influx is 'sensed' by a calcium ion sensor discovered to be synaptotagmin (Matthew et al. 1981; Fernandez-Chacon et al. 2001) and which highly conserved structure (Perin et al. 1991) has been determined to contain two calcium binding C_2 sites (Fernandez-Chacon et al., 2001; Rizo & Sudhof, 1998; Sutton,

Davletov, Berghuis, Südhof, & Sprang, 1995). Synaptotagmin interacts with the SNARE complex in a Ca^{2+}-independent manner where the protein is essential in the docking of the vesicle (Rickman et al. 2004) and in a Ca^{2+}-dependent manner where synaptotagmin relayes the calcium trigger on to the SNARE proteins for fusion.

Through protein assays the fusion essential SNARE proteins syntaxin 1, SNAP25 and Synaptobrevin were discovered and their molecular interaction revealed. However, this revealed no information on the spatial structuring of these events. Such a spatial analysis of the exocytotic components, including vesicles, SNARE proteins and voltage-gated calcium channels was later addressed through modern fluorescence microscopy.

1.4.4 The $Ca_v2.2$ Channel and the Synaptic Protein Interaction Site (Synprint)

With the involvement of multiple proteins, these have to be precisely orchestrated for fast and efficient secretion. It is therefore hypothesised that some of the proteins physically interact to be spatially connected. Vesicles first dock to the plasma membrane through SNARE proteins (Wit et al. 2006), then bind into a helical complex before the interaction of synaptotagmin with syntaxin1a as well. It is left to assume, that VGCCs ought to be close to the site of fusion and that there could be an interaction between SNARE proteins and VGCCs. In fact, the first evidence for this was when the purification of syntaxin1a showed a binding to $Ca_V2.2$ channels (Bennett et al., 1992b).

A unique site on the $Ca_v2.2$ calcium channel, which now has been termed the synaptic protein interaction (synprint) site, is shown, through protein assays, to interact with syntaxin1a (Bezprozvanny et al. 2000). First found by Catterall's group (Sheng et al. 1994), this synprint site is located in the II - III domain linker region of the calcium channel (Figure 1.4), where syntaxin1a can interact and regulate the channel activity (Bezprozvanny et al. 2000). The synprint site seems to be unique to mammals. It has been shown that invertebrates lack the synprint site and instead rely on the proteins Mint1 and CASK to perform the equivalent task (Spafford et al. 2003). The roles of different regions of the α_1 subunit of the $Ca_v2.2$ channel have been successfully characterized in experiments that delete different exons of the gene (Lin et al. 1997; Pan & Lipscombe 2000). These alternative splicing experiments can be very useful in further experiments as comparisons can be made between full functional channels and channels that have the exon of the synprint site deleted.

The $Ca_v2.2$ channel has a pore forming α_1 subunit and three G proteins $\alpha_2\delta$, β and γ, which are able to regulate calcium passage through the channel. It was demonstrated that syntaxin1a and the G proteins compete for the same site on the channel, which results in reduced open probability, indicating that syntaxin1a may be a regulator of the

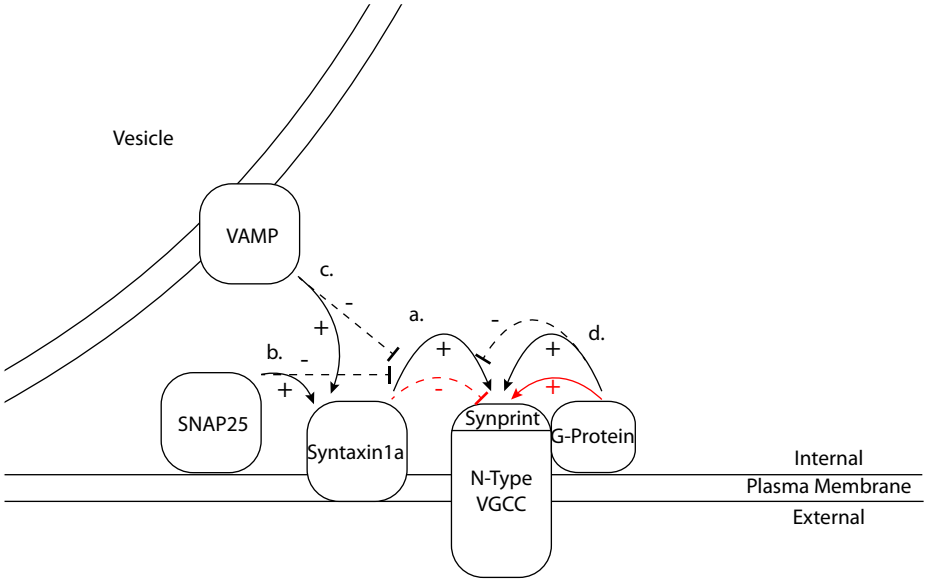

Figure 1.5 **Protein interaction and modulation of SNARE complex and $Ca_v2.2$ calcium channels.** Black arrows and dashed lines indicate either physical interaction or inhibition respectively. Red arrows and dashed lines indicate positive and negative modulation of the protein a. Syntaxin1a has a high affinity for the synprint site on the $Ca_v2.2$ (N-type) voltage-gated calcium channels but has a negative modulatory effect, lowering the opening probability of the channel. b. SNAP25 competes for syntaxin1a negatively influencing the binding of syntaxin1a to the synprint site. c. VAMP also competes for syntaxin1a and similarly negatively decreases the binding of syntaxin1a to the synprint site. d. The G-proteins of the $Ca_v2.2$ calcium channel bind to the synprint site and hence may displace syntaxin1a. The G-proteins have a positive modulatory effect on the calcium channel, increasing the opening probability.

$Ca_v2.2$ channel (Jarvis et al. 2002; Stanley & Mirotznik 1997). Two sites of interaction have been identified. One is the anchoring of syntaxin1a to the α_1 subunit and the second is a modulatory interaction, as mentioned above, which is mediated from a site located on the H3 domain of the syntaxin1a protein (Bezprozvanny et al. 2000) (Figure 1.5). In contrast to previous findings, however, it has recently been suggested that the synprint site on the calcium channel is also involved in endocytosis (Watanabe et al. 2010). This hypothesis relies on the finding that the synprint fragment blocks the interaction between synaptotagmin 1 and AP-2 (activating protein 2) (Chapman et al. 1998) and that synaptotagmin is also prominent in endocytosis. Blocking the endocytotic pathway would ultimately stop neurotransmission as the pool of vesicles becomes depleted.

Part of this thesis concentrates on the interaction of calcium channels and syntaxin1a via its synprint site, which is assumed to be an essential feature of exocytosis.

1.5 Microscopy as a Means to Understand Biological Processes

Exocytosis is a process that happens on a millisecond and nanometre scale; too fast and small for any standard microscope to directly capture the actual fusion event. However, advances in biological approaches and electrophysiology have combined with a revolution in modern microscopy techniques to provide increasingly improving high-resolution, high speed imaging. The first of these has been in the development of a pallet of fluorescent proteins (FP); each with different excitation and emission wavelengths (Shaner et al. 2007), in order to allow for diverse labelling and imaging strategies.

Secondly, the fundamental resolution limit in microscopy, the diffraction limitation, has been circumvented through a variety of advanced super resolution techniques. Conventional microscopy techniques are dominated by the diffraction limit, around 200 nm for visible light and standard microscopy optics. Proteins range from 1 – 100 nm in size and when imaging a spot of 200 nm it cannot be distinguished whether there is only one protein or several. Widefield techniques such as PALM and STORM bypass this limit through the localisation of single molecules. Confocal techniques such as STED, FLIM and FCS offer alternative approaches to explore the sub diffraction limited world (Figure 1.6). Each of these methods comes with their own advantages and disadvantages, and selection depends on the biological problem being investigated. In this thesis confocal imaging, spectral imaging and FLIM is used to quantify the association between $Ca_v2.2$ and syntaxin1a, ω-conotoxin GVIA staining of $Ca_v2.2$

channels is imaged using the PALM technique and calcium imaging is done in TIRF exploiting the properties of the sCMOS camera for fast image acquisition.

1.5.1 Fluorescent Proteins, Dyes and Energy States

Fluorescent proteins are barrel-like structured, naturally occurring proteins with the unique protein property of optical fluorescence, the ability to absorb high energy light and emit photons of lower energy. Since the discovery of these proteins in the Aequorea Victoria jellyfish, for which Martin Chalfie, Osamu Shimomura, and Roger Tsien were awarded the chemistry Nobel prize in 2008, extensive work on the molecular modification of the structure has created a huge variety of FPs in terms of absorption and emission range, with constantly improving quantum yields and performance (Tsien 1998). Not only have standard FPs been created and improved but also new proteins with niche properties, such as photoactivatable (PA) FPs have been developed, allowing unique applications in advanced microscopy systems for single molecule localization microscopy (Shaner et al. 2007). Both fluorescent proteins and conventional fluorescent dyes have an abundance of applications. To name a few examples, these small molecules can be used for immunostaining, where a dye is conjugated to the secondary antibody, or as an indicator such as calcium indicators, where the change in conformation upon calcium binding restores the fluorescence property of the dye (Cobbold & Rink 1987).

The Jablonski diagram is an energy diagram describing the photon absorption and emission by FPs and dyes (Figure 1.7). FPs and dyes absorb a high energy photon, shifting the energy state from ground state S_0 to an excited high-energy state, either S_2 or S_1 . Vibrational relaxation of electrons and internal conversion from S_2 to S_1 reduces the energy to the lowest S_1 energy state from where it releases its energy radiatively through the emission of a lower energy photon, fluorescence, to return back to the ground state S_0. This process typically takes of the orders of a few nanoseconds, the so called fluorescence lifetime. Before S_1 to S_0 radiative relaxation intersystem crossing from the singlet excited state to the triplet excited state T_1 , can occur. Due to the spin blocking and optical selection rules, the excited electrons spend an extended period of time in T_1 until the alignment of spins allows an emission of a single photon, called phosphorescence, for the FP or dye to return to the ground state S_0 .

1.5.2 Optical Resolution

To understand why super-resolution techniques such as PALM and STORM have been developed, prior understanding as to why and how the resolution is limited by the optics is essential. To be able to adequately image and sample very small specimens

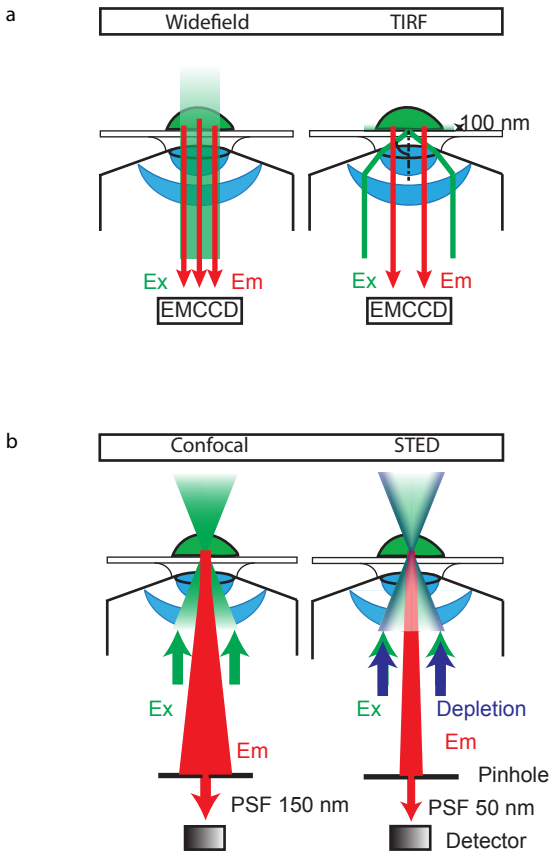

Figure 1.6 **Schematic of widefield and confocal microscopy systems.** a. On a widefield microscope the specimen is illuminated directly from below, through the inverted objective with a beam largely passing through the specimen and the emitted light is detected on an EMCCD or sCMOS camera. In TIRFM mode, the excitation beam is angled so that the light is reflected off the glass surface of the cover slip, creating an evanescence wave that penerates only a few 10's nm into the sample. b. In a confocal microscope a pinhole is used to remove the out of focus light from the collection area, and the specimen is scanned in x-y-z dimensions. A special application of confocal is the simulated emission depletion (STED) configuration, which uses a donut shaped depletion laser to reduce the PSF to about 50 nm diameter.

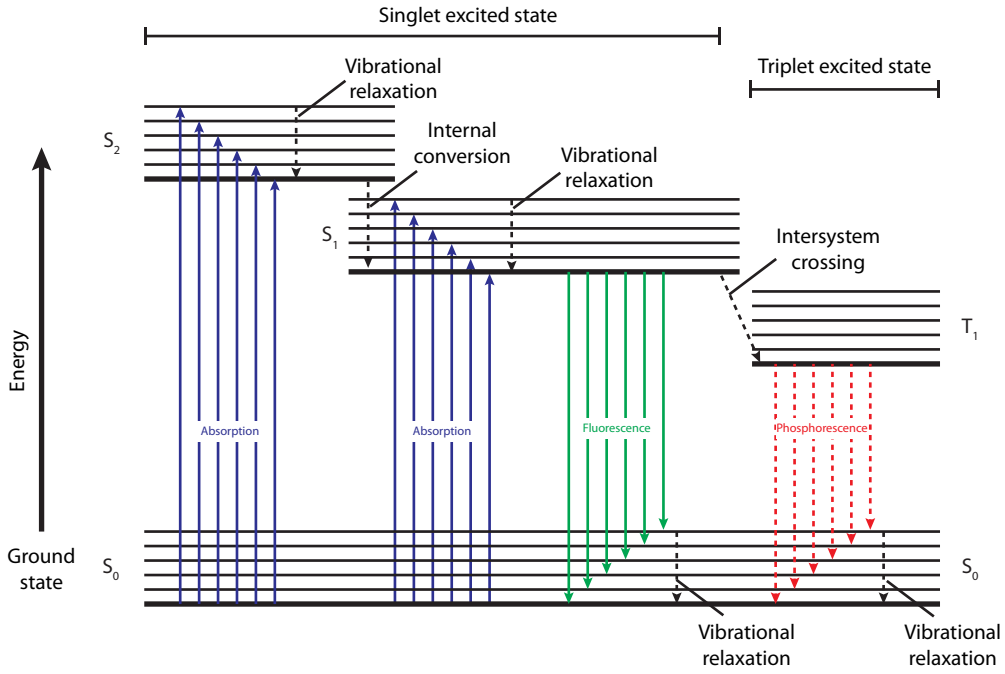

Figure 1.7 **Jablonski diagram.** The Jablonski diagram is a schematic representation of the energy diagram describing the photon absorption and emission by FPs and dyes. Energy absorption, through an incident photon, moves the electron configuration of the FP of dye into an excited state, where vibrational relaxation decreases the energy to the lowest excited energy level. Direct relaxation to the ground state, fluorescence, or multi level relaxation via triplet states, phosphorescence, returns the dye to the ground level energy state via the release of a lower energy photon.

like single cells, first of all the objectives, which have a very complex design containing multiple optical components, must have a very high magnification, typically 60x, 100x or 150x. However, irrespective of the magnification, the maximum resolution (R) is defined only by the smallest distance at which two points can be differentiated, which is defined by the wavelength (λ) and the numerical aperture of the lens (NA): $R = \lambda/2NA$. To achieve the maximum resolution it is important to have an objective with the highest NA possible. The numerical aperture can be thought of as the maximum cone of light gathered by the objective lens and is defined by the focussing power of the lens ($\sin \mu$) and the medium (n) between the front lens and the specimen, such that: $NA = n(\sin \mu)$, where μ is the angle between the focussing cone and the optical axis. The mathematical maximum NA of a lens in air is given by $\mu = 90°$, or 1 but in practice this is impossible and typical lenses have maximum values of around 0.91. To attain a higher NA, immersion oil with a refractive index of 1.51, which is very similar refractive index of the glass coverslip, gives the highest possible NA. A typical oil immersion objective has an effective NA of 1.4 – 1.45. The resolution is also defined by the wavelength, by which a shorter wavelength will create a smaller resolution. Therefore, the green FP EGFP with an emission at 507 nm will have a marginally better resolution than the red FP mCherry with the emission at 610 nm. The effect of diffraction is that, for example, when imaging a point source such as a 40 nm bead the resulting bead image on the camera will always have a larger diameter of around 200 nm. The resulting diffraction pattern will show an Airy disc, a ring pattern of light and dark ring intensities that are formed by the minuscule scattering of the light coming from the focal plane back through the specimen and due to the circular back aperture of the objective. Every single imaged spot on the EMCCD or sCMOS camera has the diameter of an Airy disc. (Figure 1.8) However, the higher the NA of an objective, the smaller the Airy discs and the better the resolution. Therefore, as mentioned previously, it is important to use an objective with a high NA to capture the best high-resolution images possible.

1.5.3 The Widefield Microscope

In cell biology the widefield microscope is commonly used for imaging the plasma membrane, capturing relatively fast events, or doing single molecule localization microscopy (SMLM). The widefield microscopes defining feature is that it uses a two dimensional array detector, a CCD or CMOS camera, to acquire a spatial image of a magnified, uniformly illuminated, field of view in a single acquisition frame (Figure 1.9). Providing sample brightness is adequate, imaging speed is therefore limited only by camera frame rate.

For biological purpose, cells are plated onto a glass coverslip and are illuminated with a selected laser or lamp through the objective. The scattered emission is collected back through the objective, with suitable optical filtering to isolate fluorescence from excitation light, and is captured on a widefield camera, typically an EMCCD or sCMOS. The advantage of the widefield system is the speed of acquisition which, when using an EMCCD camera, can be as fast as 40 ms per frame, but can be even up to 10 ms with newly developed high-speed cameras, such as the scientific complementary metal-oxide-semiconductor (sCMOS) camera.

1.5.4 High Speed Cameras

For widefield imaging a two dimensional imaging array is necessary for a snap shot image acquisition with the desired properties being excellent quantum efficiency (QE) for high photon sensitivity, low signal-to-noise ratio (SNR), and a high acquisition rate.

One of the cameras used for widefield imaging was the charge-coupled device (CCD) camera. The CCD was invented for the purpose of information storage in the early days of computer technology, but since has been developed for image acquisition and pixel-by-pixel information transfer. The CCD camera has an image registration section where photons collected from the sample hit the pixel array. These are typically between 512x512 to 1024x1024 pixels with each pixel being 5 - 16 μm in size, depending on the camera. Every photon detected on the high QE sensor is transferred into an electron signal. The image is shifted to the store section from where it is read out in the readout register pixel by pixel through an on-chip charge to voltage conversion before the analogue to digital conversion allows the information to be stored as an image file. The downfall of the CCD cameras is the high readout noise, which dominates when imaging at fast speeds due to the decreased photon numbers per imaging frame, especially when imaging faint samples where every photon matters.

In the electron multiplying charge-coupled device (EMCCD) (Figure 1.10a) an extra step is built in before the readout register, the gain register. The gain register is the electron multiplying step in which the electrons pass through a succession of multiplication stages. Each stage consists of four phases, R1, Rdc, R2 and R3. The voltage is clocked for phase R1, R2 and R3, but constant for Rdc. Through the clocked changes of voltage the electrons are shifted from one phase to the next. A big voltage step, controlled through the EM gain in the Olympus software, which controls the camera, occurs between Rdc and R2, where collision between electrons going through the large voltage field can generate new electrons, a process called ‘impact ionization’, and hence electron multiplication. Temperature has an influence on the impact ionization, with colder

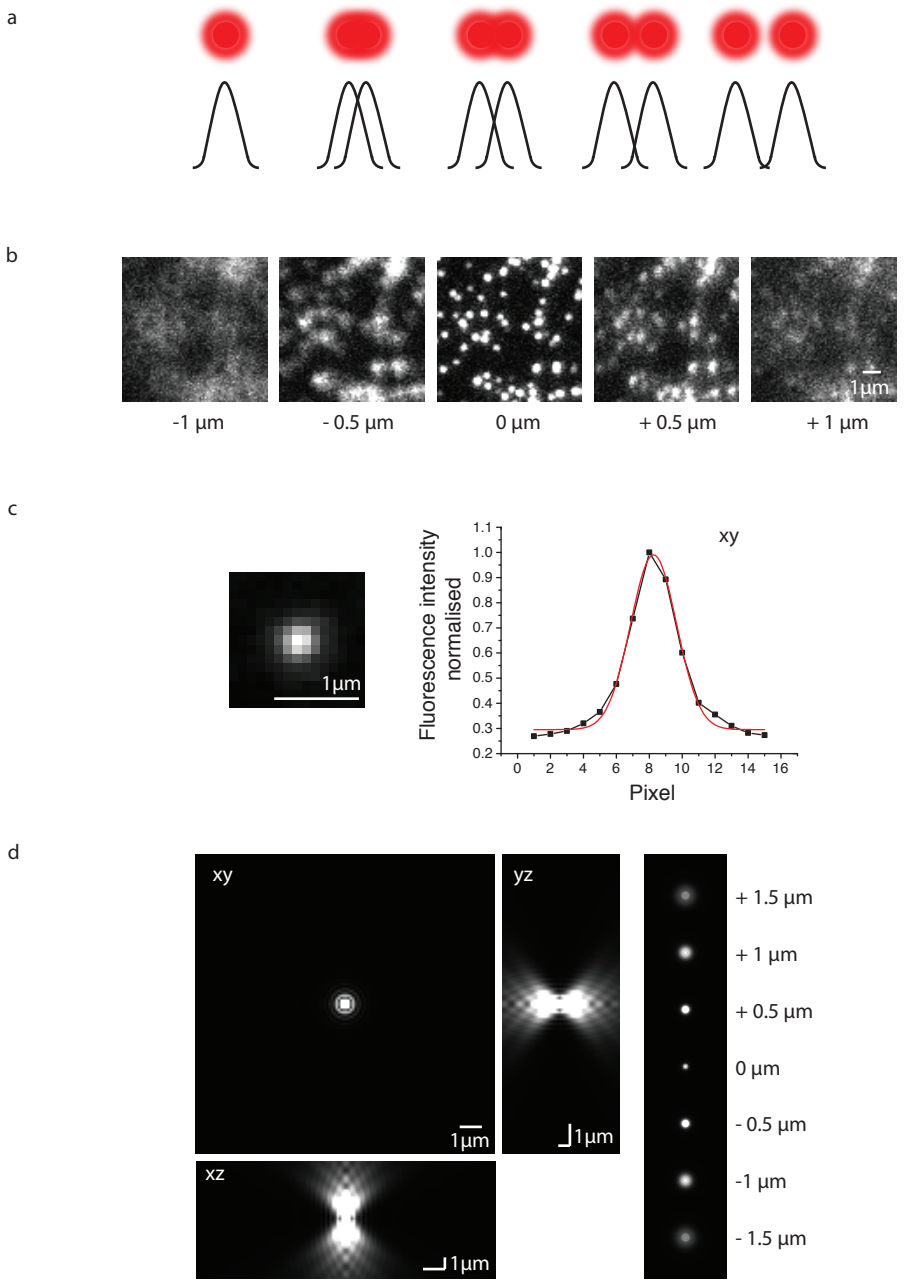

Figure 1.8 **Point spread function and optical resolution.** a. Principle of the point spread function (PSF). Due to the diffraction of light through the optics in the microscope objectives any infinitively small object will appear as a well-defined point spread function, typically 200-300 nm in size. If PSFs overlap it is impossible to distinguish between them, thus limiting optical resolution. b. 40 nm beads were imaged at different focal depth As focal depth increases or decreases the PSFs defocus and blur. c. Measured PSF of a 40 nm bead (660 nm wavelength) and the normalised xy profile was plotted and fitted with a Gaussian curve. c. Theoretical PSF calculated using the Gibson and Lanni model showing the PSF in xy and its orthogonal views as well as in xy with 0.5 µm above and below the sharpest point.

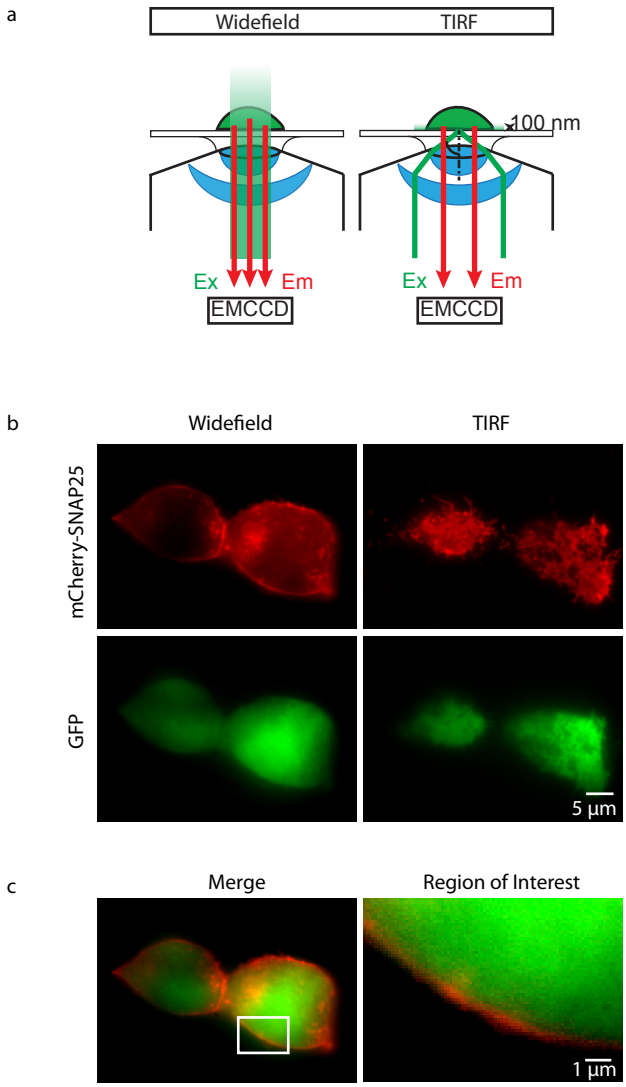

Figure 1.9 **Widefield and TIRF imaging.** a. Illustration of the widefield microscope and TIRFM setup from Figure 1.5. b. AtT20 D16:16 cells expressing transfected mCherry-SNAP25 and GFP, imaged in both widefield and TIRFM mode demonstrates both the difference in sharpness of a membrane bound protein (SNAP25) verses a cytosolic protein (GFP) and the difference between widefield (dominated by out of focus light) and TIRFM (clear membrane definition). c. The merged image and the ROI show the clear distinction between membrane bound and cytosolic proteins.

temperatures increasing the probability of electron multiplication and limiting random electron multiplication events. Conveniently, very low temperatures keeps dark noise, unwanted electron generation through thermal excitation of electrons in the CCD, at bay, so high end cameras are typically electrically and water cooled down to -80 °C. With the electron multiplication step and improved electronics, the readout noise that hampered the CCD cameras image quality, is effectively eliminated and therefore the new EMCCD camera have become standard throughout biological imaging.

Next to the EMCCD camera the newer sCMOS technology is becoming increasingly competitive. The sCMOS camera works different to the EMCCD camera in that there is no readout time limit as the readout is done simultaneously (Figure 1.10b). In the sCMOS camera the chip typically consists of 2048x2048 6.5 μm pixels, although pixel number and size may differ depending on the manufacturer, with an amplifier and an A/D converter integrated into each pixel. The advantage over the EMCCD camera is the gain in acquisition speed due to the reduced readout time, pushing the limit up to 100 Hz. However, this comes at a cost of sensitivity and higher SNR, as less photons will be captured in each frame.

Understanding how the two cameras work is essential to choose which one to use to the best of their capability. For fixed samples for slower moving processes, an EMCCD will be of advantage, but to capture fast events in the time scale of 5 – 100 ms such as calcium events, the sCMOS camera would be preferable, but only if the sample is bright enough (Long et al. 2012) .

1.5.5 Total Internal Reflection Fluorescence Microscopy

Total internal reflection fluorescence microscopy (TIRFM) is an optical technique that restricts the illumination profile to below 100 nm into the specimen, effectively removing the out of focus light in the widefield configuration, and producing a very sharp image (Steyer & Almers 2001). In biology the TIRFM setup is often used for imaging plasma membrane molecules and SMLM.

In TIRFM the incoming excitation laser beam is angled shallower than the critical angle between the sample cover slip and cell medium, which will cause the light to be reflected off the high to low refractive index interface between the glass coverslip and the liquid media (Figure 1.11a). It is important to use a high NA objective in combination with a low refractive index of the cell media to be able to exploit the properties of this interface. During TIR an evanescent wave is created at the refractive index interface, penetrating into the sample with an exponentially decreasing intensity. Viable illumination intensities are restricted to within 100 nm of the interface,

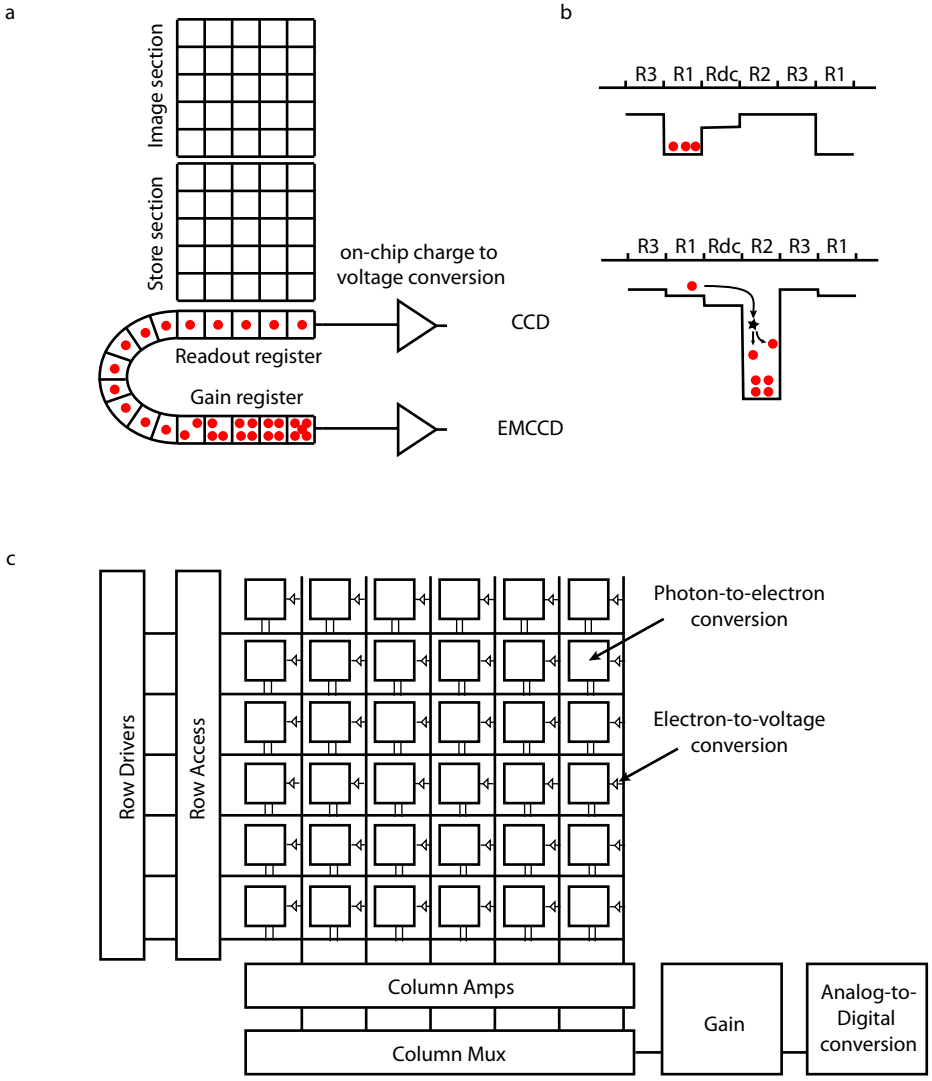

Figure 1.10 **EMCCD and sCMOS camera detectors.** a. Detection array and photon multiplication (Gain register) on the EMCCD camera. b. Voltage changes across the different R1, R2, Rdc and R3 bias regions encourage impact ionisation, increasing the photon number and effectively providing high gain detection. c. The detector in the sCMOS is an array of photon-to-electron conversion detectors and the output is immediately converted into voltage.

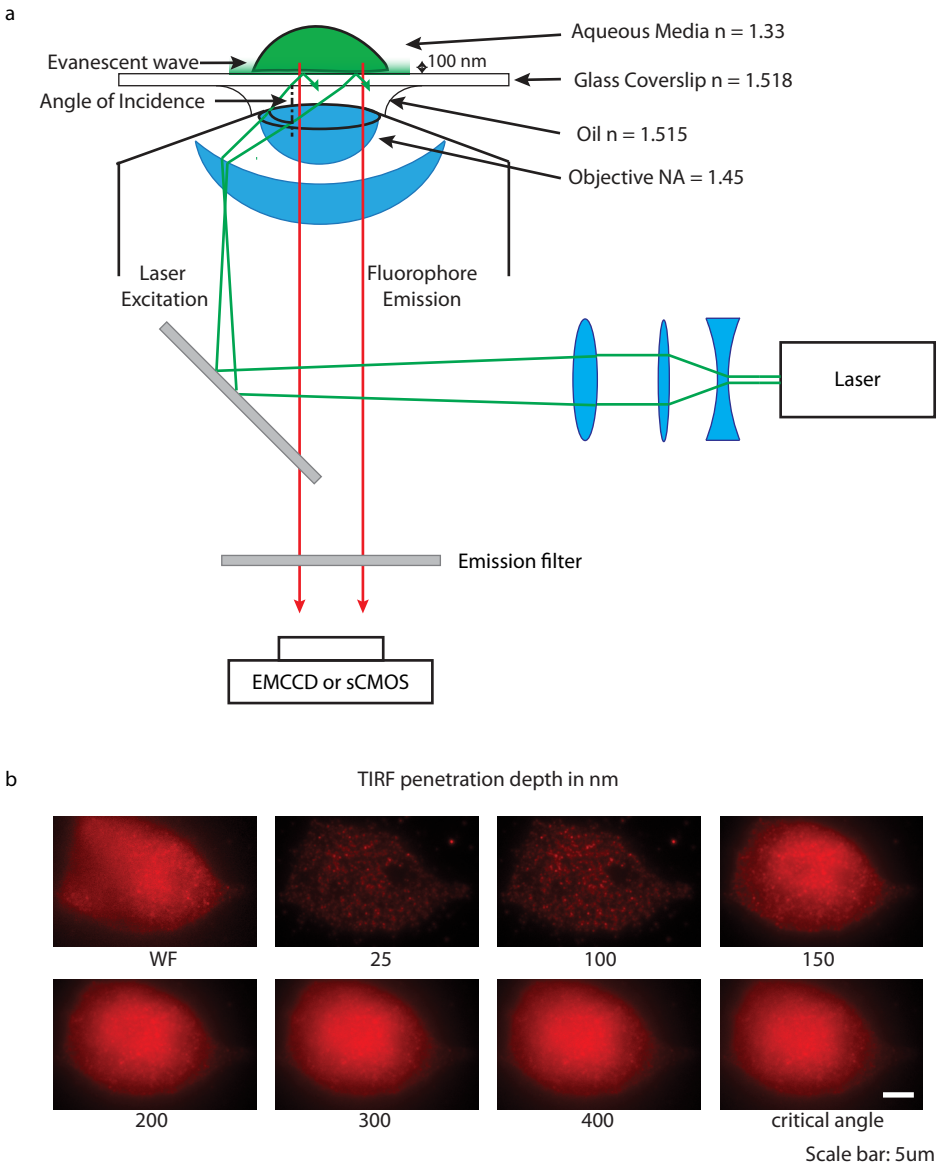

Figure 1.11 **Total Internal Reflection Fluorescence Microscopy.** a. A detailed diagram of a typical TIRFM setup, which is done on a widefield microscope. For TIRFM imaging the incident beam is set to the correct critical angle, to induce total internal reflection and avoid the evanescence wave penetrating further than around 100 nm into the sample. The high NA of the objective and the immersion oil are vital to achieving total internal reflection b. These example images of mCherry-SNAP25 demonstrate the image outcome with the illumination beam set at different angles, here ranging from 25 – 400 nm depth penetration.

restricting the illumination depth for fluorescence microscopy (Axelrod 2001). This enables a sharp image of the plasma membrane with all the membrane proteins without any background fluorescence from the intracellular compartments of the cell (Axelrod 1981) (Figure 1.11b).

1.5.6 Photoactivated Localisation Microscopy

Photoactivated localization microscopy (PALM) is a single molecule imaging technique done in TIRFM only capturing plasma membrane proteins in the here desirable 2-dimentional image acquisition method (Betzig et al. 2006). PALM avoids the problem of the optical resolution limitation, as the number of fluorescent molecules is kept sparse, ensuring non-overlapping PSF signals. Cells are transfected with the DNA encoding for a fusion protein between the protein of interest and a photoactivatable fluorescent protein, which requires activation by high energy blue laser light before the fluorescence properties resemble normal FPs (Shaner et al. 2007). By reducing the activation intensity, only a fraction of PA- molecules will become active at any one pulse, emit photons and bleach after which they cannot be switched on again (Figure 1.12a). This is repeated over and over again acquiring between 10^4 and 10^5 images in total (Hess et al. 2006). By imaging these spatially distinct PSFs, software algorithms can localise the molecules through fitting the PSFs and rendering these into a virtual image that shows the coordinate positions of all the molecules on the plasma membrane that have emitted photons (Owen et al. 2010).

A variation of PALM is the combination of the conventional PALM with live single-particle tracking (spt) named sptPALM (Manley et al. 2008), indicating the potential of development of this technique.

1.5.7 Stochastic Optical Resolution Microscopy

Stochastic optical resolution microscopy (STORM) (Rust et al. 2006) is a SMLM technique that, similar to PALM, relies on the acquisition of only a few spatially separated molecules per image frame.

The biological sample is fixed and immunostained for the protein of interest, the primary antibody targeting the endogenous protein and the secondary antibody labelling the primary. For imaging, the cells are bathed in a reducing buffer, which drives the exited fluorophors into the long lived dark triplet state (Fölling et al. 2008). From the dark state they emit a photon to return to the low-energy ground state, as explained in the Jablonski diagram. However, this process is both long lived and stochastic such that only a small subset of molecules emit at any one time. As in PALM, therefore a time series allows for the accurate rendering of isolated PSFs to form a final

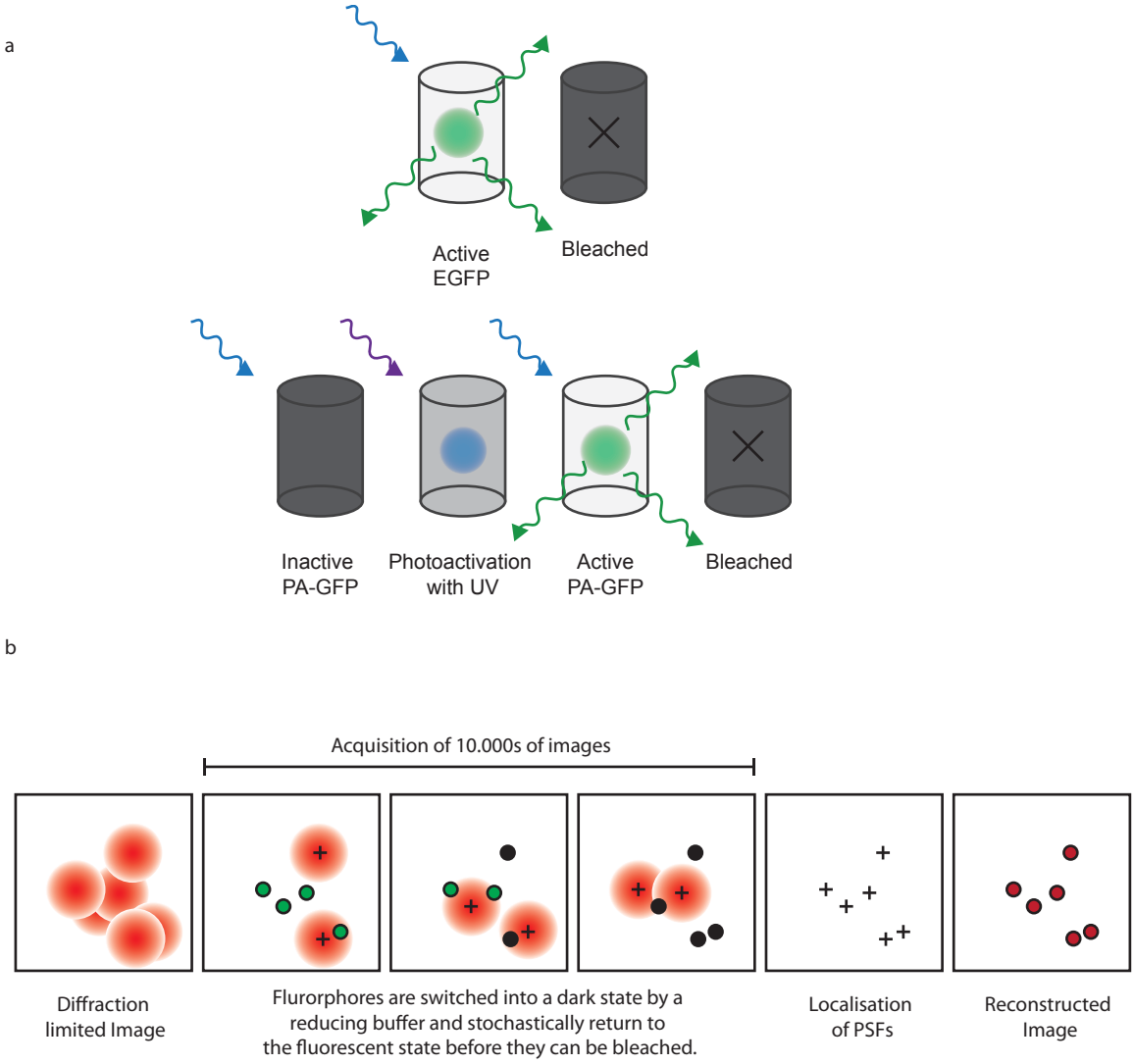

Figure 1.12 **PALM and STORM activation.** a. PALM. Standard fluorescent proteins absorb energy and emit fluorescence without restriction beyond the inherent lifetime of the proteins. Photo-activatable FPs, however, have to be activated with 405 nm light prior to normal absorption. The activation is kept at a low intensity to only switch on a subset of PA-FPs. b. STORM. Fluorescent dyes are driven into the shelved triplet state from which a small subset will at any one time randomly cycle to the fluorescently active singlet state when they return to the low energy state.

super-resolution image (Figure 1.12b). Again the final rendered image is a representation of the coordinates and accuracy of each individual spot.

The advantage of STORM is that the imaging is done on endogenous proteins, eliminating the problem of overexpression through transfection, but the disadvantage is that fluorescent dyes can 'blink' and several secondary antibody dyes can attach to the primary antibody, and therefore the number of proteins cannot be determined.

The blinking is thought to arise due to molecules that have emitted photons but did not bleach and instead have crossed into the in the dark state and then can absorb and emit photons again once they cross back into the $S_1 - S_0$ states.

1.5.8 Confocal Microscope

The original one photon confocal microscope works by illuminating the specimen through a focused beam that scans the specimen pixel-by-pixel (Minsky 1988; Pawley 1995). To eliminate all out of focus light, a pinhole is put in place in front of a single point detector that only allows photons through that come from a tightly defined, diffraction limited, focal point. The collected photons are detected typically with a high sensitivity photon multiplier tube (PMT), or single photon avalanche diode (SPAD). As this is a single point scanning methodology, this is significantly slower than the image acquisition on the widefield microscope, but the images are sharper with less out of focus light and benefit from higher sensitivity single pixel detectors. There are advanced variations of the confocal microscope such as the addition of the spinning disk, which allows faster imaging at increased complexity, as well as the 2-photon confocal microscope, where the excitation is inform the non-linear absorption of two low energy photons simultaneously that only together can excite the fluorophore in the centre of the focal beam. The advantage with the 2-photon confocal microscope is improved axial sectioning as the non-linear absorption cross section results in a tighter axial focus than conventional confocal microscopy.

1.5.9 Förster Resonance Energy Transfer and Fluorescence Lifetime Imaging Microscopy

Förster resonance energy transfer (FRET) directly utilizes the property of energy transfer between fluorescent dyes to probe protein interactions. As this interaction is only prevalent over 1 – 10 nm, FRET uniquely provides the only existing methodology to probe direct protein-protein interaction (Figure 1.13a).

FRET happens between a donor, a short wavelength, high-energy fluorescent probe and an acceptor, with a longer wavelength and lower energy properties (Figure 1.13b). Upon optical excitation the donor transfers its excited energy to the acceptor, which subsequently emits a photon (Figure 1.13c). Recording this photonic emission

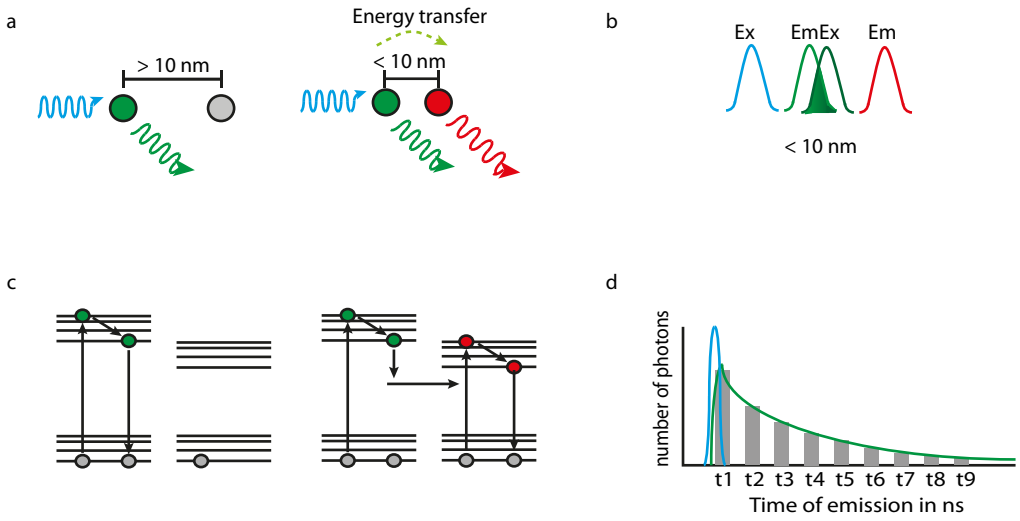

Figure 1.13 **Principle of resonance energy transfer between fluorophores.** a. Förster resonance energy transfer (FRET) is when fluorophores are in very close proximity to one another energy can transfer from one excited fluorophore, the donor, to the other, the acceptor, enabling the acceptor to fluoresce on excitation of the donor. b. and c. For FRET to occur, the emission of one fluorophore has to overlap sufficiently with the excitation spectrum of the second fluorophore. d. Fluorescence Lifetime Imaging Microscopy. The fluorescence lifetime can be measured by giving an excitation pulse at t = 0, then counting the arrival time of the emitted photons relative to the excitation event. The histogram of these photon arrival can be plotted and thus the lifetime extracted. If FRET happens, then the lifetime of the donor fluorophore will decrease.

behaviour, and the relative relationship between the donor and acceptor, indicates donor and acceptor proximity. The main requirement of probes for FRET is the energy overlap between the donor and the acceptor. The emission energy of the donor must overlap with the energy required for the excitation of the acceptor. For the energy transfer the spatial separation between the probes has to be between 1 - 10 nm, the exact distance being specific to each FRET pair. This makes FRET the only, and therefore extremely powerful, imaging tool for analysis of true protein-protein interactions.

FRET can be measured in terms of intensity or lifetime of the donor. With the transfer of energy the intensity of the donor decreases, whilst the acceptor increases, which can be imaged using a widefield microscope. However, intensity FRET can be challenging, requiring careful controls and dual colour imaging. Fluorescent lifetime is a more robust measurement of FRET. The lifetime, the length of time a fluorophore spends in the excited state before returning to the ground state, can be measured pixel-by-pixel using the SPADs on a confocal microscope and time correlated single photon counting (TCSPC), a method known as fluorescence lifetime imaging microscopy (FLIM) (Stryer & Haugland 1967; Stryer 1978) (Figure 1.13d). A shortened lifetime of the donor indicates energy transfer to the acceptor and a close proximity between the donor and acceptor, suggesting a possible interaction between the proteins of interest.

1.6 Functional Biological Imaging

1.6.1 Calcium Imaging

The importance of understanding calcium signalling cannot be overestimated; it is crucial to a variety of biological processes, function and diseases. However, due to the nature of ions, their small size and fast diffusion, it is extremely difficult to shed light on cellular calcium activated processes. However, some tricks have assisted in calcium imaging, namely calcium dyes and genetically encoded calcium indicators.

When it was understood that calcium was one of the main component in many signalling cascades the task turned to seeking to understand the mechanisms, particularly in relation to fusion sites. Estimations of calcium 'domains' have been done (Chad & Eckert 1984; Sala & Hernández-Cruz 1990), but only direct calcium imaging can confirm the local flux and diffusion of calcium ions.

One of the primary methods to achieve this is through the use of calcium dyes, which are chemical indicators that can chelate calcium ions. These chemical structures are based on an EGTA homologue BAPTA, from which Fura-2, Fluo3 and Fluo4, amongst

many others, have been derived. To allow these molecules to pass through the cell membrane, carboxyl groups are masked by acetoxymethyl ester (AM ester) groups rendering the molecule lipophilic. The AM esters are cleaved off by cytosolic esterases, inhibiting the molecules to escape back through the lipophilic membrane. Calcium binding to these dyes can either increase the quantum yield for fluorescence, in the case of the Fluo dyes, or the emission and excitation wavelength can shift, a characteristic of the Fura-2 dye.

A second method is genetically encoded calcium indicators, which have undergone significant improvement in recent years (Kotlikoff 2007; Akerboom et al. 2013). Through biochemistry and molecular biology experiments, calcium sensitive proteins were identified, one of them being calmodulin. Calmodulin is present throughout the cytoplasm and when bound to four calcium ions it changes confirmation and can bind to various target enzymes. One of these targets is the myosin light chain kinase, which in turn phosphorylates and activates the myosin light chain as one step in the muscle contraction cascade of events. The calmodulin-binding domain of the myosin light chain kinase was synthesized separately from the entire protein in an experiment to prove that calmodulin binds to the M13 section and does not require the entire protein. This synthetic protein termed M13 was then used for other calmodulin binding experiments. Taking advantage of these properties, the first GECI was designed that linked calmodulin, M13, with two FRET-paired FPs. Here, a higher calcium concentration would result in the binding of calmodulin and M13 to each other, which would therefore draw the two FPs into closer proximity allowing for FRET measurement (Miyawaki et al. 1997). GECIs were re-designed into circular permutation of FPs, where the calmodulin and M13 tagged FP was modified to a slightly more open β-barrel configuration, quenching and therefore disrupting the fluorescence properties (Griesbeck et al. 2001). However, in the presence of calcium, calmodulin binds with M13 and effectively pulls the opened β-barrel structure of the FP together to allow fluorescence (Baird et al. 1999). Herewith, a calcium indicator was created that can be transfected and expressed in cells in a minimally invasive manner and allowed complex *in vivo* calcium imaging (Tallini et al. 2006). A wide range of GECI in terms of fluorescence properties and calcium sensitivity has been created (Zhao et al. 2011). Further genetic modification by creating a recombinant protein can be done to deliver these GECI to a subcellular compartments (Su et al. 2013).

The task of understanding and probing the intercellular calcium signalling is therefore immensely abridged with the discovery and synthesis of calcium dyes and the creation of encoded indicators.

1.6.2 Optical Patching

Optical patching is a technique combining electrophysiology and microscopy imaging to simultaneously correlate temporal data of ion fluctuations across the PM with the spatial configuration of the protein or ion of interest, on the same PM.

On its own, electrophysiological recordings give out a wealth of information about behaviour and properties of ion channels in the PM. For electrophysiological recording a relatively wide glass micropipette tip is brought into close proximity to the PM and, with applied suction, a patch of the PM is drawn slightly into the micropipette forming a high resistance seal between the glass and the membrane (Neher & Sakmann 1976). This method is called 'cell attached', and recordings can be taken from the ion channels within the patch. 'Whole cell' recordings acquiring collective results of all the ion channels in the PM can be taken if the patch is broken, but the high resistance seal remains.

To date, due to the extremely high temporal resolution and precise electrical recording, most of the ion channel properties have been collected through patch clamp recordings. The downside however is the complete lack of spatial information.

With the development of ion indicators, the idea of combining electrophysiology and microscopy imaging blossomed. The simultaneously acquired temporal information from electrical recordings and the spatial information from imaging data can be pooled to understand ion channels distribution and activity at the plasma membrane.

Both techniques on their own are extremely difficult and there are very few groups within this field performing optical patching. Ian Parker and his group are one of the leading researchers electrically stimulating cells and recording calcium 'sparks' in TIRFM. Their work was focused on IP_3R calcium currents from the ER (Smith et al. 2009) and their analysis was done subjectively picking out calcium 'sparks' or 'events' (Parker & Smith 2010). These techniques are excellent tools for spatial and temporal imaging of calcium events, however the evaluation could be improved with less subjective and more objective analysis.

1.7 Biological Aims and Questions

The overall question this thesis will address focuses on understanding the spatial and functional distribution of voltage-gated calcium channels.

In the initial experimental results chapter, chapter 3, an analysis of the effect the synprint site has on the spatial interaction of $Ca_v2.2$ channels will be conducted. How much the two proteins, syntaxin1a and the complete $Ca_v2.2$ channel, or the synprint-

deleted $Ca_v2.2$ channel, interact in the spatial environment of the plasma membrane of an excitable cell will be shown through confocal co-localisation and FLIM analysis. In addition, for imaging and localising single $Ca_v2.2$ channel molecules a novel approach was developed to answer questions about the spatial distribution. Here, ω-conotoxin GVIA, a highly specific $Ca_v2.2$ channel toxin was used to localise this specific channel type using the super-resolution technique PALM.

The second experimental chapter, chapter 4, addresses the functionality of calcium channels at the plasma membrane through direct calcium imaging. TIRFM imaging was conducted to capture the plasma membrane calcium events, adding pharmacological reagents, channel specific agonists or antagonists, to manipulate the calcium flux and to single out calcium channel types. A new non-subjective global methodology was developed to analyse the images and create a functional map showing areas of high and low calcium activity.

The third experimental chapter, chapter 5, discusses the functional aspect of voltage-gated calcium channels in light of optical patching and simultaneous dual colour imaging. Optical patching, where cells were simultaneously patch clamped and imaged in TIRFM, was conducted to analyse the spatial calcium distribution in relation to the voltage potential. Knowing that the influx of calcium is on the time scale of 10-100 ms, imaging was pushed to the limit capturing the events with a high speed camera, the sCMOS, imaging at 10 ms / frame. To investigate, the spatial and temporal relationship between vesicle fusion and calcium channel opening, a dual-colour image splitter was used which allowed simultaneous imaging of the two events.

Reference

Adrian, R.H., Chandler, W.K. & Hodgkin, A.L., 1970. Voltage clamp experiments in striated muscle fibres. *The Journal of Physiology*, 208, pp.607–644.

Akerboom, J. et al., 2013. Genetically encoded calcium indicators for multi-color neural activity imaging and combination with optogenetics. *Frontiers in Molecular Neuroscience*, 6, p.2.

Albillos, A. et al., 1997. The exocytotic event in chromaffin cells revealed by patch amperometry. *Nature*, 389, pp.509–12.

Armstrong, C.M., 1969. Inactivation of the potassium conductance and related phenomena caused by quaternary ammonium ion injection in squid axons. *The Journal of general physiology*, 54(5), pp.553–75.

Armstrong, C.M., 1971. Interaction of tetraethylammonium ion derivatives with the potassium channels of giant axons. *The Journal of general physiology*, 58(4), pp.413–37.

Armstrong, C.M. & Binstock, L., 1965. Anomalous rectification in the squid giant axon injected with tetraethylammonium chloride. *The Journal of general physiology*, 48, pp.859–72.

Axelrod, D., 1981. Cell-substrate contacts illuminated by total internal reflection fluorescence. *The Journal of Cell Biology*, 89(9), pp.141–145.

Axelrod, D., 2001. Total internal reflection fluorescence microscopy in cell biology. *Traffic*, 2, pp.764–774.

Baird, G.S., Zacharias, D. a & Tsien, R.Y., 1999. Circular permutation and receptor insertion within green fluorescent proteins. *Proceedings of the National Academy of Sciences of the United States of America*, 96, pp.11241–6.

Barr, F. & Huttner, W.B., 1996. A role for ADP-ribosylation factor 1, but not COP I, in secretory vesicle biogenesis from the trans-Golgi network. *FEBS Letters*, 384, pp.65–70.

Barrett, E.F. & Stevens, C.F., 1972. The kinetics of transmitter release at the frog neuromuscular junction. *The Journal of Physiology*, 227, pp.691–708.

Bennett, M.K. et al., 1992. Synaptic vesicle membrane proteins interact to form a multimeric complex. *The Journal of Cell Biology*, 116(3), pp.761–75.

Bennett, M.K., Calakos, N. & Scheller, R.H., 1992. Syntaxin : a synaptic protein implicated in docking of synaptic vesicles at presynaptic active zones. *Science*, 257, pp.255–259.

Betzig, E. et al., 2006. Imaging intracellular fluorescent proteins at nanometer resolution. *Science*, 313, p.1642.

Bezanilla, F. & Armstrong, C.M., 1972. Negative conductance caused by entry of sodium and cesium ions into the potassium channels of squid axons. *The Journal of General Physiology*, 60(5), pp.588–608.

Bezprozvanny, I. et al., 2000. Molecular determinants of the functional interaction between syntaxin and N-type Ca 2+ channel gating. *PNAS*, 97(25), pp.2–7.

Block, M.R. et al., 1988. Purification of an N-ethylmaleimide-sensitive protein catalyzing vesicular transport. *Proceedings of the National Academy of Sciences of the United States of America*, 85, pp.7852–6.

Borst, J.G.G. & Sakmann, B., 1996. Calcium influx and transmitter release in a fast CNS synapse. *Nature*, 383, pp.431–434.

Catterall, W. a, 2000. Structure and regulation of voltage-gated Ca2+ channels. *Annual Review of Cell and Developmental Biology*, 16, pp.521–55.

Chad, J.E. & Eckert, R., 1984. Calcium domains associated with individual channels can account for anomalous voltage relations of Ca-dependent responses. *Biophysical Journal*, 45, pp.993–9.

Chapman, E.R. et al., 1998. Delineation of the oligomerization, AP-2 binding, and synprint binding region of the C2B domain of synaptotagmin. *Journal of Biological Chemistry*, 273(49), pp.32966–32972.

Choe, S., 2002. Potassium channel structures. *Nature reviews. Neuroscience*, 3(2), pp.115–121.

Clary, D.O., Griff, I.C. & Rothman, J.E., 1990. SNAPs, a family of NSF attachment proteins involved in intracellular membrane fusion in animals and yeast. *Cell*, 61, pp.709–21.

Clary, D.O. & Rothman, J.E., 1990. Purification of three related peripheral for vesicular transport membrane proteins needed. *The Journal of Biological Chemistry*, 265(17), pp.10109–10117.

Cobbold, P.H. & Rink, T.J., 1987. Fluorescence and bioluminescence measurement of cytoplasmic free calcium. *The Biochemical journal*, 248(2), pp.313–28.

Cohen, F.S., Zimmerberg, J. & Finkelstein, A., 1980. Fusion of phospholipid vesicles with planar phospholipid bilayer membranes. *The Journal of General Physiology*, 75, pp.251–270.

Cole, K.S., 1949. Dynamic electrical characteristics of the squid axon membrane. *Arch. Sci. Physiol.*, 3, pp.253–258.

Cole, K.S. & Curtis, H.J., 1939. Electric impedance of the squid giant axon during Activity. *The Journal of General physiology*, 22(5), pp.649–70.

Dalton, B. & Felix, M.D., 1956. A comparative study of the golgi complex. *Journal of Biophysical and Biochemical Cytos*, 2(4), pp.79–94.

Doyle, D.A. et al., 1998. The structure of the patassium channels: Molecular basis of K conduction and selectivity. *Science*, 280, pp.69–77.

Dunn, L.A. & Holz, R.W., 1983. Catecholamine secretion from digitonin-treated adrenal medullary chromaffin cells. *The Journal of Biological Chemistry*, 258(8), pp.4989–93.

Eisenberg, D., 1984. Three-dimensional structure of membrane and surface proteins. *Annual Review of Biochemistry*, 53, pp.595–623.

Farquhar, M.G. & Palade, G.E., 1981. The Golgi apparatus (complex)-(1954-1981)-from artifact to center stage. *The Journal of Cell Biology*, 91(1), pp.77–103.

Fasshauer, D., Bruns, D., et al., 1997. A structural change occurs upon binding of syntaxin to SNAP-25 . *Biochemistry*, 272(7), pp.4582–4590.

Fasshauer, D. et al., 2002. SNARE assembly and disassembly exhibit a pronounced hysteresis. *Pharmacia*, 9(2).

Fasshauer, D., Otto, H., et al., 1997. Structural changes are associated with soluble N-ethylmaleimide-sensitive fusion protein attachment protein receptor complex formation. *The Journal of Biological Chemistry*, 272(44), pp.28036–28041.

Fatt, B.P. & Katz, B., 1951. An analysis of the end-plate potential recorded with an intra-cellular electrode. *Journal of Physiology*, 115, pp.320–370.

Fatt, P. & Ginsborg, B.L., 1958. The ionic requirements for the production of action potentials in crustacean muscle fibres. *The Journal of Physiology*, 142, pp.516–543.

Fatt, P. & Katz, B., 1953. The electrical properties of crustacean muscle fibres. *The Journal of Physiology*, 120, pp.171–204.

Fenwick, B.Y.E.M., Martyt, A. & Nehert, E., 1982. Sodium and calcium channels in bovine chromaffin cells. *The Journal of Physiology*, 331, pp.599–635.

Fernandez-Chacon, R. et al., 2001. Synaptotagmin I functions as a calcium regulator of release probability. *Nature*, 410, pp.41–49.

Ferro-Novick, S. & Jahn, R., 1994. Vesicle fusion from yeast to man. *Nature*, 370, pp.191–193.

Fölling, J. et al., 2008. Fluorescence nanoscopy by ground-state depletion and single-molecule return. *Nature*, 5(11), pp.943–945.

Giles, W. et al., 1989. Modulation of the delayed rectifier K+ current by isoprenaline in bull-frog atrial myocytes. *Journal of Physiology*, 415, pp.233–249.

Goldin, A.L., 2001. Resurgence of sodium channel research. *Annual Review of Physiology*, 63, pp.871–894.

Goldman, D.E., 1943. Potential, impedance, and rectification in membranes. *The Journal of General Physiology*, pp.37–60.

Griesbeck, O. et al., 2001. Reducing the environmental sensitivity of yellow fluorescent protein. Mechanism and applications. *The Journal of Biological Chemistry*, 276, pp.29188–94.

Hagiwara, S. & Naka, K.I., 1964. The initiation of spike potential in barnacle muscle fibers under low intracellular Ca++. *The Journal of General Physiology*, 48, pp.141–62.

Hagiwara, S. & Nakajima, S., 1966. Effects of the intracellular Ca ion concentration upon the excitability of the muscle fibre membrane of a barnacle. *The Journal of General Physiology*, 49, pp.807–818.

Hamill, O.P. et al., 1981. Improved patch-clamp techniques for high-resolution current recording from cells and cell-rree membrane patches. *Pflugers Archiv. European Journal Of Physiology*, 391, pp.85–100.

Hayashi, T. et al., 1994. Synaptic vesicle membrane fusion complex: action of clostridial neurotoxins on assembly. *The EMBO Journal*, 13(21), pp.5051–61.

Hermann, L., 1872. *Grundriss der Physiologie* 4th Ed.,

Hermann, L., 1902. *Lehrbuch der Physiologie* 13th Ed., August Hirschwald, Berlin.

Hess, S.T., Girirajan, T.P.K. & Mason, M.D., 2006. Ultra-high resolution imaging by fluorescence photoactivation localization microscopy. *Biophysical Journal*, 91(11), pp.4258–4272.

Hille, B., 1968. Pharmacological modifications of the sodium channels of frog nerve. *The Journal of General Physiology*, 51, pp.199–219.

Hille, B., 1971. The permeability of the sodium channel to organic cations in myelinated nerve. *The Journal of General Physiology*, 58, pp.599–619.

Hodgkin, A.L. & Huxley, A.F., 1952a. A quantitative description of membrane current and its application to conduction and excitation in nerve. *Journal of Physiology*, 117, pp.500–544.

Hodgkin, A.L. & Huxley, A.F., 1939. Action potentials recorded from inside a nerve fibre. *Nature*, 114, pp.710–711.

Hodgkin, A.L. & Huxley, A.F., 1945. Resting and action potentials in single nerve fibres. *Journal of Physiology*, 104, pp.176–195.

Hodgkin, A.L. & Huxley, A.F., 1952. The components of membrane conductance in the giant axon of Loligo. *Journal of Physiology*, 116, pp.473–496.

Hodgkin, A.L. & Huxley, A.F., 1952b. The dual effect of membrane potential on sodium conductance in the giant axon of Loligo. *Journal of Physiology*, 116, pp.497–506.

Hodgkin, A.L. & Katz, B., 1949. The effects of sodium ions on the electrical activity of the giant axon of the squid. *Journal of Physiology*, 108, pp.37–77.

Jahn, R., Lang, T. & Südhof, T.C., 2003. Membrane Fusion. *Cell*, 112, pp.519–533.

Jahn, R. & Scheller, R.H., 2006. SNAREs-engines for membrane fusion. *Nature reviews. Molecular cell Biology*, 7(9), pp.631–43.

Jarvis, S.E. et al., 2002. Molecular determinants of syntaxin 1 modulation of N-type calcium channels . *Biochemistry*, 277(46), pp.44399–44407.

Kostyuk, P.G. & Krishtal, O.A., 1977. Separation of sodium and calcium current in the somatic membrane of mollusc neurones. *The Journal of Physiology*, 270, pp.545–568.

Kotlikoff, M.I., 2007. Genetically encoded Ca2+ indicators: using genetics and molecular design to understand complex physiology. *The Journal of Physiology*, 578, pp.55–67.

Lin, Z. et al., 1997. Identification of functionally distinct isoforms of the N-type Ca2+ channel in rat sympathetic ganglia and brain. *Neuron*, 18(1), pp.153–66.

Long, F., Zeng, S. & Huang, Z.-L., 2012. Localization-based super-resolution microscopy with an sCMOS camera part II: experimental methodology for comparing sCMOS with EMCCD cameras. *Optics express*, 20(16), pp.17741–59.

Manley, S. et al., 2008. High-density mapping of single-molecule trajectories with photoactivated localization microscopy. *Nature Methods*, 5(2), pp.2007–2009.

Matthew, W.D., Tsavaler, L. & Reichardt, L.F., 1981. Identification of a synaptic vesicle-specific membrane protein with a wide distribution in neuronal and neurosecretory tissue immunohistochemistry isolation of hybridoma secreting cell lines. *The Journal of Cell Biology*, 91, pp.257–269.

McNew, J.A., 2008. Regulation of SNARE-mediated membrane fusion during exocytosis. *Proteins*, pp.1669–1686.

Michaelis, L. & Menten, M.L., 1913. Die Kinetic der Invertinwirkung. *Journal of Biochemistry*, 49, pp.333–369.

Minsky, M., 1988. Memoir on inventing the confocal scanning microscope. *Scanning*, 10(4), pp.128–138.

Miyawaki, A. et al., 1997. Fluorescent indicators for Ca 2+ based on green fluorescent proteins and calmodulin. *Nature*, 388, pp.882–887.

Nakamura, Y., Nakajima, S. & Grundfest, H., 1965. Analysis of spike electrogenesis and depolarizing K inactivation in electroplaques of electrophorus electricus, L. *The Journal of General Physiology*, 49(2), pp.321–49.

Narahashi, T., Moore, J.W. & Scott, W.R., 1964. Tetrodotoxin blockage of sodium conductance increase in lobster giant axons. *The Journal of General Physiology*, 47, pp.965–74.

Neher, E. & Sakmann, B., 1976. Single-channel currents recorded from membrane of denervated frog muscle fibres. *Nature*, 260, pp.799–802.

Owen, D.M. et al., 2010. PALM imaging and cluster analysis of protein heterogeneity at the cell surface. *Journal of Biophotonics*, 3(7), pp.446–454.

Oyler, G. a et al., 1989. The identification of a novel synaptosomal-associated protein, SNAP-25, differentially expressed by neuronal subpopulations. *The Journal of Cell Biology*, 109(6), pp.3039–52.

Palay, S.L. & Palade, G.E., 1955. The Fine Structure of Neurons. *The Journal of Biophysical and Biochemical Cytology*, 1(1), pp.69–88.

Pan, J.Q. & Lipscombe, D., 2000. Alternative splicing in the cytoplasmic II-III loop of the N-type Ca channel alpha 1B subunit: functional differences are beta subunit-specific. *The Journal of Neuroscience : the official journal of the Society for Neuroscience*, 20(13), pp.4769–75.

Parker, I. & Smith, I.F., 2010. Recording single-channel activity of inositol trisphosphate receptors in intact cells with a microscope, not a patch clamp. *The Journal of General Physiology*, 136(2), pp.119–127.

Parsons, T.D. et al., 1995. Docked granules, the exocytic burst, and the need for ATP hydrolysis in endocrine cells. *Neuron*, 15, pp.1085–96.

Pawley, J., 1995. *Handbook of Biological Confocal Microscopy*, Plenum, New York.

Perin, M.S. et al., 1991. Structural and functional conservation of synaptotagmin (p65) in Drosophila and humans. *The Journal of Biological Chemistry*, 266(1), pp.615–22.

Rickman, C. et al., 2007. Functionally and spatially distinct modes of munc18-syntaxin 1 interaction. *Journal of Biological Chemistry*, 282(16), pp.12097–12103.

Rickman, C. et al., 2004. Synaptotagmin interaction with the syntaxin / SNAP-25 dimer is mediated by an evolutionarily conserved motif and is sensitive to inositol Hexakisphosphate. *The Journal of Biological Chemistry*, 279(13), pp.12574–12579.

Rickman, C. et al., 2010. t-SNARE Protein conformations patterned by the lipid. *Journal of Biological Chemistry*, 285(18), pp.13535–13541.

Rizo, J. & Sudhof, T.C., 1998. C2-domains, structure and function of a universal Ca2+ -binding domain. *The Journal of Biological Chemistry*, 273(26), pp.15879–15882.

Rothman, J.E., 1994. Methanisms of intracellular protein transport. *Nature*, 372, pp.55–63.

Rust, M.J., Bates, M. & Zhuang, X., 2006. Stochastic optical reconstruction microscopy (STORM) provides sub-diffraction-limit image resolution. *Nature Methods*, 3(10), pp.793–795.

Sala, F. & Hernández-Cruz, A., 1990. Calcium diffusion modeling in a spherical neuron. *Biophysical Journal*, 57, pp.313–24.

Schneggenburger, R. & Neher, E., 2000. Intracellular calcium dependence of transmitter release rates at a fast central synapse. *Nature*, 406, pp.889–893.

Shaner, N.C., Patterson, G.H. & Davidson, M.W., 2007. Advances in fluorescent protein technology. *Journal of Cell Science*, 120(24), pp.4247–4260.

Sheng, Z., Rettig, J. & Takahashi, M., 1994. Identification of a Syntaxin-Binding Site on N-Type Calcium Channels. *Cell*, 13, pp.1303–1313.

Smith, I.F. et al., 2009. Ca 2 + puffs originate from preestablished stable clusters of inositol trisphosphate receptors. *Science Signaling*, 2(98), pp.1–7.

Sollner, T. et al., 1993. SNAP receptors implicated in vesicle targeting and fusion. *Nature*, 362, pp.318–324.

Söllner, T. et al., 1993. A protein assembly-disassembly pathway in vitro that may correspond to sequential steps of synaptic vesicle docking, activation, and fusion. *Cell*, 75, pp.409–18.

Spafford, J.D. et al., 2003. Calcium channel structural determinants of synaptic transmission between identified invertebrate neurons. *Biochemistry*, 278(6), pp.4258–4267.

Stanley, E.F. & Mirotznik, R.R., 1997. Cleavage of syntaxin prevents G-protein regulation of presynaptic calcium channels. *Nature*, 385, pp.340–343.

Stein, A. et al., 2009. Helical extension of the neuronal SNARE complex into the membrane. *Nature*, 460(7254), pp.525–528.

Steyer, J.A. & Almers, W., 2001. A real-time view of life withing 100 nm of the plasma membrane. *Nature reviews. Molecular Cell Biology*, 2, pp.268–276.

Steyer, J.A., Horstmann, H. & Almers, W., 1997. Transport, docking and exocytosis of single secretory granules in live chromaffin cells. *Nature*, 388, pp.474–8.

Stryer, L., 1978. Fluorescence energy transfer as a spectroscopic ruler. *Annual Review of Biochemistry*, 47, pp.819–46.

Stryer, L. & Haugland, R.P., 1967. Energy transfer: a spectroscopic ruler. *Proceedings of the National Academy of Sciences of the United States of America*, 58(2), pp.719–26.

Su, S. et al., 2013. Genetically encoded calcium indicator illuminates calcium dynamics in primary cilia. *Nature Methods*, 10, pp.1105–7.

Sudhof, T.C. & Rothman, J.E., 2009. Membrane fusion : grappling with SNARE and SM proteins. *Science*, 323, pp.474–477.

Sutton, R.B. et al., 1998. Crystal structure of a SNARE complex involved in synaptic exocytosis at 2 . 4 A resolution. *Nature*, 395, pp.347–353.

Sutton, R.B. et al., 1995. Structure of the first C2 domain of synaptotagmin I: a novel Ca2+/phospholipid-binding fold. *Cell*, 80, pp.929–38.

Tallini, Y.N. et al., 2006. Imaging cellular signals in the heart in vivo: Cardiac expression of the high-signal Ca2+ indicator GCaMP2. *Proceedings of the National Academy of Sciences of the United States of America*, 103(12), pp.4753–8.

Tasaki, I. & Hagiwara, S., 1957. Demonstration of two stable potential states in the squid giant axon under tetraethylammonium chloride. *The Journal of General Physiology*, 40(6), pp.859–885.

Torday, J.S. & Rehan, V.K., 2009. Cell communication insights the evolution of cell communication : the road not taken. *Cell Communication Insights*, 2, pp.17–25.

Trimble, W.S. & Scheller, R.H., 1988. Molecular biology of synaptic vesicle-associated proteins. *TINS*, 11(6), pp.241–242.

Tsien, R.Y., 1998. The green fluorescent protein. *Annual Review of Biochemistry*, 67, pp.509–544.

Valenstein, E.S., 2002. The discovery of chemical neurotransmitters. *Brain and cognition*, 49, pp.73–95.

Watanabe, H. et al., 2010. Involvement of Ca 2ς Channel Synprint Site in Synaptic Vesicle Endocytosis. , 30(2), pp.655–660.

Weidman, P.J. et al., 1989. Binding of an N-ethylmaleimide-sensitive fusion protein to Golgi membranes requires both a soluble protein(s) and an integral membrane receptor. *The Journal of Cell Biology*, 108, pp.1589–96.

Wit, H. De et al., 2006. Docking of Secretory Vesicles Is Syntaxin Dependent. *PloS one*, 1(1), p.e126.

Young, J.Z., 1936. Structure of nerve fibres and synapses in some invertebrates. *Cold Spring Harbor Symp. Quant. Biol.*, 4, pp.1–6.

Zhao, Y. et al., 2011. An expanded palette of genetically encoded Ca2+ indicators. *Science*, 333, pp.1888–1891.

Chapter 2 Methods

Throughout the work presented in this thesis, standard cell and molecular biology techniques (Figure 2.1) provide the framework in which all subsequent research advancements are built upon. As such, standard solutions, which originated from established and pre-existing procedures and protocols, where required throughout the work and are listed here in detail and for reference and referred to throughout the thesis. Advanced, novel and new techniques developed in this thesis are presented in the associated chapters discussing the results. All chemicals were purchased from Sigma-Aldrich, unless otherwise indicted.

2.1 Molecular Biology Methods

2.1.1 Solutions

L – Broth (LB) Media

- 1 % (w/v) Tryptone
- 0.5 % (w/v) Yeast extract
- 1 % (w/v) NaCl
- ddH_2O
- pH adjusted to 7.4 (with NaOH)

LB Agar

- LB media
- 1.5 % (w/v) Agar

10 x Tris-Borate-EDTA Buffer (TBE)

- 1 M Tris
- 1 M Boric acid
- 20 mM EDTA
- ddH_2O
- pH adjusted to 8.3

1 % Agarose Gel

- 1 % (w/v) Agarose
- 1 x TBE
- 0.001 % (v/v) Sybersafe

Orange G (10x)

- 40 % (w/v) Sucrose
- 0.2 % (w/v) OrangeG
- ddH_2O

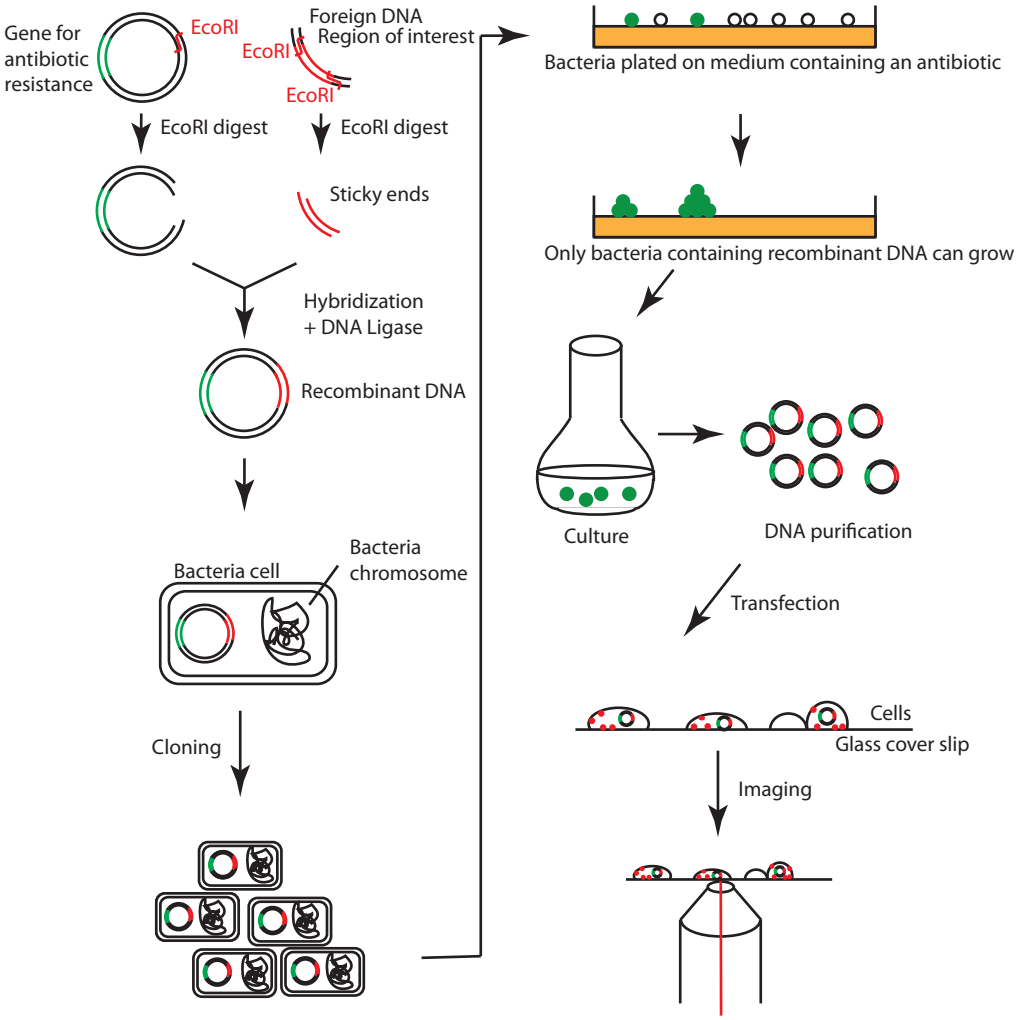

Figure 2.1 Molecular engineering. Cloning a plasmid involves cutting and ligating DNA strands to engineer the required DNA sequence, and amplifying the vectors with bacterial cultures. The vectors are transfected into cells, which express the proteins, and can be imaged.

2.1.2 DNA Constructs from Addgene

Several DNA constructs containing specific cDNA sequences were purchased from Addgene, a non-profit plasmid repository (www.addgene.org) (Table 2.1). The DNA constructs used to assemble the full $Ca_v2.2$ channel cDNA sequences included the full α_{1B} sequence, the α_{1B}-$_{\Delta 18a}$ sequence, with a few exon deletions, the β_3 subunit sequence and the $\alpha_2\delta_1$ subunit sequence. The R-GECO1.0, G-GECO1.1 and GEX-GECO1.0 DNA constructs (Zhao et al. 2011) were ordered for performing the calcium imaging experiments discussed throughout the thesis.

Table 2.1 DNA constructs from Addgene

Construct name	Plasmid number	DNA Backbone	Antibiotic resistance
CaV2.2e [a10,18a,Δ24a,31a,37b,46]	#26568	pcDNA/V5-His ABC	Ampicillin
CaV2.2e [Δa10,Δ18a,Δ24a,31a,37b,46]	#26570	pcDNA/V5-His ABC	Ampicillin
Cavb3	#26574	pcDNA3.1/Zeo	Ampicillin
CaVa2d1	#26575	pcDNA3.1/Hygro	Ampicillin
CMV-R-GECO1.0	#32444	-	Ampicillin
CMV-G-GECO1.1	#32445	-	Ampicillin
CMV-GEX-GECO1.0	#32443	-	Ampicillin

2.1.3 Standard Constructs

Several cDNA constructs are available that encode different fluorescent proteins with a multiple cloning site (MCS) at either the 5' (N) or 3' (C) end of the sequence (Clontech, UK) (Table 2.2). A number, 1, 2 or 3, indicates the reading frame of the fluorescent protein cDNA start codon relative to the MCS. A number of plasmid constructs have been cloned as part of previous research projects and are commonly used by members of the laboratory in which the main experiments of this thesis were performed. The ones used for imaging purpose in this thesis were fluorescently tagged SNAP25B and fluorescently tagged neuropeptideY (NPY).

Table 2.2 DNA plasmids

Construct	Protein DNA inserted	Antibiotic resistance	Cloned by
pmCherry-C1	-	Kanamycin	-
pEGFP-N1	-	Kanamycin	-
pEGFP-C1	-	Kanamycin	-
pEGFP-C2	SNAP25B (*M.musculus*)	Kanamycin	Colin Rickman
pmCherry-C2	SNAP25B (*M.musculus*)	Kanamycin	Colin Rickman
pmCherry-N1	NeuropeptideY (*Rattus nerwegicus*)	Kanamycin	Charlotte Hamilton
pEGFP-N1	NeuropeptideY (*Rattus norwegicus*)	Kanamycin	Colin Rickman

2.1.4 Polymerase Chain Reaction

The polymerase chain reaction (Saiki et al. 1988) is a biotechnology method of DNA amplification through enzymatic duplication of the template DNA strand. Several heating and cooling cycles allow the multiplication from just a few DNA strands to many thousand copies.

2.1.4.1 Primers

Primers are short DNA sequences used for PCRs. As the reverse complement sequence of the original sequence, the primers bind to the DNA strand from where the amplification is initiated. All custom designed primers were purchased from SigmaAldrich, UK.

2.1.4.2 Standard PCR

A standard PCR setup was prepared using the Expand kit (Roche) (Table 2.3). This enzyme mix contains the thermostable *Taq* DNA polymerase as well as the thermostable *Tpo* polymerase with proofreading properties in 3' – 5' direction. This ensures fast but accurate copying of the template DNA.

Cycle length and temperature were adjusted specific for each reaction depending on the template cDNA characteristics such as length and base pair composition (Table 2.4). The melting temperature (T_m) was approximated by using the following formula:

$$Tm = (4\,GC) + (2\,AT) \qquad 2.1$$

The optimal elongation temperature for the expand enzymes is 72°C, unless the DNA template is >3kb, at which the elongation temperature is reduced to 68°C.

Table 2.3 Standard PCR setup

Solutions	Stock concentration	Volume quantity for PCR
Template DNA	1 mg/ml	1 µl
PCR Buffer	10 x	1 µl
dNTPs	10 mM	1 µl
Forward primer	0.1 mg/ml	1 µl
Reverse primer	0.1 mg/ml	1 µl
ddH_2O	-	44 µl
Enzyme mix	-	1 µl
Total		**50 µl**

Table 2.4 Standard PCR cycle parameters

Number and length of cycles		Temperature	PCR cycle
1 x	2 min	95°C	Denaturation
30 x	30 sec	94°C	Denaturation
	30 sec	55°C	Annealing
	30 sec per 1000 bps	72°C	Elongation
1x	4 min	72°C	Extension
1x	-	4°C	Hold

2.1.4.3 Single-site Mutagenesis

The QuikChange II Site-Directed Mutagenesis (Agilent Technologies) was used for point mutations as this kit exploits the properties of *Pfu* Turbo DNA polymerase, which replicates both strands of the template DNA without displacing the mutant primers (Table 2.5).

Table 2.5 Single-site mutagenesis PCR setup

Solutions	Stock concentration	Volume quantity for single-site mutagenesis PCR
Template DNA	1 mg/ml	1 µl
PCR Buffer	10 x	5 µl
dNTPs	10 mM	1 µl
Forward primer	0.1 mg/ml	1 µl
Reverse primer	0.1 mg/ml	1 µl
QuikSolution	-	1.5 µl
ddH_2O	-	38.5 µl
Enzyme mix	-	1 µl
Total		**50 µl**

2.1.4.4 Multi-site Mutagenesis

QuikChange Lightning Multi-site directed Mutagenesis (Agilent Technologies) allows two primers to cover two separate sites of mutation (Table 2.6). Both primers initiate reading in the same direction, creating a single strand of the entire construct DNA. The template DNA is destroyed with the treatment of *Dnp*I, a restriction enzyme that only targets phosphorylated DNA, which is the template DNA. The single stranded DNA is transformed into bacteria, where they are replicated and transformed back into double stranded DNA containing the two mutated sites.

Table 2.6 Multi-site mutagenesis PCR setup

Solutions	Stock concentration	Volume quantity for multi-site mutagenesis PCR
Template DNA	1 mg/ml	1 µl
PCR Buffer	10 x	2.5 µl
dNTPs	10 mM	1 µl
Forward primer	0.1 mg/ml	1 µl
Reverse primer	0.1 mg/ml	1 µl
QuikSolution	-	1.5 µl
ddH_2O	-	16 µl
Enzyme mix	-	1 µl
Total		**25 µl**

2.1.5 Cloning Kit for PCR Products

Several kits have been produced that facilitate the insertion of PCR products into constructs. Two of these used are the CloneJet PCR Kit (ThermoScientific), specialized for blunt end PCR products, and the pGEMT EASY kit (Promega), dedicated for PCR products with adenine (A) extensions to match the thymine (T) sticky ends of the vectors.

2.1.6 Restriction Enzymes and Digests

Restriction enzymes are enzymes that cut at very specific DNA sites, usually encoded by 4 – 8 nucleotides, often in a palindromic configuration (Table 2.7). The enzyme cuts through both sugar-phosphate strands to enable DNA separation, and these cuts can be either at the exact same site, creating blunt ends, or several nucleotides apart, creating sticky ends.

Fast digest restriction enzymes supplied by Fermentas were used with the exception of *Sac*II, a slow digest enzyme. Fast digest enzymes have a 100 % efficiency in the optimal pH, glycerol condition and ionic strength given by the FastDigest buffer. A digest can be

set up with multiple FastDigest enzymes (Table 2.8), which only need a 5 – 15 minute incubation period for a full digest. In comparison to conventional enzymes, which require an hour each, this is a considerably time efficient process. All digests were set up with the DNA, restriction enzyme, digest buffer and ddH_2O and were incubated in a 37°C water bath for 15 minutes for the reaction to take place.

Table 2.7 Restriction enzymes

Restriction enzymes	DNA recognition site	Fast or slow enzyme	Supplier
***Age*I**	A|CCGG T T GGCC|A	Fast	Fermentas
***Bgl*II**	A|GATC T T CTAG|A	Fast	Fermentas
***BsrG*I (Bsp1407I)**	T|GTACA A CATG|T	Fast	Fermentas
***Dpn*I**	GA|TC CT|AG	Fast	Roche
***EcoR*I**	G|AATT C C TTAA|G	Fast	Fermentas
***Kpn*I**	G GTAC|C C|CATG G	Fast	Fermentas
***Sac*II**	CC GC|GG GG|CG CC	Slow	Fermentas

Table 2.8 Digest setup

	Test Digest	Full Digest
DNA	1 µl	3 µl
Restriction enzyme	1 µl	3 µl
Fast digest buffer	1 µl	3 µl
H_2O	7 µl	21 µl
Total volume	**10 µl**	**30 µl**

2.1.7 Ligation

The enzyme ligase (ThermoScientific) ligates two complementary ends of DNA together that have been cut with the same restriction enzyme. Ligations were set up in a 1:3, 1:1 and 3:1 ratio of vector to insert to ensure the best possible result (Table 2.9). The reaction was left to incubate for 30 minutes at room temperature. Controls were set up without the insert, as a high background would indicate the re-ligation of the vector without the insert.

Table 2.9 Ligation setup

	1:3	1:1	3:1	Control
DNA Vector	1 µl	1 µl	3 µl	1 µl
DNA Insert	3 µl	1 µl	1 µl	-
Ligase	1 µl	1 µl	1 µl	1 µl
Ligation Buffer	5 µl	5 µl	5 µl	5 µl
H_2O	-	2 µl	-	3 µl
Total volume	**10 µl**	**10 µl**	**10 µl**	**10 µl**

2.1.8 Gel Electrophoresis

Gel electrophoresis is a technique performed to separate DNA strands by size. This is either performed on samples in which DNA strands have to be isolated for further use or to ensure the DNA cloning result is correct through characteristic band sizes when cut with certain restriction enzymes. A 1 % agarose gel was prepared containing Sypersafe (Invitrogen) to visualize the DNA strands. The DNA was mixed with OrangeG dye (10:1), which is a marker diffusing similarly to very short DNA molecules. The electrophoresis was run at 100 mV for 30 - 45 minutes, depending on the expected size of the fragments.

2.1.9 DNA Extraction from Agarose Gel

For DNA extraction from an agarose gel the bands were excised from the agarose gel. The DNA was extracted using the GeneJet Gel Extraction Kit (ThermoScientific) according to manufacturers instructions. In a 1.5 ml eppendorf tube, the gel was dissolved at 50°C in 3 times its weight in a chaotopic agent, which disrupts hydrogen bonding between the agarose molecules and hence weakens the links allowing the gel to liquefy. The liquid was run through a spin column, collecting the DNA in the column. This was washed with 70 % (v/v) ethanol before the elution step of a small 30 µl volume of ddH_2O or the buffer provided in the kit.

2.1.10 Antibiotics

All the plasmids used had either a resistance gene against ampicillin or kanamycin. The antibiotics were added in a 1/1000 ratio i.e. 250 µl ampicillin into a 250 ml LB flask, to obtain a final concentration of 100 µg/ml for ampicillin and 50 µg/ml for kanamycin.

2.1.11 Bacterial Culture

XL-10 Gold bacteria (Agilent Techniolgies) *E .coli* are ultracompetent bacterial cells with an extremely high transformation efficiency of $5x10^9$ cfu/µg pUC18 DNA (Cfu – colony forming unit; pUC (plasmid University of California) plasmid size is 2.7kb).

These cells were stored at -80˚C and defrosted on ice when required for transformations.

2.1.12 Transformation

For the transformation of DNA vectors into bacterial cells XL10 Gold cells were defrosted slowly on ice. It is very important to keep everything, eg. eppendorf tubes, ice cold before the heat-shock. 45 µl of XL10 Gold cells were mixed with 5 µl of the ligation mix or 1 µl of pure 1 mg/ml DNA and left on ice for 20 minutes before the heat-shock in a 42°C water bath to enable the uptake of DNA into the bacterial cells. The cells were then incubated on ice for a recovery period of 5 minutes before 500 µl LB was added. The bacterial cells were then shaken vigorously at 37°C for 30 minutes to allow the cells to recover and express the proteins of the antibiotic resistance gene. Finally, 100 µl was plated on agar plates containing the correct antibiotics, either ampicillin or kanamycin, and placed in a 37°C incubator for 16 hours to allow for colonies to grow.

2.1.13 Plasmid Preparation

Single bacterial colonies from the agar plates were picked and separately cultured in 5 ml LB containing the correct antibiotic of either ampicillin or kanamycin. For a small amplification, a miniprep, these were cultured for 16 hours at 37°C on a shaker before extracting the DNA using the GeneJet Plasmid Miniprep Kit (ThermoScientific) following the manufacturers protocol. For a maxiprep the 5 ml starter cultures were transferred into a 250 ml LB flask and incubated for 16 hours at 37°C on a shaker before DNA extraction using the HiPure Plasmid Maxiprep Kit (Invitrogen), again following the manufacturers instructions. The extraction of plasmid DNA from bacteria follows the same procedure and principles. Pelleted cells are re-suspended in an alkaline solution containing 50 mM glucose to maintain osmotic pressure, 25 mM Tris-Cl, to buffer the cells at pH 8, and 10 mM EDTA, which binds to divalent cations in the lipid bilayer weakening the outer layer of the cell. After lysis, EDTA also prevents the degradation of DNA by binding Mg^{2+} ions. A second solution is added that contains 1 % (w/v) SDS detergent to dissolve the cellular lipid membranes sodium hydroxide (NaOH) which denatures plasmid and chromosomal DNA into single strands, however the circular plasmid DNA stay linked together. A third solution neutralizes the mixture with the addition of acetic acid to allow the plasmid DNA to re-anneal. An addition of potassium acetate precipitates the SDS-lipid-protein amalgamation, which traps the partially hybridized chromosomal strands. After filtering or centrifugation the remaining fluid containing the plasmid DNA and RNA is run through a column, washing and purifying the plasmid DNA before re-collection by elution with a TE buffer

containing 10 mM Tris-Cl and 1 mM EDTA, which limits DNA degradation through bacterial nucleases which require divalent cations as a cofactor. The final concentration for maxiprep DNA purification was adjusted to 1 mg/ml.

2.1.14 DNA Quantification

DNA quantification was performed using a NanoDrop 2000c device (ThermoScientific) to measure the nucleic acid content of the solution compared to a reference standard that was set with the same solution the DNA was dissolved in, either ddH_20 or TE elution buffer. The molecular content was adjusted to 1 mg/ml for storage in a -20°C freezer.

2.1.15 Sequencing

Sequencing is essential for the verification of DNA sequences of the cloned plasmids.

All constructs were sequenced by SourceBioscience, either requesting the use of standard or specifically designed primers that covered the DNA sequence. The sequences were checked and confirmed using an alignment feature in the software Geneious, to compare the measured sequences to the expected sequence, ensuring no random mutation has been incorporated.

2.1.16 Final Constructs

cDNA sequences were cloned into constructs to allow expression of a fusion protein of the protein of interest labelled with a fluorescent protein (Table 2.10).

The α_{1B} subunit (full length) and the α_{1B} subunit (Δ18a) of the $Ca_V2.2$ channel were cloned into EGFP-C1 and mCherry-C1 vectors. Exon 18a contains the synprint sequence, which is why one sequence with and one without 18a were obtained and cloned into constructs for comparison measurements. The other exons do not affect the synprint site, but are listed for identification purpose.

Table 2.10 Final constructs

Construct	Exon details	Antibiotic resistance
EGFP-C1- $Ca_V2.2$-α_{1B}	a10,18a,Δ24a,31a,37b,46	Kanamycin
EGFP-C1- $Ca_V2.2$-α_{1B} [Δ18a]	Δa10,Δ18a,Δ24a,31a,37b,46	Kanamycin
mCherry-C1- $Ca_V2.2$-α_{1B}	a10,18a,Δ24a,31a,37b,46	Kanamycin
mCherry-C1- $Ca_V2.2$-α_{1B} [Δ18a]	Δa10,Δ18a,Δ24a,31a,37b,46	Kanamycin
R-GECO1.0-SNAP25	-	Kanamycin

2.1.17 Immunostaining

Immunostaining is a method to visualize endogenous proteins in fixed cells by tagging them with a protein-specific primary antibody and a fluorescently labelled secondary antibody.

For the immunostaining procedure (Table 2.11) the samples were first fixed with two aldehydes, 4 % (w/v) paraformaldehyde (PFA) and 0.1 % (v/v) glutaraldehyde, which crosslink proteins together for rigidity. The sample is then treated with ammonium chloride to eliminate the autofluorescence of PFA, after which the detergent TritonX-100 is used in a 0.5 % (v/v) dilution to partially dissolve some of the lipids to allow access for the antibody staining inside the cell. This is followed by a 1 hour incubation with 0.5 % (w/v) fish skin gelatine (FSG) solution, that acts to block non-specific binding sites. The primary antibody are usually diluted in 0.5 % (w/v) FSG solution to 1:500 – 1:5000, depending on how good the antibody properties are. The sample is immersed and incubated in this solution for 3 hours, before a series of gentle but thorough washes before incubation of the secondary antibody, diluted 1:1000 in 0.5 % (w/v) FSG. The sample is covered during incubation to avoid photo-bleaching of the fluorescent probe by background lighting. The sample is washed 4 times, before being stored in the fridge ready to be imaged.

Table 2.11 Immunostaining procedure

Steps	Duration	Purpose of step
3 x PBS (1x) wash	5 min each	Clean off debris and proteins in the media
PFA + 0.1 % (v/v) glutaraldehyde	30 min	Fixation of cells
3 x PBS wash	5 min each	Clean off PFA
50 mM NH_4Cl	10 min	Suppression of PFA fluorescence
2 x PBS (1x) wash	5 min each	Wash off NH_4Cl
0.5 % (v/v) Triton X	4 min	Partially dissolves membrane lipids
2 x PBS (1x) wash	5 min each	Wash of the detergent
0.5 % (w/v) FSG	1 hour	Unspecific blocking
Primary antibody (in FSG)	3 hours	Protein-specific staining
3 x PBS (1x) wash	5 min each	Wash off any remaining primary antibody
Secondary antibody (in FSG)	1 hour	Stain for primary antibody
4 x PBS (1x) wash	5-10 min each	Remove all antibodies to keep the sample as clean as possible

2.2 Tissue Culture

2.2.1 Cell Storage

Cell line stocks were stored in the vapour phase of liquid nitrogen, at –180°C, just above the boiling point at -196°C. Confluent cells in one 75 cm^2 flask were spun down and re-suspended in a volume of 1.5 ml of complete media, which is then aliquoted in 0.5 ml volumes into three sterile cryovials. The same amount of freezing media consisting of complete media supplemented with 20 % (v/v) of a tissue culture (TC)-grade sterile cryoprotective agent dimethylsulfoxide (DMSO) is added, reducing the final DMSO concentration to 10 % (v/v). The DMSO acts to reduce the freezing temperature as well as the cooling rate to reduce the risk of ice crystal formation and hence damaging the cells. The sterile and labelled cryovial tubes, with the cells, are placed into a freezing apparatus which slows the cooling to 1°C a minute. Cells were left in a freezing vessel in a -80°C freezer overnight to ensure slow cooling, before deposited long term in a liquid nitrogen storage chamber. One tube was defrosted soon after freezing to check viability of the cells, to make sure the batch of cell line has been well preserved.

Defrosting cells has to happen fast, taking one cryovial out of the liquid nitrogen storage and defrosting in a 37°C water bath before transferring the liquid into a 15 ml Falcon tube and very gently adding 5 ml of warm complete media. Cells were either spun down and re-suspended in complete media to remove the DMSO, or they were allowed to recover and settle overnight in a 25 cm^2 flask, before replacing the DMSO containing media with fresh media.

2.2.2 Human Embryonic Kidney Cell Line, HEK293

HEK293 is a fusion cell line derived from human embryonic kidney cells with adenovirus 5 DNA inserted into the genome (Graham et al. 1977). Frank Graham's 293rd experiment resulted in the desired fusion creating a cell line with adhesive properties as well as constant cell division. These cells are not a good model for cellular processes, as with the addition of the adenovirus DNA, the functional processes of the cell are too far removed compared to cancer or neuronal cells. However, due to the easy culturing and high transfection efficiency, they are an excellent cell line to analyse protein conduct, such as ion channels in the plasma membrane, or initial testing of newly cloned plasmid constructs.

Media for HEK 293 cell culture

- Dulbecco's Modified Eagle Medium (DMEM), phenol red, high glucose (4.5 g/l D-glucose) (Gibco)
- 10 % (v/v) Fetal Bovine Serum (FBS) (Gibco)
- 1 % (v/v) Glutamax (Gibco, 100X)
- 1 % (v/v) Pen/Strep, (Gibco, 10000 units/ml, 10000 µg/ml Streptomycin)
- 1% (v/v) Sodium Pyruvate (Gibco)

Passaging cells was done twice a week with a ratio of 1:5 by removing old media from the 75 cm^2 cell culture flask, washing the cells with 5 ml of 1x Versene (Gibco) and then adding 2 ml of 0.05 % (v/v) Trypsin-EDTA (Gibco). After a 2 minute incubation at 37°C the cells were washed off the flask and titurated to break up cells clumped together. Cells were cultured in a 37°C / 5 % CO_2 incubator.

2.2.3 PC12 Cell Line

Exocytosis has been extensively studied using adrenal chromaffin cells either from mice, rats or cows. The rat phaeochromocytoma (PC12) cell line was derived from a tumour in the adrenal medulla of a rat in 1976 (Greene & Tischler 1976), exhibiting similar secretory characteristics to the adrenal chromaffin cells as well as neuronal behaviour after differentiation with nerve growth factors.

Media for PC12 cell culture

- RPMI, phenol red, enhanced with non-essential amino acids and sodium pyruvate (Gibco)
- 10 % (v/v) Horse serum (Hyclone)
- 5 % (v/v) Fetal Calf Serum (Hyclone)
- 1 % (v/v) Glutamax (Gibco, 100X)
- 0.1 % (v/v) Gentamicin (Gibco, 50 mg/ml)
- 1 % (v/v) Sodium Pyruvate

PC12 cells were split once a week, with the ratio 1:3. To split PC12 cells the media in the 75 cm^2 flask was removed and the cells washed with 1x Versene (Gibco), before adding 5 ml of 1x Versene (Gibco) to remove them from the flask by continuously washing the dissociation reagent over the cells with the stripette. The solution was transferred into a 50 ml conical falcon tube and spun in a centrifuge for 3 minutes at about 200 *g*. The solution was decanted and cells re-suspended in 9 ml RPMI media. One third was

transferred into a fresh collagen coated flask for further culturing. Cells were cultured in a 37°C / 7.5 % CO_2 incubator.

2.2.4 AtT20 D16:16, Mouse Pituitary Cell Line

The adherent AtT20 D16:16 cell line is derived from a radiation-induced mouse anterior pituitary tumour, specialized for adrenocorticotrophic hormone (ACTH) (Furth et al. 1953) and β-endorphin secretion (Reisine et al. 1985). These excitable cells exhibit frequent spontaneous bursts of action potential initiating a slow Ca^{2+}-dependent depolarization followed by a Ca^{2+}-dependent K^+-driven hyperpolarization. Secretion is stimulated by the action of corticotrophin releasing factor (CRF), vasopressin (VP), oxytocin (OXY) and angiotensin II in the body but other agents such as norepinephrine, isoproterenol and 8-bromo-cAMP can stimulate in vitro secretion. CRF induces a slight membrane depolarization, which facilitates action potential generation, eliciting Ca^{2+} transients through voltage-gated calcium channels and hence prompting secretion.

Media for AtT20 D16:16 cell culture

- Dulbecco's Modified Eagle Medium (DMEM), phenol red, high glucose (4.5 g/l D-glucose) (Gibco)
- 10 % (v/v) Fetal Bovine Serum (FBS) (Gibco)
- 1 % (v/v) Glutamax (Gibco, 100X)
- 1 % (v/v) Pen/Strep (Gibco, 10000 units/ml, 10000 µg/ml Streptomycin)
- 1 % (v/v) Sodium Pyruvate

Passaging cells was done twice a week in a ratio of 1:3 by removing old media from the flask, washing the cells with 5 ml of 1x Versene (Gibco) and then adding 2 ml of 0.05 % (v/v) Trypsine-EDTA (Gibco). After a two minute incubation at 37°C the cells were washed off the flask. These cells have to be treated with care so they were not titurated as HEK293 cells were. Cells were cultured in a 37°C and 5 % CO_2 incubator.

2.2.5 Cell Counting

The haemocytometer was used to count cells before plating them onto coverslips at a specific cell density. A 4 x 4 square corner grid, which is 0.1 mm^3 (1 mm x 1 mm x 0.1 mm) in volume, is used in which the total number of cells can be calculated according to: number of cells in 1 ml given by x = (No of cells in 4 x 4 square x 1000 µl) / 0.1 µl. Due to the different growth rate of the cell lines, they were plated at different densities to reach 80 % confluency for transfection. For PC12 cells 1.6 million cells were plated, for HEK293 0.6 million cells and AtT20 D16:16 0.8 million cells were plated per well.

2.2.6 Preparation of Coverslips

Glass coverslips had to be cleaned thoroughly to reduce the amount of machine oil and contaminants that disrupt high-resolution imaging, and they had to be coated with poly-D lysine to enhance cell adhesion to the glass.

Glass coverslips were sonicated in a detergent-containing bath for 30 seconds, before thoroughly washing off the sonication buffer with ddH_2O, and submerging them in 100 % (v/v) -ethanol and -acetate for 30 seconds each. A wash with water removed any residual acid before leaving them to coat in a 50 mM PDL solution for 1 hour. The coverslips were then dried under UV for sterilization.

2.2.7 Transfection

Transfection is a method to introduce plasmid DNA into cells for protein expression with the purpose of imaging. Two different methods were used; Lipofectamine 2000 (Invitrogen) was used for PC12 cells and TurboFect (ThermoScientific) was used for HEK293 and AtT20 D16:16 cell transfections.

The lipofectamine reagent is made up of cationic lipid subunits that assemble into liposomes in aqueous solution. These can encapsulate the plasmid DNA, cancelling out their negative charge, allowing the positively charged liposomes to merge with the negatively charged plasma membrane of the cells. This releases the plasmid DNA into the intercellular space from where it gets into the nucleus either during cell division, or by penetrating the nuclear envelope in a similar fashion as the plasma membrane.

Lipofectamine 2000 (Invitrogen) was used according to manufacturer's instruction by mixing 4 µl DNA (at 1 mg/ml) with 250 µl clear, serum free media and 10 µl Liopfectamine 2000 with 250 µl clear, serum free RPMI media in 2 separate 15 ml falcon tubes before adding them together and leaving them for 20 minutes to allow the DNA to bind to the Lipofectamine. Each well was transfected with 500 µl of transfection mix. In the case of a double transfection 2 µl of each DNA construct was used. In the case of a triple transfection, again, 2 µl of each DNA construct was used but the Lipofectamine 2000 was adjusted to 15 µl.

TurboFect is a solution of proprietary cationic polymers that envelope plasmid DNA and condense them into positively-charged complexes, which allows the penetration through the plasma membrane, as well as through the nuclear envelope.

For the TurboFect transfection, 4 µl DNA at 1 mg/ml per well was mixed with 400 µl colourless, serum-free media and 6 µl Turbofect reagent. This was left to incubate for 15 – 20 minutes before adding 400 µl to the well.

The transfected cells were left to incubate and express the proteins for a 24-48 hour

period before imaging.

2.3 Microscopy

2.3.1 Nyquist sampling rate

The Nyquist rate defines the ideal x-y-z sizes of a voxel, a single point of the image, when imaging and depends on the optics of the microscope and the excitation and emission wavelength. Sampling itself is the process of the analogue-to-digital signal conversion. The sampling density or sampling rate is the number of recorded signals per unit distance. As the images are assembled by the acquisition of PSFs, the sampling rate must at least cover the distance of a single PSF, otherwise it is impossible to distinguish between PSFs. However, the analogue-to-digital conversion the sampling rate is required to be at least twice the frequency to be able to reconstruct the original sampled image. For the widefield microscope, the lateral Δ_x and axial Δ_y sampling rate is defined by the lens immersion refractive index (n, usually of immersion oil) and the half aperture angle (α) of the objective:

$$\Delta_x = \frac{\lambda em}{4n \sin(\alpha)}$$
$$\Delta_z = \frac{\lambda em}{2n\,(1 - \cos(\alpha))} \qquad 2.1$$

The Nyquist sample rate is defined as half the Δ_x and Δ_y sampling rate and is defined as the minimum sampling required to optimally reconstruct a PSF's overall form. Images on the widefield microscope were acquired with a pixel size of 106 nm, which agrees well with the required Nyquist rate. The Nyquist sampling rate differs for the confocal microscope due to the difference in detection method induced by the pinhole. The excitation wavelength is used in the calculation and the lateral Δ_x and axial Δ_y sampling rate have to be divided by two:

$$\Delta_x = \frac{\lambda ex}{8n \sin(\alpha)}$$
$$\Delta_z = \frac{\lambda ex}{4n\,(1 - \cos(\alpha))} \qquad 2.2$$

Again the Nyquist sample rate is half the Δ_x and Δ_y sampling rate. Unlike widefield where sampling is fixed according to camera pixel size and lens NA, one advantage of

confocal microscopy is that sampling can be tuned through controlling the scan details, size and number of points in the image. Optimisation of Nyquist sampling is therefore trivial in confocal microscopy.

2.3.2 Imaging buffer

For live cell imaging, KREB's buffer was used to maintain the physiological ion balance. HEPES was added to buffer and maintain physiological pH, which can fluctuate due to CO_2 concentration changes, keeping the cells in the best condition possible while imaging.

KREB's – HEPES Buffer

- 145 mM NaCl
- 5 mM KCl
- 1 mM $MgSO_4$
- 0.5 mM Na_2HPO_4
- 6 mM Glucose
- 10 mM HEPES at pH7.4 with NaOH
- 1 mM $CaCl_2$
- ddH_2O

The osmolarity was adjusted to 290 mOsm by adding 1 mM glucose for an increase of 1 mOsm, or by adding ddH_2O to decrease the osmolarity. PBS was used for imaging fixed cells.

STORM relies on the switching of fluorescent proteins or dyes into the long-lived, non-fluorescent state (the dark state). To achieve this, cells are bathed in a specific enzymatic oxygen-scavenging buffer containing the enzymes glucose oxidase and catalase, which removes oxygen from the buffer in order to increase photobleaching of the fluorophores. This increases the probability of driving the fluorophores into the dark state before non-reversible bleaching quenching the emission.

The combination glucose oxidase and catalase is very reactive and can result in acidification of the buffer after time, requiring a specific buffer protocol to avoid any pre-imaging reactions.

STORM Imaging Buffer for Alexa 647

- 50 mM 2-Mecaptoethylamine (MEA /Cysteamine)
- 1x PBS
- 0.5 mg/ml glucose oxidase
- 40 µg/ml catalase
- 10% (w/v) glucose

First, an initial buffer is made up by adding 2 g of glucose and 0.1929 g of MEA to 20 ml 1x PBS. The second buffer is a small volume of a 1:100 dilution of catalase formed by adding 0.004 g to 1 ml of the glucose/MEA solution. To make the STORM buffer, 50 µl of diluted catalase is added to 5 ml glucose/MEA solution. Then 0.0025 g glucose oxidase is dissolved in the 5 ml solution, which is put through a SpinX column (Sigma Aldrich, Corning Costar) to filter any non-dissolved particles before using it as the imaging media. The glucose/MEA solution and the diluted catalase solution can be stored in a fridge throughout the day, but the complete STORM buffer has to be made fresh each time and was replaced every two hours.

2.3.3 Confocal Laser Scanning Microscopy

Confocal images were acquired using a Leica SP5 single molecule detection (SMD) gated-STED laser scanning confocal microscope with a HCX PL APO 63x 1.4 NA oil immersion lens. The required wavelength was chosen either on the supercontinuum white light laser (CW) spectrum (470 -670 nm), or by using the argon laser (for 488 nm) or the Helium/Neon (He/Ne) laser (for 633 nm). For 3D imaging the z-steps were set to 100 nm and the x-y sizes were set to the Nyquist sampling rate. PMT detectors were used for image and spectral scan acquisition and Single Photon Avalanche Photodiodes (SPAD) detectors (MicroPhoton Devices, Italy) were used for FLIM detection. Using the Picoquant software, the photons were acquired at microsecond rates using external SPAD detectors.

2.3.4 Widefield and TIRF Microscopy

Widefield and TIRFM imaging were done using an Olympus IX-81 TIRF+ microscope with a 150x 1.45 NA immersion oil lens. The main camera used was the EMCCD camera (Hamamatsu, UK), which has a pixel array of 512 x 512 16 µm pixels, resulting in an effective pixel size of 106 nm when using the 150x lens. The sCMOS camera (Hamamatsu, UK) was used for extremely fast imaging (over 16 Hz), and with the pixel array binned 4 x 4 from 2048 x 2048 to 512 x 512. With an original pixel size of 6.5 μm^2 and using the 150x lens, the resulting effective pixel size is 178 nm. The excitation

sources were 100 mW laser diodes producing 405 nm, 491 nm, 561 nm and 640 nm wavelength excitation beams. The TIRFM angle illumination setting was regulated through the Olympus software Xcellence (Advanced Live Cell Imaging Software), setting the correct angle for each laser excitation beam individually.

For single molecule imaging of the caged dye conjugated to ω-conotoxin GVIA acquisition was done setting multiple cycles of uncaging with 405 nm illumination followed by imaging with the 561 nm illumination in TIRFM mode with a long exposure. Calcium imaging was done in the TIRFM mode using the 561 nm illumination imaging at 60 ms/frame (16 Hz) when capturing the images with the EMCCD camera, or imaging at 10 ms/frame (100 Hz) when acquiring with the sCMOS camera. Because of the addition of toxins during imaging and the complex electrophysiology setup, the temperature could not be held at a consistent 37 °C and therefore calcium imaging was done at 22 °C throughout. As the main limitation is the speed of acquisition, the slight change in kinetics caused by the lower temperature is insignificant.

2.4 Image Analysis

2.4.1 Deconvolution

Confocal microscopy offers a hardware-based solution to significantly reduce the out-of-focus signals of 3D images when compared to the widefield alternative by reshaping the PSF through the introduction of a pinhole to suppress out-of focus light. However, confocal microscopy is not perfect and is susceptible to practical limitations in terms of the ability to truly idealise axially confined 3D point spread functions. As such, and in all work presented here, all three-dimensional images taken on the confocal microscope were deconvolved before further data analysis. Devonvolution is a method that uses an understanding of the system's PSFs to mathematically remove the effect of out-of-focus light by using algorithm-based processing to reconstruct the three-dimensional stack without the PSF distortion. The method utilises either a theoretical PSF, calculated from established optical models using the specific parameters of the microscope, or an experimentally measured PSF from a sub-diffraction limit sized bead imaged under the same conditions as the experiment. By distinguishing the distribution of point sources of light from the overlapping PSF with the actual object image signal, the image stack is reconstructed as accurately as possible without the distortion induced by the PSFs extended shape. Importantly, deconvolution does not improve optical resolution. Information from within the optically defined PSF cannot be recovered, but returns an idealised image without the out-of-focus distortion. The result is a sharper, better

sectioned 3D stack with significantly reduced background.

Deconvolution is a commonly used and established image processing method, which greatly aids further image analysis, such as signal co-localisation analysis (see 2.4.2), where better signal-to-noise show noticeably improved analysis results. However, deconvolution is limited and it is challenging to account for altering PSFs due to depth dependent aberrations and refractive index changes in the sample. However, in this work state-of-the-art methods are applied at the forefront of image processing through the use of the Huygens image software (Scientific Volume Imaging, The Netherlands). Huygens was used to reconstruct the image stacks acquired on the confocal microscope, with the theoretical PSF calculated from the microscope parameters.

2.4.2 Co-localisation Analysis

Co-localisation analysis is an evaluation of the degree of signal overlap between two different channels in an image. A pixel-by-pixel spatial co-localisation analysis is done using either Pearson's or Mander's co-localisation algorithms depending on the sample. Pearson's co-localisation analysis is intensity insensitive but relies heavily on the number of objects in the image. With R and G representing two channels, the average is subtracted from the pixel index *i* in the calculation, making the coefficient independent from the background:

$$r_p = \frac{\sum((R_i - R_{ave})(G_i - G_{ave}))}{\sqrt{\sum(R_i - R_{ave})^2 \sum(G_i - G_{ave})^2}} \qquad 2.3$$

The Pearson's coefficient r_p describes how well the two channels are related by a linear equation and returns a values between -1 and 1. Values close to +/- 1, indicate a higher linear relationship between the voxels of the two channels. Pearson's co-localisation method provides an effective statistic to measure the overall relationship between two fluorescently tagged proteins, but does not provide a measure for the quantity of overlap between the two channels. Mander's co-localisation analysis provides the measure of both fractions of overlap with the other channel. Mander's analysis is calculated based on the intensity of each signal in every pixel (Manders et al. 1993).

$$M_1 = \frac{\sum(R_{i,coloc})}{\sum R_i}$$
$$M_2 = \frac{\sum(G_{i,coloc})}{\sum G_i} \qquad 2.4$$

$R_{i,coloc} = R_i$ if $G_i > 0$ and $R_{i,coloc} = 0$ if $G_i = 0$ and vice versa $G_{i,coloc} = G_i$ if $R_i > 0$ and $G_{i,coloc} = 0$ if $R_i = 0$. This method measured the co-occurrence irrespective of signal proportionality (Dunn et al. 2011).

The Mander's co-localisation method was applied to the image stacks to measure the $Ca_v2.2$ calcium channel trafficking to the plasma membrane and Manders's was again used for the co-localisation analysis of the spatial relationship between $Ca_v2.2$ calcium channels and syntaxin1a. The ImageJ Coloc2 plugin was used for the co-localisation analysis.

2.4.3 Single Molecule Localisation Analysis

Single molecule localisation was analysed by using a Matlab script kindly supplied by Dr Samuel Hess (University of Maine). The script is designed to distinguish PSFs in the single molecule localisation images and determine the coordinates of each molecule. The output is a virtual image of the combined coordinates of each localised molecule.

2.5 Electrophysiology

Cells were observed and selected by light microscopy (Olympus inverted microscope) and subjected to whole- cell voltage clamp using an Axoclamp 2B amplifier (Molecular Devices, LLC CA, United States) operating in continuous mode. The data were acquired (digitized) and stored using 'Clampex' and analysed using 'Clampfit' software (both Molecular Devices, LLC CA, United States, versions 10.3). Series resistance was compensated to 70% and liquid junction potentials were measured but not subtracted. Recordings were made at 22°C using $AgCl_2$ electrodes and filamented borosilicate glass pipettes with resistances of between 3-7 MΩ. The bath solution contained (mM): 140 NaCl, 4 KCl, 1.8 CaCl2, 1 MgCl2, 10 HEPES, 10 Glucose, pH = 7.4. The pipette solution contained (mM): 100 mM CsCl, MgCl, 10 EGTA, 40 HEPES free acid, 5 Na-ATP, 5 GTP, pH = 7.2 (295 mOsm/kg). Recordings were judged suitable for analysis if under voltage clamp, the holding current at -60 mV was less than -100 pA. Voltage clamped currents were recorded in 10mV steps from -70 to +80mV every 2 s.

References

Dunn, K.W., Kamocka, M.M. & McDonald, J.H., 2011. A practical guide to evaluating colocalization in biological microscopy. *American journal of physiology. Cell physiology*, 300(4), pp.723–42.

Furth, J., Gadsen, E.L. & Upton, A.C., 1953. ACTH secreting transplantable pituitary tumors. *Experimental Biology and Medicine*, 84(1), pp.253–254.

Graham, F.L. et al., 1977. Characteristics of a human cell line transformed by DNA from human adenovirus type 5. *The Journal of general Virology*, 36, pp.59–72.

Greene, L.A. & Tischler, A.S., 1976. Establishment of a noradrenergic clonal line of rat adrenal pheochromocytoma cells which respond to nerve growth factor. *Proceedings of the National Academy of Sciences of the United States of America*, 73(7), pp.2424–8.

Manders, E.M.M., Verbeek, F.J. & Aten, J.A., 1993. Measurement of co-localization of objects in dual-colour confocal images. *Journal of Microscopy*, 169, pp.375–382.

Reisine, T. et al., 1985. Corticotropin-releasing factor-induced adrenocorticotropin hormone release and synthesis is blocked by incorporation of the inhibitor of cyclic AMP-dependent protein kinase into anterior pituitary tumor cells by liposomes. *Proceedings of the National Academy of Sciences of the United States of America*, 82, pp.8261–5.

Saiki, R.K. et al., 1988. Primer-directed enzymatic amplification fo DNA with a thermostable DNA polymerase. *Science*, 239(4839), pp.487–491.

Zhao, Y. et al., 2011. An expanded palette of genetically encoded Ca2+ indicators. *Science*, 333, pp.1888–1891.

Chapter 3 $Ca_v2.2$ Calcium Channel Interactions and Distributions at the Plasma Membrane

The $Ca_v2.2$ calcium channel plays a prominent role in synaptic neurotransmission. The first part of this chapter addresses the spatial relationship of these calcium channels to SNARE proteins, and specifically their functional interaction with syntaxin1a, through the use of several laser-scanning confocal microscopy and spectroscopy techniques, including FLIM-FRET. The second part of this chapter focuses on the development of a new method for single-molecule resolution imaging of $Ca_v2.2$ calcium channels through the development and action of the channel specific toxin ω-conotoxin GVIA.

3.1 Spatial Distribution of $Ca_v2.2$ at the Plasma Membrane

Regulated exocytosis is tightly controlled both temporally and spatially and relies on fast protein-protein interaction in order to enable this efficient process. The proteins involved, SNARE proteins and calcium channels, need to be appropriately spatially arranged to explain this rapid and effective information transfer. Distinct active zones have been identified in synaptic terminals, where vesicles dock and fuse (Ruiz et al. 2011), from which it was concluded that synaptic proteins and calcium channels must be able to interact at the fusion site in a manner that enables efficient conduction of fusion events. In this chapter the focus is on understanding the spatial distribution of $Ca_v2.2$ calcium channels. The initial attention is on the functional interaction between $Ca_v2.2$ channels with the SNARE protein syntaxin1a, which has an impact on the overall spatial distribution of the channels across the plasma membrane. Then the emphasis will be on the development of a unique staining method using ω-conotoxin GVIA to enable single molecule imaging of the $Ca_v2.2$ calcium channel in order to experimentally reveal, with super-resolution imaging the spatial distribution of endogenous $Ca_v2.2$ calcium channels.

3.1.1 Synaptic Protein Interaction Site

The first evidence of SNARE and $Ca_v2.2$ channel binding was through immunoprecipitation analysis, where syntaxin1a was found to bind to $Ca_v2.2$ channels *in vitro* (Bennett et al. 1992). This led to the hypothesis that $Ca_v2.2$ channels are essential not only to generate the calcium signal for fusion, but also for vesicle docking and priming (Sheng et al. 1998). Searching for the interaction site of $Ca_v2.2$ for SNARE proteins, binding assays were developed by separately expressing the intracellular regions of the $Ca_v2.2$ channel and measuring the binding activity to syntaxin1a (Sheng et al. 1994). They found that syntaxin1a binds to the intracellular II-III loop (718-1145 in the amino acid sequence) of the α_{1B}-subunit (Figure 1.4). This was followed up by further investigation narrowing the identified sequence to between amino acids 773 and 859, which structural properties contain three helices linked by two loop sections (Sheng et al. 1994). This binding site was coined *syn*aptic *pr*otein *int*eraction site (synprint) (Sheng et al. 1998) by Catteralls group, who were prominent in researching this interaction.

In addition to syntaxin1a, SNAP-25 and synaptotagmin were also found, again by immunoprecipitation, to bind to the synprint site of α_{1B}-subunit (Sheng et al. 1997). More importantly, however, the synprint motif and synaptotagmin were found to competitively interact with syntaxin1a, suggesting a complex mechanism in which the

channel interacts in a Ca^{2+}-dependent manner, with different SNARE proteins during the pre-fusion phase of exocytosis (Sheng et al. 1997). The importance of the synprint site became apparent by a complete block of exocytosis in the presence of intracellularly injected synprint peptides, which was postulated to competitively bind to syntaxin1a and therefore increase the distance between the docked vesicle and the calcium channel, reducing the probability of fusion (Sheng et al. 1998). At this time, around 1998, a working hypothesis was developed as to how the calcium channels and SNARE proteins would arrange and bind, taking into consideration that different Ca^{2+} concentration alters protein affinities; a biphasic effect leading to spatial rearrangement. This hypothesis put forward that, in resting Ca^{2+} concentration (<10 μM) levels, the vesicle would loosely dock to a low-affinity complex of $Ca_v2.2$, binding to syntaxin1a and SNAP-25. With a Ca^{2+} concentration increase to 10-20 μM the affinity of the complex coupling increases in strength. However, a Ca^{2+} concentration threshold of > 20 μM reduces the affinity of syntaxin 1a and SNAP-25 for the synprint site, which instead bind to synaptotagmin in order to fuse (Sheng et al. 1998).

The working hypothesis outlined above, which was mainly deduced by *in vitro* protein biochemistry, was supported by several experiments observing the functional behaviour related to the synprint site, which revealed important modulatory effects of syntaxin1a on $Ca_v2.2$ channels. The phosphorylation of the synprint site by protein kinase C (PKC) or calcium/calmodulin dependent protein kinase II (CaMKII) inhibits syntaxin1a binding (Yokoyama et al. 1997), which suggests that, depending on molecular arrangement with other synaptic proteins, the modulatory effect of syntaxin1a on $Ca_v2.2$ can be switched on and off (Yokoyama et al. 2005). This modulatory binding effect, demonstrated by using a mutated syntaxin1a, where the ability to bind to the synprint site through the H3 domain is abolished, turned out to be an inhibition of $Ca_v2.2$ opening through syntaxin1a binding to the synprint site (Wu et al. 1999). The reverse experiment, the expression of a splice variant α_{1B}-subunit lacking of the synprint site, showed the same result; a decrease in channel activity when bound to syntaxin1a (Bezprozxanny et al. 1995). However, the removal of the synprint site, and hence the increased spontaneous calcium channel activity did not increase the overall fusion activity (Harkins et al. 2004). This presented a seemingly conflicting result, however it led to the conclusion that syntaxin1a bound to $Ca_v2.2$ channels would inhibit spontaneous activity and avoid unnecessary calcium entry that may trigger unwanted fusion. At fusion sites though, the assembly and interaction of synaptic proteins with synatxin1a and the phosphorylation of the synprint site provides a

mechanism to ensure selective opening of channels at fusion sites (Keith et al. 2007; Zamponi 2003).

The experiments and work described above underline the significance of precisely regulated protein-protein interaction for exocytosis. Much of these results have derived from *in vitro* protein biochemistry and electrophysiological data, which to date have provided a substantial array of information about binding and channel modulation. However, these techniques don't reveal any spatial information about the hypothesised interaction between the $Ca_v2.2$ calcium channel and syntaxin1a across the plasma membrane, which is crucial for understanding the details of the docking process of vesicles in exocytosis and importantly, it remains unknown whether a direct interaction occurs at all in cells. In addition, the *in vitro* biochemical approach creates a controversy over the amount of spatial interaction through the overexpression of proteins and saturating the samples. The delicately balanced interactions between the $Ca_v2.2$ calcium channel and syntaxin1a proteins have to be analysed *in situ* through high-resolution imaging to be able to draw concise and robust conclusions about the behaviour at the plasma membrane.

This chapter directly addresses this challenge by studying the spatial localisation between the $Ca_v2.2$ calcium channels and syntaxin1a, using several advanced microscopy techniques to, for the first time, directly visualise the interaction between these two proteins *in situ*. In order to achieve this, fluorescently labelled $Ca_v2.2$ calcium channels in the full length sequence and a splice variant lacking exon 18a (Lin et al. 2004), which incorporates the synprint region, were genetically engineered, so that base comparisons about the different spatial interaction between the full length and the splice variant $Ca_v2.2$ calcium channel can be explored. Co-localisation, spectral scans and FLIM analysis were performed on calcium channel transfected and syntaxin1a immunostained AtT20 cells to draw conclusions as to how the synprint site affects the spatial interaction between these two proteins.

3.1.2 ω-Conotoxin GVIA

Cone snails are a species of venomous predatory marine molluscs that produce a cocktail of up to 100 different peptide toxins used for prey capture, defence or competitor deterrence (Terlau & Olivera 2004). Cone snails and their venomous toxins were identified in the 1950s (Kohn 1956) and an attempt was made to purify the venom in the 1970s (Endean et al. 1974), but is wasn't until advanced purification technology emerged around 1980 - 1990 (Smith et al. 1988) that detailed study of the venoms composition became possible. It was found that the venoms of different cone

snails were a complex mixture of distinctive peptides, each specifically targeting different ion channels (Terlau & Olivera 2004). Amongst the array of peptides, ω-conotoxin was purified (Olivera et al. 1984) and found to inhibit presynaptic action potentials (Kerr & Yoshikami 1984). ω-Conotoxin was identified as binding to $Ca_v2.2$ calcium channels with extremely high affinity and selectivity (Gray et al. 1988) sparking high interest for pharmacology studies as neuronal $Ca_v2.2$ calcium channels were postulated to have a major implication in the neuropathic pain pathway (Vink & Alewood 2012).

ω-Conotoxins are small, positively charged (net charge between +5e - +7e) peptides of 24 to 31 amino acids, exhibiting commonly six cysteine peptides, which are key for the four-loop scaffold linked by disulphide bonds (Nielsen et al. 2000). Peptides have been sub-classified according to sequence homology, giving names such as GVIA (from *C. geographus*) or MVIIA (from *C. magus*). ω-Conotoxin GVIA was found to be one of the most $Ca_v2.2$ calcium channel specific toxins, and is therefore commonly used for $Ca_v2.2$ calcium channel targeting experiments. The site of interaction on the $Ca_v2.2$ calcium channel was found to be located on the extracellular loop in domain III (Chen & Chung 2013; Witcher et al. 1993) and binding of the ω-conotoxin peptide was discovered to modulate the channel by destabilizing the open states (Yarotskyy & Elmslie 2009).

Electrophysiology experiments have mainly been performed to study the effect of ω-conotoxin on $Ca_v2.2$ calcium channels, but microscopy offers the only method to study the spatial distribution of toxin binding on the plasma membrane, through the direct visualisation of fluorescent versions of the peptides. Early imaging attempts were made not long after the original purification of conotoxins by synthesizing biotinylated analogues of peptides for imaging purpose (Jones & So 1993; Haack et al. 1993). However, these attempts were hindered by the imaging technology available at the time, the key limitations being the inability to image single molecules and the slow rate at which images could be acquired. It was at the turn of the century that techniques such as TIRFM, along with high sensitivity detectors, became readily available. In this thesis, a novel method to perform live single endogenous calcium channel molecule imaging is presented that utilises an improved and advanced directly labelled ω-conotoxin GVIA for single molecule imaging. This method provides a novel means to perform live single molecule calcium channel imaging.

3.2 Cloning and Expression of the FP-$Ca_v2.2$ Calcium Channel Fusion Protein

3.2.1 Cloning the α_1-subunit and α_1-subunit(Δ18a) into a FP Expressing Vector

Two cDNA constructs of the α_{1B}-subunit of the $Ca_v2.2$ channel were acquired from Addgene as specified in the methods section (see section 2.1.2). One of the cDNA constructs contains the full sequence of the $Ca_v2.2$ α_{1B}-subunit and a mutated sequence $Ca_v2.2$ α_{1B}-subunit(Δ18a), which has two sections deleted out of the sequence, one of which is the synprint sequence, exon 18a (Figure 3.1a).

The initial cloning strategy was to perform a polymerase chain reaction (PCR) of the two entire sequences and insert them separately into a range of mammalian expression vectors containing different sequences of fluorescent proteins, thus creating palette of fusion proteins 'colours' for both the α_1-subunit and its mutant.

For calcium channels the fluorescent protein is tagged to the N-terminal of the protein, encoded by the 5' proximal end of the DNA sequence. The initial strategy was to perform a PCR, which would have allowed the insertion of the calcium channel DNA into a vector encoding a fluorescent protein in one step (Figure 3.1b and Figure 3.2a). However, this proved intractable. The percentage of CG-content in the first 200 base pairs is extremely high (Figure 3.1c), which hindered the denaturing phase during a PCR and gave a poor PCR replication result.

An alternative, more complex multi-step approach was thus developed to construct the vector containing a $Ca_v2.2$-fluorescent fusion protein. Here, a larger number of restriction enzyme unique sites had to be used, which was difficult as the α_{1B}-subunit DNA is 7kb and the chance of unique restriction sites occurring within the sequence is low. The option of excising the calcium channel cDNA from the plasmid and inserting it into the vector in one step was not feasible. Therefore, the first step was the preparation of the vector (pmCer-C1; Clontech), which had to be modified at two sites of the multiple cloning site (MCS) by multi-site mutagenesis (Figure 3.1b and Figure 3.2b). The second step was to insert different FP encoding cDNAs in substitution of the Cerulean FP. The third step was to insert the cDNA of the two α_1-subunits in two separate stages (Figure 3.2b).

The multi-site mutagenesis was performed to replace a *Bgl* II restriction site with a *Sac* II restriction site and deleting the original *Sac* II site that was located 3' of the *Kpn* I site. The successful mutation, as determined by digestion with *Bgl* II and sequencing, was used as the vector template (Figure 3.1b).

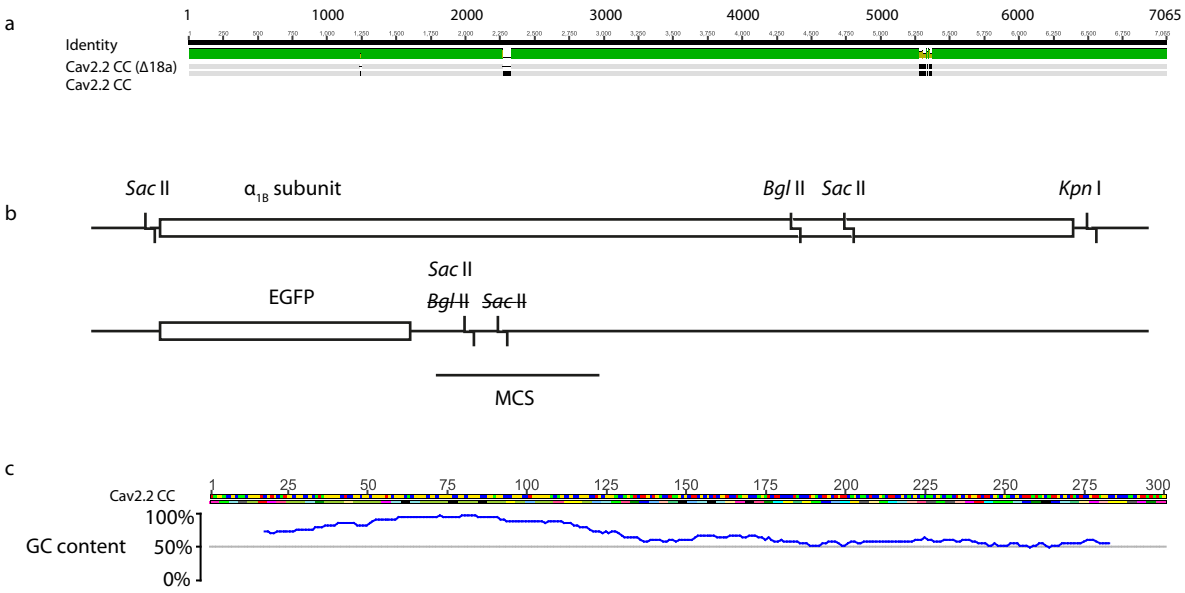

Figure 3.1 **The full length $Ca_v2.2$ α_{1B}-subunit and the splice variant $Ca_v2.2$ α_{1B}-subunit (Δ18a).** a. The cDNA sequence alignment of the $Ca_v2.2$ α_{1B}-subunit and $Ca_v2.2$ α_{1B}-subunit(Δ18a) highlights the segments deleted in the splice variant sequence. b. Schematic diagram of the α_{1B}-subunit sequence with the locations of the restriction sites used and the vector showing the sites of multi-mutagenesis in the multiple cloning site (MCS). c. The α_{1B}-subunit displayed an extremely high GC content percentage at the beginning of the cDNA sequence.

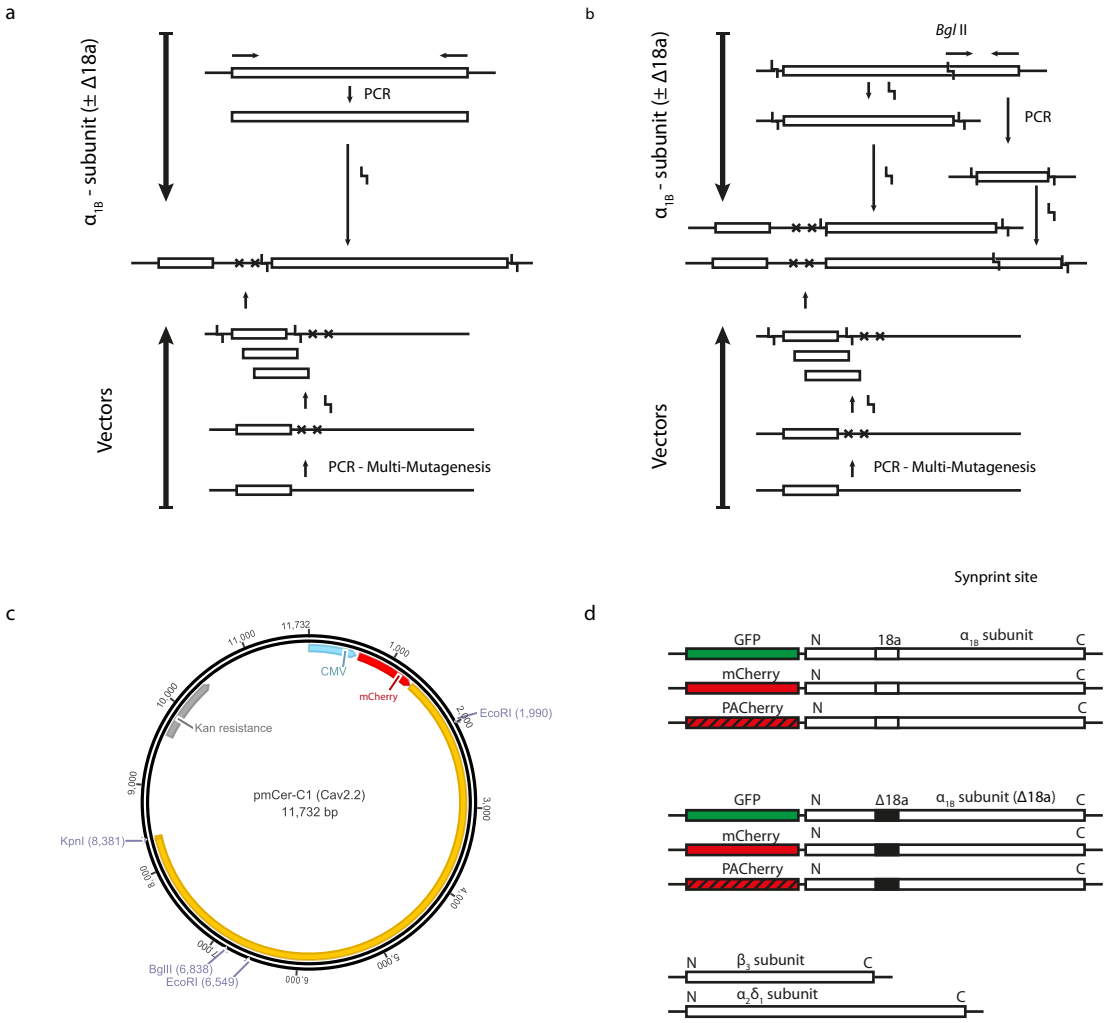

Figure 3.2 **Schematic diagram of the molecular engineering strategy**. a. The initial cloning strategy was to perform a PCR to replicate the cDNA sequence of the α_{1B}-subunit and insert it directly into a mutated C1 vector. b. The second more complex cloning strategy involves separately inserting the 5' proximal and then the 3' proximal sequenced into the mutated C1 vectors. c. Shown is an example of the final cDNA vector containing a fluorescent protein sequence at the 5' proximal end of the α_{1B}-subunit cDNA sequence. d. Schematic diagram of all the engineered vectors and the β_3 and $\alpha_2\delta_1$.

To have a palette of template vectors each containing a different fluorophore-encoding gene, Cerulean (Cer) (Rizzo et al. 2004) had to be swapped for EGFP, Cherry and PACherry. A restriction digest was performed with *Age* I and *BsrG* I to excise the fluorophore-encoding-cDNA from their original vectors and insert them into the new MCS pmCer-C1 vector, of which the Cerulean was previously cut out with the same enzymes. Thus several template vectors were created, all with the same mutated polylinker site, but each containing a different fluorescent protein. The cDNAs encoding the α_1-subunit and its mutant, had to be inserted into all of the vector templates that were engineered. The α_{1B}-subunit cDNA had to be transferred in two sections, referred to as the 5' and the 3' proximal end for simplicity. To achieve this, the 5' proximal end of each α_{1B}-subunit gene, was cut out with *Sac* II and inserted into the new MCS pm[FP]-C1 vector. To test the correct ligation of the insertion of the 5' proximal end of the calcium channel DNA into the new MCS vector, a digest was performed using *EcoR* I. The digestion pattern of bands on the gel electrophoresis, indicating the DNA strand sizes, revealed whether the DNA was inserted in the correct orientation. The 3' proximal end was amplified by PCR and inserted into a CloneJet (Fermentas) or pGEM-T easy (Promega) vector. It was then cut out with the restriction enzymes *Kpn* I and *Bgl* II to insert it into the pm[FP]-C1 - 5' proximal end vector. The new constructs had the cDNA of the α_{1B}-subunit or α_{1B}-subunit(Δ18a) inserted, to which the fluorescent proteins would attach to the N-terminus when translated (Figure 3.2c and Figure 3.2d).

3.2.2 Sample Preparation for FP-Ca_v2.2 Calcium Channel Expression Analysis

The sample preparation for the expression analysis of the FP-α_{1B}-subunit and FP-α_{1B}-subunit(Δ18a) fusion proteins was done using HEK293 and AtT20 D16:16 cells. These were plated on glass coverslips 24 hours before transfection with Turbofect, which were prepared as a single (GFP-α_1-subunit or mCherry-α_1-subunit), double (GFP-α_1-subunit or mCherry-α_1-subunit and the β-subunit) and triple transfection (GFP-α_{1B}-subunit or mCherry-α_{1B}-subunit and both β- and $\alpha_2\delta_1$-subunits). After a 48-hour incubation with the transfection reagent/DNA mixture, cells were fixed and kept in 1xPBS and imaging was done on the widefield microscope in the widefield (WF) and TIRFM modality, using the 491 and 561 nm lasers.

For membrane location analysis, HEK293 cells were plated as specified above and transfected with GFP-α_{1B}-subunit or GFP-α_{1B}-subunit(Δ18a) and the β- and $\alpha_2\delta_1$-subunits. After the 48 hour incubation period, cells were washed in 1x PBS and subjected to a 5 minute incubation at 37°C with the CellMask Deep Red plasma

membrane stain (Invitrogen), the concentrated solution diluted 1:1000 in 1xPBS. The cells were fixed immediately after the staining and left in 1xPBS for confocal imaging.

3.2.3 Expression of FP-Ca_v2.2 Calcium Channel Fusion Protein

The expression of channels (and all fusion proteins in general) may be altered by the addition of the large (about 27 kDa) FP to its structure. It is therefore important to confirm the channels are targeting correctly to the plasma membrane and that they correctly function when in location. In addition to this calcium channels are known to traffic best with the β-, and $\alpha_2\delta_1$-subunits. However, as for all systems biology experiments, the least invasive method is preferred, which in this case would be the transfection of only the GFP-α_{1B}-subunit or GFP-α_{1B}-subunit(Δ18a) cDNA without its supplementary subunit cDNA, reducing the amount of protein expression causing toxicity to cells. However, as shown in the imaging data presented in Figure 3.3, the expression of mCherry-α_{1B}-subunit (Figure 3.3a) and GFP-α_{1B}-subunit (Figure 3.3b) in a single transfection seems to produce a largely homogenous distribution within the cytosol of the cell and is clearly not located to the plasma membrane. The double transfection with the β_3-subunit shows evidence of some improvement over the single transfection, as significantly less fluorescence in the intra-cellular area can be observed, but it remains clear the expression is not located predominantly at the membrane. However the triple transfection with the β_3-, and $\alpha_2\delta_1$-subunits, is clearly marked by a distinctive outline of the cell, and very little intra-cellular labelling, thus illustrating the necessity of all three subunits for efficient targeting. The conclusions drawn from the WF images are reflected in the TIRFM images, which show sharper and more defined calcium channel locations with the triple transfection compared to the single or double transfection.

It has been postulated that the synprint site is preferable, but not necessary for the translocation of the α_1-subunit (Szabo et al. 2006). Dual-colour co-localisation microscopy provides an opportunity to verify this claim (see section 2.4.2), by comparing the degree of spatial localisation of the transfected calcium channel to a membrane stain. For this analysis, confocal images are deconvolved (see section 2.4.1), as even with confocal, the small reduction of out of focus signal delivers significantly improved co-localisation analysis results. The co-localisation is done between the GFP-α_{1B}-subunit and a standard membrane dye CellMask Deep Red in addition to the GFP-α_{1B}-subunit(Δ18a) and CellMask Deep Red (Figure 3.4a). Mander's co-localisation is a methodology based on determining the spatial overlap between two spectrally fluorescently labelled proteins. The co- localisation analysis returns two co-efficients,

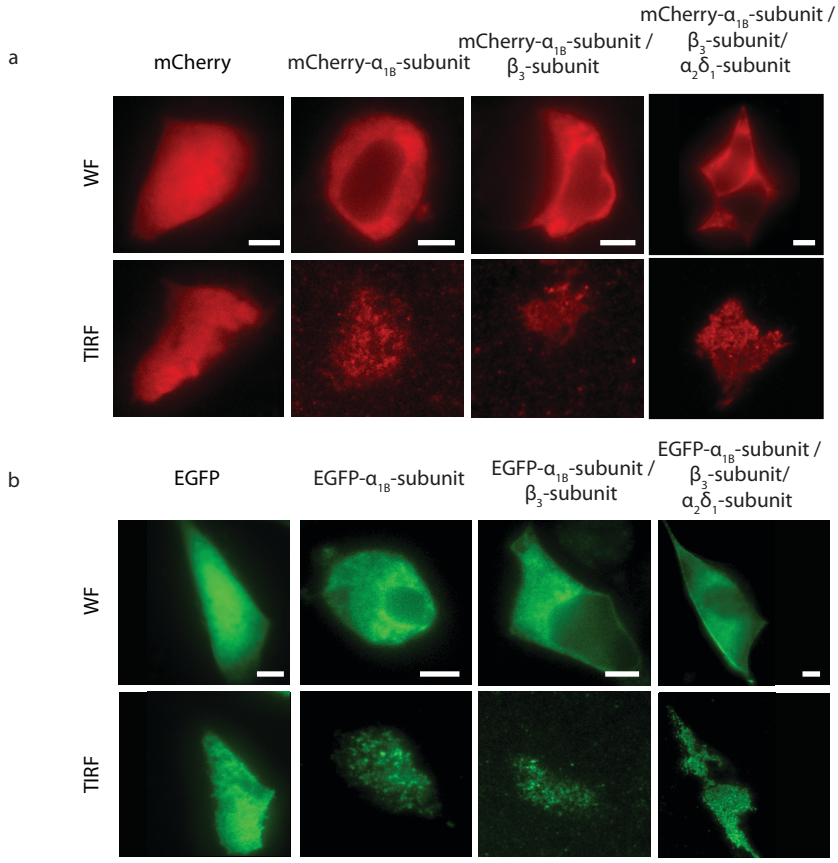

Figure 3.3 **Widefield and TIRFM imaging showing the expression of the fluorescently labelled $Ca_v2.2$ calcium channel.** a. AtT20 D16:16 cells were transfected with (i) mCherry (ii) mCherry-α_{1B}-subunit (iii) mCherry-α_{1B}-subunit and β_3 –subunit and (iv) mCherry-α_{1B}-subunit, β_3-subunit and $\alpha_2\delta_1$-subunits. All four conditions were imaged in WF and TIRFM to visually assess the best transfection efficiency b. Equivalent images to (a) but using the EGFP-α_{1B} subunit instead of mCherry. Scale bar: 5µm.

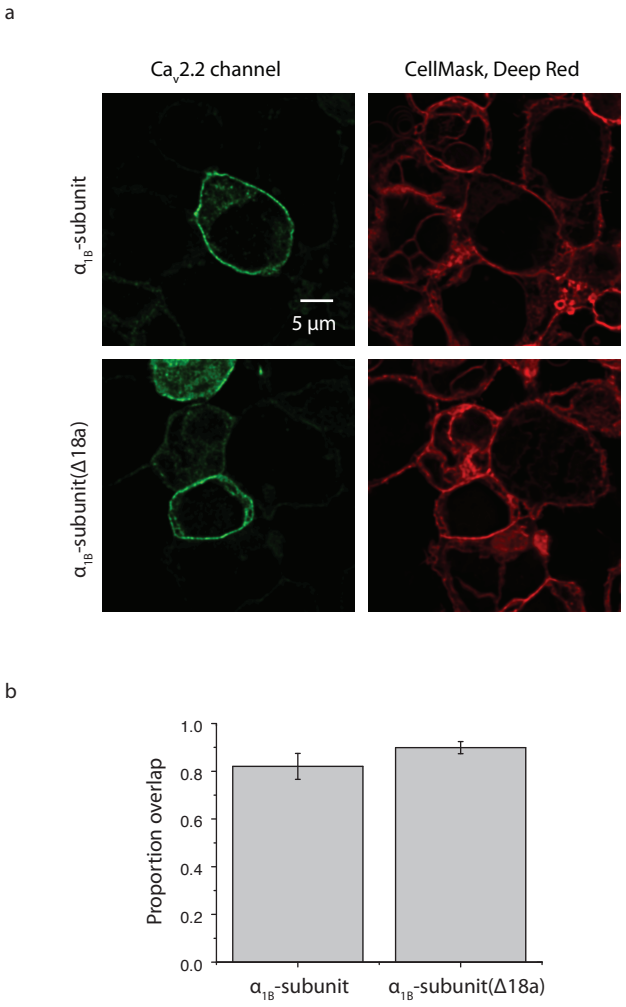

Figure 3.4 **Localisation of the Ca$_v$2.2 calcium channel to the plasma membrane.** a. Shown are deconvolved images of EGFP-α_{1B} / β_3 / $\alpha_2\delta_1$ subunits and EGFP-α_{1B} (Δ18a)/ β_3 / $\alpha_2\delta_1$ subunits transfected HEK293 cells (green). The xyz stacks were taken on the confocal microscope. A far red membrane dye (red) was used to stain the plasma membrane in order to determine the localisation of the Ca$_v$2.2 calcium channels. b. Manders' co-localisation was performed on the image stack. EGFP-α_{1B} showed a co-localisation, tM_2, of 0.82 (± 0.05 SEM, n = 10) and the EGFP-α_{1B} (Δ18a) showed a co-localisation of 0.89 (± 0.03 SEM, n = 6).

tM1 and tM2, which represent the 'red-with-green' and 'green-with-red' overlap. Using the ImageJ co-localisation analysis tool the Manders' coefficients were calculated from the image stacks. The Mander's co-localisation analysis of CellMask Deep Red with both the α_{1B}-subunits is not valid here, due to the staining of surrounding cells, which skews the results. As such, only the Manders of GFP-α_{1B}-subunit(w/o Δ18a) was taken into account to analyse the membrane localisation. The images show a high localisation of both the full length and splice variant α_{1B}-subunit, with the GFP-α_{1B}-subunit transfected cells revealing a co-localisation of 0.82 (±0.054 SEM, n = 10) and the GFP-α_{1B}-subunit(Δ18a) transfected cells displaying a co-localisation of 0.89 (±0.025 SEM, n =6) (Figure 3.4b). Calculated with the Mann-Whitney U test, there is no significant difference (p = 0.367) between the two co-localisation data sets, which reflects the plasma membrane localisation efficiency. The high co-localisation of both the full length and splice variant GFP-α_{1B}-subunit confirm through imaging that the GFP molecule does not hinder the trafficking of the calcium channel to the plasma membrane.

3.2.4 Electrophysiological Analysis of the Expression of EGFP-$Ca_v2.2$ α_{1B}-subunit

Electrophysiology experiments were performed to assess if the the electrical properties of the fluorescently labelled full length and splice variant $Ca_v2.2$ calcium channels have remained comparable. The intention was to verify that the voltage-dependent gating properties have remained similar to the unlabelled full length $Ca_v2.2$ calcium channel and that the voltage-current profiles have not shifted significantly to either more positive or more negative voltages. This work was done in collaboration with Dr. Euan Brown and Matthew Euston (Institute of Biological Chemistry, Biophysics and Bioengineering, Heriot-Watt University, Edinburgh).

For AtT20 D16:16 cells, Tetrodotoxin, TTX, at a concentration of 1 µM, was added to the extracellular media, Kreb's HEPES buffer, in order to inhibit sodium current. This is common practice, as the large inwardly rectifying sodium current masks the smaller calcium current. Whole cell patch clamping was performed to measure the current of all channels in the plasma membrane, which provides a significantly better quantification of the overall current-voltage relationship when compared to cell-attached or single cell patching. The electrophysiology data were collected by recording the current change ΔI at controlled and constant voltage steps of 10 mV, each lasting 300 ms, so called voltage sweeps. The voltage sweeps were started at a holding potential of -90 mV, the resting potential where no inward calcium current was detected, and was stepped up to +40 mV in 10 mV steps, returning back to the holding

potential of -90 mV between every sweep. The maximum calcium current at a given voltage can be measured from the voltage-current relationship profile (Figure 3.5a).

For the GFP-$Ca_v2.2$ $\alpha_{1B}/\beta_3/\alpha_2\delta_1$ expressing cells, the sample preparation was prepared as described in section 3.2.2, by allowing a 48-hour transfection of all three subunits in HEK293 cells before patching. A CCD camera (Hamamatsu) enabled the detection of fluorescently labelled cells. A stable cell line of Chinese Hamster Ovary (CHO) cells, created to express the full length $Ca_v2.2$ calcium channels (Human $Ca_v2.2/\beta_3/\alpha_2\delta_1$ calcium channel cell line, ChanTest, www.chantest.com) was acquired for control reference of the voltage-current relationship of these calcium channels. These cells had to be defrosted, plated and patched within one to two days.

GFP-$Ca_v2.2$ $\alpha_{1B}/\beta_3/\alpha_2\delta_1$ transfected HEK293 cells were patched and from a holding potential of -90 mV the current was recorded for every 10 mV depolarisation step (Figure 3.5a). These cells generated the maximum calcium current when depolarised to +10 mV (Figure 3.5a and b). The HEK cells were additionally tested for further calcium current. $Ca_v2.1$ calcium channels activate from a holding potential higher holding potential of around -60 mV compared to the $Ca_v2.2$ calcium channels (Catterall 2000). Electrical measurements displayed a current, although much smaller, which indicated the presence of further voltage-gated calcium channels on the plasma membrane (Figure 3.5b). Untransfected cells served for control measurements and these displayed no detectable $Ca_v2.2$ calcium channel current. The electrophysiological properties were compared to stable $Ca_v2.2$ calcium channels transfected CHO cells, which served as a control. The CHO cells displayed a maximum current at +20 mV. Within a batch of stable transfected cells there are always some cells, about 1:40, that do not express $Ca_v2.2$ calcium channels. These cells, patched by chance, displayed no calcium current at all (Figure 3.5b). The slightly positive current arises due to very small potassium current.

The analysis of the current indicates that the maximum current in GFP-$Ca_v2.2$ $\alpha_{1B}/\beta_3/\alpha_2\delta_1$ transfected HEK293 cells is the same as for $Ca_v2.2$ calcium channel expressing CHO cells. This result demonstrates that the fusion of the fluorescent protein to the $Ca_v2.2$ α_{1B}-subunit does not compromise the electrophysiological properties of the voltage gated calcium channel.

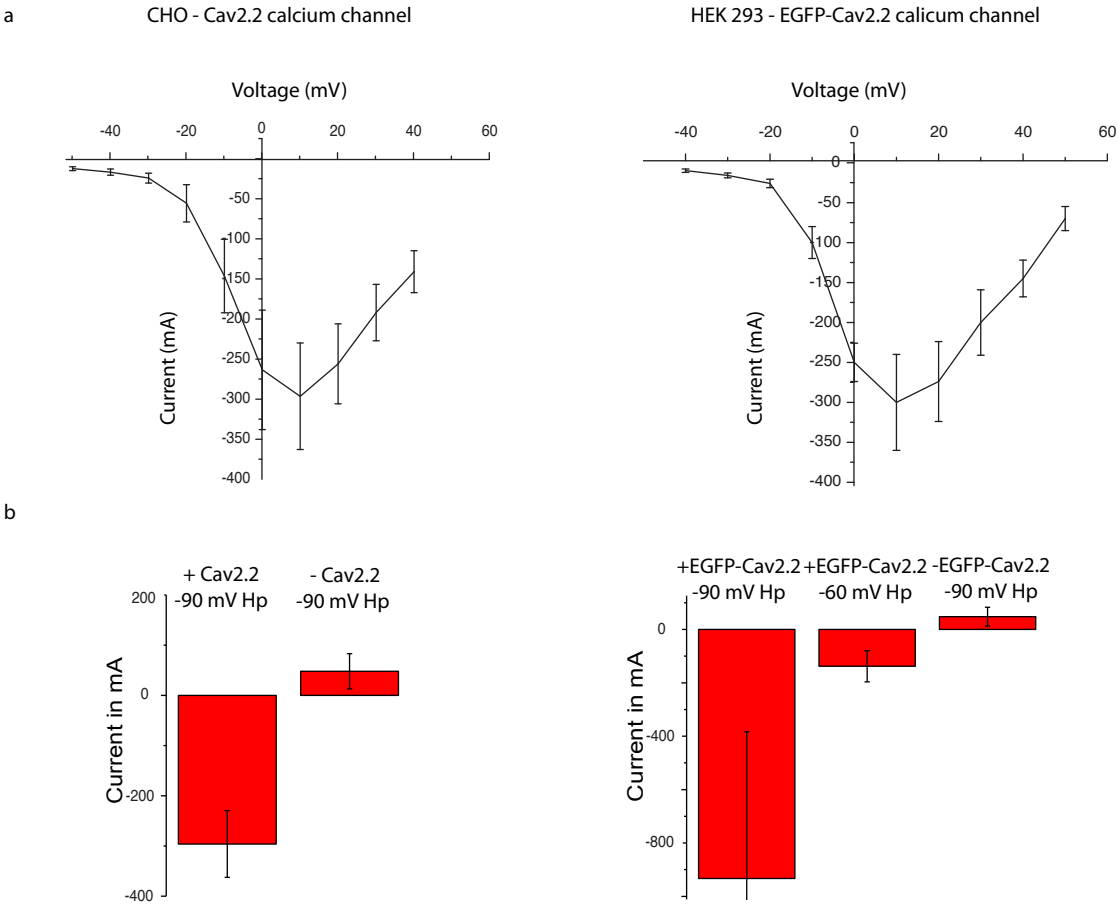

Figure 3.5 **Electrophysiological testing of the EGFP-α_{1B} subunit construct.** a. $Ca_v2.2$ calcium channel expressing CHO cells and EGFP-α_{1B} / β_3 / $\alpha_2\delta_1$ subunits, transfected HEK293 cells were tested for calcium current. Cells were depolarised from a holding potential of -90 mv, for 200 ms with different depolarisation steps, in 10 mV increments. The current-voltage plots measured for $Ca_v2.2$ calcium channel expressing CHO cells and EGFP-α_{1B} / β_3 / $\alpha_2\delta_1$ subunits, transfected HEK293 cells (n = 10 for each cell type and voltage condition). There is no shift between the native $Ca_v2.2$ calcium channel (CHO cells) and the EGFP-α_{1B} / β_3 / $\alpha_2\delta_1$ calcium channel. b. The maximum currents for different conditions.

3.3 Spatial Interaction of $Ca_v2.2$ Calcium Channels and Syntaxin1a through the Synprint Site

With successful functional expression of the labelled syntaxin1a and $Ca_v2.2$ calcium channel verified and electrophysiology evidence that neither the attached GFP nor the mutation alter the electrical activity, fluorescence imaging was performed to quantify the spatial interaction between the $Ca_v2.2$ calcium channel and syntaxin1a. A variety of imaging approaches were employed to reveal the amount of spatial overlap of the spectrally distinct FP labels or dyes, thus revealing if these proteins are in close enough proximity to physically interact. Three analysis methods were chosen to interpret the relationship of these proteins on the plasma membrane. Firstly, co-localisation was preformed to quantify the space, to within the ~200 nm lateral diffraction limit, that they share on the membrane. Secondly, intensity based spectral scans were performed to give an indication of whether fluorescence resonance energy transfer (FRET) was occurring between the EGFP-labelled calcium channels and the Alexa 568-immunostained syntaxin1a. As FRET is only detected between fluorophores separated by less than ~5 nm, the spectral scan would give an indication of a molecular radii-sized spatial co-localisation. The third imaging technique was FLIM, which measures FRET directly via the excited-state fluorescence lifetime of a fluorescent protein. FLIM is a more robust tool than intensity quantification for revealing FRET (Medine et al. 2007). As the lifetime of the donor protein is dependent on the degree of FRET, decreasing with increasing FRET due to quenching by the acceptor, FLIM provides an intensity insensitive, definitive marker of FRET and therefore, strongly implies protein-protein interaction (Duncan 2006). All these techniques, from the simpler but cruder co-localisation to the more complex but increasingly accurate FLIM-FRET, provide information on if the $Ca_v2.2$ calcium channel and syntaxin1a are spatially arranged, and co-localised in the plasma membrane, which is something hitherto unknown at these levels.

The sample preparations were the same for all the different imaging and analysis approaches. AtT20 D16:16 cells were plated on glass coverslips 24 hours before the Turbofect transfection with GFP-α_{1B}-subunit vector or GFP-α_{1B}-subunit(Δ18a) vector and with the two supplementary β-, and $\alpha_2\delta_1$- subunit vectors. After an incubation period of 48 hours to allow functional expression, the cells were fixed and immunostained for syntaxin1a, using HPC-1 (monoclonal mouse antibody; Sigma) and the secondary antibody anti-mouse 568 (Invitrogen). Prior to imaging, cells were left in

the 1xPBS solution. Controls were prepared by immunostaining of transfected and non-transfected cells with the secondary antibody only, or no immunostaining at all.

3.3.1 Co-localisation Analysis of the Spatial Overlap of $Ca_v2.2$ Calcium Channel and Syntaxin1a

Co-localisation experiments were performed between transfected $Ca_v2.2$ channels (EGFP-α_{1B}-subunit or EGFP-α_{1B}-subunit(Δ18a) along with the β_3 and $\alpha_2\delta_1$- subunits) and endogenous HPC-1-immunostained syntaxin1a in order to reveal the diffraction-limited spatial overlap between the two proteins (Figure 3.6a). The hypothesis is that any difference between the GFP-α_{1B}-subunit and GFP-α_{1B}-subunit(Δ18a) co-localisation with syntaxin1a will give an indication of how essential the synprint site is for regulated exocytosis, or targeting and localisation of the SNARE or the channels, in terms of spatial distribution of the $Ca_v2.2$ calcium channel and syntaxin1a. For the co-localisation analysis, xyz-dimensional stacks were acquired using the confocal microscope. Before analysis, all stacks were deconvolved as discussed in section 2.4.1.

Again, using the ImageJ co-localisation analysis tool the Manders' coefficient was calculated from the deconvolved image data stacks. As the focus was on the interaction of $Ca_v2.2$ calcium channel with syntaxin1a, the fraction of green pixels (EGFP-$Ca_v2.2$) overlapping with red (immunostained syntaxin1a) was used for analysis. The co-localisation analysis revealed a high spatial overlap between the EGFP-$Ca_v2.2$ calcium channel and syntaxin1a. Those cells transfected with the EGFP-α_{1B}-subunit returned a Manders' co-localisation fraction of 0.52 (±0.09 SEM, n = 10) and those transfected with GFP-α_{1B}-subunit(Δ18a) displayed a Manders' co-localisation fraction of 0.41 (± 0.08 SEM, n = 10) (Figure 3.6c). The Mann-Whitney U test revealed that there is no significant difference between the two data sets ($p = 0.235$). Controls without staining (Figure 3.6b) showed no co-localisation at all. With this technique limited to the size of the PSF of both the AlexaFluor568-labelled syntaxin1a and the EGFP-$Ca_v2.2$ calcium channel, the results therefore reflect the spatial areas that these proteins share on the membrane, but do not reveal any interaction as such. To do so, further investigation using sub-diffraction limited approaches has to be performed to accurately determine the spatial interaction of the $Ca_v2.2$ calcium channel and sytaxin1a.

3.3.2 Spectral Scanning to Reveal FRET Interaction between the $Ca_v2.2$ Calcium Channel and Syntaxin1a

The co-localisation analysis gives a good indication of the spatial proximity of the $Ca_v2.2$ calcium channels and syntaxin1a molecules on the plasma membrane. However,

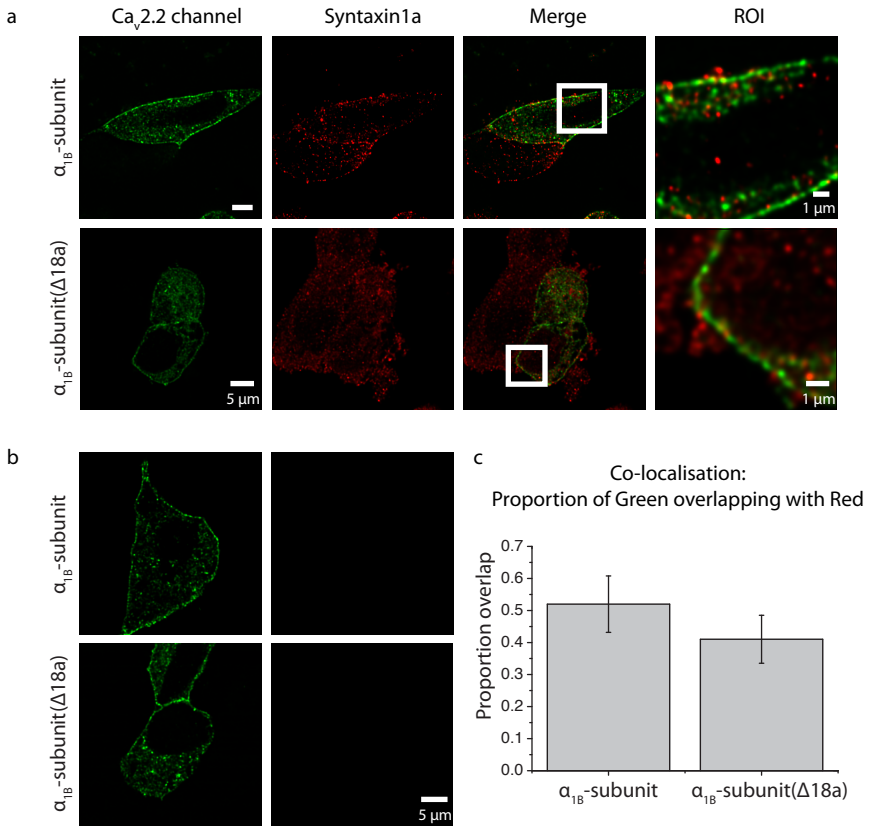

Figure 3.6 **Co-localisation of the α_{1B}-subunit and the α_{1B}-subunit (Δ18a) with syntaxin1a.** a. Confocal imaging (xyz stack) and co-localisation of AtT20 D16:16 cells that were transfected with either the EGFP-α_{1B}-subunit or the EGFP-α_{1B}-subunit (Δ18a) along with the two supplementary subunits, β_3 and $\alpha_2\delta_1$ (green) and then immunostained with HPC-1 (anti-syntaxin) and AlexaFluor 568 (red). b. Control samples were transfected as stated above and stained only with the secondary antibodies, AlexaFluor 568, to ensure no unspecific binding. c. Mander's co-localisation analysis was performed to assess the overlap of the green signal with the red signal. EGFP-α_{1B} showed a co-localisation of 0.52 (± 0.09 SEM, n = 10) and the EGFP-α_{1B}(Δ18a) showed a co-localisation of 0.41 (± 0.08 SEM, n = 10). The controls showed no co-localisation at all.

this analysis is limited by the 200 nm diffraction-limit and therefore does not, and cannot, reveal if there is in fact molecular interaction between the proteins. However, a FRET-based approach can provide evidence of protein-protein interaction by inferring spatial co-localisation to molecular distances. FRET works through the measurement of the amount of energy transfer from a donor to an acceptor molecule, which reveals itself through either the presence of acceptor emission through donor excitation, or a reduced donor lifetime. Importantly, the transfer is not a re-absorption of photon emission, but it is resonant transfer of energy. FRET only occurs when the donor emission and acceptor absorption spectrally overlap. This spectral overlap is a minimal prerequisite for FRET, however an added complexity for efficient resonance transfer is correct dipole orientation, lifetime and quantum yield, which is why not all spectrally overlapping fluorophores show FRET. To establish whether EGFP and the AlexaFluor 568 dye show possible FRET, spectral scanning was performed to analyse the energy transfer between the EGFP labelled channels and the AlexaFluor 568 dye-tagged syntaxin1a. The 491 nm excitation wavelength only excites EGFP-labelled proteins and not the AlexaFluor 568-dye molecules that syntaxin1a is immuno-identified with. If there is FRET transfer, can the AlexaFluor 568-dye acquire energy to emit fluorescence Therefore, evidence of AlexaFluor 568 emission under 491 nm excitation, would provide strong evidence of a FRET interaction.

Spectral scanning acquired on the confocal microscope is effectively imaging in xyλ dimensions, where each pixel is excited with the 491 nm laser ling and then emission-scanned through the spectral range from 500 nm to 700 nm, with the λ steps set to a 10 nm width acquiring in 5 nm steps (Figure 3.7a). The integrated intensity over the whole image, all the pixels, at each λ-step is used to establish the spectral signature. A region at the plasma membrane was manually selected and the intensity summed, then the spectral scan curves (n = 5 for each condition) were normalised to the maximum intensity and averaged to produce the final result.

First, spectral scans on the transfected full length and splice variant GFP-Ca_v2.2 calcium channels without syntaxin1a-immunostaining were performed to measure the spectral property of EGFP alone (Figure 3.7b). These curves fit well with two Gaussians, one centred at 509 nm characterising the main emission peak (blue curve), and a second one centred at 514 nm, fitting the characteristic longer wavelength emission that arises due to the vibrational states (green curve), as shown in the Jablonsky diagram (see section 1.5.1). Secondly, spectral scans were done on samples transfected with full length and splice variant GFP-Ca_v2.2 calcium channels and stained with the secondary

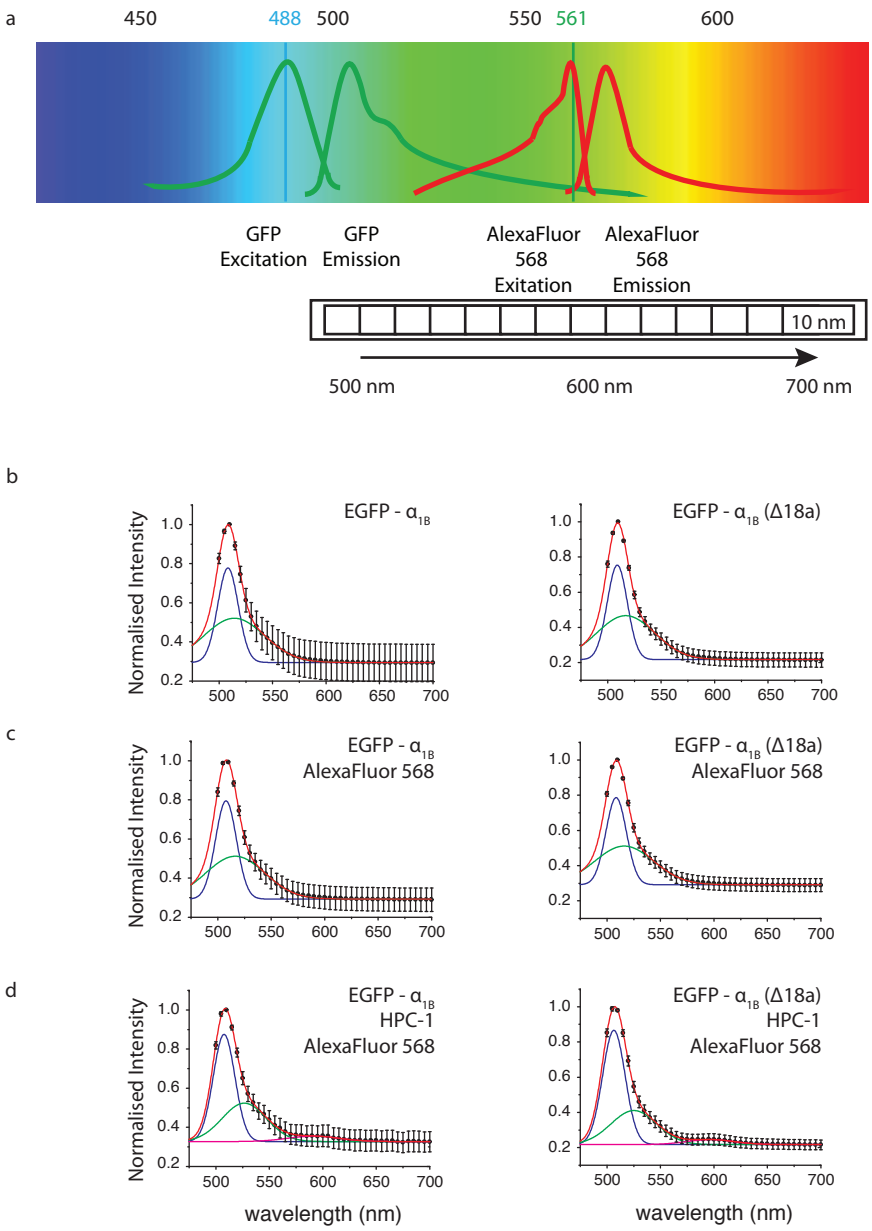

Figure 3.7 **Spectral scanning to reveal FRET.** a. Schematic diagram of the spectral properties of EGFP and AlexaFluor568 and the spectral acquisition methodology. b. Spectral scans of EGFP-α_{1B} and EGFP-α_{1B}(Δ18a) fitted with two Gaussians, characteristic for EGFP, blue representing the primary fluorescence transition and the green representing the vibrational state transitions. c. Spectral scans of EGFP-α_{1B} and EGFP-α_{1B}(Δ18a) samples with secondary AlexaFluor568 staining, again fitted with two Gaussians characteristic for EGFP. d. Spectral scans of EGFP-α_{1B} and EGFP-α_{1B}(Δ18a) samples with immunostaining for syntaxin1a. Both curves were fitted with the same two Gaussians characteristic for EGFP and a now third Gaussian (purple) centred around 597 nm, which indicates FRET transfer.

antibody AlexaFluor 568 in the absence of anti-syntaxin1a primary antibody. This control, which is not expected to show any FRET between EGFP and AlexaFluor 568 was done to verify that there is no detectable emission at longer wavelengths, above 600 nm, due to unspecific staining of the secondary antibody. As for the first control, these curves are also well described by two Gaussians that fit the characteristic EGFP emission, and did not show any measurable fluorescence at the AlexaFluor 568 emission band around 600 nm (Figure 3.7c). The full length and splice variant GFP-$Ca_v2.2$ calcium channels transfected, and for syntaxin1a immuno-labelled AtT20 D16:16 samples, both demonstrated a faint fluorescence at the emission spectrum of the AlexaFluor 568 centred at 600 nm (Figure 3.7d). The spectra now fit well to a three Gaussian model, one centred at 508 nm, one at 525 nm and the third at 597 nm. The third Gaussian describes clearly the lower energy, longer wavelength, peak at 600 nm. This clear spectral signature typical of AlexaFluor 568 and not present in the control cells, provides strong evidence of a FRET interaction of the GFP molecule with the AlexaFluor 568 acceptor dye. This evidence therefore suggests close contact of the GFP-$Ca_v2.2$ calcium channels to syntaxin1a. Although the FRET signature is relatively weak in comparison to the main GFP signal, this result is encouraging and justified further investigation into the spatial interaction between these two proteins.

The spectral scan method is useful, simple, and indicative of evidence of FRET between donor and acceptor labels, in this case a protein and dye. However, a more robust methodology to reveal FRET measures the lifetime of the donor protein, in this case the GFP molecule of tagged $Ca_v2.2$ calcium channels, which is quenched (decreases) when the donor experiences FRET.

3.3.3 FLIM Analysis of the Spatial Interaction of $Ca_v2.2$ Calcium Channel and Syntaxin1a

FLIM-FRET is a more direct and robust sub-resolution method than spectral scanning. The information about a close interaction of two fluorescently labelled proteins is extracted by measuring the lifetime of the fluorescent donor, which will be shortened through FRET interaction between the donor and acceptor labels. FLIM-FRET provides the strongest optical evidence of protein-protein interaction. The aim here is to measure the interaction between the $Ca_v2.2$ calcium channel and syntaxin1a, and thereby reveal the spatial relationship that these two proteins share on the plasma membrane. For this purpose, the expression of the complete $Ca_v2.2$ calcium channel sequence was compared to the synprint-lacking $Ca_v2.2$ calcium channel, and thereby revealing for the first time the proportion of syntaxin1a-interacting $Ca_v2.2$ calcium channel molecules. The aim here is to reveal direct evidence of the global interaction

behaviour, which may contribute a great deal to the understanding of the spatially defined interaction of SNARE proteins and calcium channels in respect to fusion sites.

The result of the spectral scans above indicated a likely direct interaction between $Ca_v2.2$ calcium channels and syntaxin1a, expressing separately the full length and splice variant calcium channel constructs. However, this method does not have the sufficient sensitivity to accurately measure and quantify the proportion of interaction within the cell. However, what is crucial is that the spectral scanning method confirmed the likelihood of FRET and the FRET compatibility of EGFP and the AlexaFluor 568 as a donor and acceptor pair. Based on this, the sample preparation for the FLIM measurements were prepared in the same manner as previously for the co-localisation and spectral scan analysis detailed above (see 3.3).

FLIM is a photon counting technique based on time-correlated single photon counting (TCSPC) (Becker 2005). A pulsed, picosecond, excitation laser excites the sample and the corresponding emission is collected on a single photon avalanche diode (SPADs). The time between excitation and photon collection is recorded through TCSPC electronics and a fluorescence lifetime decay histogram is built through repeated measurements. The distribution of the timed photon collection is plotted over time and the lifetime, corresponding to the statistically average time a fluorophore spends in its excited state, is extracted through exponential fitting of the decays. For FLIM the lifetime of the donor, in this case the EGFP protein labelling the $Ca_v2.2$ calcium channels, was measured using the external SPAD detectors on the Leica SP5 confocal microscope. EGFP molecules typically returns a single lifetime, τ, through the fit of a mono-exponential decay, with an inherent lifetime value within the 2 – 3 nanosecond range (Broussard et al. 2013). A donor in close proximity to an acceptor will undergo FRET, transferring energy from the donor to the acceptor. As this process is temporal and statistical, it naturally quenches the donor emission and thereby decreases its lifetime. Under ideal conditions where all donor molecules in the sample undergo FRET a single faster mono-exponential decay will be recorded. However, in practice only a fraction of donor molecules will undergo FRET due to excessive donor labelling or inactive donor-acceptor pairs. Therefore, usually a mono-exponential no longer describes the data and instead a bi-exponential relationship is necessary to accurately describe the fast (FRET) and slow (native) components of the overall sample decay. This is shown schematically in Figure 3.8, where theoretical curves, with added Gaussian noise, are plotted to demonstrate the principal of native GFP lifetime vs FRET reduced GFP lifetime in a sample where around 30% of molecules show a clear FRET signature.

Mono-exponential $$y(x) = z + Ae^{-x/\tau}$$ 3.1

Bi-exponential $$y(x) = z + A_1 e^{-x/\tau_1} + A_2 e^{-x/\tau_2}$$

Figure 3.9a shows whole cell FLIM data, created by estimated spatial lifetime distribution across the cell using a fast-FLIM (Symphotime) method. Fast-FLIM estimates lifetime based on temporal weighting of the decay curves. These images give an indication of varying lifetime across the cell. However, in this work the plasma membrane proximal activity is of main interest. Therefore, the main FLIM analysis in this work was done by manually selecting a region of interest that showed only the plasma membrane (Figure 3.9a) and producing lifetime decay curves that was the total of all pixels in these regions. Summing the lifetime curves provides adequate signal to noise to perform high reliability lifetime fits. The data was fitted by selecting a curve, mono or bi-exponential that best described the decay with the smallest number of terms.

The non-immunostained control data, expressing the full length EGFP-Ca_v2.2 calcium channel fitted with a mono-exponential with a characteristic lifetime around 2.39 ns (± 0.02 SEM, n = 6), which is in agreement with the literature describing the fluorescent lifetime of EGFP (Broussard et al. 2013). The qualities of the fits are described through the residuals, the weighted differences between the fit and the data. The residuals for the full length EGFP-Ca_v2.2 calcium channel and the HPC-1-immunostained splice variant EGFP-Ca_v2.2 calcium channel show little or no oscillations around the zero baseline, and are dominated only by noise. The mono-exponentials returned a lifetime of 2.37 ns (± 0.02 SEM, n = 6). The HPC-1-immunostained full length EGFP-Ca_v2.2 calcium channel data did not fit well to a mono-exponential function, with the residuals showing a clear oscillation around the baseline. This is characteristic of a poor fit. A bi-exponential fitted much better, with little or no residual oscillations (Figure 3.9b), returning two lifetimes, one at 2.50 ns (± 0.03 SEM, n = 6), which is similar to the non-FRET EGFP lifetime, and the other typically 1.30 ns (± 0.08 SEM, n = 6), which is significantly shorter that the non-FRET EGFP lifetime (Figure 3.10a). This is strong evidence of FRET. The FLIM result from the synprint-lacking EGFP-Ca_v2.2 calcium channel, once again fitted to a mono-exponential curve, with a lifetime of 2.4 nm, indicating no FRET interaction. Now that a clear molecular interaction had been established by measuring FRET, it was important to consider the proportion of

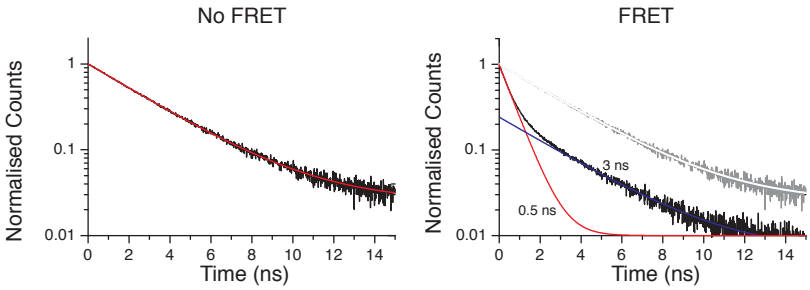

Figure 3.8 **Modelled FLIM-FRET lifetime data.** a. The synthetic lifetime, representing for example, pure EGFP with no FRET energy transfer, is fitted with a mono-exponential decay giving a single lifetime of 3 ns. b. Synthetic data, representing EGFP donor with a significant FRET energy transfer, is fitted with a bi-exponential decay giving a fast component of 0.5 ns (30% decay contribution, red curve) and a slow component of 3 ns (70% decay contribution, blue curve). The mono-exponential decay from a. (gray) is displayed for comparison.

channels that are modulated by syntaxin1a. This can be calculated using the two amplitudes in the decay equation, which relate to the proportion that each lifetime component contributes to the overall decay curve. The relative percentage that each lifetime contributes to the decay is given by:

$$\tau_1\% = \frac{A_1\tau_1}{A_1\tau_1 + A_2\tau_2} \cdot 100$$

$$\tau_2\% = \frac{A_2\tau_2}{A_1\tau_1 + A_2\tau_2} \cdot 100 \qquad 3.2$$

In a mono-exponential decay only one lifetime describes the curve and it contributes to 100% of the decay. This applied to both the EGFP control and the EGFP-$Ca_v2.2$ calcium channel (Δ18a) samples. For the EGFP-$Ca_v2.2$ calcium channels the percentage of each lifetime contributing to the fitted exponential decay was calculated. The result showed that 87.94% (± 2.56 SEM, n = 6) of EGFP-$Ca_v2.2$ calcium channel were not interacting with syntaxin1a, but that 12.01% (± 2.56 SEM, n = 6) were spatially interacting with syntaxin1a at the plasma membrane (Figure 3.10b). This confirms for the first time through the means of sub-resolution optical measurement the theory that syntaxin1a spatially interacts with the $Ca_v2.2$ calcium channel at the synprint site at the plasma membrane.

3.3.4 Conclusion of the Spatial Relationship of Syntaxin1 and $Ca_v2.2$ Calcium Channels

The aim of this piece of work was to investigate the spatial interaction that syntaxin1a has with the $Ca_v2.2$ calcium channel through the channel-located synprint site. The co-localisation analysis between the full length- and splice variant- $Ca_v2.2$ calcium channel and syntaxin1a showed that only about 52% of the EGFP-α_{1B}-subunit signal overlapped with the syntaxin1a signal, whereas the EGFP-α_{1B}-subunit(Δ18a) only overlapped by around 41%. This suggests that the synprint site does, at least in part, affect the overall spatial arrangement of $Ca_v2.2$ calcium channels in relation to syntaxin1a. The sub-resolution analysis performed through spectral scanning and quantified with the FLIM-FRET experiment revealed that only about 12% of $Ca_v2.2$ calcium channels interact through the synprint site. This suggests a non-uniform spatial distribution, where calcium channels across the plasma membrane are spatially and possibly temporally regulated by the interaction with syntaxin1a. In a uniformly distributed $Ca_v2.2$ calcium channel arrangement one could expect a higher interaction percentage as all $Ca_v2.2$ calcium channels are in a similar environment surrounded by a relatively high density

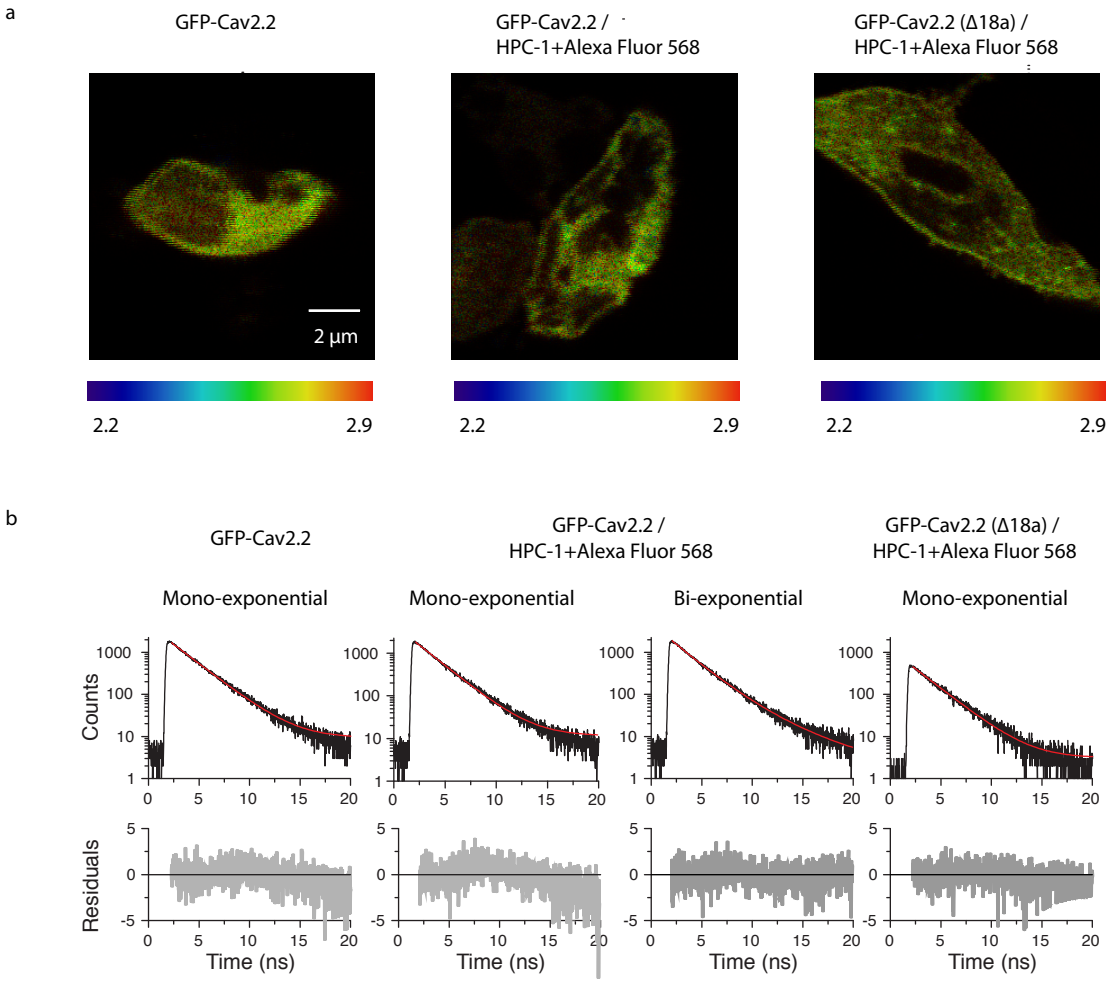

Figure 3.9 **FLIM-FRET on the full length and splice variant EGFP- $Ca_v2.2$ calcium channel with syntaxin1a immunostaining.** a. Representative fluorescence lifetime (FLIM) images of AtT20 D16:16 cells transfected with the full length EGFP-$Ca_v2.2$, full length EGFP-$Ca_v2.2$ with syntaxin1a immunostaining and splice variant EGFP-$Ca_v2.2$ with syntaxin1a immunostaining. Scale is in nanoseconds. b. Representative summed fluorescence lifetime data from a selected region of the plasma membrane of the data shown in (a). Shown are the decays, the fitted lifetimes and the weighted residuals. The standard deviation of the residuals are 1.34, 1.50, 1.09, 1.19 respectively. The full length EGFP-$Ca_v2.2$ fitted to a mono-exponential decay curve of lifetime 2.35 ns. The full length EGFP-$Ca_v2.2$ with syntaxin1a immunostaining did not fit to a mono-exponential, but well with a bi-exponential decay curve, lifetimes 2.5 and 1.3 ns. The splice variant EGFP-$Ca_v2.2$ with syntaxin1a immunostaining fitted with a mono-exponential decay curve, lifetime 2.35 ns.

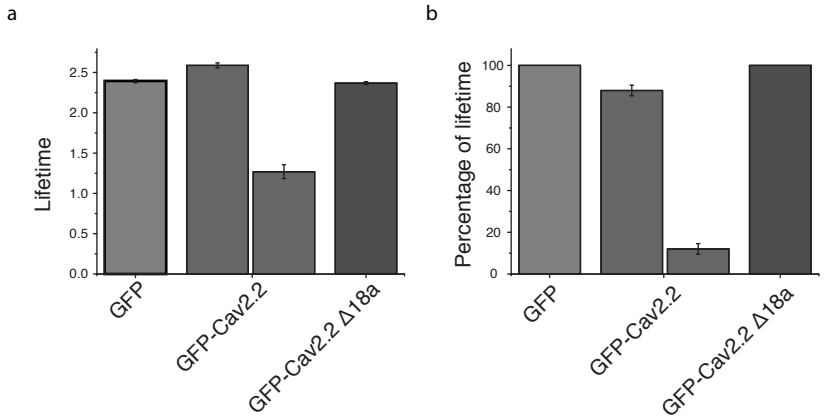

Figure 3.10 **Lifetime of EGFP-Ca_v2.2 affected by the synprint site.** a. Both the EGFP-Ca_v2.2 (control) and splice variant EGFP-Ca_v2.2 (with syntaxin1a staining) transfected in AtT20 D16:16 cells returned a single lifetime of 2.39 ns (± 0.02 SEM, n = 6) and 2.37 (±0.02 SEM, n = 6) respectively. The full length EGFP-Ca_v2.2 calcium channel (with syntaxin1a staining) shows a clear bi-exponential decay, with a longer 2.50 ns (± 0.03 SEM, n = 6) component and a shorter 1.30 ns (± 0.08 SEM, n = 6) component. b. The percentage contribution for each lifetime component to the overall decay curve was determined. For the longer 2.50 ns component it calculated to be 87.94% (± 2.56 SEM, n = 6). For the shorter, 1.30 ns component it was calculated to be 12.01% (± 2.56 SEM, n = 6).

of syntaxin1a molecules. However, the low interaction percentage suggests a mixed arrangement of single and clustered calcium channels across the plasma membrane, in which one of the configurations is preferred for the sytaxin1a interaction. Since clusters probably represent the higher proportion of total $Ca_v2.2$ calcium channels, it is more plausible that the interaction between $Ca_v2.2$ calcium channels and syntaxin1a via the synprint site arise in spatially isolated areas. This leads on to speculations about the how the protein-protein interaction affects the spatial arrangement in relations of the fusion site. A possible hypothesis explaining the results is that only isolated syntaxin1a-binding $Ca_v2.2$ calcium channels are located in proximity to docked vesicles. However, more evidence of the spatial arrangement of $Ca_v2.2$ calcium channel across the plasma membrane is necessary to support this hypothesis. For this, a completely novel single molecule localisation method was developed, which is discussed in the following section.

3.4 Single-Molecule Imaging of the $Ca_v2.2$ Calcium Channel

The above work described how the spatial relationship between the transfected α_{1B}-subunit (w/o Δ18a), along with the β_3 and $\alpha_2\delta_1$, and the immunostained syntaxin1a has been revealed through the means of sub-resolution spectral and temporal microscopy. Confocal imaging and co-localisation data have shown the importance of the synprint site for syntaxin1a interaction and highlight the necessity of the synprint site for overall channel localisation. The spectral scan and FLIM-FRET data demonstrate that there is direct interaction between the $Ca_v2.2$ calcium channel and syntaxin1a. These techniques are useful for an overall interpretation, where the population of expressed protein molecules reflects the global behaviour.

However, single molecule localisation microscopy is required to appraise the detailed arrangement in molecular spatial distribution. Here, the intention is to understand the spatial arrangement of endogenous $Ca_v2.2$ calcium channels at the plasma membrane.

The aim was to create a new method that allows specific $Ca_v2.2$ calcium channel targeting and labelling for live-cell single-molecule imaging. When immunostaining with the anti-Cacna1b antibody (Abcam) against α_{1B}-subunits, these were found to not target efficiently, and did not give reliable results (Figure 3.11a). Therefore a new approach was developed that allowed specific targeting of endogenous $Ca_v2.2$ calcium channel through ω-conotoxin GVIA. Initially, biotinylated ω-conotoxin GVIA and a streptavidin-alexa647 conjugation were used for primary and secondary labelling respectively (Figure 3.11b). However, an innovative approach using a purposely conjugated ω-conotoxin GVIA with a caged dye, developed by Almac Group, UK

(www.almacgroup.com) was tested for its viability as a labelling strategy for super-resolution imaging of $Ca_v2.2$ calcium channels in live cells (Figure 3.11c).

3.4.1 A ω-Conotoxin-Biotin, Streptavidin-Alexa647 Staining Method

The feasibility of using ω-conotoxin GVIA for $Ca_v2.2$ calcium channel single molecule imaging was tested by staining cells with biotinylated ω-conotoxin GVIA (BAChem, Germany, www.bachem.com) and streptavidin-alexa647 (Invitrogen). This novel approach shares similarities with the concept of immunostaining, where a primary antibody binds the target protein, and a secondary antibody targets the primary antibody. There are some key drawbacks with immunostaining for single molecule localisation imaging using STORM. Firstly, primary antibodies vary in specificity. Secondly, multiple secondary antibodies tag to one primary antibody, leaving one target protein labelled with several fluorescent dyes (Figure 3.11a). Thirdly, IgG molecules have larger dimensions than the resolution of the single molecule imaging techniques now available, such as PALM and STORM. In addition to the issue of multiple dyes conjugated to each secondary IgG, secondary detection can cross-link primary targets into macromolecular complexes. Together, this means that the use of immunodetection with single molecule imaging is undesirable and small, single-dye-conjugated, high affinity ligands are required to deliver the maximum resolution and reliability, together with quantitative information about molecular numbers and organisation.

For the ω-conotoxin GVIA staining method, initially, Alexa647-labelled streptavidin (Invitrogen) was used, which is a molecule with a high affinity for biotin. The tetrameric structure of streptavidin means that there are 4 biotin binding sites, of which one is blocked though the attachment of the dye. Through biotin binding, this molecule acts to fluorescently label biotinylated ω-conotoxin GVIA (Figure 3.11b). In principle, the staining with these two conjugated molecules, the biotinylated ω-conotoxin GVIA and the streptavidin-alexa647, results in each $Ca_v2.2$ calcium channel being tagged with only one single fluorescent dye. This unique staining method therefore provides an ideal biological sample for STORM-type single molecule imaging of $Ca_v2.2$ calcium channel.

Similar to conventional immunostaining procedures, pre-blocking steps had to be done to eliminate unspecific binding. Due to the naturally high biotin content in cells (Tytgat et al. 2014), a 10-minute pre-incubation with avidin (0.001% w/v in PBS) and biotin (0.001 % w/v in PBS) (Avidin/Biotin blocking kit, Life Technologies) successively was necessary to minimise binding of streptavidin-alexa647 to endogenous biotin

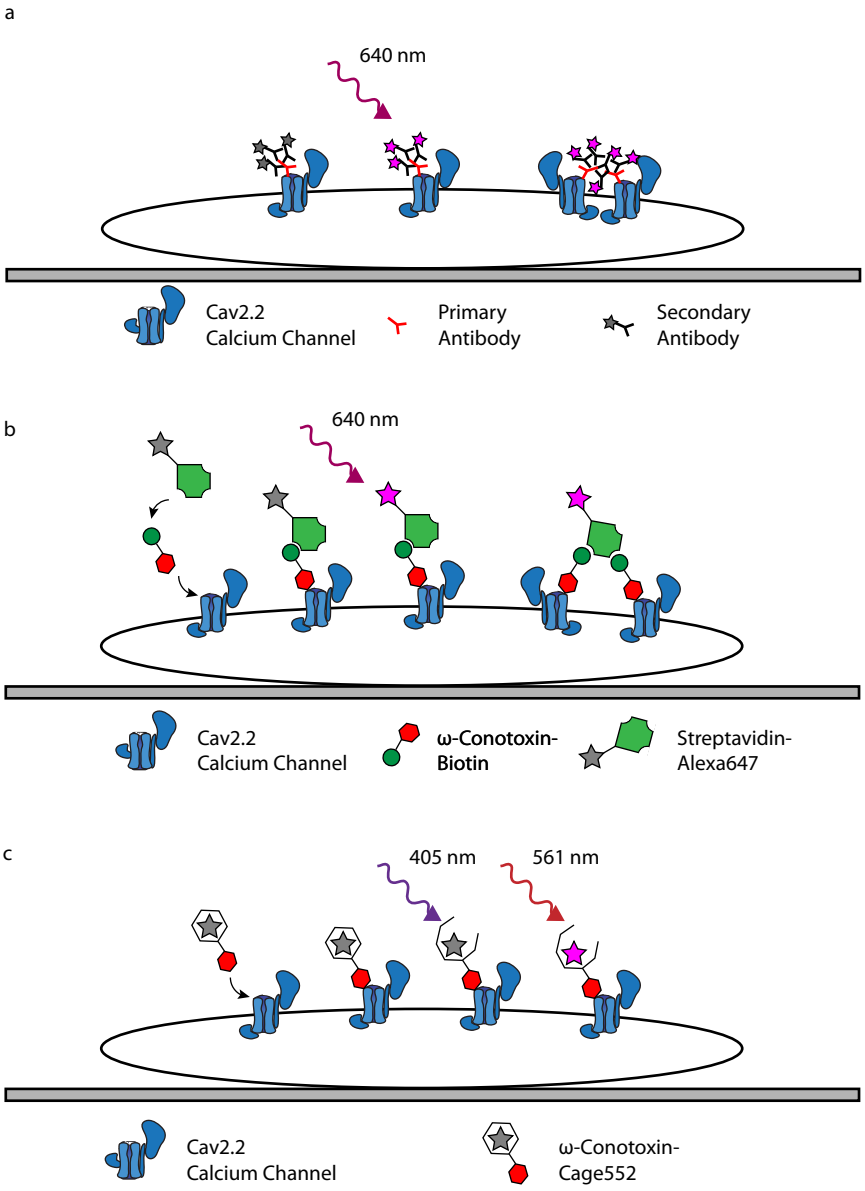

Figure 3.11 **. Principle of $Ca_v2.2$ calcium channel staining for SMLM.** a. Immunostaining is the standard technique to label and visualise the proteins. The protein specific primary antibody targets the channel directly and the secondary antibody labels the primary antibody. This can lead to multiple labelling of one channel. b. ω-Conotoxin GVIA is a highly specific $Ca_v2.2$ calcium channel toxin. Biotinylated ω-conotoxin GVIA targets the mouth of the $Ca_v2.2$ calcium channel with high affinity and can also be targeted with streptavidin bound to Alexa647. c. A new staining technique developed using ω-conotoxin GVIA conjugated to Cage552 for highly specific, single site labelling for SMLM.

molecules. Additionally, as established in immunostaining procedures, cells were pre-incubated with 0.5% (w/v) FSG to further reduce unspecific binding.

Biotinylated ω-conotoxin GVIA (MW: 3376.85) was used at a concentration 1 ng/ml. A serial dilution was done for the streptavidin-Alexa647, reducing the original concentration of 1 mg/ml by 1:1000, 1:2000 and 1:5000, with the aim to eliminate unspecific background staining. Imaging was conducted on the Olympus IX81 microscope in TIRFM mode and using PC12 cells.

In Figure 3.12 it can be seen from the TIRFM images that the staining is concentrated on the cell membrane relative to the background. The biotinylated ω-conotoxin GVIA and streptavidin-Alexa647 staining resulted in a concentration dependent fluorescent intensity, where the overall, averaged fluorescence reflected the amount of concentration of either the biotinylated ω-conotoxin GVIA or streptavidin-alexa647. The control images, where the staining was done with streptavidin-Alexa647 alone, showed a concentration-dependent staining as well (Figure 3.12a). Additionally, the average fluorescence from each staining condition highlights the high level of unspecific binding (Figure 3.12b). This problem is most likely due to targeting of biotin and streptavidin molecules to either endogenous molecules or residues from the pre-blocking incubations with avidin and biotin. Together this demonstrates that the use of biotin and streptavidin as a staining method is not sufficiently robust for single molecule imaging. Additionally, as schematically presented in Figure 3.11, the inherent issue with the streptavidin molecule is that the tetrameric structure can bind a biotin molecule at three of its four interfaces, with the fourth biotin-binding site being blocked due to the covalently bonded alexa647 dye. This may cause crosslinking of $Ca_v2.2$ calcium channels through the binding of several channel-bound biotinylated ω-conotoxin GVIA to one streptavidin-alexa647 molecule (Tytgat et al. 2014).

The above conclusions called for an improved ω-conotoxin GVIA staining method that eliminates the secondary incubation step by directly labelling ω-conotoxin GVIA with a fluorescent dye.

3.4.2 Single Molecule Imaging with Conjugated Cage552-ω-conotoxin GVIA

The single molecule imaging methods PALM and STORM both have their advantages and disadvantages to assess the spatial behaviour of a protein of interest. The advantage of PALM is the reliability of the mono-labelled, encoded fusion protein to only switch on once, after which the bleached molecules are irreversibly destroyed. For assessing the number of molecules, this method provides consistency, although the result of absolute numbers is skewed by the overexpression of proteins. Alternatively,

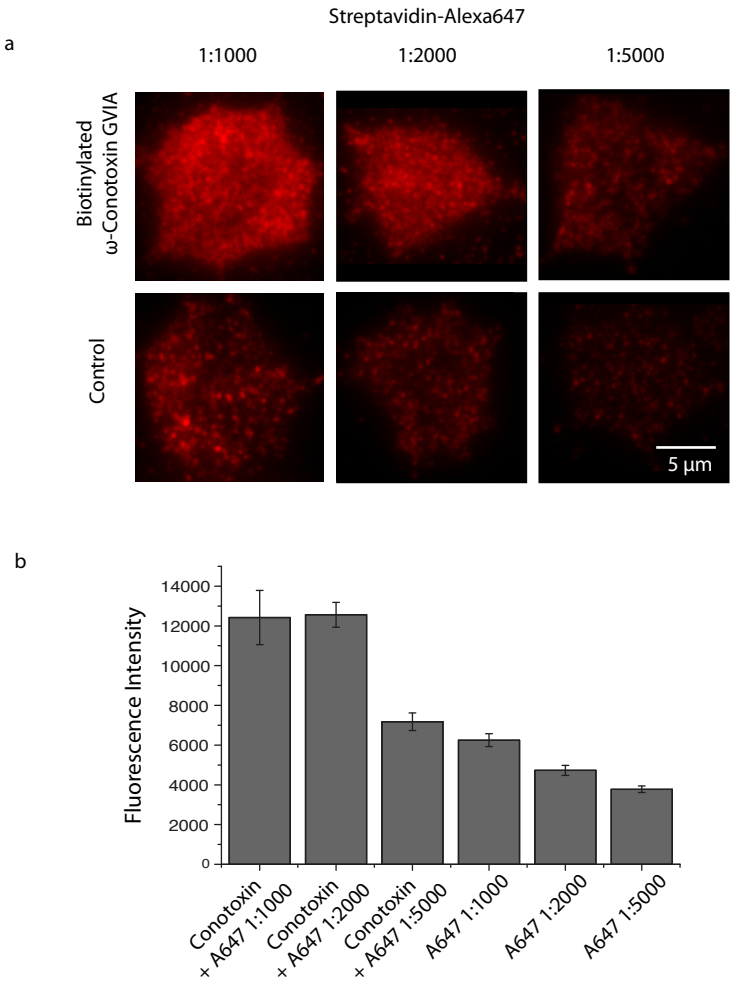

Figure 3.12 **$Ca_v2.2$ calcium channel staining with biotinylated ω-conotoxin GVIA and streptavidin-alexa647.** A. Representative TIRFM images of PC12 cells showing the staining with and without biotinylated ω-conotoxin GVIA and with different dilutions of streptavidin-alexa647. b. The average fluorescence intensity of different conditions showing the overall effect of background staining.

STORM provides a means to image, with single molecule precision, endogenous protein molecules. However, due to the very nature of STORM the fluorescent dyes cycle through the high and low energy states several times, causing blinking, which in turn causes multiple counts of a single molecule. In addition, the immunostaining of cells causes each protein of interest to be labelled with several dyes. This arises through the multiple labelling of the primary antibody with numerous secondary antibodies, each conjugated with multiple dyes, which again leads to multiple counts of a single molecule. As with the biotin-streptavidin method, cross-linking through the secondary antibodies (Figure 3.11a) may be a problem. In this work, a new approach was specifically developed and tested using directly labelled caged dye -ω-conotoxin GVIA to allow for endogenous single molecule imaging of $Ca_v2.2$ calcium channel, circumventing the above-mentioned issues of conventional SMLM. The direct labelling method also eliminates problematic secondary staining, which causes a considerable amount of unspecific signal. Most importantly, however, is this new method provides a 1:1 stoichiometry between the dye molecule and the toxin. This novel approach therefore combines the advantages of both the PALM and STORM techniques.

The chemical conjugation of ω-conotoxin GVIA and the caged dye (Abberior-Cage552, www.abberior.com) was done as a commercial sub-contract by Almac Group UK. The Cage552 dye effectively behaves similarly to photoactivatable proteins, which have to be activated with high energy light, typically 405 nm. After activation, the protein or dye is receptive to the 561 nm excitation wavelength in order to fluoresce. For the Cage552 photoactivation, the principle is the same, although the 405 light uncages the molecule rather than activates it (Figure 3.11c).

Initial tests were performed on the Cage552 dye itself to confirm its performance. Low density, sparse, dye molecules were attached onto glass coverslips using CellTak (Becton-Dickson). The samples were bathed in 1xPBS for SMLM imaging which was done by repeatedly uncaging the dye with the 405 nm laser light before imaging with the 561 nm excitation using a long 200 ms exposure (Figure 3.13a) (see section 1.5.6). A proportion of the dye molecules that were stuck onto the glass were aggregated in clumps, which worked well for the purpose of testing and visually demonstrating the properties of the dye subjected to uncageing. From the images it can be seen that each cycle of uncaging activates more molecules that then decrease in intensity (if aggregated) or activate and bleach in a quantal step, if a single molecule is examined (Figure 3.13b). As a control, an area containing no fluorescent molecules was subjected to the same activation and image sequence. The images showed only a very slight increase, which is probably a result of contaminants on the

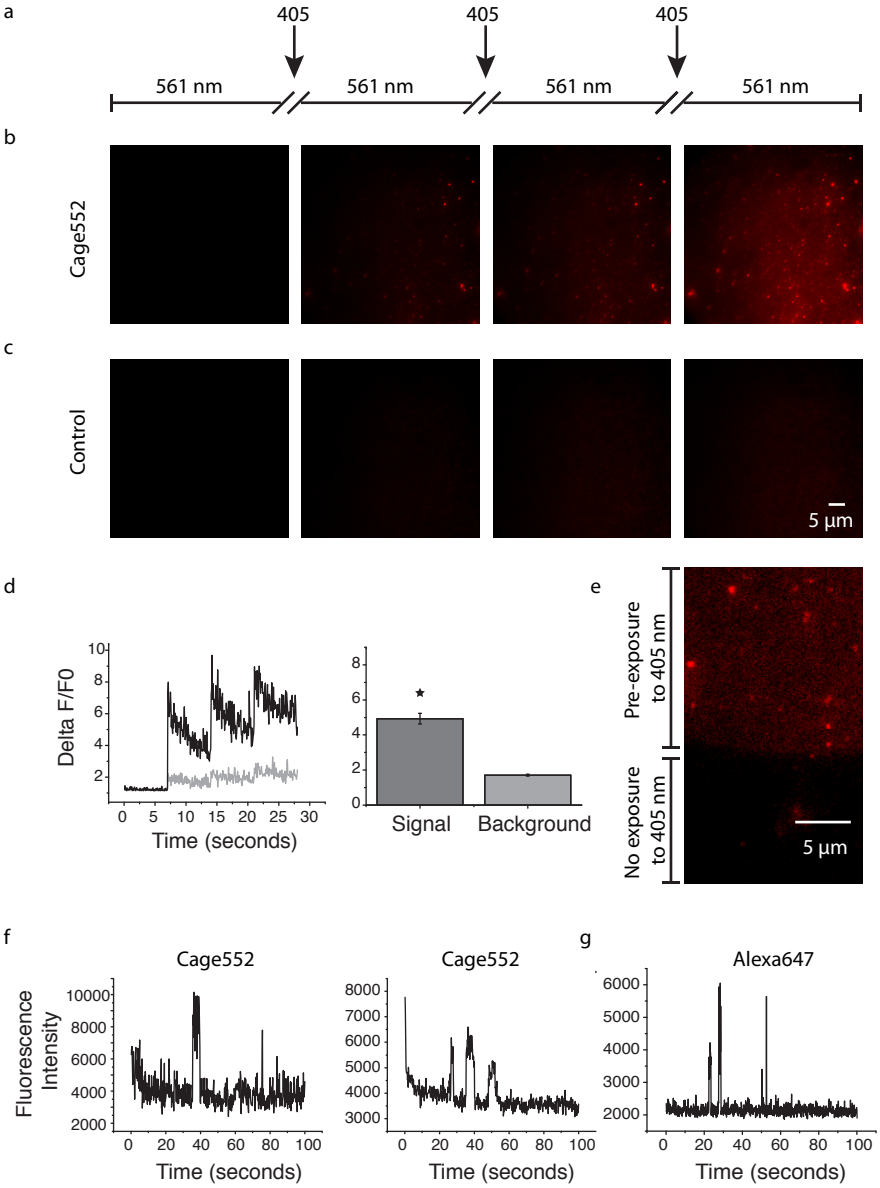

Figure 3.13 **Single molecule localisation testing with Cage552 adhered to the glass surface with CellTak.** a. Schematic diagram of the image acquisition sequence. 405 nm activation excitation is periodically used to activate the 561 nm excited Cage552 molecules. b. Representative images before, then after each uncaging pulse. c. Representative images of an alternative field of view of the same sample but without Cage552 molecules demonstrating the lack of any background contamination. d. Time trace of an aggregate of Cage552 and of the background ROI. The fluorescence difference between the baseline and the maximum fluorescence after the first pulse for both the aggregates and the background is shown in the bar graph. e. Image showing activated (top) and unactivated (bottom) regions further confirming the role of activation on the caged molecules. f. Two representative time traces of single molecules switching on and off. g. An equivalent time trace from a STORM image.

glass coverslip or Cage552 molecules that detached from the CellTak and diffused within the buffer (Figure 3.13c). These behaviours are reflected when plotting the fluorescence profile of an aggregate of dye molecules and an equally sized area in the control image sequence and the average fold increase was plotted, showing a significant difference between the fluorescence signal and the background (Figure 3.13d). Further, evidence that 405 nm light activates Cage552 is demonstrated in Figure 3.13e, where only one half of the image frame was activated, and it can be clearly seen that the molecules were uncaged in the activated region, and those molecules outwith the activated region remain unresponsive to 561 nm excitation. Figure 3.13f shows two individual time traces from a 4x4 pixel (~400 x 400 nm) ROI from Figure 3.13b. Demonstrated here is the switching on and off of molecules. Once molecules are bleached, they cannot fluoresce again, and therefore, if another molecule switches on at the same spot, this can be confidently identified as a different molecule. In contrast to this, Figure 3.13g shows a time trace taken from a STORM image train using Alexa647. Since Alexa647 molecules can blink, it cannot be established if these signals arise from one or several molecules spatially co-localised. The Cage552 test gives confidence in using this labelling molecule for the conjugation to ω-conotoxin GVIA.

A major reason for using ω-conotoxin GVIA, apart from the obvious advantage that these are highly $Ca_v2.2$ calcium channel-specific, is that it may be possible to achieve $Ca_v2.2$ calcium channel imaging in live cells. Consequently, with confidence in the conjugation of this molecule by Almac Group, UK, the Cage552- ω-conotoxin GVIA was used for live cell SMLM experiments. However, as mentioned previously the synthesis of the unique Cage552-ω-conotoxin GVIA conjugate was specifically requested from Almac Group, UK. Unfortunately, the initial test batch of synthesised Cage552-ω-conotoxin GVIA that was available for these experiments did not contain enough molecules to additionally test the pharmacological properties of this specific conjugate molecule through electrophysiological measurements and so the live cell experiment was limited to proof-of-principle SMLM tests.

For the live cell SMLM experiments AtT20 D16:16 cells were transfected with the EGFP-NPY construct. The cells were subjected to a 15 minute incubation at 37°C with Cage552-ω-conotoxin GVIA at a concentration of 1 μM to allow for the $Ca_v2.2$ calcium channel targeting. This was followed by two washes with KREB's HEPES media to eliminate free, unbound Cage552-ω-conotoxin GVIA molecules. The imaging was performed in TIRFM by first taking an image of the vesicles using the 491 nm laser, which usually show very limited movement in AtT20 D16:16 cells, and then imaged the Cage552-ω-conotoxin GVIA as described for the Cage552 imaging. The single molecule

localisation rendering was executed using the SMLM Matlab script generously provided by Dr Sam Hess (Maine) that was specifically designed for single molecule localisation (see section 2.4.3).

In Figure 3.14 two typical image examples are shown of the rendered Cage552-ω-conotoxin GVIA super-resolution localised image overlaid with the diffraction limited vesicle image (green). From the uncropped image it can be seen that Cage552-ω-conotoxin GVIA molecules overlay with the vesicle containing area, which as this is TIRFM imaging, can therefore be assumed to be at the plasma membrane of the transfected cell. There are some molecules detected outwith the area of the base of the EGFP-NPY expressing cells. On careful visual inspection, there seem to be clear areas of higher density localisations and areas of very little localisations. This is likely due to the fact that not all cells are transfected with NPY-EGFP, however all cells are stained with Cage552-ω-conotoxin GVIA. Exploring the localisation within the base of the cell more carefully reveals direct information on the spatial organisation of the calcium channels in relation to the vesicles. In the indicated and expanded ROI region it can be seen by eye that Cage552-ω-conotoxin GVIA is not usually located directly below the centre of the larger (around 400 nm diameter) vesicle. However, the channels seem to be located in close proximity of vesicles, suggesting that the activity of a single calcium channel may trigger fusion. Together this gives confidence that the Cage552-ω-conotoxin GVIA is an excellent new method for SMLM through highly specific $Ca_v2.2$ calcium channel targeting, but further analysis of the images will have to be done to confirm the above speculations.

3.4.3 Conclusion from the Labelling Method using ω-Conotoxin GVIA

The lack of highly specific and effective $Ca_v2.2$ calcium channel antibodies and the drawbacks of current SMLM approaches motivated the search for a new technique to reliably stain $Ca_v2.2$ calcium channels for SMLM. Toxins have evolved to be highly specialised molecules that bind only to specific channels or other proteins, commonly with molar affinity. This property of highly specific binding makes the use of toxins ideal as a labelling method. With ω-conotoxin GVIA being a specific $Ca_v2.2$ calcium channel blocker, it has been successfully shown to be an ideal new method for SMLM.

The first labelling method attempted was performed by using biotinylated- ω-conotoxin GVIA as a primary label to directly target the $Ca_v2.2$ calcium channel and streptavidin-Alexa647 as a secondary label to bind the biotin molecule. However, this proved inefficient, as there was simply too much background staining.

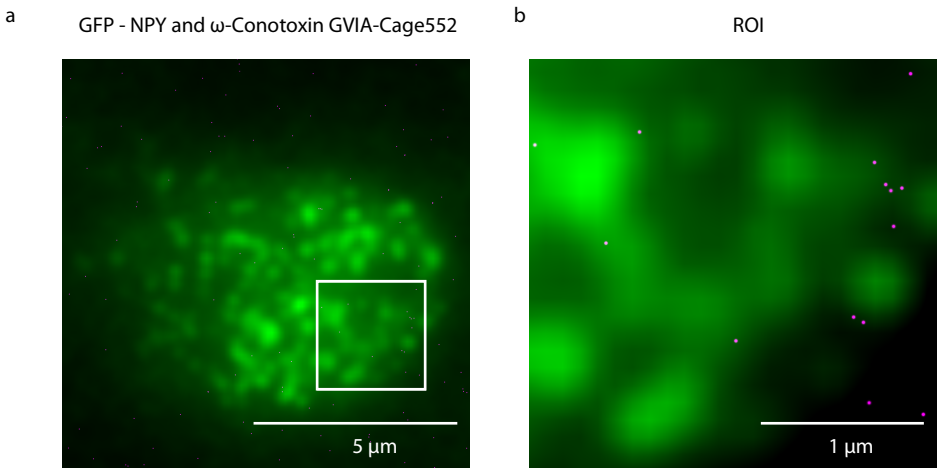

Figure 3.14 **ω-conotoxin GVIA - Cage552 labelling of endogenous $Ca_v2.2$ calcium channels.** a. Live AtT20 D16:16 cells, transfected with EGFP-NPY, were incubated with ω-conotoxin GVIA - Cage552 for labelling of endogenous $Ca_v2.2$ calcium channels. The single-molecule signals of ω-conotoxin GVIA - Cage552 in the images were localised (magenta) and overlaid with an image of vesicles (green). b. The right image is the enlarged ROI indicated by the box in the left image.

Instead, a new idea was pursued, where the ω-conotoxin GVIA molecule was mono-conjugated to a Cage552 molecule, thereby achieving a 1:1 stoichiometry between the toxin and the dye. SMLM using Cage552-ω-conotoxin GVIA was successfully tested on live cells. The proof-of-principle SMLM work promisingly showed that this unique labelling method is effective with little unspecific background staining detected. The spatial distribution of the calcium channels showed that calcium channels were arranged individually across the plasma membrane. This direct evidence suggests that the spatial arrangement of $Ca_v2.2$ calcium channels do not assemble into clusters. There was no evidence of the sparse calcium channels being located directly below the centre of a vesicle, although they remain closely associated. This may suggest tight coupling between vesicle docking and single calcium channels.

The proof-of-principle of this newly designed technique of using Cage552-ω-conotoxin GVIA for SMLM shows great potential, not only for further understanding the spatial relationship of single $Ca_v2.2$ calcium channels with SNARE other proteins or vesicles, but for any spatially sensitive exploration of calcium activity across the plasma membrane.

3.5 Conclusion

The aim in this chapter was to characterise the interaction of the $Ca_v2.2$ calcium channel molecule with syntaxin1a and analyse the distribution of the $Ca_v2.2$ calcium channel at the plasma membrane. The overarching goal is to lay a framework in order to further understand the specific details of the involvement of these channels, in particular for the study of exocytosis. This characterisation was achieved through two different approaches. Firstly, $Ca_v2.2$ calcium channels were studied in relation to syntaxin1a through sub-resolution measurements. Co-localisation demonstrated evidence of a spatial localisation of the synprint site with the $Ca_v2.2$ calcium channel, which was confirmed with FRET-based spectroscopy using both spectral scanning and FLIM-FRET. The FLIM-FRET data shows that the synprint site is necessary for the spatial interaction of the $Ca_v2.2$ calcium channel and syntaxin1a at the plasma membrane. Secondly, through the development and application of a novel method of single $Ca_v2.2$ calcium channel targeting, single molecule imaging was achieved. The initial idea of using biotinylated-ω-conotoxin GVIA and streptavidin-alexa647 was disregarded due to high unspecific staining. Alternatively, cage552-ω-conotoxin GVIA, proved highly successful ,after thorough visual inspection of the images, in specifically labelling the $Ca_v2.2$ calcium channels. The data showed sparse and isolated $Ca_v2.2$ calcium channels and,

when compared to spatial position of labelled vesicles, suggests that single calcium channels are sufficient to trigger fusion. These conclusions are on the basis of visual inspection of the cage552-ω-conotoxin GVIA images and would have to be further analyse to quantify the spatial distribution and increase the confidence in these results.

These results, from both FLIM-FRET and SMLM, support the hypothesis that only sparsely isolated $Ca_v2.2$ calcium channels are located at functionally relevant distances to the vesicle docking sites. Although this conclusion is somewhat speculative, the evidence pointing to the importance of isolated channels to fusion may suggest that, through the interaction of syntaxin1a only few $Ca_v2.2$ calcium channels are receptive to fusion vesicles. Together, this implies that calcium activity and fusion are spatially tightly coupled.

References

Becker, W., 2005. *Advanced Time-Correlated Single Photon Counting Techniques* A. W. Castleman, J. P. Toennies, & W. Zinth, eds., Berlin, Heidelberg: Springer Berlin Heidelberg.

Bennett, M.K., Calakos, N. & Scheller, R.H., 1992. Syntaxin : A Synaptic Protein Implicated in Docking of Synaptic Vesicles at Presynaptic Active Zones. *Science*, 257, pp.255–259.

Bezprozxanny, I., Scheller, R.H. & Tsien, R.W., 1995. Functional impact of syntaxin on gating of N-type and Q-type calcium channels. *Nature*, 378, pp.623–626.

Broussard, J.A. et al., 2013. Fluorescence resonance energy transfer microscopy as demonstrated by measuring the activation of the serine/threonine kinase Akt. *Nature protocols*, 8(2), pp.265–81.

Catterall, W. a, 2000. Structure and regulation of voltage-gated Ca2+ channels. *Annual Review of Cell and Developmental Biology*, 16, pp.521–55.

Chen, R. & Chung, S., 2013. Complex structures between the N-type calcium channel (Cav2.2) and w-conotoxin GVIA predicted via molecular dynamics. *Biochemistry*, 52, pp.3765–3772.

Duncan, R.R., 2006. Fluorescence lifetime imaging microscopy (FLIM) to quantify protein-protein interactions inside cells. *Biochem Soc Trans*, 34, pp.679–682.

Endean, R., Parish, G. & Gyr, P., 1974. Pharmacology of the venom of Conus geographus. *Toxicon*, 12(2), pp.131–8.

Gray, W.R., Olivera, B.M. & Cruz, L.J., 1988. Peptide toxins from venomous Conus snails. *Annual Review of Biochemistry*, 57, pp.665–700.

Haack, J.A. et al., 1993. Biotinylated derivatives of w-conotoxins GVIA and MVIID: probes for neuronal calcium channels. *Neuropharmacology*, 32(11), pp.1151–1159.

Harkins, A.B. et al., 2004. Deletion of the synaptic protein interaction site of the N-type (Ca V 2 . 2) calcium channel inhibits secretion in mouse pheochromocytoma cells. *PNAS*, 101(42), pp.15219-15224.

Jones, O.T. & So, A.P., 1993. Preparation and characterization of biotinylated analogs of the calcium channel blocker w-conotoxin. *Analytical Biochemistry*, 214, pp.227–232.

Keith, R.K. et al., 2007. Bidirectional modulation of transmitter release by calcium channel / syntaxin interactions In vivo. *The Journal of Neuroscience*, 27(2), pp.265–269.

Kerr, L.M. & Yoshikami, D., 1984. A venom peptide with a novel presynaptic blocking action. *Nature*, 308(5956), pp.282–4.

Kohn, A.J., 1956. Piscivorous gastropods of the genus conus. *Zoology*, 42, pp.168–171.

Lin, Y., McDonough, S.I. & Lipscombe, D., 2004. Alternative splicing in the voltage-sensing region of N-Type CaV2.2 channels modulates channel kinetics. *Journal of Neurophysiology*, 92, pp.2820–30.

Medine, C.N. et al., 2007. Time-correlated single photon counting FLIM : some considerations for physiologists. *Microscopy Research and Technique*, 425, pp.420–425.

Nielsen, K.J., Schroeder, T. & Lewis, R., 2000. Structure – activity relationships of v -conotoxins at N-type voltage-sensitive calcium channels. *Journal of Molecular Recognition*, 13, pp.55–70.

Olivera, B.M. et al., 1984. Purification and sequence of a presynaptic peptide toxin from Conus geographus venom. *Biochemistry*, 23(22), pp.5087–90.

Rizzo, M.A. et al., 2004. An improved cyan fluorescent protein variant useful for FRET. *Nature Biotechnology*, 22(4), pp.445–9.

Ruiz, R. et al., 2011. Active zones and the readily releasable pool of synaptic vesicles at the neuromuscular junction of the mouse. *The Journal of Neuroscience*, 31(6), pp.2000–2008.

Sheng, Z. et al., 1994. Identification of a syntaxin-binding site on N-type calcium channels. *Neuron*, 13, pp.1303–1313.

Sheng, Z., Westenbroek, R.E. & Catterall, W.A., 1998. Physical link and functional coupling of presynaptic calcium channels and the synaptic vesicle docking / fusion machinery. *Journal of Bioenergetics and Biomembranes*, 30(4), pp.335–345.

Sheng, Z.-H., Yokoyama, C.T. & Catterall, W.A., 1997. Interaction of the synprint site of N-type Ca 2 + channels with the C2B domain of synaptotagmin I. *PNAS*, 94, pp.5405–5410.

Smith, M.C. et al., 1988. Chelating peptide-immobilized metal ion affinity chromatography. *The Journal of Biological Chemistry*, 263(15), pp.7211–7215.

Szabo, Z. et al., 2006. Role of the synprint site in presynaptic targeting of the calcium channel Ca V 2.2 in hippocampal neurons. *European Journal of Neuroscience*, 24, pp.709–718.

Terlau, H. & Olivera, B.M., 2004. Conus venoms: a rich source of novel ion channel-targeted peptides. *Physiological reviews*, 84, pp.41–68.

Tytgat, H.L.P. et al., 2014. Endogenous biotin-binding proteins: an overlooked factor causing false positives in streptavidin-based protein detection. *Microbial biotechnology*.

Vink, S. & Alewood, P.F., 2012. Targeting voltage-gated calcium channels: developments in peptide and small-molecule inhibitors for the treatment of neuropathic pain. *British Journal of Pharmacology*, 167, pp.970–89.

Witcher, D.R., Waard, M.D.E. & Campbell, K.P., 1993. Characterization of the purified N-type Ca2+ channel and the cation sensitivity of w-conotoxin GVIA binding. *Neuropharmacology*, 32(11), pp.1127–1139.

Wu, M.N. et al., 1999. Syntaxin 1A interacts with multiple exocytic proteins to regulate neurotransmitter release In vivo. *Neuron*, 23, pp.593–605.

Yarotskyy, V. & Elmslie, K.S., 2009. ω -Conotoxin GVIA alters gating charge movement of N-type (CaV2 . 2) calcium channels. *Journal of Neurophysiology*, 101, pp.332–340.

Yokoyama, C.T. et al., 2005. Mechanism of SNARE protein binding and regulation of Ca v 2 channels by phosphorylation of the synaptic protein interaction site. *Molecular and Cellular Neuroscience*, 28, pp.1–17.

Yokoyama, C.T., Sheng, Z. & Catterall, W.A., 1997. Phosphorylation of the synaptic protein interaction site on N-type calcium channels inhibits interactions with SNARE proteins. *The Journal of Neuroscience* , 17(18), pp.6929–6938.

Zamponi, G.W., 2003. Regulation of presynaptic calcium channels by synaptic proteins. *Journal of Pharmacological Sciences*, 92, pp.79–83.

Chapter 4 Imaging and Quantifying Voltage-Gated Calcium Channel Activity in Cells

This chapter focuses on improving the acquisition of calcium imaging and the analysis of calcium activity due to the opening of plasma membrane located voltage-gated calcium channels. Firstly, by creating a new fusion protein between an existing genetically encoded calcium indicator, R-GECO1, and SNAP25, the calcium indicator was targeted directly to the plasma membrane. The restricted movement of the indicator itself significantly improved TIRFM imaging of the calcium activity at the plasma membrane, compared to the use of soluble calcium indicators such as Fluo4. Secondly, a new method to analyse the spatial and temporal distribution of functional voltage-gated calcium channels in a non-subjective, intensity insensitive manner, was developed. The result was a map of the cell showing the amount of calcium activity dynamic behaviour at each pixel.

4.1 Imaging the Dynamics of Intracellular Calcium

The cellular regulation of calcium channels controlling the calcium flux at the plasma membrane is a dynamic event that dictates the spatial and temporal properties of regulated exocytosis. Early mathematical modelling attempted to estimate the spatial calcium activity, taking into consideration all the parameters such as ionic current and number of channels (Chad & Eckert 1984; Sala & Hernández-Cruz 1990). Such work concluded that the calcium influx centred on individual calcium channels can be modelled, but not the spatial extent of the calcium domains, as this varies with the different types of calcium channels with their individual gating properties as well as with their distribution, essentially whether the proteins are clustered or individual. Therefore, only live calcium imaging can truly reveal the spatio-temporal dynamics of calcium flux at the plasma membrane.

In the 1990s a method of calcium imaging was developed using calcium dyes to try and capture single channel events (Zou et al. 1999). Initially, calcium-binding dyes, which have a high affinity for calcium ions and through the binding of calcium ions dramatically increase their fluorescence absorption and emission properties were used to image intracellular calcium flux (Figure 4.1a). Examples commonly include Fluo-3 (Zou et al. 1999) or Rhod-2 (Robinson et al. 1996). Calcium imaging was used to try and image the calcium events at the plasma membrane through TIRFM imaging or to try and reveal Ca^{2+}-triggered Ca^{2+} release (Wang et al. 2001). Experimental work on observed calcium events showed they were large in size, with a fitted curve measuring a full width half maximum (FWHM) of 600 nm (Demuro & Parker 2004). However, a thorough mathematical analysis of Fluo-4 imaging, another calcium indicator with slightly different fluorescence and affinity properties than Fluo-3 or Rhod-2, which took into account all parameters from affinity to diffusion rate, resulted in a theoretical calcium event with a FWHM of 250 nm during a 10 ms channel opening (Shuai & Parker 2005). For precise spatial analysis of calcium events the above discrepancy highlights the call for a better solution of a biological calcium dye.

Roger Tsien and his group were the first to develop a FRET based genetically encoded calcium indicator (GECI) based on calmodulin, M13 and two FP (Miyawaki et al. 1997) (Figure 4.1b). The big advantage of GECIs is that they can be targeted to certain cellular compartments by genetically linking them to a protein that locates to the region of interest. GECIs were further developed and fluorescent properties improved (Zhao et al. 2011; Yamada & Mikoshiba 2012; Ohkura et al. 2012) as discussed in Chapter 1, section 1.6, and various different GECIs have been methodically analysed to thoroughly understand their properties, especially in light of neuronal activity

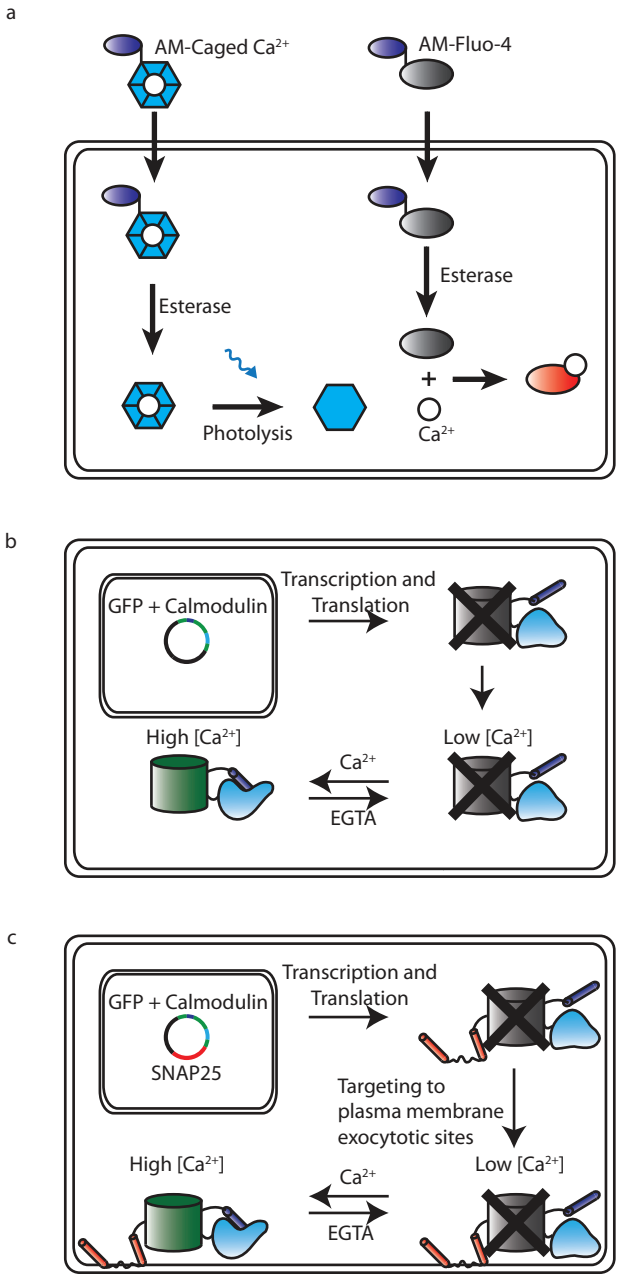

Figure 4.1 **Calcium dyes and detection methods for calcium imaging.** a. Fluo4 and Caged-Ca^{2+} pass through the plasma membrane into the cell, where esterases cleave off the ester side-chain, preventing the molecule from exiting the cell. With natural calcium or uncaged calcium binding to the Fluo4 dye, an increase in calcium concentration can be detected. b. Genetically encoded calcium indicators are transfected, then expressed by the cell. c. A fusion protein of the genetically encoded calcium indicator with SNAP25 was created to ensure plasma membrane localisation of the calcium indicator.

(Akerboom et al. 2012; Akerboom et al. 2013). GECI's have been implemented to image calcium during the retinal response to electrical stimulation (Weitz et al. 2013), as well as the calcium dynamics in primary cilia (Su et al. 2013). This thesis expands on previous work on calcium behaviour at the plasma membrane of secretory cells, by genetically linking the GECI, R-GECO1, to SNAP25 to enable TIRFM imaging of calcium activity on the membrane (Figure 4.1c).

To date, most calcium imaging activity has been analysed using similar methodology, namely by F/F_0, which divides all the images in a time varying image movie sequence by the reference 'baseline' image, the first frame, F_0. This approach gives an indication of percentage increase of fluorescence over time. An alternative but similar approach, $\Delta F/F_0$, calculates and rescales the fluorescence intensity by the equation $(F-F_0/F_0)$. These approaches highlight intensity changes in the trace, and are good for exploring representative traces or as a rough demonstration of high calcium activity areas in cells when summing the images over the time domain. However, the intensity profile is different from cell to cell, which eliminates the use of absolute fluorescence values. In addition, different calcium channels have distinctive gating and the small and short events would disappear through the summation of several hundred images and be disregarded. The widely accepted approach of singling out by select calcium events for analysis is very subjective and, as before, smaller events are often neglected in favour for the obviously high activity and bright events (Demuro & Parker 2003). Crucially, selecting individual events does not provide any information on the spatial distribution of the calcium activity, essential for understanding processes such as exocytosis. An ideal approach would offer a non-subjective analysis over the entire image and be sensitive to all activity types and event durations whilst successfully ignoring noise and inactive regions. In this chapter, a new analysis approach that combines novel biological probes, new imaging techniques and temporal autocorrelation analysis is presented. This approach is insensitive to intensity as well as to subjective data handling; this will be explained in more detail in section 4.4. A calcium activity map is created from the TIRFM images of calcium imaged over a period of time. Through a pixel-by-pixel analysis by autocorrelation of the z-axis profile, a map is created differentiating pixels with a highly active intensity profile displaying a high correlation with itself from those pixels that do not exhibit high activity. The map is therefore a pure representative of calcium activity.

4.2 Genetically Encoded Calcium Indicators fused to SNAP25

The primary aim of this chapter was to improve the spatial and temporal acquisition of calcium imaging. The localisation of a genetically encoded calcium indicator, R-GECO1, to the plasma membrane was done by creating a fusion protein with the SNARE protein SNAP25. The fluorescence property of R-GECO1 in response to different calcium concentrations was examined and the correct expression and localisation of the fusion protein R-GECO1-C1-SNAP25 was determined through widefield and TIRFM microscopy.

4.2.1 Cellular Expression of R- GECO1

To evaluate the effectiveness of the probe to different calcium concentrations the R-GECO1 cDNA was transfected into AtT20 D16:16 cells and the total fluorescence increase measured at different calcium concentrations by flooding the cell with calcium. The plasma membranes were made Ca^{2+} permeate by adding an ionophore, which are lipid soluble molecules that can transport ions across lipid membranes. Specifically, the ionophore ionomycin, produced by *Streptomyces conglobatus*, was used, which are specific Ca^{2+} ion carriers. The untargeted R-GECO1 filling the cytoplasm of the cell binds to the free calcium ions, restoring its fluorescence properties. For imaging single calcium events, the maximum intensity change occurs at the mouth of the channel (Sala & Hernández-Cruz 1990), which is why it is important to gauge the dynamic range of the indicator fluorescence. The difference in baseline fluorescence of the entire cells was compared to the maximum fluorescence after the 1 µM ionomycin addition (Figure 4.2a). This was done in different calcium concentrations, adjusting the EGTA/calcium molar amount in the extracellular KREBs buffer to give 0 mM, 0.1 mM, 1 mM, 3mM and 10 mM free Ca^{2+}. Calculated for each cell individually, the baseline fluorescence was defined as the average fluorescence of the first 10 frames and, after the addition of ionomycin, the peak increase, judged by the intensity profile of the overall intensity changes, was also an average of 10 frames (Figure 4.2b). The average intensity change was plotted (Figure 4.2c), showing a maximum change between 1 mM (fold increase 1.78 ± 0.35 SEM) and 3 mM (fold increase 1.67 ± 0.34 SEM) free extracellular Ca^{2+}. This was reflected in the maximum values (Figure 4.2d), which show a marked increase again between 1 mM (fold increase 4.55 ± 0.56 SEM) and 3 mM (fold increase 4.72 ± 0.65 SEM) free Ca^{2+}. During the opening event of a calcium channel the highest internal calcium concentration will be closest to the mouth of the channel and the calcium concentration will decrease with distance from the centre of the channel. The intensity of an imaged calcium event should reflect these concentrations.

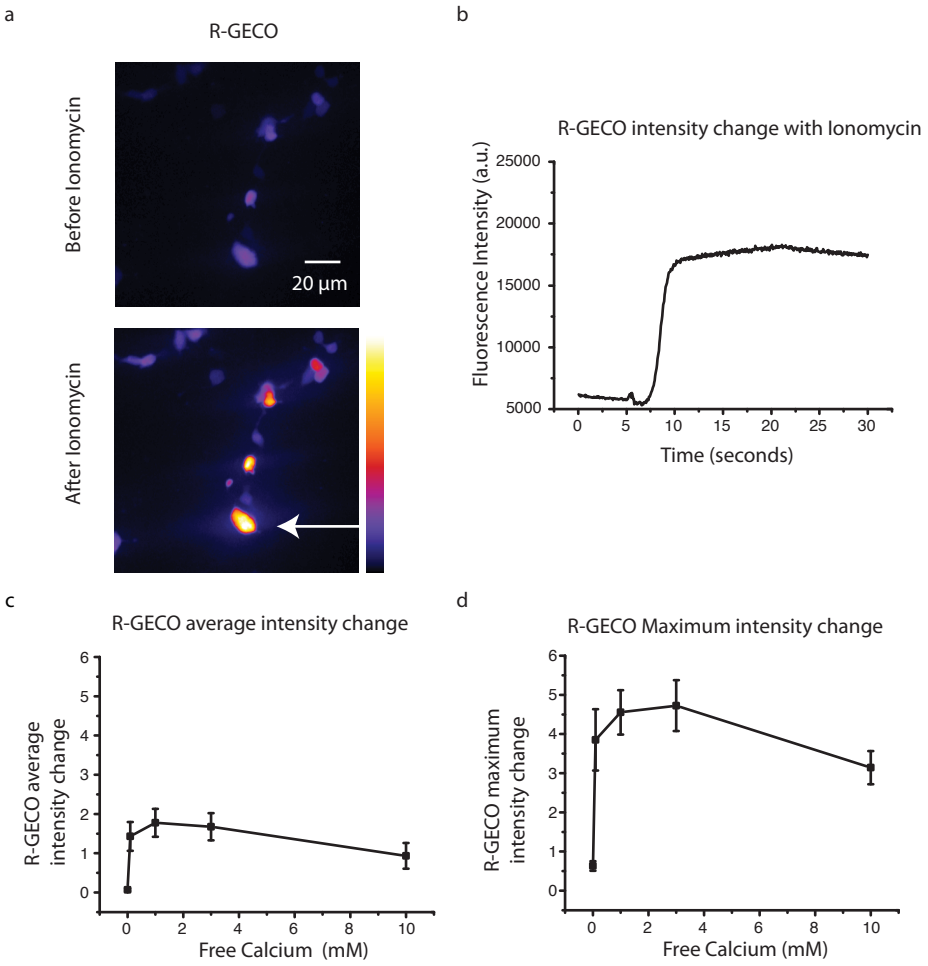

Figure 4.2 **Fluorescence intensity profile of R-GECO1.** a. AtT20 D16:16 cells transfected with R-GECO1 were subjected to 1 µM ionomycin to measure the fluorescence increase. b. Example trace of the average fluorescence profile with the addition of 1 µM ionomycin in a 1 mM Ca2+ containing KERB's buffer. c. The average intensity change over the entire cells at different extracellular calcium concentrations. d. The maximum intensity change in each cell at different extracellular calcium concentrations.

Judging from the data presented in figure 4.3 the optimal extracellular concentration for calcium imaging is between 1 and 3 mM free Ca^{2+}. As the physiologically optimal calcium concentration in KREBs buffers is 1 mM, this value was the concentration used for all following experiments.

4.2.2 Molecular Engineering of the R-GECO-C1-SNAP25 Vector

As a relatively small protein of only 25 kDa with very high plasma membrane locatlisation efficiency, SNAP25 was chosen to create a fusion protein with R-GECO1. The cDNA of R-GECO1 was mutated by PCR to eliminate the two *BrsG* I sites, and was inserted into the CloneJet vector. The sequence was then excised using the *Age* I and *BrsG* I restriction enzymes to replace the EGFP sequence in the EGFP-C1-SNAP25 vector. The final R-GECO1-C1-SNAP25 vector was used for all following plasma membrane calcium imaging.

4.2.3 Expression of R-GECO-C1-SNAP25 in AtT20 Cells

The R-GECO1-C1-SNAP25 vector was transfected into AtT20 D16:16 to confirm the plasma membrane targeting of the R-GECO1. Imaging was done on the widefield Olympus IX81 Cell^{+} TIRF microscope with the Hammamatsu EMCCD camera at a frame rate of 16.6 Hz (60 ms/frame) giving a stack of images in xy and t. The EMgain and laser power were consistently set to 500 and 15 % respectively. The intensity profiles over time were extracted by choosing a region of interest (ROI) on the stack and using the z-axis profile application in the ImageJ software.

Widefield images show a faint fluorescence lining the plasma membrane of the cell. The addition of 1 µM ionomycin elicited a sharp fluorescence increase at the plasma membrane (Figure 4.3a), shown in the fluorescence intensity profile (Figure 4.3b). The cells were then imaged in TIRFM without addition of ionomycin. Background fluorescence is unavoidable due to the nature of very low intracellular calcium, but in the TIRFM images clear events turn on and off (Figure 4.3c). The intensity profiles for single events, an example shown in Figure 4.3d, show short increases of fluorescence for just a few frames, though varying in duration. This confirms that the R-GECO1-C1-SNAP25 is restricted to the plasma membrane and successfully shows clear and punctate calcium activity. The next step is to analyse calcium activity in detail.

4.3 Analysing Full Cell Calcium Activity

The calcium images in TIRFM, such as the example shown in Figure 4.4a, seem to show a temporally uncoordinated activity of spatially distinct calcium channels. The distinct

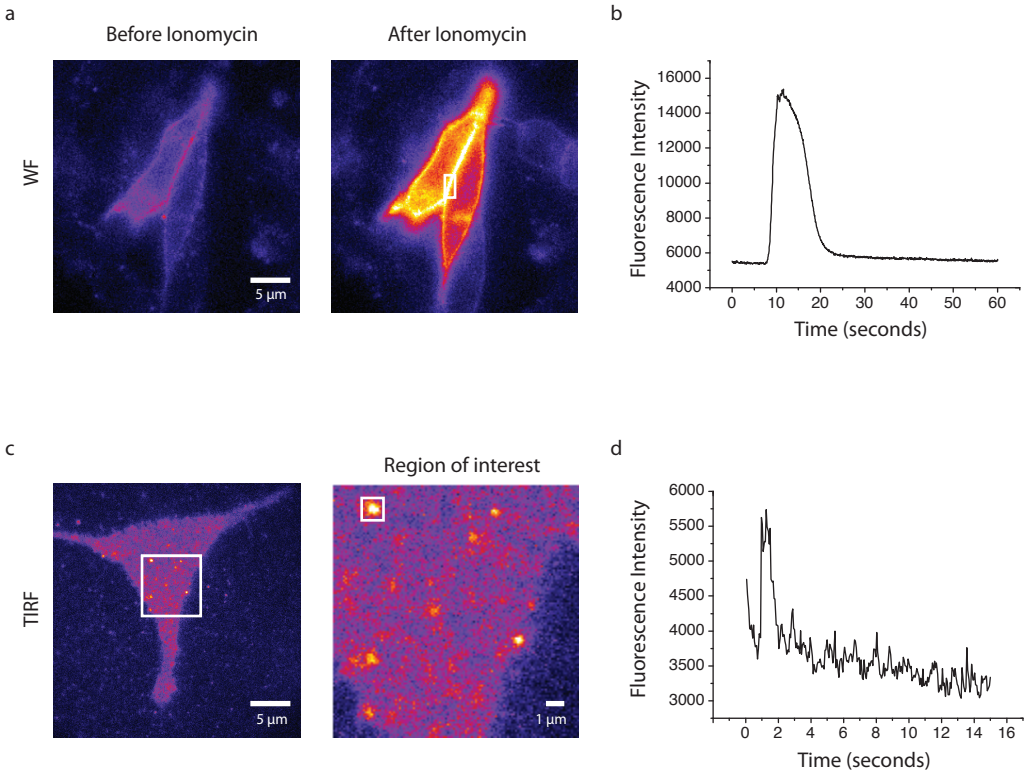

Figure 4.3 **Expression of the R-GECO-SNAP25 fusion protein.** a. Widefield images of AtT20 D16:16 cells expressing R-GECO1-SNAP25 before and after the addition of 1 µM ionomycin. b. The fluorescence intensity profile at the plasma membrane (from the ROI indicated in (a)). c. TIRFM images of R-GECO1-SNAP25 transfected AtT20 D16:16 cells. d. The fluorescence intensity profile of the square indicated within the ROI image in (c).

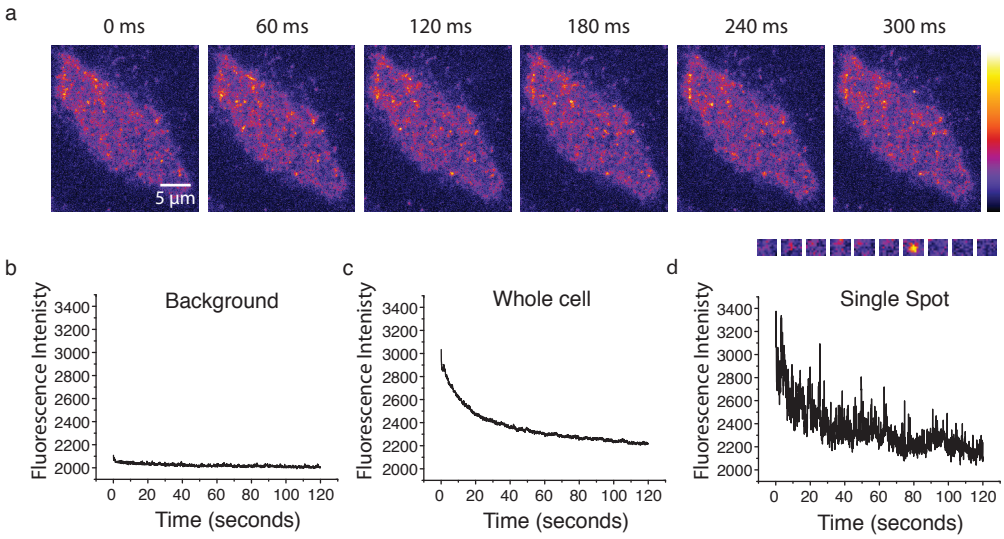

Figure 4.4 **Overall calcium activity.** a. Successive sequence of images of a R-GECO-SNAP25 transfected AtT20 D16:16 cell taken in TIRFM mode with a frame rate of 16.6 Hz (60 ms/frame). b. The fluorescence intensity profile of the background. c. The fluorescence intensity profile of the whole cell. d. The fluorescence intensity profile of a 3x3 pixel (300x300 nm) ROI.

spatial and temporal variation of calcium activity across the cell strongly suggests that a complete spatio-temporal analysis over the entire TIRFM image is required in order to reveal the underlying dynamic behaviour of calcium channel activity and subsequent channel populations. Image analysis using the overall cell activity, by averaging the intensity over each frame (Figure 4.4b), demonstrates explicitly an inability to distinguish detailed calcium activity as the distinct spatial information across the cell is masked by the averaging. However, of interest here is the overall exponentially decreasing decay (Figure 4.4c), suggesting clear photobleaching properties, which detracts the impact of the raw signal in each pixel (Figure 4.4d). Simple bleach correction done on the entire stack using the ImageJ application fits a single exponential to the overall bleach rate and corrects all pixels with the same equation. This approach adequately corrects the bleaching for superficial interpretation but is limited for detailed analysis. While the overall intensity is corrected with the a global bleach correction, careful analysis of every single pixel shows that not every pixel is corrected adequately. Many still display a decay, while others are overcorrected and show a rise, meaning that the each pixel has a slightly varying decay constant.

The inability for full cell analysis to reveal detailed calcium activity is highlighted through single pixels selectively chosen, which show a range of activity. Again, bleach correction is required on each trace to reveal true behaviour. Within the cell, some pixels display no activity, with the baseline being fairly high but not uniform across the cell surface. Active pixels, where the fluorescence show obvious jumps in intensity, display a wide variety of activity in terms of amount of fluorescence increase, the duration of activity, as well as the number of active events. These details, and how to extract them over the whole image, will be discussed in depth in section 4.4.

Though most cells did not show any overall, synchronised calcium activity, some do by exhibiting clear calcium 'waves', which appear to be a simultaneous or coordinated opening of very many calcium channels at the plasma membrane (Figure 4.5). This phenomenon has been observed in cells for a number of functions such as cell division, keeping up the rhythmic beating of the heart, as well as for slow continuous secretion of hormones (Hodson et al. 2012). Specifically in pituitary cells such as AtT20 D16:16 this calcium 'wave' like behaviour has been observed before and is postulated to increase the secretion of hormones (Stojilkovic 2012). The calcium 'waves' shown were detected with the R-GECO1-C1-SNAP25, and, although not ideal for single calcium channel activity imaging as they dominate the cell behaviour, provide a means to demonstrate that indeed the calcium imaging was capturing the events at or near the plasma membrane. The addition of an L-type VGCC blocker, Nifedipine, at 1 μM, to the KREBs

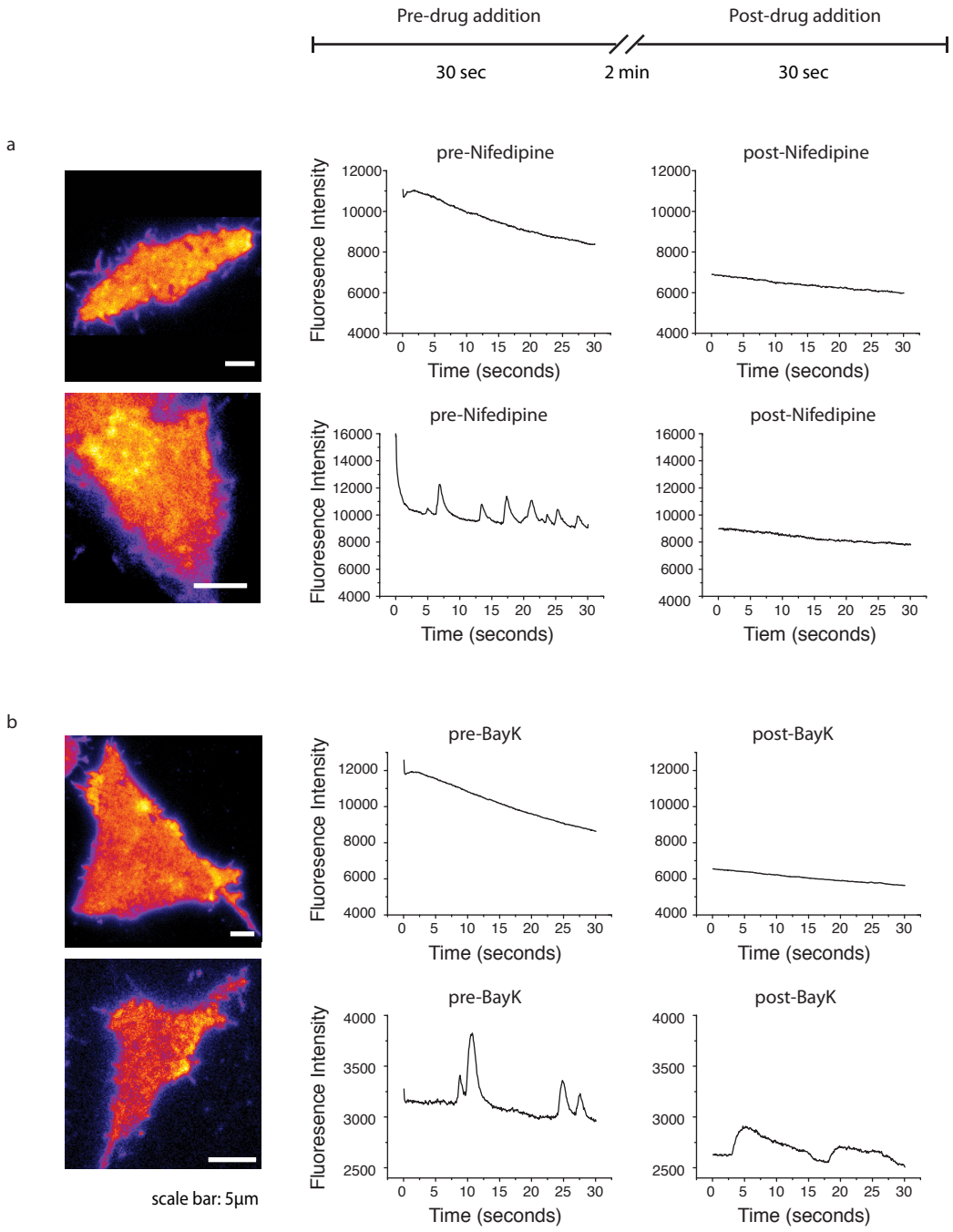

Figure 4.5 **Calcium oscillation were altered by addition of drugs.** a. R-GECO-SNAP25 transfected AtT20 D16:16 cells were imaged before and after the addition of 1 μM Nifedipine. b. R-GECO-SNAP25 transfected AtT20 D16:16 cells were imaged before and after the addition of 1 μM BayK.

buffer inhibited the calcium 'waves' (Figure 4.5a) and vice versa, the 1 μM addition of an L-type VGCC agonist increased the opening time of the channels, increasing the length of the calcium 'waves' (Figure 4.5b). As the antagonist and agonist can only bind and act on the extracellular channel domain, the blocking and enhancement of calcium activity demonstrates that the TIRFM images truly arise from activity at the plasma membrane.

4.4 Analysing Single Calcium Events

Full cell analysis, although useful under specific conditions such as for calcium 'waves', is not a suitable means to analyse the diverse activity displayed in every pixel arising from different calcium channels, emphasizing the need for a more complex method. Ideally, this analysis has to be non-subjective, be pixel-by-pixel to retain the original imaging resolution, and be over the entire time stack due to the nature of activity variation. Furthermore, the choice of analysis also has to be intensity insensitive, to eliminate the difference in baseline fluorescence skewing the results. All this points to a pixel-by-pixel analysis to create a map showing the spatial and temporal activity.

As shown in Figure 4.6 many different types of calcium activity are displayed in the time traces. The background, the region outside the defined cell boundary, shows a trace dominated by noise, a very slightly decaying trace with an intensity value of around 1500 – 1600. This background is of no interest to the calcium imaging as such, but does have to be taken into consideration for the analysis of the entire image. Inactive traces are those within the cell boundary that display a noise dominated but heavily sloping trace, with no clear intensity fluctuations above the bleaching decay, with the starting intensity values varying significantly between pixels. This demonstrates the absolute intensity values are a non-ideal and non-robust method for further image analysis, making an intensity insensitive choice of analysis preferred. Active traces, again dominated by the sloping effect of bleaching, are defined as showing a range of spikes varying in duration and fluorescence intensity as well as frequency. With calcium channel activity ranging from 1 – 100 ms, all calcium events, including those lasting only one frame, would ideally be accounted for. Crude analysis attempts involving summing or averaging the time stack will only lead to biasing high baseline fluorescence areas and high calcium activity, but will obscure short and faint calcium activity.

As discussed in section 4.1, F/F_0 and $\Delta F/F_0$ are often used for data representation and analysis. Furthermore, analysis commonly consists of subjectively picking out events

and showing single representative traces. This approach is acceptable for illustrative purpose, however considering that there are a wide variety of calcium channels in the plasma membrane, each with different channel gating, manually picking out events would lead to side-lining the fainter events as the bright events have a higher demonstrative impact. The $\Delta F/F_0$ method essentially rescales the traces to highlight intensity changes and returns another stack representing the rescaled traces in the same format as the original stack. This gives no analytical interpretation of the activity as such and the information still needs to be extracted from the time stack. What is needed is a conversion of the 3D temporal information into 2D, done in a non-subjective unbiased way that accurately represents the spatial distribution of calcium activity.

4.4.1 Autocorrelation: Pixel-by-Pixel

To analyse single calcium events in conjunction to other biological processes, such as exocytosis, the need for an accurate analysis of the spatial and temporal calcium activity at the plasma membrane is apparent. Summing the images of the $\Delta F/F_0$ stack is one way to gauge where areas of activity are. However, as discussed above, given that an imaging stack may consist of more than 1000s of single images in total, summing the images will mask the small and short events and only the large and frequent events will be spatially highlighted.

Given the limitation with the $\Delta F/F_0$ approach, an alternative methodology is developed here to create a full spatial map to take into account the temporal and spatial calcium activity. This approach is based on autocorrelation analysis. Autocorrelation is a measure that compares the degree of similarity of the intensity profile to itself over successive time lag intervals. Largely insensitive to noise and intensity level, autocorrelation is a standard approach for quantifying temporal fluctuations in order to highlight the time constants of any underlying processes, including extracting information on rapid temporal events close to the acquisition rate. Autocorrelation is used for a number of applications, which deal with fluctuating traces; a prime example being Fluorescence Correlation Spectroscopy (FCS), where it is used to extract the local concentrations, mobility coefficients and characteristic rate constants of inter and intra molecular interactions of diffusing molecules in low concentration solutions (Hess et al. 2002). Full FCS analysis is reliant on complex model fitting to extract the above, but the underlying analysis begins with a calculation of the autocorrelation function of the intensity fluctuations in the recorded photon counting trace. Another example of autocorrelation analysis is in classifying the photo-physical dynamics in single molecule

spectroscopy. For example in studying isolated conjugated polymers (Yip et al. 1998). Here single molecules are isolated, in solution, and the temporal fluctuation is used to characterise the underlying photo-physical behaviour, which varies with polymer confirmation. Autocorrelation again extracts the underlying dynamics, this time of the molecules' conformational restructuring. A similar approach was used in a study of tethered, isolated conjugated polymers in solution (Dalgarno et al. 2013). The second order autocorrelation is also the underlying principle behind detection single photon emission from a single molecule or single quantum dot in directly experimentally measured photon anti-bunching work (Michler et al. 2000; Lounis & Moerner 2000). All these applications demonstrate the power of autocorrelation for the analysis and extraction of dynamic processes in complex time traces. In this thesis the motivation is to compress the temporal information from the autocorrelation traces into a single value in order to create a 2D spatial map that displays temporal behaviour in each pixel.
Autocorrelation is a standard statistical approach to extract the cross correlation of a signal with itself. Autocorrelation, G, of a given signal, I, is defined as the time average of the original signal, I(t), with the lagged signal, I(t+τ), over all time lags, and normalised by the overall intensity of the original signal (Fox n.d.).

$$G'(\tau) = \frac{\langle I(t)I(t+\tau)\rangle}{\langle I(t)\rangle^2} \qquad 4.1$$

G'(τ) returns normalised values between -1 (negatively correlated) and 1 (fully positively correlated) and can include zero (completely uncorrelated).
Conceptually, autocorrelation is relatively simple. Overlaying the trace with the exact same trace, at zero time lag, gives 100% identical match and in the autocorrelation analysis is represented as the value 1. As the overlaid trace is shifted frame by frame (ie. the lag), the autocorrelation value changes according to how similar the trace remains to its original zero lag behaviour. For traces with little similarity, the autocorrelation curve falls quickly towards zero. If different parts of the intensity trace are similar, the degree of similarity remains high, which again is reflected in the autocorrelation number. In reverse, if two parts of the traces display opposite behaviours, it will display as a negative correlation. A significant advantage is that autocorrelation is sensitive in extracting rapid time events on the order of one lag, or one imaging frame, allowing for the extraction of events on time scales inaccessible by other conventional means.

Calcium imaging is marked by 'spontaneous' intensity up-ticks, which show no obvious rigid pattern, and autocorrelation is a method that extracts information from these traces. As discussed F/F_0 does not provide a robust methodology to extract full spatial mapped behaviour as it requires subjective region of interest selection and thus favours highly active behaviour. Autocorrelation on the other hand is non subjective and extracts the distinct temporal behaviour over all trace types (background, inactive and active). It has therefore been employed here to create, for the first time, a complete spatial map of the temporal activity over the whole plasma membrane.

The idea that autocorrelation would display the expected result was initially tested on single pixels selectively chosen to show a range of calcium activity: from inactive highly active regions. For consistency throughout the analysis, four traces from single pixels (background, inactive, active, very active) were chosen subjectively by hand to illustrate the process. The analysis of these traces helped determine how useful this approach was as well as flag up any errors and areas that needed further improvement.

Shown in Figure 4.6, are the uncorrected intensity traces of the four selected points, shown alongside a time averaged image of the original data stack. For the active points, each pixel displays a bleaching decay common to temporal fluorescence imaging, as discussed in section 4.3, with active intensity fluctuations superimposed on top. For the inactive trace only a bleaching decay is evident with no evidence of intensity spikes. For the background, where there is no, or little fluorescence, only noise fluctuations are present. Unfortunately, photobleaching presents one of the dominant challenges in performing accurate autocorrelation analysis; as discussed briefly above, photobleaching confounds all image analysis approaches if not correctly appropriated and this is extremely prevalent for autocorrelation analysis. Without bleach correction the autocorrelation of the background gives a rapid fall to zero after a single frame, and is marked by a noisy trace around zero (Figure 4.7) which is the expected result for a non-bleaching noise dominated trace. For the inactive trace, however, the bleach decay skews the result as the autocorrelation trace is dominated by the characteristic 'slow fall and low dip below zero' that is typical for an exponential decay curve and the same problem arises for the active and very active curves (Figure 4.7). This presents a problem to the autocorrelation analysis as all intensity traces display exponential bleaching, and thus most of the information that the autocorrelation extracts is masked. As discussed previously (section 4.3), a 'whole cell' bleach correction is not sufficient to successfully straighten all the intensity traces and the autocorrelation curves on the 'whole cell' bleach corrected traces confirm that there is still a decay problem as every pixel exhibits a different decay exponential. This supports the necessity for a method,

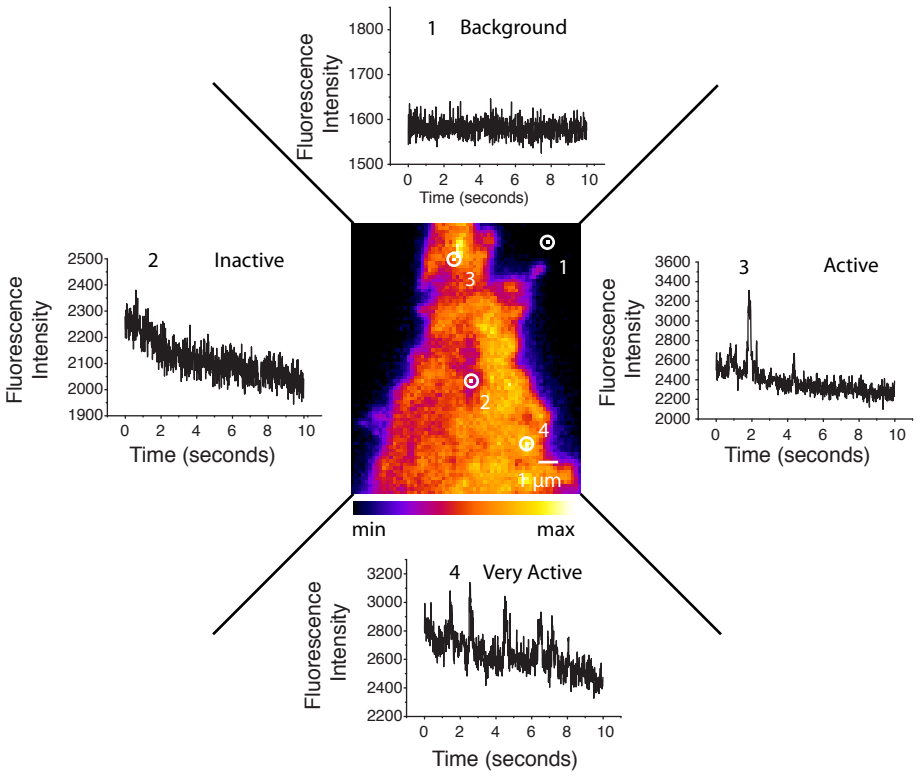

Figure 4.6 **Raw calcium traces.** An AtT20 D16:16 cell transfected with R-GECO-SNAP25, imaged in TIRFM with a frame rate of 16 frames/second, was used for demonstration purpose of calcium activity. The single pixels were subjectively chosen to demonstrate different types of calcium activity (1) background, (2) inactive, (3) active and (4) very active.

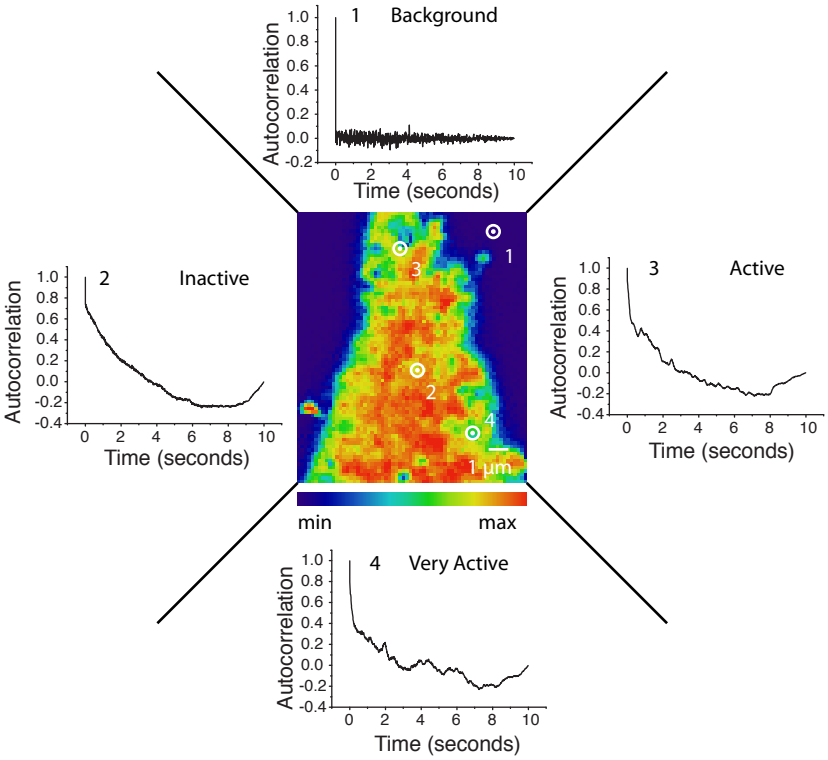

Figure 4.7 **Autocorrelation of raw calcium traces.** The same R-GECO1-SNAP25 transfected AtT20 D16:16 as in Figure 4.6, imaged in TIRFM, was used to demonstrate the autocorrelation of the raw calcium traces. The calcium intensity traces of the single pixels of the original calcium imaging stack were autocorrelated, showing the result of (1) background, (2) inactive, (3) active and (4) very active.

which independently corrects each pixel. An approach based on fluorescence lifetime fitting is employed to perform this correction. A FLIM application software called TRI2 (https://www.assembla.com/spaces/ATD_TRI/wiki) was used as, like all FLIM analysis, it is designed to extract the fluorescence lifetime by fitting an exponential decay curve to every pixels' intensity trace. A key feature is that, as the calcium activity is predominantly short intensity fluctuations over a background bleaching decay, FLIM-type exponential fitting will adequately fit the bleaching background. Upon uploading the original cell data into the software, a series of single pixels are selected to determine if, on average the majority of pixels were fitted best with a mono- or bi-exponential curve and one of the functions, that successfully describe the data with the minimum number of exponential terms, was chosen.

$$y = z + a\, e^{(-\frac{t}{\tau})}$$

or

$$y = z + a_1\, e^{(-\frac{t}{\tau_1})} + a_2\, e^{(-\frac{t}{\tau_2})} \qquad 4.2$$

TRI2 displays each pixel fit on selection along with the chi-squared fit metric that signifies degree of accuracy of the fit to the data. The range of the Chi squared values was capped though user selection to eliminate poorly-fitted pixels, and these non-fitted pixels are given the value zero in the output by TRI2. Importantly poorly fitted pixels return Chi squared values many orders of magnitude above well fitted pixels, making thresholding robust and straightforward. The result of the TRI2 fitting returns an image for each component a_1 (and a_2), τ_1 (and τ_2) and z of the exponential decay curve (Figure 4.8a). These images are used to create a stack representing the fitted decay curves in every pixel through simple image calculation transform in ImageJ. A reference time stack, t, was required, created by dividing the original cell stack with itself in ImageJ to return every value to 1, then a macro applying v=z+1 (where v is pixel value and z is frame number) to every frame extended the values linearly from 1 (first frame) to 1000 (last frame). This stack was then divided by 1000 to keep the range between 0 and 1, which was necessary as the time values used in TRI2 defaulted to the same range. These stacks and images were then combined using the ImageJ image calculator according to the mono- or bi-exponential equation to generate a stack representing the decay curve of each pixel (Figure 4.8b). To eliminate all the values of the pixels that were not fitted in the TRI2 software, the τ image was divided by itself, making all the

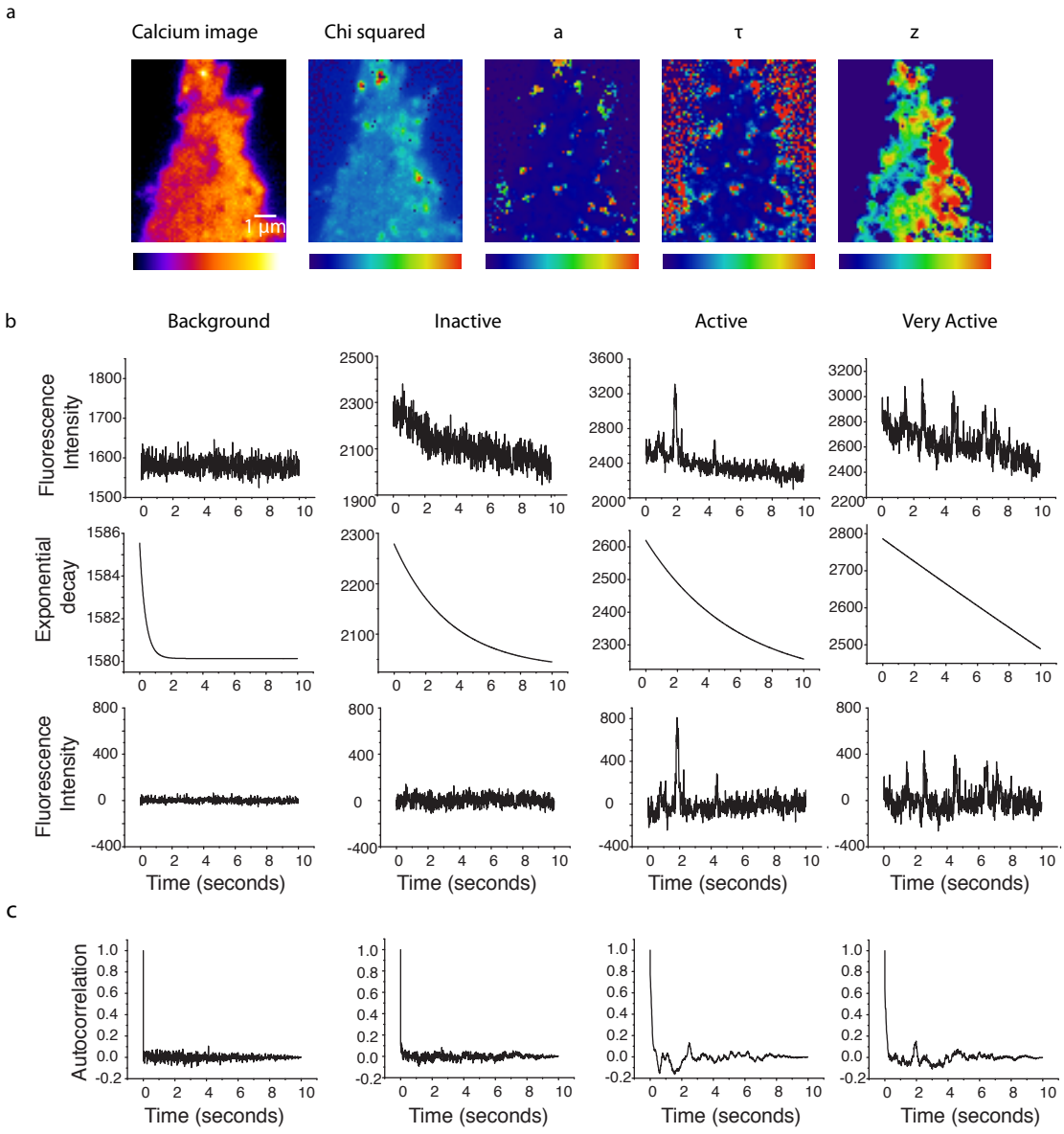

Figure 4.8 **Pixel-by-pixel bleach correction.** The same AtT20 D16:16 cell transfected with R-GECO1-SNAP25 as in Figure 4.6 was used to demonstrate the pixel-by-pixel bleach correction. a. The TRI2 program fits each pixel with a decay curve and returns several images from which the decay can be calculated. b. The decay curves were subtracted from each pixel of the original data. c. The bleach corrected traces were autocorrelated.

zero valued pixels NaN (not a number) and all other values '1' and this was multiplied with the decay stack. This process created a new image stack, of identical dimensions to the original data, where each pixel independently represents a fitted exponential decay representing the bleach dynamics at that particular point. The final fitted decay stack was subtracted from the original stack of images, leaving a pixel-by-pixel bleach corrected stack with the baseline around zero (Figure 4.8b), which were then autocorrelated (Figure 4.8c)

The fact that every pixel was fitted and corrected individually with a bespoke exponential, means that the pixel-to-pixel fluorescence intensity relationship has been altered and therefore absolute values cannot used to compare fluorescence differences between pixels. However, crucially autocorrelation analysis is independent of absolute intensity and so therefore this issue is not of a concern here.

An autocorrelation plug-in for ImageJ was developed that calculates the autocorrelation of every single pixel. The plug-in subtracts the mean of each trace so that the bleach-corrected intensity trace oscillates around zero, as required for the autocorrelation, and then performs autocorrelation on every individual pixel, calculated according to the equation 5.1. The plug-in then returns a new time series image stack that shows the autocorrelation of each pixel as function of lag. The autocorrelation plug-in was developed and written with assistance from Eric Pitkeathly and Dr. Paul Dalgarno (Institute of Biological Chemistry, Biophysics and Bioengineering, Heriot-Watt University, Edinburgh).

To compress the autocorrelation stack into a single metric representation of the temporal behaviour a 2D image has to be generated that compresses the temporal information into a single parameter indicating the level of activity. Unlike FCS and other work using autocorrelation, there is no known model that can be used to extract specific information from the autocorrelation curves. However, autocorrelation still provides a valid framework to extract such information. Summing the area under the curve will give a good indication of the degree of activity, as in contrast to the inactive traces, the active traces, whether positively or negatively correlated, display a much larger area under the curve. The area under the curve, A, is given by the square and square root of the sum of each lag x subtracted by the average of all lag values $\bar{x}$:

$$A = \sqrt{\Sigma\,(x - \bar{x})^2} \qquad 4.3$$

An alternative notation, favoured here, used the standard deviation (STD), which is proportional to the area under the curve and is a measure of the spread of the data around the mean value with n being the number of lags:

$$\sigma = \sqrt{\frac{\Sigma\,(x - \bar{x})^2}{n}} \qquad 4.4$$

The STD was used to represent in a single value the activity level at each point of the autocorrelation stack (Figure 4.9). ImageJ was used to calculate the STD for every pixel and a map was created that represents the activity level at each pixel. For the data shown in Figure 4.9 the background pixel from outwith the cell had the lowest STD of 0.039, this non-zero value originates from a small and rapid correlation from within the background signal, likely due to artefacts of the inherent frame rate of the imaging system. The inactive pixel from inside the cell showed a similar value of 0.040. Therefore, despite the significant absolute fluorescence signal from all pixels inside the cell, the degree of temporal activity at the inactive regions is essentially zero. The active pixels showed autocorrelation STD values of 0.085 and 0.069, higher values reflecting the increase in dynamic activity. Together these data showed that the pixel-by-pixel bleach correction and the STD of the autocorrelation is a good approach to the problem of calcium imaging analysis.

Figure 4.10 shows the a full cell intensity average image of the original stack alongside a false coloured version and false coloured autocorrelation STD map of every pixel produced as described above. In the correlation map areas of high correlation, and therefore high overall calcium activity appear red, areas of low correlation and therefore low activity appear blue. We observe a few notable features. Some of the cell area displays little or no correlation with a level similar to the non-cell background, implying a lack of calcium channels, or at least a lack of active channels. Very active areas appear sparsely distributed across the plasma membrane. There is however a consistent, although non-homogeneous, low activity level across much of the cell. This points to a clearly defined and diverse spatial organisation of the calcium activity across the plasma membrane.

4.4.2 Investigating the Influence of Calcium Agonists

The pixel-by-pixel bleach correction and the standard deviation spatial map from the autocorrelated data provide a reliable and robust method to reflect the overall degree of calcium activity across the plasma membrane. Direct comparison on the degree and nature of spatially distinct calcium activity are now viable. As autocorrelation is normally intensity independent, it is possible to compare cells under subsequent illuminations without further consideration of photobleaching. To this effect cells were

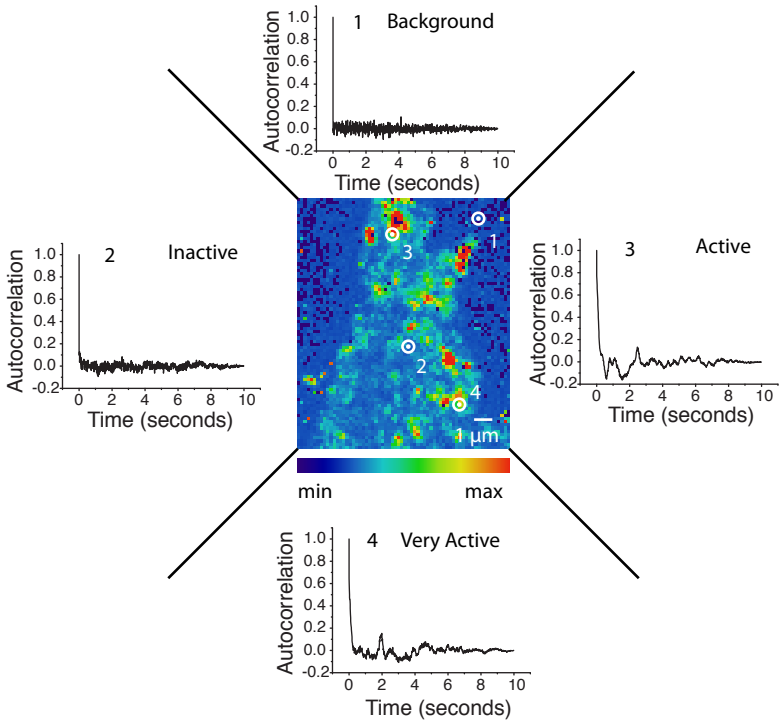

Figure 4.9 **Autocorrelation of the bleach corrected calcium traces.** The same R-GECO1-SNAP25 transfected AtT20 D16:16 cell, imaged in TIRFM, as in Figure 4.6 was used to demonstrate the autocorrelation of the bleach corrected calcium traces a. The single pixels of the original calcium imaging stack were bleach corrected and then autocorrelated, showing the result of (1) background (autocorrelation STD, 0.039), (2) inactive (autocorrelation STD, 0.04), (3) active (autocorrelation STD, 0.085), and (4) very active (autocorrelation STD, 0.069).

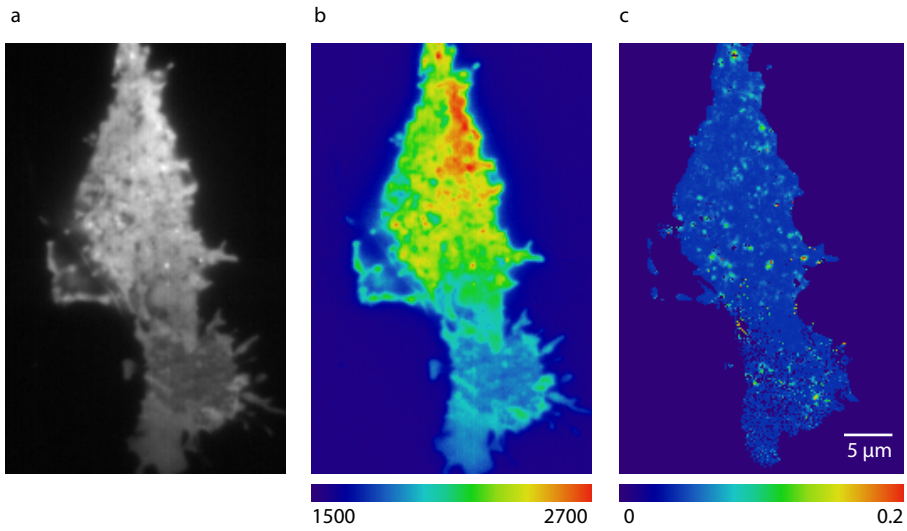

Figure 4.10 **Fluorescence intensity vs autocorrelation.** Comparative calcium activity visualisation of a R-GECO1-SNAP25 transfected AtT20 D16:16 cell. a. The raw data of a calcium imaging stack of 1000 frames averaged. b. The average presented in false colour. c. The autocorrelation STD representation of the same stack.

subjected to two different conditions to allow comparisons between the resulting map representing the calcium activity. First, in the example shown above in Figure 4.10 the cells were imaged in only KREB's buffer to reveal the natural calcium activity. Second, the $Ca_v2.1$ calcium channel agonist BayK was added to the bath for a 5-minute incubation period before imaging the same cell a second time. BayK prolongs the opening time of calcium channels, which was confirmed previously by the increased length of calcium waves in the full cell oscillation data, Figure 4.5b. This allowed direct comparison between the calcium activities, with the predicted result being that the calcium activity would increase after the addition of BayK.

Figure 4.11a shows the pre- and post- BayK intensity images alongside the autocorrelation STD maps. There is a subtle but non-zero difference between the two levels of activity seen in the intensity histograms of the autocorrelation map of the two differing conditions. The histograms are formed by defining a ROI around the cell, using the average intensity of the original data stack, copying it to the autocorrelation STD map and setting al background values outwith the ROI to NaN. This avoids incorporating the low STD values from non-cell background data, discussed above, from effecting the low histogram values. The histograms show that the BayK treatment supresses short lived dynamic events (low STD values) and favours long-lived openings of $Ca_v2.1$ calcium channels in the plasma membrane (Figure 4.11b). Although this effect is slight, it provides confidence that the autocorrelation STD map accurately reflects calcium activity across the plasma membrane.

Ideally, due to the intensity insensitive nature of the autocorrelation map the above approach would allow us to compare cells imaged under different conditions. An example of this is shown in Figure 4.12 which shows the intensity, autocorrelation STD map and combined histograms of different cells imaged with both Nifedipine and Mibefradil both a calcium channel blockers. It is clear that direct comparisons remain challenging due to the STD ranges being largely different. This may be reflective of the underlying dynamics, but also may be due, in part, to differing noise floors between different samples imposing a non standard baseline for the correlation statistics. It is not known at this stage. However, what is clear from Figure 4.12 is that the range of STD values, and therefore calcium activity is different for Mibrefradil and Nifedipine than BayK, showing noticeably shorter events, as may be expected for an channel blocker over an antagonist. This analysis method provides the potential to further study the biological role of the calcium channel blockers and antagonists in a spatial manner.

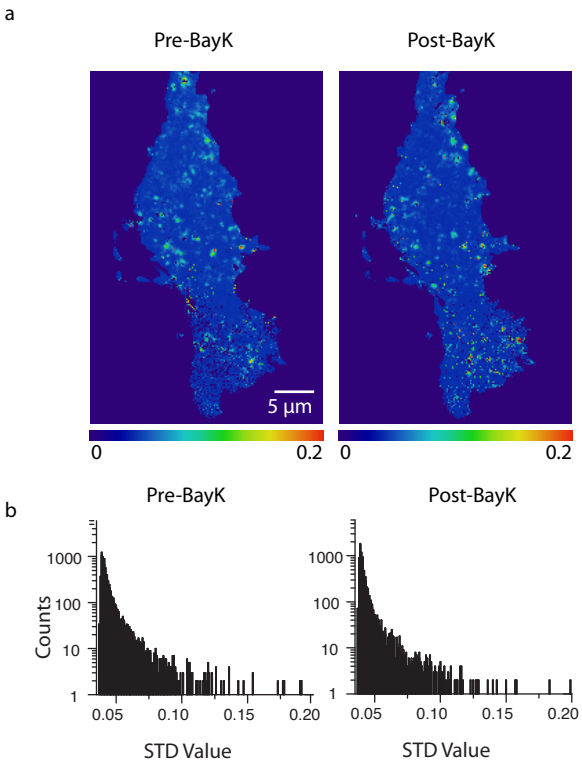

Figure 4.11 **Calcium activity pre-and post-BayK addition.** a. Calcium activity map represented through the standard deviation of the autocorrelated calcium images stack of pre-and post-BayK addition. b. Histograms of the cells autocorrelation STD values pre- and post-BayK addition. The calcium images were taken in TIRFM mode of a R-GECO1-SNAP25 transfected AtT10 D16:16 cell.

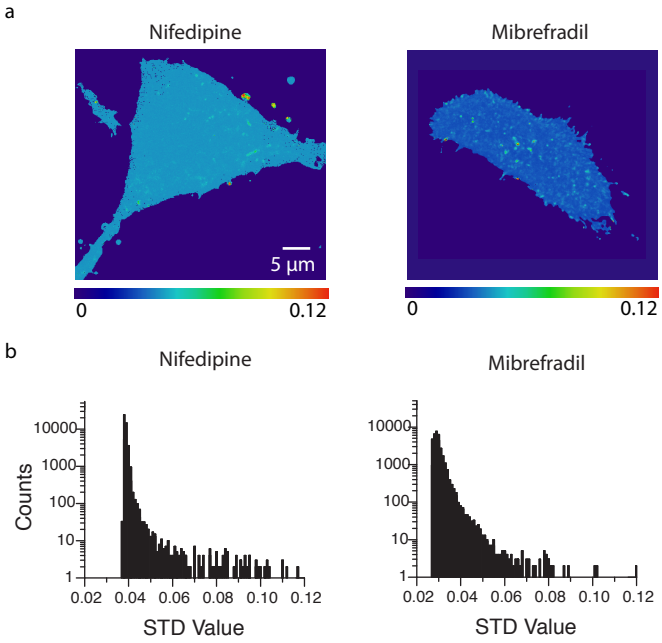

Figure 4.12 **4.12. Calcium activity of cells treated with Nifedipine and Mibefradil.** a. Representative calcium activity map of Nifedipine and Mibefradil treated cells. b. Histograms of the Nifedipine and Mibefradil treated cells. The calcium images were taken in TIRFM mode of R-GECO1-SNAP25 transfected AtT10 D16:16 cells.

4.5 Conclusion

The aims of this chapter were firstly to improve calcium imaging and secondly to design a different and novel image processing method to analyse the spatial behaviour of calcium activity. The fusion protein of R-GECO1-C1-SNAP25 was found to be more successful for calcium imaging in TIRFM mode than the use of Fluo4, providing sharper and more membrane bound imaging of calcium activity than previously available. The autocorrelation map to determine the spatial distribution of calcium activity across the membrane using pixel-by-pixel analysis and independent bleach correction also proved successful to represent the calcium activity. The result of the standard deviation numbers reflecting the calcium activity demonstrated two important conclusions. Firstly, the background region outwith the cell displayed very similar, low STD values to large numbers of pixels within the cell. This shows that there are regions inside the cell with little or no calcium activity. Secondly, large regions of high STD values reflect areas of high dynamic activity, which are dispersed throughout the cell membrane. The STD maps successfully reflect changes in the dynamic behaviour initiated through the use of external channel agonists and blockers. However, the autocorrelation STD values return only the overall amount of activity at each point and not necessarily accurately represent the level of that activity, specifically the duration of the individual calcium fluctuation events. Due to the nature of autocorrelation, very active traces with a short duration peaks could return similar or even lower STD values than one with a small number of long duration peaks. To account for this, the images would have to be weighted by the number of active events.

This clearly requires further work but one methodology may be to fit the oscillatory nature of the autocorrelation traces in order to extract the frequencies of the correlated signals, which may reflect the number of dynamic events within the traces and therefore relate to average channel opening times. Preliminary work to this effect has been explored with the assistance of Eric Pitkeathly and Dr. Paul Dalgarno and is shown in Figure 4.13, where three example single pixel bleach corrected intensity traces are shown alongside the autocorrelations of those traces and a corresponding fit using a damped sine function of the form:

$$y = y_0 + Aexp^{-x/t_0} sin\left(\pi \frac{x - x_c}{\omega}\right) \quad 4.5$$

Where t_0 represents the damping rate of the exponential decaying envelope function and ω the period of the oscillation, thus the inverse of the frequency. Y_0, A and x_c are for

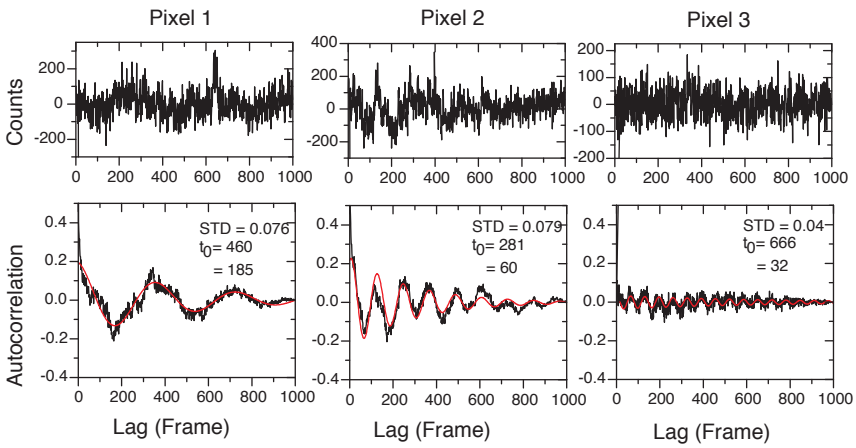

Figure 4.13 **Damped sine wave fitting.** a. Example shows bleach corrected calcium intensity traces of three pixels displaying different activity. b. The autocorrelation traces of each fitted with damped sine functions.

the offset (largely zero in our case) the amplitude and the phase shift. The damping reflects the rate at which the original decay ceases to become similar to itself, the period (frequency) reflects the number of times the original traces looks similar to itself, and therefore reflects the number of events in the original trace. The hypothesis is that the period therefore relates to the duration of the active calcium events, and therefore the channel opening times. In the three examples shown in Figure 4.13, pixel 1 shows a small number of clear channel openings, and is reflected in a high STD value and period (low frequency), pixel two has a similar STD activity value, but a larger number of events and thus a lower period (higher frequency). Point 3, a background trace, has a low STD value but very high frequency.

Fits of this form may be used to weight the STD maps with the frequencies to create a 2D plot of overall channel activity weighted by estimate of the activity duration at each pixel. This would be a complete non-subjective representation of the entire calcium channel behaviour across the cell membrane. Unfortunately global fitting over the entire cell is challenging and beyond the scope of this thesis: shown in Figure 4.13 are exemplary traces easily described by the model. More work needs to be done to investigate this further but the framework is presented here as an example of how this may be achieved.

This chapter has demonstrated the use of a novel labelling strategy for improved calcium channel imaging in TIRFM along with a newly developed image processing method to display the channel activity across the cell membrane. The combined result is a clear ability to distinguish varying regions of calcium activity distribution across the cell. These advances are now applied further in the following chapter to explore functional calcium activity through optical patching and simultaneous vesicle and channel imaging methods.

References

Akerboom, J. et al., 2013. Genetically encoded calcium indicators for multi-color neural activity imaging and combination with optogenetics. *Frontiers in Molecular Neuroscience*, 6, pp.1–29.

Akerboom, J. et al., 2012. Optimization of a GCaMP calcium indicator for neural activity imaging. *The Journal of Neuroscience*, 32(40), pp.13819–40.

Chad, J.E. & Eckert, R., 1984. Calcium domains associated with individual channels can account for anomalous voltage relations of Ca-dependent responses. *Biophysical journal*, 45, pp.993–9.

Dalgarno, P.A. et al., 2013. Solution-based single molecule imaging of surface-immobilized conjugated polymers. *Journal of the American Chemical Society*, 135, pp.7187–7193.

Demuro, A. & Parker, I., 2004. Imaging the activity and localization of single voltage-gated Ca 2+ channels by total internal reflection fluorescence microscopy. *Biophysical Journal*, 86, pp.3250–3259.

Demuro, A. & Parker, I., 2003. Optical single-channel recording: imaging Ca2+ flux through individual N-type voltage-gated channels expressed in Xenopus oocytes. *Cell Calcium*, 34, pp.499–509.

Fox, M., *Quantum Optics: An Introduction*, Oxford: Oxford University Press.

Hess, S.T. et al., 2002. Biological and chemical applications of fluorescence correlation spectroscopy. *Biochemistry*, 41(3), pp.697–706.

Hodson, D.J. et al., 2012. Coordination of calcium signals by pituitary endocrine cells in situ. *Cell Calcium*, 51, pp.222–230.

Lounis, B. & Moerner, W.E., 2000. Single photons on demand from a single molecule at room temperature. *Nature*, 407, pp.491–493.

Michler, P. et al., 2000. Quantum correlation among photons from a single quantum dot at room temperature. *Nature*, 406, pp.968–970.

Miyawaki, A. et al., 1997. Fluorescent indicators for Ca 2+ based on green fluorescent proteins and calmodulin. *Nature*, 388, pp.882–887.

Ohkura, M. et al., 2012. An improved genetically encoded red fluorescent Ca2+ indicator for detecting optically evoked action potentials. *PloS one*, 7(7), p.e39933.

Robinson, M. et al., 1996. Specialized chromaffin release zones cells examined imaging in with pulsed-laser imaging. *Cell Calcium*, 20(2), pp.181 – 201.

Sala, F. & Hernández-Cruz, A., 1990. Calcium diffusion modeling in a spherical neuron. *Biophysical journal*, 57, pp.313–24.

Shuai, J. & Parker, I., 2005. Optical single-channel recording by imaging Ca 2 + flux through individual ion channels : theoretical considerations and limits to resolution. *Cell Calcium*, 37, pp.283–299.

Stojilkovic, S.S., 2012. Cell Calcium Molecular mechanisms of pituitary endocrine cell calcium handling. *Cell Calcium*, 51, pp.212–221.

Su, S. et al., 2013. Genetically encoded calcium indicator illuminates calcium dynamics in primary cilia. *Nature methods*, 10, pp.1105–7.

Wang, S. et al., 2001. Ca 2 + signalling between single L-type Ca 2 + channels and ryanodine receptors in heart cells. *Nature*, 410, pp.592–956.

Weitz, A.C. et al., 2013. Imaging the retina's response to electrical stimulation with genetically encoded calcium indicators. *Journal of Neurophysiology*, 109(7), pp.1979–1988.

Yamada, Y. & Mikoshiba, K., 2012. Quantitative comparison of novel GCaMP-type genetically encoded Ca2+ indicators in mammalian neurons. *Frontiers in Cellular Neuroscience*, 6, pp.1–9.

Yip, W. et al., 1998. Classifying the Photophysical Dynamics of Single- and Multiple-Chromophoric Molecules by Single Molecule Spectroscopy. *Journal of physical chemistry*, 102, pp.7564–7575.

Zhao, Y. et al., 2011. An expanded palette of genetically encoded Ca2+ indicators. *Science*, 333, pp.1888–1891.

Zou, H. et al., 1999. Imaging Ca 2+ Entering the Cytoplasm through a Single Opening of a Plasma Membrane Cation Channel. *Journal of General Physiology*, 114, pp.575–588.

Chapter 5 Towards Imaging Single Calcium Channel Activity and Exocytosis by Integrating Novel Technologies

Functional calcium imaging aims to reveal information about how voltage-gated calcium channels are integrated within the exocytotic process. This chapter presents two novel methodologies to achieve this. First, optical patching, the combination of simultaneously performing electrophysiological patch clamping and fluorescence optical imaging (Wang et al. 2001), was conducted to analyse the role that voltage-gated calcium channels play in the initiation of exocytosis. Second, simultaneous calcium- and secretory vesicle- imaging was performed to correlate plasma membrane calcium activity with exocytosis. This dual-colour imaging was achieved by using a dichroic-based image splitting device to spatially separate the synchronously acquired images on a single imaging camera.

Earlier work in the field has either modelled mathematically (Shuai and Parker 2005), or visualised calcium 'sparks' (Demuro and Parker 2004), caused by multiple channel openings, in proximity to vesicles. However, this work and other work from the same group are too low in temporal and spatial resolution to address several key questions. Firstly, how many times and how close to a vesicle does calcium influx need to occur to elicit fusion? Secondly, how are calcium channel activities distributed across the cell surface in relation to vesicle locations and thirdly, how much time separates calcium influx and exocytosis? Finally, a long-standing question remains completely unanswered and intractable: what happens to the membrane architecture at the site of vesicle fusion? These questions are addressed, at least in part, using the novel imaging modalities presented in this chapter.

5.1 Functional Imaging

Functional imaging is challenging, as it requires advanced imaging modalities with the ability to both probe and manipulate multiple aspects of calcium channel behaviour in a single experiment. Here two such methods are presented. The first combines high-resolution optical imaging with patch clamping, a technique that was coined *optical patching* (Wang et al. 2001). The second utilises a dual-colour image splitter to perform live cell multi-colour imaging simultaneously on both vesicles and calcium activity. These methods are both complimentary and unique in that they both explore the direct role of calcium in exocytosis, whilst also pushing the boundaries of what is possible for super-resolution functional imaging.

Optical patching is conceptually simple: simply the simultaneous combination of voltage clamping and fluorescent imaging. Through voltage clamping of cells, and the induction of specific voltage changes, the simultaneous acquisition of the highest possible temporal resolution image data provides information about the spatially dependent activity of VGCCs in response to controllable external stimuli. This visual link between induced activity and spatial response across the cell provides clear understanding of the calcium triggering process of exocytosis.

Optical patching experiments have been extensively investigated by Ian Parker's group since about 2000 (Wang et al. 2001). This method was initially performed using a confocal microscope, but the relatively slow confocal scanning method limited the temporal resolution. Only by using single line scanning was it possible to increase the kinetic resolution to 10 ms (Demuro & Parker 2003; Wang et al. 2001). However, increased temporal resolution through line scanning comes at a considerable cost of spatial resolution, effectively limiting the experiment to one-dimensional image slices. Parker's group subsequently established the combination of electrophysiology and TIRFM to investigate calcium imaging using *Xenopus* oocytes expressing heterologous $Ca_v2.2$ calcium channels (Demuro and Parker 2004). Supported by theoretical modelling, these experiments showed that TIRFM imaging is sensitive enough to resolve events as brief as 1 ms, even though the acquisition was not that fast (Shuai and Parker 2005). Their focus then turned to IP_3 receptors, which are calcium channels located in the ER membrane, where they proceeded to analyse the functional behaviour of those channels (Smith et al. 2012; Wiltgen et al. 2010; Parker & Smith 2010), selected for their large conductances and therefore robust fluorescent signals. They concluded that calcium events originate from pre-established and clustered IP_3 receptors, with no lateral movement in the ER membrane. What has been addressed through this work, and that of others, is primarily the dynamics from large conductance, heterologous

calcium channel imaging. However this has not yet been put into context with native plasma membrane calcium channels and exocytosis.

In the first part of this chapter, the motivation is to investigate the functionality of VGCCs in the plasma membrane, activated by voltage depolarisations. The aim is that these experiments will show the spatial distribution of functional VGCCs through high-speed and high spatial-resolution imaging of fluorescent signals. By actively controlling the opening of channels, the functionality of these can be analysed in relation to their spatial arrangement. This new approach provides a method to investigate long-standing questions concerning fusion sites. One of these questions concerns the spatial arrangement and density of active VGCCs: does a fusion site require just one isolated calcium channel within a short distance, or do clusters of calcium channels act in unison and allow a big calcium event, which diffuses to nearby docked vesicles? Unfortunately neither standard imaging, super-resolution imaging, nor even optical patching can directly address these questions alone. To do this what is required is to directly address the amount of calcium activity spatially aligned with further cellular activity, such as vesicle fusion, or the associated proteins, such as the SNARE proteins, involved in exocytosis. The second part of this chapter addresses this challenge, where simultaneous calcium and vesicle imaging was conducted to understand precisely the amount of calcium activity at known fusions sites.

The process of exocytosis only extends over a period of 10s of milliseconds and therefore it is vital to increase the temporal resolution as much as possible without compromising the image quality. For standard dual-colour imaging, performed by taking separate successive images of each colour, the excitation and emission filter sets have to be changed between each acquisition. In modern microscopes the use of electrically triggered and synchronised lasers and multi-pass filters circumvent the need to change the excitation filters, but the emission filters still need to be changed between channels. The speed of the electronic filter changer that mechanically changes the filter settings prolong the frame rate on the Olympus X81 system used in this thesis, or any other microscope for that matter. When acquiring with an EMCCD camera, the minimum frame rate for a full 512x512 pixel image is limited to 70 ms/frame, thus leaving 140 ms between frames of the same colour channel during standard dual-colour imaging, which represents severe under-sampling of 10 ms events. Thus, conventional dual-colour imaging is not suitable for the time scale required. To simultaneously image two spectral channels, a dual-colour image splitting device was used to both split and filter the light, such that the resulting image on the camera contained two identical field of views, with each showing one of the two wavelengths. Using an established ImageJ

application and dual coloured bead sample as a reference image, the images were reconstructed to overlay each other with pixel level accuracy. From these data it can be seen how calcium channel activity before and after fusion is spatially related to the fusion of vesicles.

5.2 Optical Patching

Optical patching is very challenging due to the integration of, what are essentially in themselves, two highly demanding techniques. In this thesis a new experimental set-up was developed to achieve optical patching. Particular attention needed to be made to ensure that the fundamental requirements for both high-resolution TIRFM imaging and electrophysiology were not compromised during the setup. These experiments were performed in collaboration with Dr. Euan Brown and Matthew Euston (Institute of Biological Chemistry, Biophysics and Bioengineering, Heriot-Watt University, Edinburgh), who provided both expert advice and the electrophysiology equipment (see section 2.6).

5.2.1 Linking the Electrophysiology and Widefield Microscope Systems Together

The complex optical patching setup required a re-arrangement of the widefield microscope to accommodate the electrophysiology equipment (Figure 5.1a). First, the heat insulation box surrounding the microscope had to be dismantled, which meant that all measurements and images were acquired at 22°C; this is common for electrophysiology experiments. Second, particular care needed to be taken to electrically isolate the experiment, including ensuring common grounding and extensive electrical noise elimination precautions to block all noise sources thus ensuring clean electrical measurements (Figure 5.1b). Third, the electrophysiology and imaging system needed to be synchronised and this was achieved differently depending on the camera that was used. A synchronised timing TTL (Transistor-Transistor-Logic) trigger was connected between the TTL output port on the electrophysiology system and the TTL input port on the PC running the Olympus Xcellence software, with the acquisition setting set to external trigger mode. The acquisition on the sCMOS camera was done similarly, but here the camera itself was directly activated through a synchronised timing TTL trigger (Figure 5.1a). The TTL start signal was triggered by the start of the electrophysiology depolarisation sequence and ensured simultaneous

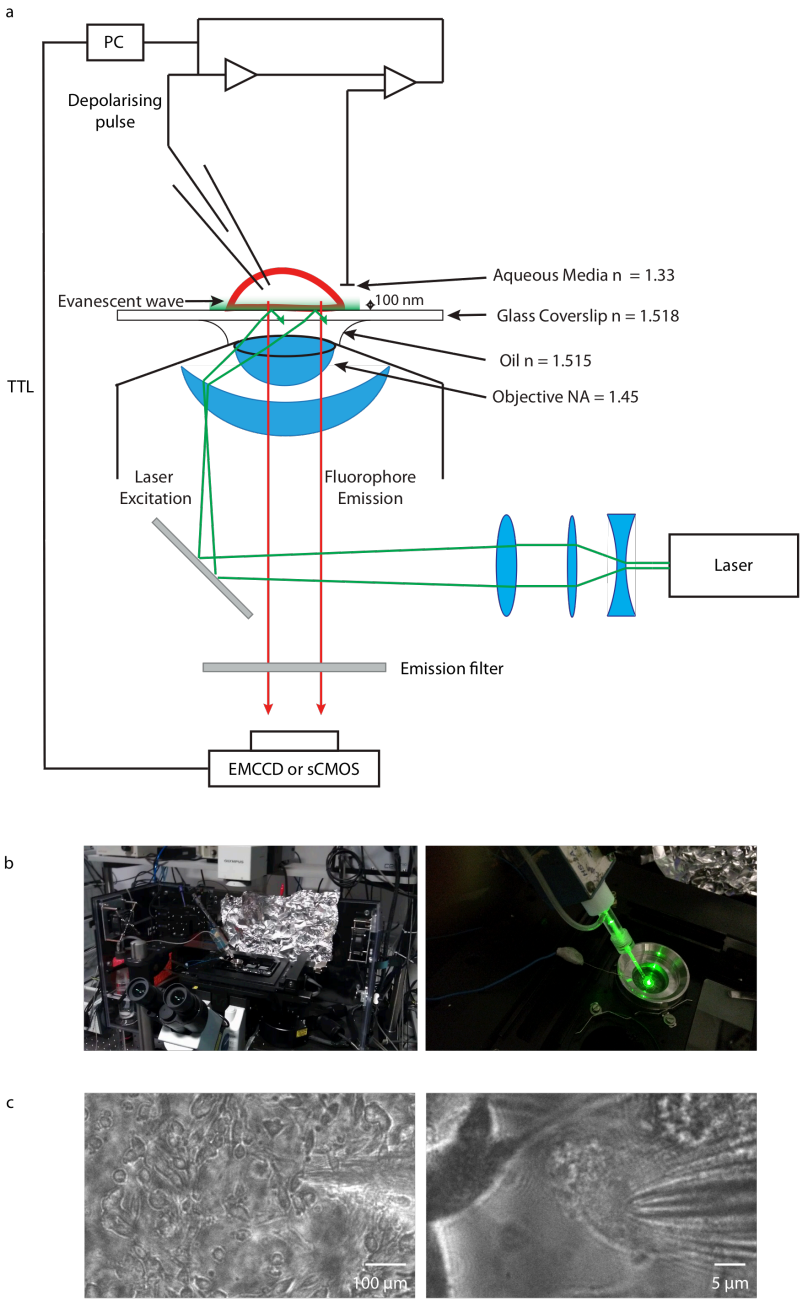

Figure 5.1 **Optical patching setup.** a. Schematic diagram of the setup of the microscope including the electrophysiology equipment. Imaging was performed in TIRFM mode and the cell was either transfected with R-GECO-SNAP25 or filled with Fluo4 through the pipette. A TTL cable was connected between the two systems for synchronised electrophysiology and imaging acquisition. b. Pictures of the microscope and electrophysiology setup, specifically showing the pipette delivery mechanism. c. Bright-field images of the pipette relative to the cell and of the cells using the 10x and 150x objective respectively.

acquisition of electrical measurements and images. This also allowed easy identification of images in terms of voltage change application. Finally, care was taken to ensure that, both the voltage clamping and optical imaging were performed optimally to ensure that neither approach has been compromised during the setup. Unfortunately a few minor challenges were not overcome. The incompatibility between the Olympus Xcellence software that controls the microscope and the sCMOS camera software made the imaging procedure more challenging. The inability to synchronise the lasers to the sCMOS camera meant that for each cell the lasers must be set on constant illumination. Bleaching therefore became a more pressing issue than normal and care was suitably required to minimize bleaching through manually terminating cell illumination between acquisitions.

The biological samples were prepared using either CHO cells, stably expressing $Ca_v2.2$ calcium channels, or AtT20 D16:16 cells transiently transfected with the novel calcium indicator R-GECO-SNAP25, localised to the inner leaflet of the plasma membrane (see section 4.3). This latter experimental system provided exceptional contrast and resolution by targeting the fluorescent indicator to the cell surface, limiting out of focus blur and haze. Furthermore, as SNAP-25 is a SNARE protein, it is predicted that this indicator would be localised preferentially to sites of vesicle fusion.

Tetrodotoxin (TTX) was added to the KREB's HEPES media at a final concentration of 1 μM to block all sodium channels that mask the calcium currents during the electrical recordings. Simultaneous electrical and optical recording of each cell required multiple steps. First, a transfected cell had to be located with the 150x objective and visual assessment of cell standard and suitability established. Then the objective was changed to 10x magnification to be able to find the glass patch pipette and position the tip in proximity to the cell surface (Figure 5.1c). The objective was rotated back to the 150x lens for the final whole-cell patching, after which the microscope was used in TIRFM mode. With the EMCCD or sCMOS controlled by external triggering and the lasers switched on, simultaneous current and image acquisition was started with the start trigger on the electrophysiology Clampex software.

5.2.2 Imaging Voltage-Induced Calcium Activity

The aim of these experiments was to analyse the cellular calcium response through plasma membrane located voltage-gated calcium channels. The first step was to test the overall calcium response through the induction of depolarisation steps across the plasma membrane by measuring the fold increase of an intracellular calcium indicator. This was done using stable $Ca_v2.2$ calcium channel-expressing CHO cells. The green,

soluble calcium indicator Fluo4 was chosen as the fluorescent calcium marker, because these cells cannot be transfected and the initial aim here is not to investigate single calcium events, but the overall cellular response. Fluo4 was added to the intracellular fluid, which, upon whole cell patching, diffused from the pipette into the cytoplasm of the cell. For these experiments the resting potential was held at -80 mV and then, depending on experiment, switched to either -40, -20, 0, +10 or +20 mV for a 5 second period, before returning back to the -80 mV holding potential. The cellular calcium response was imaged throughout the voltage manipulation in the widefield setting or TIRFM with the EMCCD camera at a frame rate of 60 ms/frame (16.6 Hz). The fluorescence intensity profile of the overall image stack was analysed to show the maximum fold increase resulting through the depolarisation, which was done by dividing the average of the first frame (manually selected ROI of the entire cell to eliminate background) (Figure 5.2a) with the maximum intensity value within the image stack (F_{max}/F_0). Figure 5.2b shows the fold increase of each tested condition. A fold-increase of 1.8-times was seen in the WF image, depolarised from -80 mV to +10 mV; considerably higher than compared to the equivalent TIRFM results. The depolarisation in WF was performed to image the intra-cellular response. From the images in can be seen that the depolarisation causes a huge, uniform and calcium-dependant fluorescence increase. This disparity can be explained by the fluorescence acquisition of an increased amount of Fluo4 molecules diffuse within the wider focal section in the widefield images, demonstrating again the unsuitability of widefield calcium imaging. In the TIRFM images, the depolarisations to -40 mV and -20 mV did not elicit any calcium activity at the plasma membrane and therefore the maximum intensity value remains similar to the first frame, which equates to a fold increase of around 1. However, the depolarisations to 0 mV, +10 mV and +20 mV elicit a fold-increase of around 1.2, 1.43 and 1.25-times, respectively. This quantifies the increase in fluorescence due to the increased calcium activity through the channels and reflects the previous electrophysiologically measured calcium current. This demonstrates through imaging that the induced depolarisations activate plasma membrane embedded VGCCs.

The next step in analysing the response of VGCCs on the plasma membrane was to test different depolarisation sequences to find the optimal depolarisation length that would allow the visualisation of the activity of calcium channels. Voltage-gated calcium channels are most likely to open during, or as a result of, abrupt voltage changes, brought about through action potentials. Based on this, different depolarisation phases were induced to test the visual response to calcium, acquired in TIRFM with the EMCCD

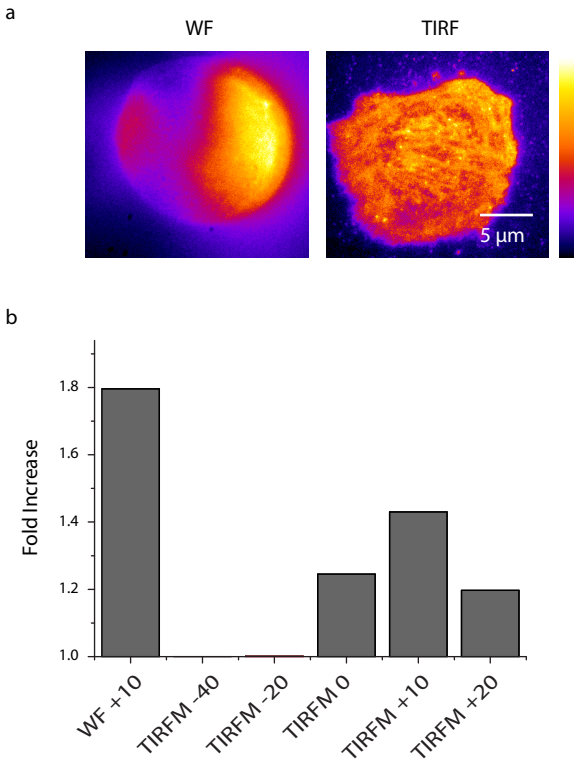

Figure 5.2 **Calcium response to voltage depolarisation.** a. Preliminary images of a patched AtT20 D16:16 cell in widefield and TIRFM mode. b. Shows the maximum fold increase in widefield and TIRFM recorded during the 5 second depolarisation from a holding potential of -80 mV to either -40, -20, 0, 10 or 20 mV.

camera at a frame rate of 60 ms/frame (16.6 Hz). The first set of experiment was designed with one depolarisation pulse of 100 ms from -80 mV to +10 mV and back to -80 mV. From the fluorescence intensity traces averaged over the entire cell it can be seen that the 100 ms depolarisation elicits a short-lived spike and the fluorescence returns to the original fluorescence level (Figure 5.3b). The depolarisation pattern was then changed to a 1-second duration depolarisation phase to observe the response to prolonged depolarisation. As before, the voltage changes were set from -80 mV to +20 mV and back to -80 mV. The trace outlining the overall calcium response for the 1-second activation shows an immediate fluorescence increase and a slow diffusion and bleaching of the calcium-bound Fluo4 (Figure 5.3c). For the next set of experiments the depolarisation from -80 mV to +10 mV and back to -80 mV was held for 5 seconds. The lengthy 5 second depolarisation caused a large calcium influx, overwhelming intracellular buffering and leading to a build-up of the intracellular Ca^{2+} concentration. The diffusion of calcium caused a blurring and masking of the single channel activity (Figure 5.3d). The control trace, with no depolarisation applied, showed no calcium activity (Figure 5.3a).

The above demonstrated visually, through the use of Fluo4, that the depolarisation of the plasma membrane actively opens membrane embedded VGCCs. However, as discussed in Chapter 3, Fluo4 is not targeted to the plasma membrane and instead diffuses throughout the cell. The direct fluorescence visualisation of calcium through R-GECO1-SNAP25 compared to Fluo4 was therefore tested for optical patching. For these experiments, the temporal acquisition with the sCMOS camera was increased to 100 Hz (10 ms/frame) to be able to capture very fast events. This allows imaging at a temporal resolution that approaches the short opening times of some voltage-gated calcium channels. Figure 5.4a shows the same patched cell, imaged in TIRFM mode with both Fluo4 and R-GECO1-SNAP25. Again, the clear improvement of calcium image quality is apparent with R-GECO-SNAP25. To manipulate the cell potential, the cell was subjected to two successive 2-second depolarisations, with a 1-second gap in between and each from a holding potential of -60 mV and depolarised to +10 mV. The fluorescence intensity traces of the whole cell, although showing a clear photobleaching during the acquisition, showed an overall increase in both the Flou4 and the R-GECO1-SNAP25 channels during the depolarisation. However, there are stark differences between the Fluo4 and the R-GECO-SNAP25 traces. The Fluo4 trace shows a sudden increase at the beginning of each depolarisation followed by a steady incline in fluorescence during the depolarisation. On the returning to the holding potential, the fluorescence returns rapidly to the bleaching background behaviour. In comparison, although the R-GECO1-

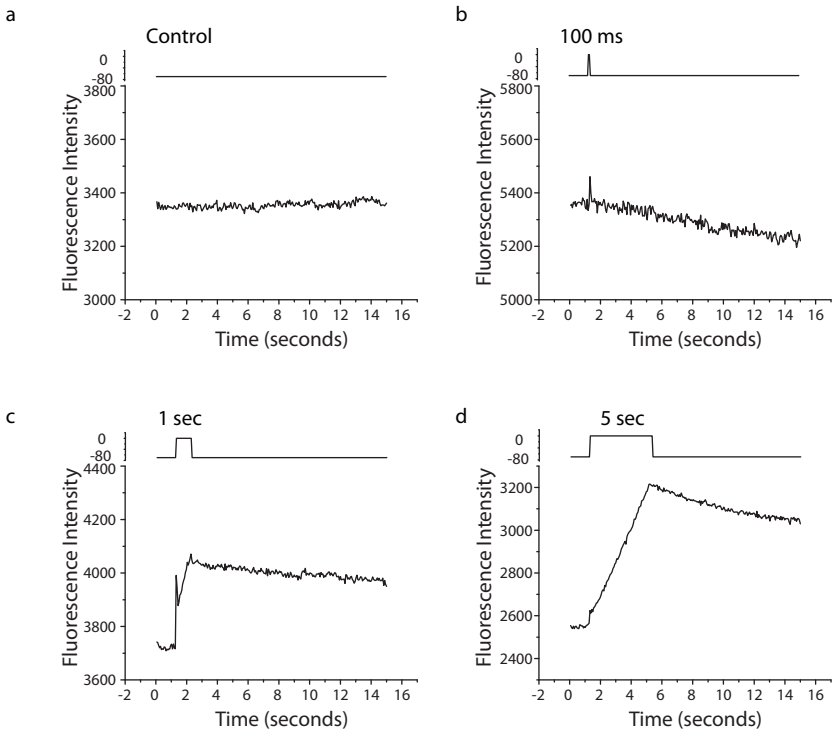

Figure 5.3 **Calcium response to depolarisation length.** The depolarisation from the holding potential of -80 mV to +10mV was held for different length. All four measurements (intensity profiles) were taken from the same AtT20 D16:16 cell that was transfected with R-GECO1-SNAP25 and imaged in TIRFM. The overall cellular fluorescence intensity traces are shown for a. no depolarisation, b. 100 ms depolarisation, c. 1 s depolarisation and d. 5 s depolarisation.

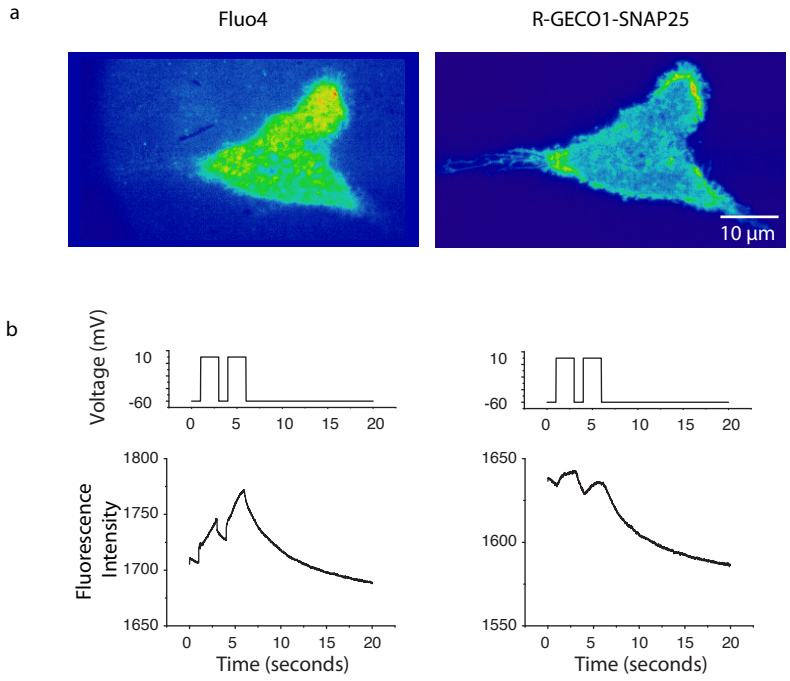

Figure 5.4 **Depolarisation profile of Fluo4 vs R-GECO1-SNAP25.** a. Representative AtT20 D16:16 cell imaged in TIRFM showing the Fluo4 and the R-GECO1-SNAP25 average intensity images, each imaged independently. b. The cell was successively depolarised, twice, to +10 mV for 2 seconds from a holding potential of -60 mV with a 1 second interval between steps. The overall fluorescence intensity response was recorded for both labels, both a frame rate of 10 ms/frame (100 Hz).

SNAP25 also displayed an overall increase during the depolarisations, it did not show a sudden jump on depolarisation and instead displayed a gradual rise that plateaued before during the depolarisation period. On returning to the holding potential, the fluorescence again rapidly returned to the bleaching background. The key difference is the rise of the Fluo4 intensity during the depolarisation compared to the plateau of the R-GECO1-SNAP25 during the same period. As these signals are superimposed over a constant bleaching background, the significant Fluo4 rise is completely dominant and indicative of the diffusion heavy reporting of Fluo4 discussed previously and in Chapter 3. This suggests that Fluo4 is non-efficient in the reporting of calcium activity, even in controlled experiments such as in optical patching. Furthermore, the clear rise and plateau of the fluorescence from the R-GECO1-SNAP25 is in keeping with electrical current measurements of the overall calcium channels activity and effectively reports well a defined calcium activity bound to the membrane. Channels tend to open at the beginning of the depolarisation phase and close after 10s of milliseconds, after which they are inactivated, which can be concluded from these traces. The plateau in the fluorescence trace shows that the R-GECO1-SNAP25 is significantly more sensitive to the changes of the surrounding calcium activity than Fluo4 and not necessarily influenced by the increasing build-up of calcium concentration.

To further explore the effect on calcium activity during the depolarisation steps, an autocorrelation STD map was made for both the Fluo4 and R-GECO1-SNAP25 calcium images to investigate specifically the spatial calcium changes in detail. Although demonstrated on a different cell, the depolarisation procedure is exactly as discussed for Figure 5.4, a -60 mV holding potential to a +10 mV depolarisation in two 2-second steps with a 1 second gap. The reason behind the having two 2 second steps is that firstly, two calcium events will be detected more efficiently in the autocorrelation analysis and secondly, a pre-activation depolarisation results in a higher opening probability on the second depolarisation. Figure 5.5a shows, for the same cell in Fluo4 and R-GECO1-SNAP25, the average intensity of a temporal image stack alongside the autocorrelation STD maps, generated as discussed in Chapter 4. The average intensity maps suggest a high concentration of activity near the centre of the cell for Fluo4, whereas activity regions are located around the perimeter of the footprint for the R-GECO1-SNAP25. The Fluo4 autocorrelation STD map reflects this distribution, displaying large areas of high activity, with no spatial distinction between the individual events. The autocorrelation STD map for the R-GECO1-SNAP25, however, shows very distinct pixels of high activity. It is worth noting that due to the very high frame rate of

10 ms/frame, these R-GECO1-SNAP25 signals were only just above the noise level, and this shows that the autocorrelation can successfully extract underlying fluorescence intensity fluctuations from these are near noise limited traces. The difference between the STD maps is clarified through investigating the fluorescence intensity traces of pixels across the cell. Shown in Figure 5.5b are a few examples for the pixel-by-pixel bleach corrected traces used to generate the autocorrelation STD maps. It can be seen that in the Fluo4 images, there is reduced correlation between the depolarisation steps and the fluorescence intensity, although there is evidence of increased calcium activity during the depolarisation. The intensity seemed to increase with a lot of activity throughout the time trace and also significantly after the depolarisation ends. Conversely, this was found to not be the case with R-GECO1-SNAP25 calcium traces (Figure 5.5b). The R-GECO1-SNAP25 calcium traces only showed activity during the depolarisation phases, and, although the signal of these rapid 10 ms acquisition makes detailed visual interpretation challenging, this activity is clearly correlated to the rise and fall of the depolarisation voltages.

The increases in Fluo4 signal during depolarisation is likely due to Fluo4 reporting internally located calcium channel activity. As only the plasma membrane is controlled by the voltage clamp, this activity is not regulated through the clamping and there is therefore little correlation between the voltages and the fluorescence activity. R-GECO1-SNAP25 however, only reports membrane bound calcium activity and therefore is fully correlated to the voltage changes. This result, only attainable through optical patching demonstrates clearly the huge potential of R-GECO1-SNAP25 as a calcium indicator for imaging the activity of plasma membrane located voltage-gated calcium channels.

5.2.3 Conclusions from the Optical Patching

Optical patching offers a unique ability to spatially probe ion channel activity across the cell membrane under strictly controlled conditions to manipulate channel activity. Although experimentally challenging, it therefore holds great potential to fully understand the spatial distribution of voltage-gated calcium channels. To date optical patching to visualise calcium channels was mainly performed using Fluo4 as a calcium indicator. However, Fluo4 is clearly non-ideal for accurately reporting the membrane bound channel activity. The optical patching presented here shows little correlation between the applied depolarisation steps and the fluorescence activity changes, raising questions as to the accuracy of any spatial map of calcium activity using Fluo4. However, the newly developed R-GECO1-SNAP25 indicator has none of these issues and

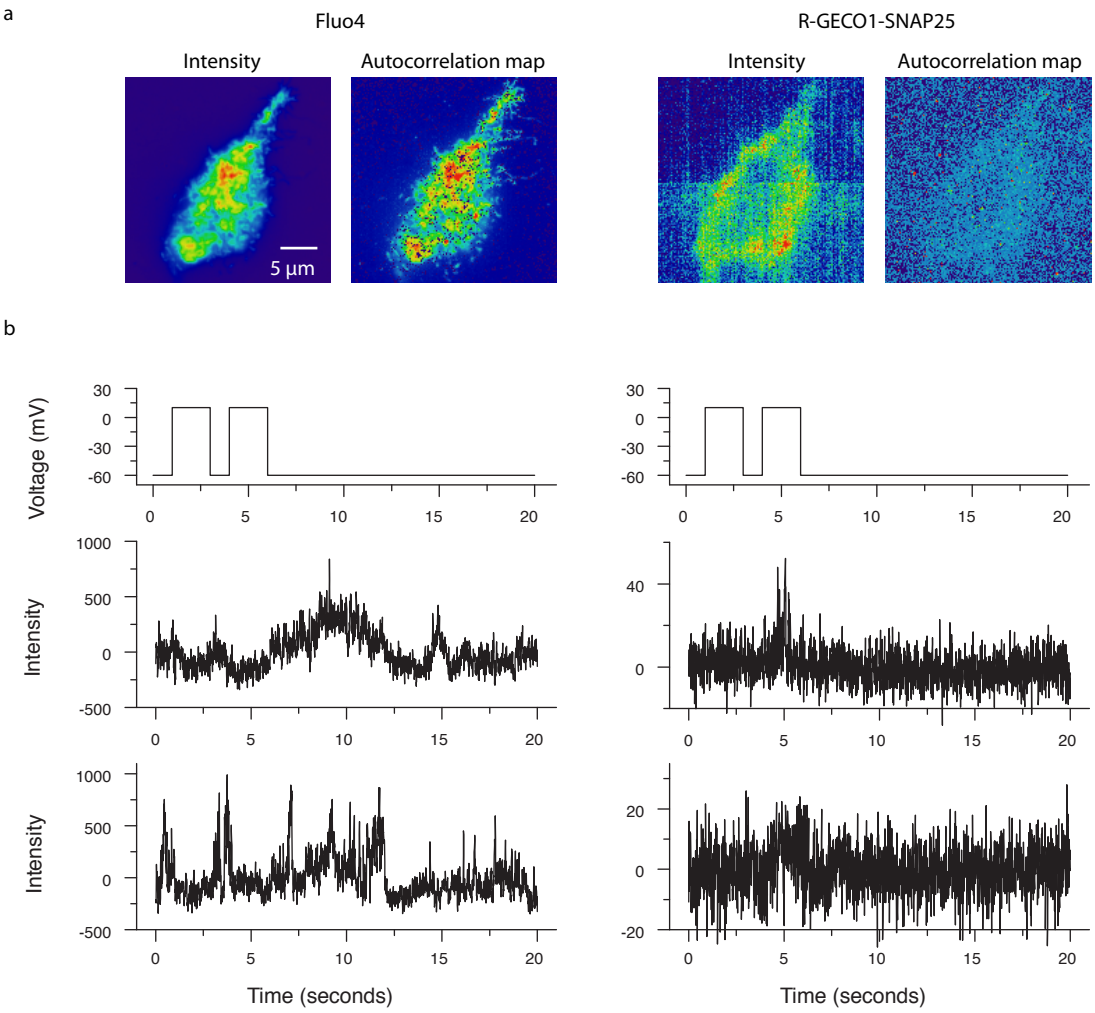

Figure 5.5 **Spatial activity map of the calcium response to depolarisation** a. Average intensity and autocorrelation STD map of the same cell with Fluo4 and R-GECO1-SNAP25. b. Individual traces, two examples each from the Fluo4 and R-GECO1-SNAP25 image stacks, of 4x4 pixels showing calcium activity during the depolarisation sequence.

the optical patching provides strong evidence that it accurately reports membrane bound calcium activity with full correlation between the depolarisation and the fluorescence signature. In addition to demonstrating the effectiveness and potential of optical patching to better understand calcium channel activity, R-GECO1-SNAP25 is therefore confirmed as an effective new approach for membrane calcium imaging. These new techniques may therefore be key for improved spatial identification of the activity in the future.

5.3 Simultaneous Imaging of Ion Channel Activity and Vesicle Dynamics

The understanding of calcium activity on the plasma membrane is in itself very important and, as demonstrated through this thesis, both challenging and rewarding to study in isolation. However, calcium influx is part of a much more complex picture involving the many different stages of exocytosis, which include the recruitment of vesicles, the docking stage, and the final fusion event (Becherer et al. 2003; Becherer & Rettig 2006; Brunger 2000; Gundelfinger et al. 2003). It even plays a part in endocytosis. To understand this complex process, vesicle movement and fusion has to be studied simultaneously with calcium imaging. However, the challenge in combining both is to preserve the spatial and temporal resolution, which has underpinned all calcium imaging in this work to date. To address this challenge a new approach, using a dual-colour image splitter, is utilised that preserves the temporal resolution of each single channel imaging modality.

Simultaneous dual-colour imaging was conducted to analyse the spatial and temporal characteristics of calcium events at fusion sites. For this, a dual-colour image splitter was used, which allows the acquisition of two channels at the same time by projecting both channels spatially separated onto the detection array of the camera. Using this type of experimental setup, and a membrane targeted calcium indicator, is a novel way of investigating calcium events in relation to fusion with the highest possible spatial and temporal resolution.

R-GECO-SNAP25 was used as the calcium indicator and pre-neuropeptide Y-EGFP (NPY-EGFP) acted as a marker for vesicles. NPY-EGFP is quenched when inside the low pH environment of the vesicle lumen and increases intensity on exocytosis as the molecules are exposed to the extracellular physiological pH, producing a rapid and spatially defined ‘flash’ in the green channel that indicates the fusion of a vesicle. This distinct increase in fluorescence indicates the release of the GFP-NPY into the space between the cell and the coverslip, which is immediately followed by a marked drop of fluorescence intensity indicating the diffusion of the peptides and dissipation of the

vesicle when the vesicle membrane is integrated into the plasma membrane. From the simultaneous imaging of calcium and fusion, information about the calcium activity before and after the fusion event can help understand the implication of calcium events in trigging fusion, as well as providing direct spatial information about fusion sites.

5.3.1 Dual-Colour Image Splitter

A dual-colour image splitting device (OptoSplit II SL Image Splitter, Cairn) was used as the image splitting platform, see Figure 5.6 for an optical schematic. Mounted at the main exit port of the Olympus IX81 microscope, it sits between the microscope and the EMCCD camera. Dual-colour imaging requires the microscope filter setting to be appropriately configured. The excitation setting was changed to a dual-view optic to simultaneously illuminate the sample with both the 488 and 561 nm excitation lasers for the GFP and R-GECO1 respectively. A dual-pass dichroic was utilised in the IX81 to allow for the transmission and collection of the two excitation, and the corresponding emission, wavelengths simultaneously. Additionally, the emission filter, normally a single band bandpass filter aligned to the emission wavelength, was removed to allow all light to pass unfiltered to the OptoSplit device. The image splitting device was fitted with a further dichroic filter (Chroma Technology Corp., 565 DCXR) that divides the light by wavelength; light shorter than 565 nm passes through the filter, but light longer than 565 nm is reflected (Figure 5.6b, black curve). The separate paths were additionally fitted with bandpass filters for the specific emission bandwidth of each fluorophore. The filters used, produced by Chroma Technology Corp., were ET 525/50 and ET 632/60 (Figure 5.6b, green and red curves), which covered the collection bandwith of EGFP and mCherry emission (Figure 5.6, green and red dotted lines respectively), for the EGFP-NPY and R-GECO-SNAP25 transfected cells. The R-GECO-SNAP25 emission was faint and therefore had to be imaged with the EMgain setting on the EMCCD camera at 500. However, this high EMgain then meant that the NPY-EGFP channel was overexposed, even on the lowest laser power setting. Therefore, an additional filter, a 0.3 neutral density filter, was inserted into the light path of the EGFP channel, which reduced the amount of light by 50% to avoid overexposure. The image splitting device, operating under these conditions, projects a spatially separated green and red filtered image onto the detection chip of the camera. An adjustable aperture, positioned at the entrance of the OptoSplit, in the image plane of the IX81 microscope, controls the field of view in each channel to prevent overlap of the spectrally, and now spatially, distinct images (Figure 5.7a).

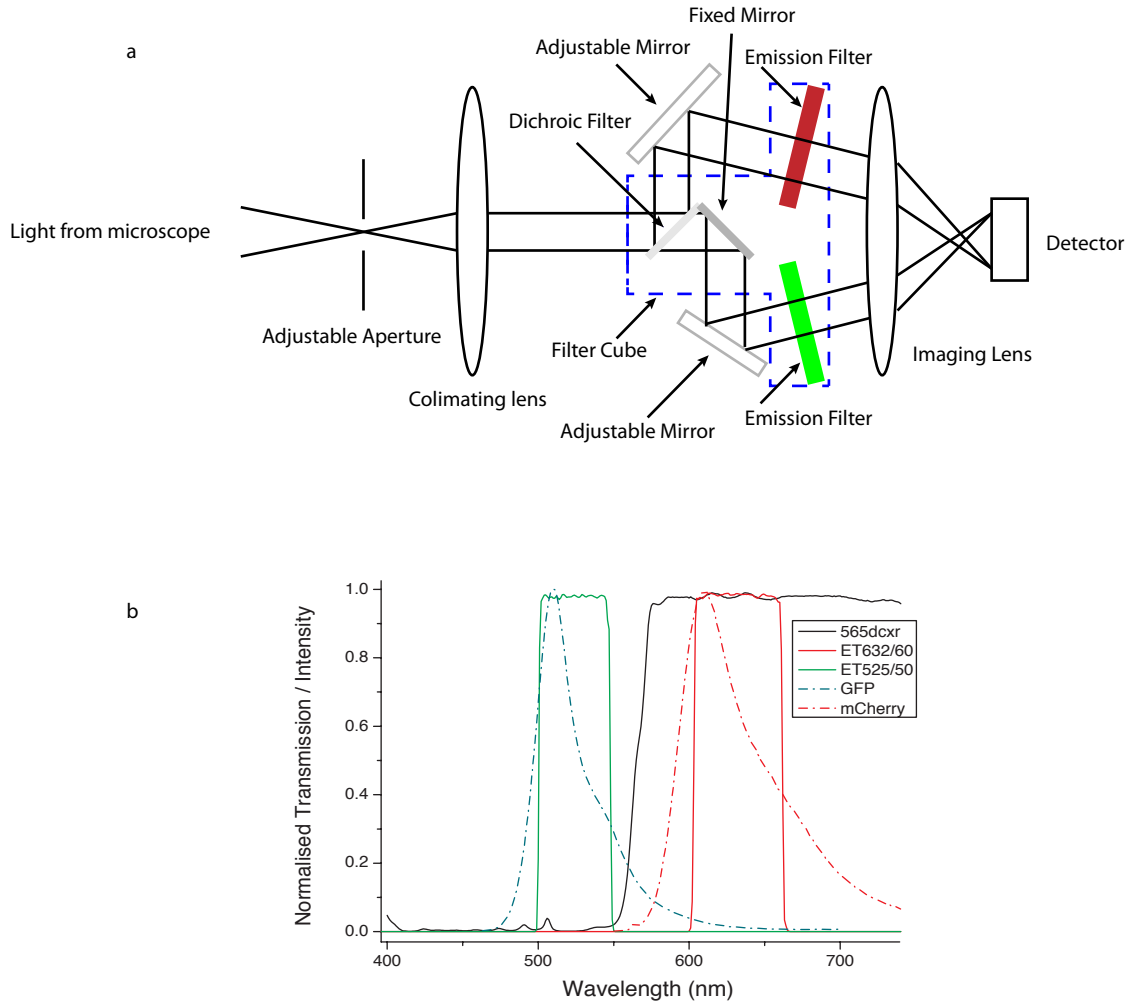

Figure 5.6 **Setup for simultaneous imaging.** a. Schematic diagram of the optical pathway through the Cairn Optosplit II dual-colour image splitter. Of note is the dichroic filter to separate the two channels followed by delivery optics to impose each channel on the single camera. b. Spectral properties of the filters and used in the image splitter (525 nm emission bandpass -solid green, 632 nm emission bandpass - red and 565 nm dichroic - black line) overlaid with the EGFP and mCherry emission (EGFP - dotted green and mCherry -red line).

To process dual-view images, the two side-by-side images have to be precisely overlaid. To achieve this, a sample containing fixed 100 nm beads labelled with blue, green, orange and dark red fluorophores (TetraSpec, Microspheres 0.1 µm blue / green / orange / dark red) was imaged as a ground-truth reference (Figure 5.7a). To align the colour channels, this reference was used in the ImageJ plugin Auto-Align (Pitkeathly et al. 2012). Auto-Align, developed for this very purpose, uses the ground-truth reference to create a coordinate offset map, to split and superimpose the original dual-colour image to pixel level accuracy (Figure 5.7b). Auto-Align accounts for both minor magnification and angular differences between the two colour channels. All images were acquired with a frame rate of 70 ms/frame.

5.3.2 Calcium triggering Exocytosis and Endocytosis

AtT20 D16:16 cells expressing R-GECO-SNAP25 and EGFP-NPY were stimulated with BayK to initiate fusion by increasing the opening probability of L-type calcium channels as shown previously (see section 4.4.2). The activation by BayK, and not through high extracellular K^+ or ATP, ensures that the fusion is actually initiated through the prolonged opening of calcium channels. The images, acquired on the widefield microscope in TIRFM mode using the dual-colour image splitter, were separated and aligned with the Auto-Align plugin (Figure 5.7). As discussed in chapter 4, and a pixel-by-pixel bleach correction and subtraction using the TRI2 program, was done on the red (R-GECO-SNAP25) channel. This correction provides a convenient way to study the corresponding calcium fluctuations on a non-varying bleaching background. As the green (NPY-GFP) channel showed considerably less bleaching, for the purpose of single pixel comparisons between the red and the green channel, the green channel was not bleach corrected. The information in the red (R-GECO-SNAP25) channel describes the spatial and temporal activity of calcium channels (Figure 5.8a). The green (NPY-GFP) channel shows the dynamics of vesicles (Figure 5.8a) and importantly the fusion events, marked by a flash then the disappearance of the vesicle. Both events, calcium influx and vesicle fusion, only last for one, or very few frames, which underlines the importance of the simultaneous dual-colour imaging and high frame rates (Figure 5.8b). Together, simultaneous imaging therefore allows for a direct spatial and temporal measurement of the action between vesicle fusion and calcium influx. The bleach-corrected, and overall average subtracted, red calcium channel shows the intensity of R-GECO-SNAP25. The addition of BayK increases the opening probability and open dwell-time of $Ca_v2.1$ calcium channels, therefore allowing more calcium into the cell at the mouth of those channel molecules, which is predicted to increase the probability of vesicle fusion.

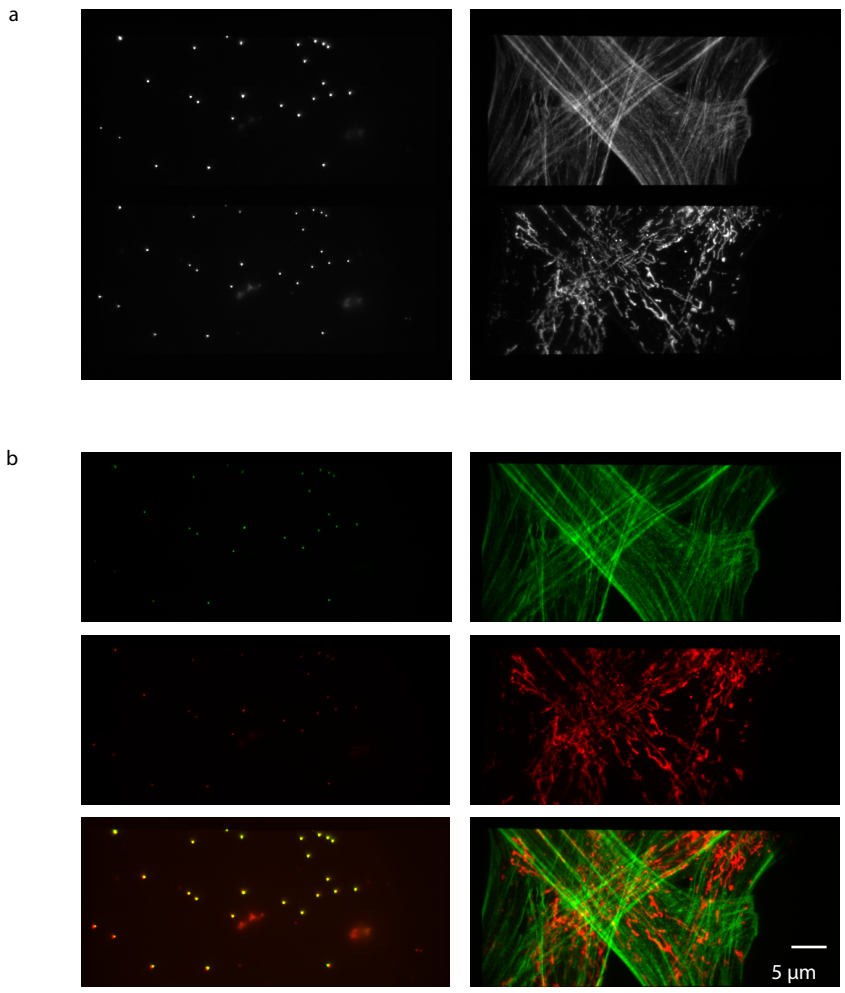

Figure 5.7 **Alignment of the dual colour images.** a. The dual-colour image splitter projected the red and green images spatially separated on the single camera detection chip. TetraSpec bead images were acquired, left, before imaging the Invitrogen FluoCell prepared slide #6, stained for Phalloidin and TO-PRO-3, test sample shown on the right. b. The AutoAlign ImageJ plugin is used to separate and overlay the simultaneously acquired images split through the alignment of the bead sample.

To understand calcium activity at the site of exocytosis, fusion events were located in the green (NPY-GFP) channel and compared to spatially identical pixels in the red channel. Example traces are shown in Figure 5.8b. Every fusion event was initiated by a spatially and temporally corrected spike in calcium, shown in the calcium intensity trace. Of interest here is the underlying calcium activity in terms of spatial organization of active voltage-gated calcium channels and fusion sites, which will be further discussed in section 5.3.3.

Also apparent in the data is the appearance of post-fusion spikes of calcium, as seen in Figure 5.8b. This is a novel result, available here for the first time due to the increased spatial and temporal resolution of the experiment. It has been postulated that calcium not only initiates exocytosis, but is also implicated in the recycling of fused vesicles back into the cytoplasm, a process called endocytosis (Hallermann 2014). In addition to this, electrophysiological capacitance measurements quantifying the change in surface area of the cell have shown that endocytosis starts as soon as exocytosis is triggered (Thomas et al. 1994). Hence, the post-fusion calcium spike recorded in the dual-colour images may indicate the initiation of endocytosis. Should this be the case, further understanding about the lateral movement of calcium channels within the plasma membrane could be revealed. A second calcium event at the same spatial location in the membrane would indicate little, or restricted movement of voltage-gated calcium channels after full exocytosis of a vesicle has occurred. Incidentally, a proteomic screen revealing binding partners to the $Ca_v2.2$ calcium channel showed that proteins involved in exocytosis, endocytosis and the cytoplasmic matrix can bind to the channel (Khanna et al. 2007). Taking this into consideration, along with indication from the calcium activity traces that calcium channels are stationary, all this points towards a highly organised fusion site coupled to a vesicle-recycling site, which are centred on an anchored voltage-gated calcium channel.

Questions dissecting the presence of either the full fusion or kiss-and-run exocytosis may be addressed in future work using the tools developed here. A full fusion of the vesicle causing the vesicle membrane to be inserted into the plasma membrane would be predicted to radically rearrange and reposition membrane proteins including calcium channels. However, a kiss-and-run fusion, where only a fusion pore opens but the vesicle otherwise stays intact, could explain the little lateral movement of calcium channels.

Many of these questions would require further work, however key to addressing these issues is to create a map of calcium activity and locate the fusion sites. The spatial

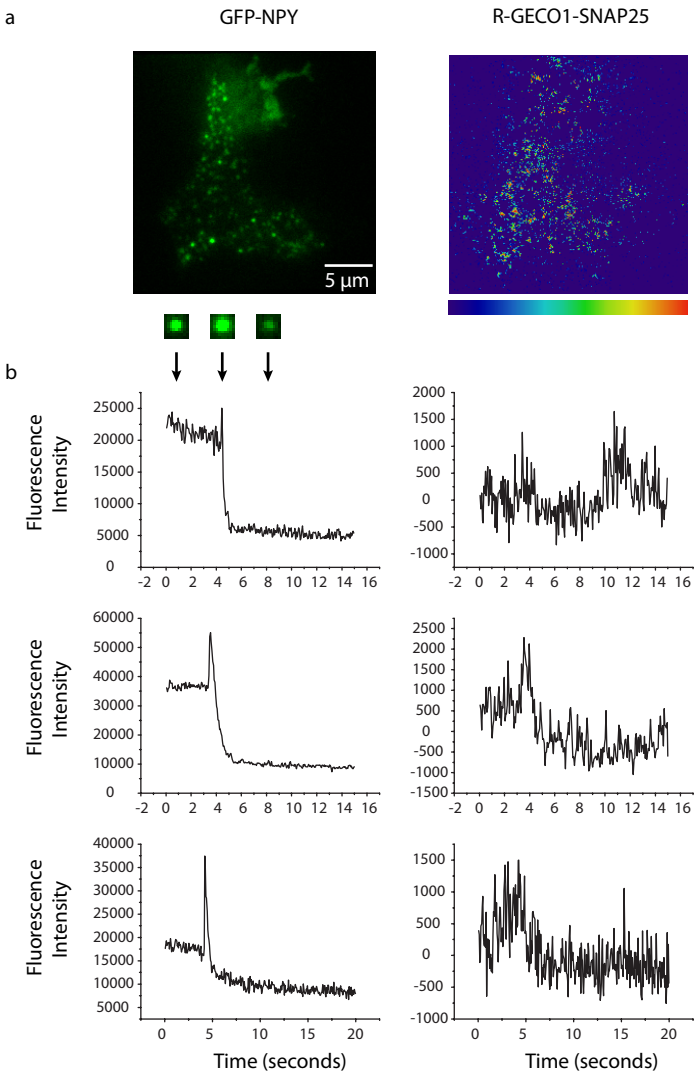

Figure 5.8 **Simultaneous calcium and vesicle imaging.** a. Images show vesicles (EGFP-NPY) and calcium (R-GECO1-SNAP25) in an AtT20 d16:16 cell, bleach corrected. b. Addition of BayK (1 µM) during imaging initiated fusion, as can be seen in the three example traces showing the vesicle and calcium traces in different pixels.

dimensions of calcium activity at fusion sites may therefore help understand some of the questions addressed above.

5.3.3 Spatial Analysis of Fusion in Relation to High Calcium Activity

The spatial relationship of calcium activity and fusion requires an image that represents the activity level of calcium and a correlated image that highlights precisely the pixels where fusion occurred. These two images could therefore be overlaid to analyse the full spatial correlation between calcium and fusion.

Full spatial analysis of the red (R-GECO1-SNAP25) channel was conducted the same way as described in detail in Chapter 4. Thus, an exponential background based pixel-by-pixel bleach correction and subtraction was performed using the TRI2 program and from a pixel-by-pixel autocorrelation analysis on the corrected stack the standard deviation (STD) was extracted. Just as in chapter 4, this spatially varying STD value, that represents the overall degree of calcium activity at each pixel, created a map of the spatial activity of calcium channels.

To spatially correlate the fusion events with the calcium activity, the green channel had to be analysed with a similarly non-subjective spatially complete pixel-by-bixel methodology extract and highlight the fusion events. The goal is to create an equivalent spatial map of the calcium channel activity in order to overlay the dynamic behaviour. For this a method had to be developed, which non-subjectively extracts the large intensity decrease in a manner that allows for easy identification of those pixels in which a fusion occurred. The autocorrelation STD analysis is not valid as vesicle fusion is a single, isolated and therefore uncorrelated temporal event. An image calculation approach called ΔF-down was utilised that calculates the intensity difference of each pixel between each successive frame by subtracting from each frame the previous frame. This was done applying the ΔF-down plugin in ImageJ to the image stack. ΔF-down acts like an extreme high pass filter where slowly fluctuating changes that occur over many pixels and frames, such as a vesicle moving in to a pixel and away again, do not show up on the ΔF-down trace, because the change in intensity happens gradually over several frames and therefore does not produce a large spike in the ΔF-down trace. However, the sudden changes in intensity caused by fusion are significantly larger and faster than the small intensity fluctuations. The ΔF-down stacks are dimensionally compressed into 2D images using a z-projection of the maximum intensity value, in which the brightest values from each pixels time trace is extracted. The resulting image highlights areas that have undergone fast and large intensity decreases. This 2D image effectively represents the spatial locations of fusion sites (Figure 5.9a). This method is

not fully robust, however, because of the larger noise fluctuation in high intensity areas (Figure 5.9b). In addition, every single pixel naturally displays a non-zero value in the z-projection image of the ΔF-down stack, forcing a threshold to be set to visualise the areas of high intensity fluctuations. However, the pixel in the centre of a fusing vesicle always displayed a correlation between the maximum value in the ΔF-down trace and the fusion of a vesicle in the raw intensity trace, whereas those surrounding the centre were not as reliable. Therefore, although this method is not robust, it does seem to successfully reflect the areas where fusion has occurred.

Using the previous discussed Auto-Align plug-in the two representative images of calcium activity and fusion sites can be overlaid to analyse the spatial correlation between these two channels. This is a novel way of spatially representing and comparing the fusion site and the calcium activity in one image. There is direct evidence of a high correlation between the fusion sites and areas of high calcium activity observable in yellow areas in the overlay image (Figure 5.10a). This is in agreement with the general concept that fusion events are triggered by an increase in calcium concentration (Neher 2012). However, the more specific question of how calcium channels are distributed in relation to fusion sites is now addressable through this method. From the images, it can be seen that the centre of the similarly sized fusion site and calcium event are always shifted by about 1-2 pixels (Figure 5.10b). This was further investigated by subjectively drawing a line through the centres of the fusion and the calcium events in the images and plotting the profile of each (Figure 5.11a). The profiles were normalised from 0-1 and fitted with Gaussian curves to extract the centre of each object. Sub-resolution object localisation is valid due to the high signal to noise of the data and the corresponding high quality fits. The distance from the centre of each Gaussian curve were calculated and the average distance between the fusion and calcium events were found to be 93 nm (± 11 SEM, n = 4) (Figure 5.10b). The finding that the centre of the fusion site and the centre of the source of calcium are within a distance of 100 nm is unique to high quality spatial imaging presented here and strongly suggests a spatially controlled fusion environment at the plasma membrane.

The width (full width half maximum) of the Gaussian fit for the fusion event was averaged out as 342 nm (± 36 SEM, n = 4). Although the ΔF-down is not a true representative of the vesicle itself but instead of the area of the largest intensity changes in the time domain, effectively the size of fusion, it provides a good approximation to the width of the fusion does reflect the size of a vesicle. The width of the high calcium activity area calculated from the calcium activity map averaged to be 220 nm (± 22 SEM, n = 4). With this being at the limit of optical resolution, the actual

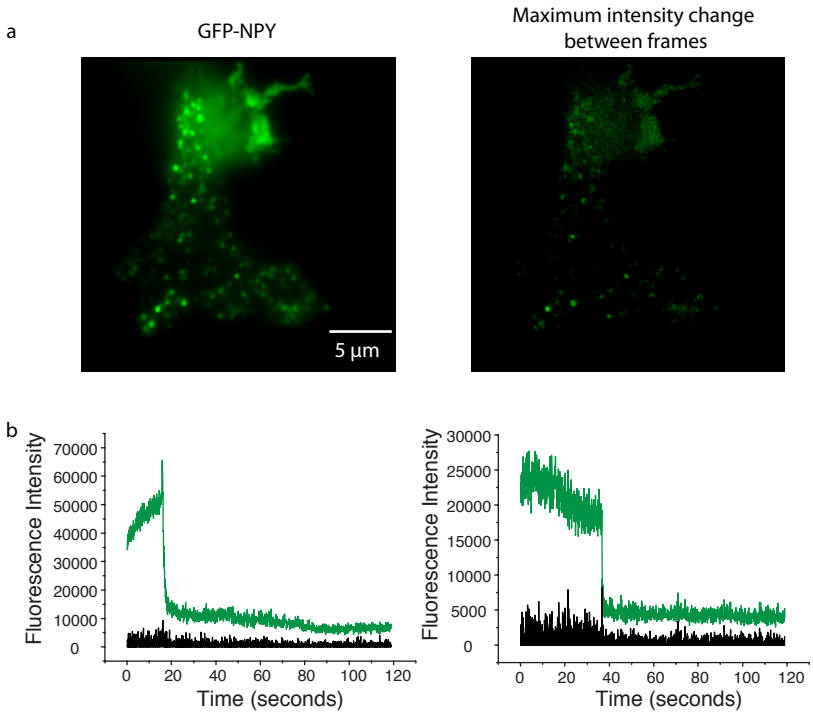

Figure 5.9 **Localising fusion events.** a. Example images of an EGFP-NPY transfected AtT20 d16:16 cell in standard TIRFM mode and of the processed maximum intensity change between frames, ΔF_{down}. b. Representative traces of fusion events (green) (from a single pixel) and the corresponding ΔF_{down} fluorescence intensity trace (black).

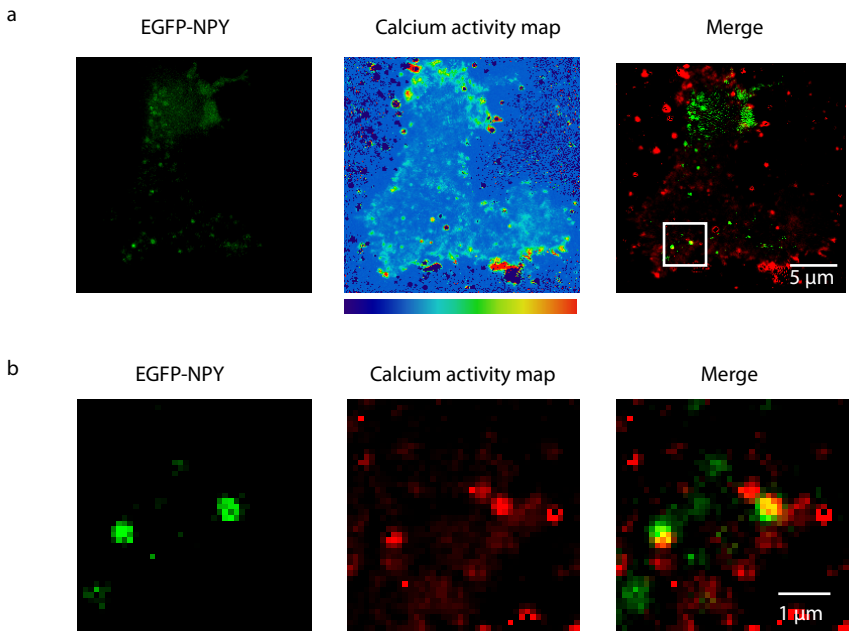

Figure 5.10 **Spatial correlation of fusion and calcium events.** a. Images of the same AtT20 D16:16 cell showing the maximum projection of ΔF_{down} and of the calcium activity map represented, through the standard deviation of the autocorrelation of each pixel in the original calcium image traces. The right image shows a merge of the two, the calcium activity map was converted to red for easier visualisation in the merged image. b. Same plots as (a) but showing the ROI from the highlighted region in (a).

size of the event cannot be calculated. However, the radius of the calcium activity area of maximally 110 nm strengthens the finding that the source of calcium must be within a distance of 100 nm from the centre of the docked vesicle to trigger the fusion. This has never been imaged before in such high spatial and temporal resolution. Simultaneous dual-colour imaging has a huge potential to further understand the implication of calcium within the mechanism of exocytosis.

5.3.4 Conclusions from Simultaneous Imaging of Ion Channel Activity and Vesicle Dynamics

The dual-colour image splitter, has been shown to allow capturing of unprecedented high temporally and spatially resolved images of calcium and associated fusion events. Using this technology, calcium events were detected immediately prior and sometimes after fusion. This reveals several conclusions about the spatial localisation and movement of the calcium channels. First, the detection of pre-fusion calcium events at fusion sites suggests close proximity of calcium channels to fusion events. This has been previously imaged at lower temporal resolution (Becherer et al. 2003). However, the overarching question concerns the location and lateral movement of calcium channels for which high spatial and temporal resolution imaging is necessary. This is inherently linked to the question of whether or not calcium channels are anchored at the plasma membrane though cellular scaffolding, the cytoplasmic matrix. There are two working models of vesicle fusion itself, which need to be considered before drawing conclusions about the precise spatial movement of calcium channels. The first is a full fusion of the vesicle, during which the vesicle membrane becomes fully incorporating into the plasma membrane (Jahn et al. 2003). This would lead to spatial dispersion and remodelling of plasma membrane proteins at the fusion site, presumably including the calcium channels. The second model was coined 'kiss-and-run' fusion, and describes a fusion where a fusion pore is opened through the interaction of SNARE proteins to release the vesicular cargo, but closes again and the vesicle structure remains intact (Jaiswal et al. 2009). This would have a reduced impact on the spatial arrangement of plasma membrane proteins. Before drawing conclusions, it is important to consider a further aspect of calcium activity, endocytosis, which is suggested by the post-fusion calcium events detected in the dual-colour traces. Exocytosis and endocytosis are thought to be tightly linked and it has been shown that exocytosis is followed by endocytosis within seconds of fusion (Thomas et al. 1994). It is also thought that endocytosis is initiated though an increased calcium concentration (Hallermann 2014).

a

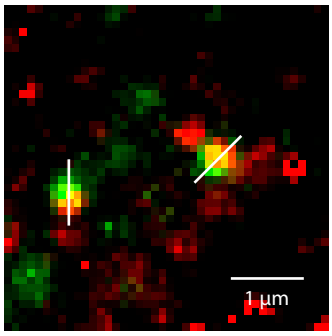

b

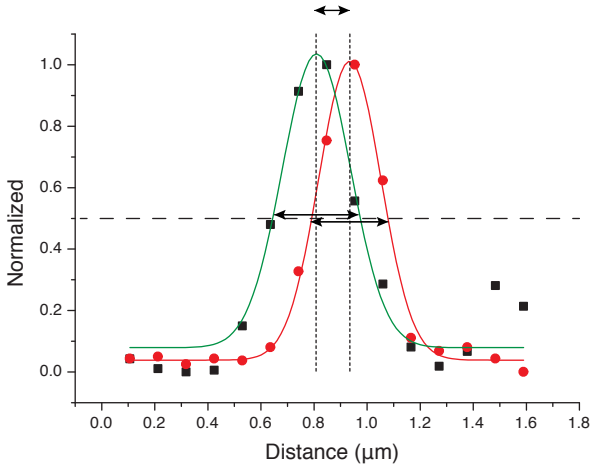

Figure 5.11 **Distance between the calcium and fusion event.** a. Merge image of ΔF_{down} (green) and calcium activity (red) shown in Figure 5.10. For distance analysis, lines were manually drawn through the centre of the fusion and calcium events as shown. b. The intensity profile of the fusion and calcium events were fitted with a Gaussian curve. The average distance between Gaussian peaks was 93 nm (± 11 SEM, n = 4). The average size for the fusion event was 342 (± 36 SEM, n = 4) and 220 (± 22 SEM, n = 4).

Assuming that calcium channel openings are tightly controlled by the cellular environment, it is unlikely that the channels will open again after fusion withoutspecifically targeting a certain process. However, having captured the post-fusion event, this may suggest that a second calcium event initiates the endocytotic process. Furthermore, the post-fusion calcium event within the same pixel of the pre-fusion calcium event suggests a minimal lateral movement of calcium channels that strengthens the hypothesis that calcium channels are spatially anchored through the cytoplasmic matrix. Taking into account the two models of fusion events, full fusion and kiss-and-run, the observation of a second, post-fusion calcium event within the same pixel favours the kiss-and-run fusion model. This speculation would however have to be backed up with further experimental evidence.

There are several scenarios of possible arrangements for calcium channels in relation to docked vesicles. First, calcium channels could be evenly distributed across the plasma membrane and several calcium channels around the fusion site could contribute to a single fusion event. Second, a single calcium channel in very close proximity of the docked vesicle may suffice to trigger one fusion event. Third, a cluster of calcium channels is speculated to generate a calcium microdomain, which can trigger fusion from a greater distance.

To support the first theory, the expected finding on the images would be a larger diameter calcium activity area around the fusion site. However, the images show that the similarly sized fusion and calcium events are slightly shifted, which suggests that calcium enters into the cytoplasm from one point and not several points around the docked vesicle. The second and third theories are harder to distinguish due to the sub diffraction limited size of the calcium event. However, the fact that the two signals do not perfectly overlap indicates that the vesicle does not physically dock directly to a calcium channel, but to nearby SNARE proteins. Considering the size of the vesicle (around 300-400 nm) and the distance of under 100 nm from the fusion pore to the centre of calcium event, the calcium channels must be located underneath the vesicle. The influx of calcium ions may be restricted in terms of space and therefore slower to diffuse, which may mean that this molecular arrangement may increase the likelihood of the fusion event. Further mathematical modelling of the calcium influx through voltage-gated calcium channels and the restricted spatial diffusion would complement this hypothesis.

5.4 Conclusion

Calcium ion flux across the plasma membrane is part of a complex process and by nature extremely difficult to image. Several different techniques were applied to understand the common aim of how the spatial and temporal behaviour of voltage-gated calcium channels on the plasma membrane behave at a fusion site and how calcium influx triggers the fusion event. This chapter focused on combining an electrophysiology system with a high-resolution microscope and using a dual-colour image splitter to maximally push the temporal resolution in order to visualise the extremely fast sequence of calcium triggering of the fusion event.

The optical patching experiments have proved successful for calcium imaging at the plasma membrane. The spatial resolution was considerably enhanced by replacing the soluble Fluo-4 with transfected R-GECO-SNAP25, which gives a less blurry and sharper image at the plasma membrane when opening VGCCs through depolarisation. The depolarisation actively opened the VGCCs and the calcium was visualised in TIRFM though the membrane targeted R-GECO-SNAP25 calcium indicator.

The dual-colour imaging has allowed for unprecedented spatial and temporal analysis of calcium and fusion events by simultaneous acquisition. The calcium event necessary for triggering was found to be within a distance of 100 nm from the centre of the fusion event.

Separately, the optical patching using R-GECO-SNAP25 as the calcium indicator and the simultaneous dual-colour image acquisition both proved successful techniques for the purpose of understanding the role of VGCCs within the process of exocytosis. A project for future work would be to combine optical patching and dual-colour imaging. This would give voltage control over the opening of calcium channels, whilst spatially determining the calcium flux and fusion of vesicles through simultaneous imaging. Furthermore, the addition of drugs as demonstrated in section 4.4.2, whether VGCC agonists or antagonists, may reveal the sub-types of VGCCs that are implicated in the triggering of exocytosis.

Considering the complexity and difficulty of each of these techniques on their own, a project combining all these together would be hugely ambitious. However, it may prove immensely beneficial in understanding the spatial and temporal behaviour of voltage-gated calcium channels involved in exocytosis.

References

Becherer, U. et al., 2003. Calcium regulates exocytosis at the level of single vesicles. *Nature Neuroscience*, 6(8), pp.846–53.

Becherer, U. & Rettig, J., 2006. Vesicle pools, docking, priming, and release. *Cell and Tissue Research*, 326(2), pp.393–407.

Brunger, A.T., 2000. Structural insights into the molecular mechanism of Ca(2+)-dependent exocytosis. *Current Opinion in Neurobiology*, 10, pp.293–302.

Demuro, A. & Parker, I., 2004. Imaging the activity and localization of single voltage-gated Ca 2+ channels by total internal reflection fluorescence microscopy. *Biophysical Journal*, 86(5), pp.3250–3259.

Demuro, A. & Parker, I., 2003. Optical single-channel recording: imaging Ca2+ flux through individual N-type voltage-gated channels expressed in Xenopus oocytes. *Cell Calcium*, 34, pp.499–509.

Gundelfinger, E.D., Kessels, M.M. & Qualmann, B., 2003. Temporal and spatial coordination of exocytosis and endocytosis. *Nature Reviews. Molecular Cell Biology*, 4(2), pp.127–39.

Hallermann, S., 2014. Calcium channels for endocytosis. *Journal of Physiology*, 15, pp.3343–4.

Jahn, R., Lang, T. & Südhof, T.C., 2003. Membrane Fusion. *Cell*, 112, pp.519–533.

Jaiswal, J.K., Rivera, V.M. & Simon, S.M., 2009. Exocytosis of post-Golgi vesicles is regulated by components of the endocytic machinery. *Cell*, 137(7), pp.1308–19.

Khanna, R. et al., 2007. The presynaptic CaV2 . 2 channel – transmitter release site core complex. *Neuroscience*, 26(May), pp.547–559.

Neher, E., 2012. Introduction : Regulated exocytosis. *Cell Calcium*, 52(3-4), pp.196–198.

Parker, I. & Smith, I.F., 2010. Recording single-channel activity of inositol trisphosphate receptors in intact cells with a microscope , not a patch clamp. *The Journal of General Physiology*, 136(2), pp.119–127.

Pitkeathly, W.T.E. et al., 2012. Auto-align - multi-modality fluorescence microscopy image co-registration. *Traffic*, 13, pp.204–17.

Shuai, J. & Parker, I., 2005. Optical single-channel recording by imaging Ca 2 + flux through individual ion channels : theoretical considerations and limits to resolution. *Cell Calcium*, 37, pp.283–299.

Smith, S.M. et al., 2012. Calcium regulation of spontaneous and asynchronous neurotransmitter release. *Cell Calcium*, 52(3-4), pp.226–233.

Thomas, E. et al., 1994. A triggered mechanism retrieves membrane in seconds after Ca2+-stimulated exocytosis in single pituitary cells. *The Journal of Cell Biology*, 124(5), pp.667–675.

Wang, S. et al., 2001. Ca 2 + signalling between single L-type Ca 2 + channels and ryanodine receptors in heart cells. *Nature*, 410, pp.592–956.

Wiltgen, S.M., Smith, I.F. & Parker, I., 2010. Superresolution localization of single functional IP 3 R channels utilizing Ca 2+ flux as a readout. *Biophysical Journal*, 99, pp.437–446.

Chapter 6 Discussion and Future Work

Calcium ions are the initiators of the vesicle fusion pathway and thereby a vital player in the sequence of events that are encompassed in exocytosis. It is the depolarisation of the membrane that initiates the opening of voltage-gated calcium channels embedded in the plasma membrane. Even though extensive work has been done to try and understand in detail the role of calcium in exocytosis, the majority of approaches were biochemical techniques. Unfortunately, these approaches often disassemble the process into individual components, and consequently the spatial and functional details of the endogenous proteins are lost. In this thesis, high and super-resolution optical imaging was successfully employed to interpret the spatial and functional behaviour of voltage-gated calcium channels in living cells, and relate these findings in particular to exocytosis. Together, the novel tools developed here provide a strong foundation for the future of calcium imaging and can be widely applied.

6.1 Summary of Major Experiments and Findings

The work in this thesis was driven by both the demand for the development of imaging techniques and analysis and the challenge of uncovering and understanding the spatial and functional distribution of calcium channels regulating exocytosis. In light of this, the first aim was to understand the spatial distribution of $Ca_v2.2$ calcium channels in relation to exocytosis. To begin, with this was done by co-localisation and FLIM-FRET measurements of the fluorescent fusion-$Ca_v2.2$ calcium channels and labelled syntaxin1a. Furthermore, a novel conception of a $Ca_v2.2$ calcium channel specific staining method was investigated and developed for single molecule imaging by using ω-conotoxin GVIA – Cage552. The second aim was to perform high resolution calcium detection at the plasma membrane by using R-GECO-SNAP25 and to establish a novel method of extracting the temporal information and projecting them in a 2D spatial map. The third aim was to advance the understanding of the spatial configuration of calcium and fusion by combining electrophysiology and several advanced microscopy techniques.

Advances in biology are often made in conjunction with advances in technology. In this thesis, the challenges set by the biological questions, whether those of single molecule imaging or those working towards rapid real time calcium event imaging, required simultaneous advances in methodology, analysis and technology and this proved to be successful, delivering a suite of new tools that can, with only modest further refinement, now be used in new biological discovery programmes.

6.1.1 Spatial Interaction with Syntaxin1a and Spatial Distribution of $Ca_v2.2$ Calcium Channels

To date not much is understood about the spatial distribution of $Ca_v2.2$ calcium channels in relation to the exocytotic machinery, in particular the fusion site. What is clear is that $Ca_v2.2$ calcium channels display a syntaxin1a specific binding site, the synprint site, and that these two proteins interact (Sheng et al. 1994). However, it is not well understood what the implication of this interaction site has for the spatial arrangement of the $Ca_v2.2$ calcium channels at the plasma membrane and this lack of information hinders the ability to construct a complete picture of the exact role of calcium in exocytosis.

In this thesis super-resolution imaging techniques were employed to reveal the spatial interaction of $Ca_v2.2$ calcium channels and syntaxin1a. A novel biological $Ca_v2.2$ calcium channel staining method was also developed that allows for the locations of the endogenous $Ca_v2.2$ calcium channels in relation to vesicles to be established with nanometre accuracy.

The sub-resolution imaging was achieved using a full length and a splice variant of $Ca_v2.2$ calcium channels, genetically engineered to be inserted into a fluorescent protein-encoding cDNA plasmid. The interaction of transfected $Ca_v2.2$ calcium channels, expressed with either the GFP-α_{1B}-subunit or GFP-α_{1B}-subunit(Δ18a), and syntaxin1a, immunostained with HPC-1 and alexa568, was confirmed via FLIM-FRET, after preliminary co-localisation and spectral scanning confirmed the likelihood of the interaction (Chapter 3). The positive FRET interaction, observed through a notable 50% decrease in the lifetime of 10% of the EGFP donor molecules, confirmed, for the first time, that the synprint site is necessary for the spatial interaction of the $Ca_v2.2$ calcium channel and syntaxin1a at the plasma membrane. This is the first direct demonstration of this interaction in intact secretory cells.

In addition, a novel method for $Ca_v2.2$ calcium channel detection with single molecule sensitivity was developed that uses ω-conotoxin GVIA with a single conjugated Cage552 dye. Compared to immunostaining, this method offers high specificity, a 1:1 stoichiometry of the toxin to the dye, and single activation photo-uncaging events, giving high confidence in the rendered image of the single molecule localisations. This novel staining method was used to establish the $Ca_v2.2$ calcium channel molecular distribution at the plasma membrane (Chapter 3). In the rendered images, little or no clustering is suggested by the distribution of localised $Ca_v2.2$ calcium channels, but instead the molecules appear to be sparsely distributed. Another observation is that, although many individual channels appeared within close proximity to docking sites, these channels were not found to be directly beneath the centre of vesicles, but they were within functionally relevant distances for exocytosis triggering.

6.1.2 Technical Advances in Calcium Imaging

Visualizing dynamic calcium activity in living cells is challenging due to the extremely rapid nature of the ion transport. Furthermore, the calcium ions cannot be directly labelled, and to date the established approach has been through the use of binding activated fluorescent calcium indicators, which freely diffuse within the cytoplasm of the cell, blurring the image and reducing spatial and temporal resolution. In chapter 4, a novel genetically encoded calcium indicator (GECI) was used to target the calcium

indicator to the inner leaflet of the plasma membrane. This R-GECO1-SNAP25 construct was highly specific, minimised diffusion and was further significantly improved by combining with high-speed TIRFM imaging. The result was sharper and more detailed images of calcium activity at the plasma membrane, and compared to previous calcium imaging, seemed the most convincing demonstration of single calcium channel activity in living cells.

Once such unparalleled imaging of calcium activity was established the challenge moved onto creating a full spatial map of temporal calcium activity without the subjective and partial isolation of specific events. A novel method was developed that, for each pixel of the original time dependent image stack, calculated the standard deviation of the temporal autocorrelation of the independently bleach corrected time traces. The result was a 2D image that accurately and non-subjectively reflects the degree of dynamic behaviour across the cell and with a high sensitivity to fast and weak temporal events. Compared to the established method of applying ratiometric $\Delta F/F_0$ analysis on select time traces within a larger image, the autocorrelation temporal map showed the spatial distribution of the whole cell calcium activity.

In addition to revealing optically the effect of pharmacological agents on perturbing ionic activity, the autocorrelation maps show a clear high and low density of dynamic calcium activity. This spatial diversity in the dynamic behaviour is only revealed through a combination of the novel labelling and analysis strategy.

6.1.3 Calcium Imaging at the Site of Exocytosis

In chapter 5, the focus was to observe the spatial and temporal role of calcium in relation to the triggering of exocytosis. This was done by electrically and physiologically manipulating the intracellular environment using two distinct methods. First, optical patching was performed to investigate the spatial cellular response of voltage-gated calcium channel activity elicited by plasma membrane voltage potential manipulation. The results indicated improved imaging of calcium activity over commonly used current techniques such as cell permeant dyes including Fluo4. Second, calcium activity and fusion events were imaged simultaneously by using a dual-colour image splitter. This revealed that the spatial arrangement of active calcium channels are not directly at the centre of the fusion event, but instead are located around 100 nm away from the fusion pore. This integration of electrophysiology with new probes, new high-speed imaging, new detectors, new optical setups that permit simultaneous dual-channel imaging and new analytical techniques have thus delivered a basis for directly determining the spatial and temporal arrangement of the secretory machinery.

6.2 The Spatial Role of Calcium Channels in Exocytosis

Two rather opposing theories exist about the origin of the calcium trigger for exocytosis. First, biochemical data show that $Ca_v2.2$ calcium channels interact with SNARE proteins, suggesting close proximity to fusion sites (Sheng et al. 1998). Secondly, it has been suggested that calcium cannels act in unison across large areas on the plasma membrane to elicit fusion (Wu et al. 2009). Regarding the first theory that calcium channels interact with SNARE proteins, extensive *in vitro* biochemistry work has inferred close physical interaction between the $Ca_v2.2$ calcium channel and the SNARE protein syntaxin1a (Sheng et al. 1994). This is also the case for the SM protein Munc18. However, as these experiments are performed *in vitro*, there is no indication or information about the spatial relationship between the $Ca_v2.2$ calcium channels and the SNARE and SM proteins, nor any information on their spatial correlation to fusion sites. However, the information gained from the biochemical experiments suggested that $Ca_v2.2$ calcium channels create a platform for the assembly of the SNARE complex (Keith et al. 2007) and for the docking of vesicles through a Munc18-synaptotagmin bridge (Chan et al. 2007; de Wit 2010). The indication of the $Ca_v2.2$ calcium channel being an anchor for the assembly for fusion points towards the existence of highly organised and dedicated fusion sites. The FLIM-FRET data in chapter 3 that suggest that only about 10% of the $Ca_v2.2$ calcium channel molecular pool is actively involved in syntaxin1a interaction is directly related to this argument. This small percentage implies that the majority of $Ca_v2.2$ calcium channels are not implicated directly in the organisation of fusion sites and, through this disconnection, may therefore not contribute to the triggering of the fusion. This is an important discovery as it suggests a large redundancy of calcium channels, at least in relation to exocytosis. The single molecule resolution images in the same chapter supports this hypothesis, indicating that $Ca_v2.2$ calcium channels were rarely directly underneath a vesicle. This is consistent with the finding that vesicles preferentially localise to low density areas of SNAP25 (Yang et al. 2012). This suggests that only few isolated $Ca_v2.2$ calcium channels and SNARE proteins contribute to the anchoring of the fusion site. Together, this points towards a well-defined arrangement of proteins at the fusion site where possibly only one $Ca_v2.2$ calcium channel provides a platform for vesicle docking and fusion. Both the spatial disconnection of the majority of $Ca_v2.2$ calcium channels and the close proximity of only few single $Ca_v2.2$ calcium channels to the site of fusion suggests that the triggering of fusion may originate from only one single tightly coupled $Ca_v2.2$ calcium channel.

The hypothesis outlined above has been established through the visualised arrangement of $Ca_v2.2$ calcium channels. However, it may be further strengthened by additional functional calcium imaging to reveal the true calcium behaviour at the plasma membrane. In the plasma membrane of the pituitary cell line AtT20 D16:16 several voltage-gated channel types are expressed (Hodson et al. 2012) and therefore differentiation of each type by calcium imaging alone is challenging and not yet established. The calcium activity map from chapter 4 showed a range of spatial activity, varying from few high activity areas of about 1 µm in size to many smaller diameter and punctate areas with low activity. This may relate to the type of voltage gated calcium channel, where the high activity may be a reflection of a large calcium influx of, for example $Ca_v2.1$ calcium channels, and the small activity areas may be due to short calcium openings arising from $Ca_v2.2$ calcium channels. This high, diverse variability in the degree of calcium activity across the plasma membrane may also be related to the spatial configuration of where vesicles dock and fuse. Previous work using calcium imaging showed large 1 – 2 µm calcium events from which it was concluded that calcium events originate from clusters of calcium channels (Neher & Sakaba 2008). However, this was not directly linked to exocytosis and it remains viable that these high activity areas may even fulfil a different role unrelated to exocytosis. Wu, in 2009, directly addressed calcium activity with exocytosis and concluded that VGCCs co-operate over a distance of micrometres creating a dominant calcium signal rather than a single microdomain from a cluster of calcium channels (Wu et al. 2009). This is in conflict with the result of the autocorrelation map, where calcium activity areas are punctate and spatially defined. Instead, the finding through the correlation of the calcium activity map and fusion points towards single channel triggering, which is consistent with the Chapter 3 result that suggests the close proximity of the calcium event to the fusion event. The finding in Chapter 5, that the average diameter of the calcium event at the fusion site is around 220 nm, which is at the limit of resolution, supports the hypothesis that only one single voltage-gated calcium channel is sufficient to trigger fusion.

The results in this thesis specifically the single molecule imaging in Chapter 3 and the dynamic mapping in Chapter 4, support the theory that a close proximity of the calcium channels and fusion site are required for exocytosis. The results indicate that very few $Ca_v2.2$ calcium channels act as a platform for fusion sites and that it is most likely only these channels that contribute to the triggering of fusion.

6.3 Future work

The work in this thesis has established an array of technical advances and novel techniques developed for the purpose of the spatial and functional calcium channel imaging. Consequently, there is significant potential to apply these techniques to further experiments and biological questions.

The application of ω-conotoxin GVIA – Cage552 as a staining method for $Ca_V2.2$ calcium channels, an alternative to immunostaining, is a novel idea and the proof-of-principle that was demonstrated in Chapter 3 is encouraging to further pursue the application of this unique method. Taken forward this detection method may provide hitherto untapped information about endogenous $Ca_V2.2$ calcium channels in relation to other proteins involved in exocytosis. Further work, such as testing different blocking strategies, would enhance the reliable imaging of ω-conotoxin GVIA – Cage552 by improving the blocking of unspecific binding. Once the staining method is sufficiently robust, the distribution of single molecules at the plasma membrane can be explored further, for example by using Ripley's Kfunction. This describes the pattern of localised points by analysis of the distance of points from each single point. By doing so, it can be determined whether the molecules are in a clustered conformation, or whether they are randomly distributed. Furthermore, the distribution of single calcium channel molecules can be related to vesicles. Here, both the molecules and the vesicles are simultaneously localised, and nearest-neighbour analysis can be conducted which measures the distance from each vesicle to all the molecules in close proximity and thereby determines the distribution of distances of molecules to the vesicle. An ambitious project would be to create a library of toxins against various ion channels labelled with different dyes. This would open up to numerous experiments requiring single molecule localisation of ion channels.

A solid foundation was laid with the development of the novel image processing to extract the temporal dynamics of calcium activity and display this in a 2D map. Through the standard deviation of the autocorrelation of fluorescence at each pixel, the calcium activity is reflected in the spatial map. To build on this, the map could be weighted by the number of events at each pixel, as was discussed in detail in chapter 4 with the use of a damped sine function fit. Since larger events outweigh shorter events in the STD map, a weighting by the number of events would improve the representation map of activity. However, this is an ambitious task, made more challenging by the nature of the traces and the noise levels when running at the limit of acquisition speeds.

Together, optical patching and simultaneous calcium and vesicle imaging techniques show great potential to further understand the spatial and temporal relationship

between VGCCs and fusion. Several future experiments could further enhance this understanding. First, optical patching could be used to investigate the characteristics of the spatial distribution of calcium activity. Relating the total current measured through the electrophysiology device to the overall area of calcium activity may reveal the spatial arrangement of calcium channels on the plasma membrane and help confirm if calcium events arise from single active channel, or from channel clusters. Furthermore, the spatial distribution of different VGCCs families may be dissected through applying and depolarising from different holding potentials. For example, $Ca_v2.1$ calcium channels respond better from a holding potential of -60 mV rather than the -80 mV of $Ca_v2.2$ channels. Following on from this, different drugs, whether agonists or antagonists, could be used to block or enhance calcium response. Together, these suggestions address the spatial distribution of different families of calcium channels. Second, the dual-colour imaging of calcium activity and vesicle movement and fusion can be further enhanced by increasing the temporal resolution. Initially, this can be done by using the sCMOS camera, which allows a frame rate as fast as 100 Hz (10 ms / frame). However next generation single photon avalanche diode array cameras, which have MHz frame rates with single photon sensitivity, may provide an idealised camera to explore calcium activity. As a first instance example, a FCS type single point measurement that uses a sole single photon detector could demonstrate the principle on select points across the cell. Considering the opening kinetics of VGCCs, which range from just a few milliseconds up to 100 ms, the extremely fast frame rate of such a camera, in addition to the simultaneous dual-colour imaging would reach the optimal sampling rate. Third, optical patching and simultaneous dual-colour imaging could be combined for calcium and vesicle imaging in a very ambitious and technically difficult experiment. However, the ability to electrically manipulate the cell membrane and thereby selectively, through choosing different holding potentials, open only certain VGCCs may reveal which channel types are involved in exocytosis, and also to what extent. Although this is extremely ambitious, it may further reveal the spatial behaviour of VGCCs in relation to fusion.

6.4 Final Conclusions

The aims in this thesis were to image the spatial and functional distribution of single voltage-gated calcium channels involved in exocytosis. Achieving these goals required the design of novel staining methods, analysis approach and imaging techniques. With these new methods established, a unique foundation has been laid to further expand on

and apply these to a variety of applications across ion transport and exocytosis. The ω-conotoxin GVIA – Cage552 approach for single molecule labelling is unique and novel and it's impact for significant improved imaging has been clearly demonstrated in this thesis. In addition, the analysis strategy of applying a pixel-by-pixel bleach correction and autocorrelation to extract the activity level at each pixel has very high potential. It is an intensity independent approach that fundamentally differs from all current calcium image processing, to create a 2D map of the calcium activity allowing spatial analysis of the functional calcium channels. The combination of the optical patching with R-GECO1-SNAP25 suggested improved imaging of calcium activity over the use of Fluo4. The application of TIRFM imaging and simultaneous dual-colour imaging was implemented due to the lack of temporally adequate traditional imaging strategies. By using this technique for R-GECO1-SNAP25 and EGFP-NPY imaging, this is to date the most temporally precise approach to image calcium and fusion.

In summary, the work in this thesis has established new integrative methods and techniques that allowed improved imaging of the spatial and functional dynamics of calcium channels in relation to fusion. Only with the improvement of single molecule imaging, calcium imaging and analysis, was it possible to create the hypothesis about the tightly coupled spatial relationship between voltage-gated calcium channels and fusion events. This demonstrates that, to establish new insights into biology the existing challenges need to be approached by developing methods, analysis and technology.

References

Chan, A.W. et al., 2007. Munc18: A presynaptic transmitter release site N type (Cav2.2) calcium channel interacting protein. *Channels*, 1(1), pp.11–20.

Hodson, D.J. et al., 2012. Coordination of calcium signals by pituitary endocrine cells in situ. *Cell Calcium*, 51, pp.222–230.

Keith, R.K. et al., 2007. Bidirectional modulation of transmitter release by calcium channel / syntaxin interactions in vivo. *The Journal of Neuroscience*, 27(2), pp.265–269.

Neher, E. & Sakaba, T., 2008. Multiple roles of calcium ions in the regulation of neurotransmitter release. *Neuron*, 59(6), pp.861–72.

Sheng, Z., Rettig, J. & Takahashi, M., 1994. Identification of a syntaxin-bindingsSite on N-type calcium channels. *Cell*, 13, pp.1303–1313.

Sheng, Z., Westenbroek, R.E. & Catterall, W.A., 1998. Physical link and functional coupling of presynaptic calcium channels and the synaptic vesicle Docking / fusion machinery. *Journal Of Bioenergetics and Biomembranes*, 30(4), pp.335–345.

De Wit, H., 2010. Morphological docking of secretory vesicles. *Histochemistry and Cell Biology*, 134, pp.103–13.

Wu, M.M., Llobet, A. & Lagnado, L., 2009. Loose coupling between calcium channels and sites of exocytosis in chromaffin cells. *The Journal of Physiology*, 22, pp.5377–5391.

Yang, L. et al., 2012. Secretory vesicles are preferentially targeted to areas of low molecular SNARE density. *PloS one*, 7(11), p.e49514.